INFORMATION TO USERS

This manuscript has been reproduced from the microfilm master. UMI films the text directly from the original or copy submitted. Thus, some thesis and dissertation copies are in typewriter face, while others may be from any type of computer printer.

The quality of this reproduction is dependent upon the quality of the copy submitted. Broken or indistinct print, colored or poor quality illustrations and photographs, print bleedthrough, substandard margins, and improper alignment can adversely affect reproduction.

In the unlikely event that the author did not send UMI a complete manuscript and there are missing pages, these will be noted. Also, if unauthorized copyright material had to be removed, a note will indicate the deletion.

Oversize materials (e.g., maps, drawings, charts) are reproduced by sectioning the original, beginning at the upper left-hand corner and continuing from left to right in equal sections with small overlaps.

Photographs included in the original manuscript have been reproduced xerographically in this copy. Higher quality 6" x 9" black and white photographic prints are available for any photographs or illustrations appearing in this copy for an additional charge. Contact UMI directly to order.

Bell & Howell Information and Learning
300 North Zeeb Road, Ann Arbor, MI 48106-1346 USA
800-521-0600

Reproduced with permission of the copyright owner. Further reproduction prohibited without permission.

DISSERTATION

BAROTROPIC INSTABILITY AND ASYMMETRIC MIXING IN HURRICANES WITH PRIMARY AND SECONDARY EYEWALLS

Submitted by

James P. Kossin

Department of Atmospheric Science

In partial fulfillment of the requirements

for the Degree of Doctor of Philosophy

Colorado State University

Fort Collins, Colorado 80523

Spring 2000

Reproduced with permission of the copyright owner. Further reproduction prohibited without permission.

UMI Number: 9981349

UMI®

UMI Microform 9981349
Copyright 2000 by Bell & Howell Information and Learning Company.
All rights reserved. This microform edition is protected against
unauthorized copying under Title 17, United States Code.

Bell & Howell Information and Learning Company
300 North Zeeb Road
P.O. Box 1346
Ann Arbor, MI 48106-1346

Reproduced with permission of the copyright owner. Further reproduction prohibited without permission.

COLORADO STATE UNIVERSITY

4 February 2000

WE HEREBY RECOMMEND THAT THE DISSERTATION PREPARED UNDER OUR SUPERVISION BY JAMES P. KOSSIN ENTITLED BAROTROPIC INSTABILITY AND ASYMMETRIC MIXING IN HURRICANES WITH PRIMARY AND SECONDARY EYEWALLS BE ACCEPTED AS FULFILLING IN PART REQUIREMENTS FOR THE DEGREE OF DOCTOR OF PHILOSOPHY.

Committee on Graduate Work

Michael T. Montgomery

William M. Gray

Gerald D. Taylor

Mark DeMaria

Wayne Schubert

Adviser

S. A. Rutledge

Department Head

Reproduced with permission of the copyright owner. Further reproduction prohibited without permission.

ABSTRACT OF DISSERTATION

BAROTROPIC INSTABILITY AND ASYMMETRIC MIXING IN HURRICANES WITH PRIMARY AND SECONDARY EYEWALLS

Asymmetric vorticity mixing in hurricanes is studied in the context of a nondivergent barotropic framework. The stability of primary and secondary eyewalls is considered through linear analyses and numerical experiments using a pseudospectral model. For the case of unstable primary eyewalls, which are idealized as annular rings of enhanced vorticity embedded in relatively weak vorticity, nonlinear rearrangement occurs in which most of the vorticity initially in the eyewall is transported inward. During this evolution, distinct mesovortices form, orbit the eye, and eventually merge and axisymmetrize near the vortex center. The end state of this type of evolution is an axisymmetric and monotonic vorticity field. Observational evidence of this process occuring in real hurricanes is introduced using aircraft flight-level data.

For the case of hurricanes with secondary eyewalls, which are idealized as annular rings of enhanced vorticity with intense vortices at their center, two types of instabilities are discussed. With the first type (type 1), the instability is realized across the secondary eyewall. The nonlinear mixing associated with type 1 instability results in a broader and weaker secondary eyewall. The end state is axisymmetric and stable,

Reproduced with permission of the copyright owner. Further reproduction prohibited without permission.

but is not monotonic. Secondary wind maxima associated with secondary eyewalls are maintained during this type of mixing.

In the second type (type 2), the instability is realized across the moat between the secondary eyewall and the central vortex. The nonlinear mixing associated with type 2 instability perturbs the central vortex and can result in the formation of a nearly steady tripole-like structure. The formation of a tripole offers an explanation for the observed formation and persistence of elliptical eyewalls in hurricanes.

James P. Kossin
Department of Atmospheric Science
Colorado State University
Fort Collins, Colorado 80523
Spring 2000

Reproduced with permission of the copyright owner. Further reproduction prohibited without permission.

ACKNOWLEDGEMENTS

I would like to thank my advisor, Dr. Wayne Schubert for his mentorship, accessibility, and patience. I can only aspire to achieve his encyclopaedic scope of knowledge. I also wish to thank my committee members, Drs. William Gray, Michael Montgomery, Mark DeMaria, and Gerald Taylor for many helpful discussions and for their great involvement in my work. I have been very fortunate to have such a varied and notable group of scientists in my corner.

Special thanks must go to Ricardo Prieto, Rick Taft, Scott Hausman, Paul Reasor, John Knaff, Vince Larson, Hung-Chi Kuo, Mel Nicholls, Scott Fulton, Lloyd Shapiro, Dominique Möller, and David Nolan who have improved this work in a variety of ways. Hugh Willoughby, Frank Marks, Peter Dodge, and Peter Black have also advanced my work through many helpful discussions.

I would especially like to thank Matthew Eastin for his great contribution to chapter 4 of this study.

I am grateful to Hugh Willoughby, Chris Landsea, and Ed Rahn of the Hurricane Research Division for their efforts in making the flight-level data, used in chapter 4, available.

This work was supported by NSF Grant ATM-9729970 and by NOAA Grant NA67RJ0152 (Amendment 19).

Reproduced with permission of the copyright owner. Further reproduction prohibited without permission.

TABLE OF CONTENTS

Reproduced with permission of the copyright owner. Further reproduction prohibited without permission.

Reproduced with permission of the copyright owner. Further reproduction prohibited without permission.

LIST OF FIGURES

Reproduced with permission of the copyright owner. Further reproduction prohibited without permission.

Reproduced with permission of the copyright owner. Further reproduction prohibited without permission.

Reproduced with permission of the copyright owner. Further reproduction prohibited without permission.

Reproduced with permission of the copyright owner. Further reproduction prohibited without permission.

Reproduced with permission of the copyright owner. Further reproduction prohibited without permission.

Reproduced with permission of the copyright owner. Further reproduction prohibited without permission.

Reproduced with permission of the copyright owner. Further reproduction prohibited without permission.

LIST OF TABLES

Reproduced with permission of the copyright owner. Further reproduction prohibited without permission.

Chapter 1

INTRODUCTION

> I am an old man now, and when I die and go to Heaven there are two matters on which I hope for enlightenment. One is quantum electrodynamics, and the other is the turbulent motion of fluids. About the former I am rather optimistic. *Horace Lamb* to the British Association for the Advancement of Science

> It is only when we use systematically imperfect equations or initial conditions that we can begin to gain further understanding of the phenomena which we observe. *Edward Lorenz*

The inner core of a hurricane is a region of intense convection and strong winds. The convection typically consists of cells or "hot towers" (Malkus 1958; Riehl and Malkus 1961), on the order of a few kilometers in diameter, which are organized into an annulus known as the eyewall. The strongest winds are typically found in the eyewall, where potential vorticity (PV) production by the diabatic effects of deep convection is generally large. In strong hurricanes, the eyewall is typically flanked on both sides by regions of subsidence and clear air or stratiform clouds. At the center of the hurricane and within the eyewall is found the eye while the clear or stratiform region outside of the eyewall is referred to as the moat. Warming associated with upper and mid-level subsidence within the eye results in baroclinity, and thermal balance requires that updrafts within the eyewall slope outward with height as they approximately conserve angular momentum. Meanwhile, the inner core is embedded in the larger environment of the hurricane outer core[1]. The extent of the outer core varies but

[1]Here we define the outer core as the region outside a radius of 1° latitude or 111 km.

Reproduced with permission of the copyright owner. Further reproduction prohibited without permission.

is generally a few hundred kilometers in radius. In intense hurricanes, cyclonic flow and inflowing radial wind can be found at distances greater than 1000 km from the center (Frank 1977; Gray 1979). The theory of Conditional Instability of the Second Kind, or CISK (Charney and Eliassen 1964; Ooyama 1964), poses a link between the outer and inner cores. Convective scale motions in the inner core create a horizontal gradient of latent heat release which then acts to drive the large scale inflow. The inflow then imports moist energy from the outer to the inner core which increases the latent heat release and further intensifies the large scale circulation, and so on. Thus hurricane flows are largely three-dimensional and non-conservative, and the dynamics occur on a broad range of physically unseparable scales from synoptic ($\sim 10^3$ km) to convective ($\sim 10^0$ km). Numerical modeling of such flows is a formidable task.

A widely applied simplification is the assumption of axisymmetry which, given the apparently near-circular nature of hurricanes, is a natural choice. The evolution of axisymmetric models may arguably be traced to the work of Eliassen (1952) after which a large number of numerical studies have applied axisymmetric models to hurricanes. Axisymmetric models effectively couple the primary (azimuthal) and secondary (radial and vertical) circulations through parametrization of diabatic and frictional processes and have been successful in replicating a number of the observed features of the hurricane flow field. The parametrization of the collective effects of convective clouds generally involves some type of statistical treatment of the small-scale convective eddies. One complication of this type of parametrization lies in the fact that in addition to serving as a transport mechanism, the convective eddies also introduce energy to the system. Using a simple axisymmetric balance model, Emanuel (1997) argued that the inclusion of such parameterized diabatic energy production leads to frontogenesis near the inner edge of the eyewall and ultimate eyewall collapse, i.e., the local vorticity approaches a vortex sheet. Rotunno and Emanuel (1987) and Emanuel (1997) further note that to combat the formation of such discontinuities, axisymmetric models must incorporate some type of diffusion as a parameterization

Reproduced with permission of the copyright owner. Further reproduction prohibited without permission.

of subgrid scale mixing processes. The amount of diffusion applied varies, but if large, it can spin down an unforced vortex in an unrealistically short time. This is especially problematic in small vortices such as those which might be chosen to describe an intense hurricane. A more detailed examination of this issue is made in chapter 5 which considers the diffusive evolution of a barotropically unstable flow, described by an annular ring of enhanced vorticity confined to an axisymmetric framework.

Consideration of *asymmetries* in the flow fields of hurricanes has previously been motivated by questions regarding hurricane motion (e.g., Shapiro and Franklin 1999, and references therein), formation (e.g., Challa and Pfeffer 1992; Montgomery and Farrell 1993) and intensification (e.g., Molinari, et al. 1998, and references therein). The present work can be considered as part of a recent trend of studies which consider the significance of asymmetric horizontal advective processes in the inner core evolution of hurricane-like vortices. Much of the pertinent dynamics of such flows can be understood in the context of vortex Rossby waves and asymmetric PV rearrangement in a nondivergent framework. Guinn and Schubert (1993), and Montgomery and Kallenbach (1997), elaborating on earlier work by MacDonald (1968), found that spiral bands can be well explained solely in terms of nondivergent vortex Rossby wave theory. Schubert et al. (1999) and Reasor et al. (1999) proposed instability of an annular ring of elevated vorticity as a source for polygonal and elliptical eyewalls respectively. Montgomery and Enagonio (1998) proposed vortex merger and axisymmetrization as a key mechanism in the transformation of a mid-level vortex to a deep layer warm core vortex, an important event in tropical cyclogenesis. Vortex intensification by the mechanism of convectively forced vortex Rossby waves was proposed by Montgomery and Kallenbach (1997) and recently extended by Möller and Montgomery (1999).

Here, we consider the unforced evolution of unstable primary and secondary eyewalls in hurricanes. We abandon the assumption of axisymmetry but introduce the assumption of nondivergent barotropic (two-dimensional) flow. The hurricane's secondary circulation and all baroclinic effects are thus not directly considered. Asymmetric and

Reproduced with permission of the copyright owner. Further reproduction prohibited without permission.

axisymmetric processes are by no means mutually exclusive and our results should be considered a step towards the alliance of two methodologies. Our goal is to complement the axisymmetric theory while offering more consistent dynamical explanations for observed hurricane features.

In chapter 2, we describe a physical mechanism for the development of combined barotropic and baroclinic instability in the region of a hurricane's primary or secondary eyewall. The development of such instability can lead to nonlinear asymmetric mixing which acts to stabilize the flow by rearranging the PV into a monotonic state. Chapter 3 considers the linear stability and nonlinear evolution of an unstable primary eyewall in an idealized nondivergent barotropic framework, and introduces a statistical mechanics approach for obtaining end states of initially unstable flows. Using aircraft flight-level data obtained in a number of hurricanes, chapter 4 demonstrates that during intensification, radial vorticity profiles are observed to be sharply peaked within the eyewalls and suggest barotropically unstable flows. When intensification ceases, a marked transition of the flow is observed as the vorticity relaxes to an approximately monotonic, and hence stable, profile. Comparisons of the observations with the theoretical and numerical predictions of chapter 3 offer compelling evidence that nondivergent barotropic processes can well explain much of the observed evolution of a hurricane's eyewall.

In addition to primary eyewalls, intense tropical cyclones often exhibit secondary (concentric) eyewall patterns in their radar reflectivity. Deep convection within the inner, or primary eyewall is surrounded by an echo-free moat, which in turn is surrounded by an outer, or secondary ring of deep convection. Both convective regions typically contain well-defined tangential wind maxima. The primary wind maximum is associated with large vorticity just inside the radius of maximum wind, while the secondary wind maximum is usually associated with relatively enhanced vorticity embedded in the outer ring. In contrast, the moat is a region of relatively low, but positive, vorticity. If the vorticity profile across the eye and inner eyewall is ap-

Reproduced with permission of the copyright owner. Further reproduction prohibited without permission.

proximated as monotonic, the resulting radial profile of vorticity still satisfies the Rayleigh necessary condition for instability as the radial gradient twice changes sign. In chapters 6 and 7, we investigate the stability of such structures and, in the case of instability, we simulate the nonlinear evolution into a more stable structure using a nondivergent barotropic model.

Because the radial gradient of vorticity changes sign twice, two types of instability and vorticity rearrangement are identified: (1) instability across the outer ring of enhanced vorticity, and (2) instability across the moat. Type 1 instability occurs when the outer ring of enhanced vorticity is sufficiently narrow and when the circulation of the central vortex is sufficiently weak (compared to the outer ring) that it does not induce enough differential rotation across the outer ring to stabilize it. The nonlinear mixing associated with type 1 instability results in a broader and weaker vorticity ring but still maintains a significant secondary wind maximum. The central vortex induces strong differential rotation (and associated enstrophy cascade) in the moat region which then acts as a barrier to inward mixing of small (but finite) amplitude asymmetric vorticity disturbances. Type 1 instability is discussed in chapter 6.

Type 2 instability occurs when the radial extent of the moat is sufficiently narrow so that unstable interactions may occur between the central vortex and the inner edge of the ring. Because the vortex induced differential rotation across the ring is large when the ring is close to the vortex, type 2 instability typically precludes type 1 instability except in the case of very thin rings. The nonlinear mixing from type 2 instability can perturb the vortex into a variety of shapes, and one possible outcome is that the vortex and moat evolve into a nearly steady tripole structure. Such an evolution to a tripole is the most likely outcome in the case of a contracting secondary ring of enhanced vorticity and offers a mechanism for the formation and persistence of elliptical eyewalls. Type 2 instability is discussed in chapter 7.

Reproduced with permission of the copyright owner. Further reproduction prohibited without permission.

Chapter 2

DEVELOPMENT OF BAROTROPIC INSTABILITY IN HURRICANES

The thing about PV is that it's more V than P. *William Gray*

The azimuthal mean tangential winds observed inside the radius of maximum wind (RMW) of hurricanes often exhibit a "U-shaped", or concave upwards profile, while outside the RMW, the mean tangential winds typically decrease significantly with radius (e.g., Willoughby et al., 1982, Fig. 14). The symmetric part of the vorticity associated with such flows consists of an annular ring of enhanced vorticity in the eyewall with relatively weak vorticity inside (in the eye) and outside (in the moat). The association between vorticity and U-shaped tangential wind profiles can be understood as follows. Consider a family of idealized tangential wind profiles

$$\frac{v(r)}{v_0} = \begin{cases} (r/a)^x & 0 \le r \le a, \\ a/r & a \le r < \infty, \end{cases} \tag{2.1}$$

where v_0 is the maximum wind, a is the RMW, and $x > 0$. The associated vorticity is given by

$$\frac{\zeta(r)}{v_0/a} = \begin{cases} (x+1)(r/a)^{x-1} & 0 \le r \le a, \\ 0 & a < r < \infty. \end{cases} \tag{2.2}$$

When $x = 1$, $v(r)$ increases linearly with radius inside the RMW and the vorticity is piecewise-constant. This type of flow is referred to as a Rankine vortex. When $x < 1$, the tangential wind inside the RMW may be described as "concave downwards" and the vorticity decreases monotonically with radius. For the case when $x > 1$, $v(r)$ is U-shaped and the vorticity increases with radius until $r = a$ outside of which the

Reproduced with permission of the copyright owner. Further reproduction prohibited without permission.

flow is irrotational. This vorticity profile forms an annular ring. Profiles of $v(r)$ and $\zeta(r)$ for selected values of x are shown in Fig. 2.1. Note that for large values of x the tangential wind becomes increasingly U-shaped and the annular ring of vorticity becomes increasingly strong and radially narrow. The limiting case as $x \to \infty$ is a circular "vortex sheet" at $r = a$.

An observed example of a ring of elevated PV in a hurricane eyewall can be seen in Fig. 2.2 which identifies an annular ring of high PV in the region of the eyewall of Hurricane Hilda (1964). The ring of enhanced PV achieves its maximum in the layer between 763 mb and 667 mb and is evident throughout the vertical extent of Hilda. Also evident is an increase with height of the radius of the PV maximum while the maximum decreases with height above 667 mb. The association between the convective regions and flow fields in Hurricane Andrew (1992) is shown in Fig. 2.3 and demonstrates the elevated vorticity embedded in the highly convective eyewall. In this chapter, the physical mechanisms responsible for the development of such flows are addressed.

For fully three-dimensional nonhydrostatic motions with diabatic and frictional effects, the Ertel potential vorticity equation is $DP/Dt = \alpha(\nabla \times \mathbf{F}) \cdot \nabla\theta + \alpha\boldsymbol{\zeta}_a \cdot \nabla\dot{\theta}$, where D/Dt is the material derivative, $P = \alpha\boldsymbol{\zeta}_a \cdot \nabla\theta$ the potential vorticity, α the specific volume, $\boldsymbol{\zeta}_a = 2\boldsymbol{\Omega} + \nabla \times \mathbf{u}$ the absolute vorticity vector, $\mathbf{u}$ the three dimensional velocity vector, θ the potential temperature, $\dot{\theta}$ the diabatic heating, and $\mathbf{F}$ the frictional force per unit mass. Defining $\mathbf{j} = \nabla\theta/|\nabla\theta|$ as a unit vector perpendicular to the θ-surface, and $\mathbf{k} = \boldsymbol{\zeta}_a/|\boldsymbol{\zeta}_a|$ as a unit vector pointing along the absolute vorticity vector. We can then write the potential vorticity equation as

$$\frac{DP}{Dt} = P\left(\frac{\mathbf{j}\cdot(\nabla\times\mathbf{F})}{\mathbf{j}\cdot\boldsymbol{\zeta}_a} + \frac{\mathbf{k}\cdot\nabla\dot{\theta}}{\mathbf{k}\cdot\nabla\theta}\right). \tag{2.3}$$

In the intense convective regions of a hurricane, the diabatic term is particularly important and the exponential nature of (2.3) demonstrates that PV production is greatest where regions of high PV are congruent with regions where $\mathbf{k}\cdot\nabla\dot{\theta}/\mathbf{k}\cdot\nabla\theta$ is

Reproduced with permission of the copyright owner. Further reproduction prohibited without permission.

positive and large. In the middle troposphere and near the relatively warm region of the hurricane center, $\mathbf{k}$ tends to point upward and radially outward while $\nabla\theta$ tends to point upward and radially inward. The outward tilt of $\mathbf{k}$ is due to the decrease of tangential wind with height while the inward tilt of $\nabla\theta$ is due to isentropic surfaces which are bulged downwards in the warm region. Both of these effects are related to the baroclinity resulting from the diabatic warming within the convective region. Since the heating $\dot{\theta}$ tends to be maximized in the midtroposphere, $\nabla\dot{\theta}$ tends to be positive below the maximum and negative above. We might then expect the vertical distribution of PV to be that of a dipole with $P > 0$ in the lower troposphere and $P < 0$ in the upper troposphere, but this is typically not observed (e.g., see Fig. 2.2) due to the large values of lower and mid-tropospheric PV which are carried aloft by strong updrafts.

In the case of hurricanes which exhibit well defined eyes, the diabatic production of PV is greatest in the convective region of the eyewall and is relatively small in the eye and moat where latent heat release is not typically large. The resulting spatial structure of the PV field might then be expected to be a hollow tower of high PV (Möller and Smith 1994; Schubert et al. 1999) where large values of PV would not be found in the eye unless they were transported in from the eyewall. An important consequence of the formation of such a PV structure is that its radial gradient of PV changes sign and thus can set the stage for dynamic instability. This will be addressed in greater detail in chapter 3.

For the case of hurricanes which exhibit concentric eyewalls, diabatic production of PV in the outer eyewall can result in a second annular ring of enhanced PV. The dynamic stability of the flow associated with secondary eyewalls is complicated by the presence of the primary eyewall and will be discussed in chapters 6 and 7.

Reproduced with permission of the copyright owner. Further reproduction prohibited without permission.

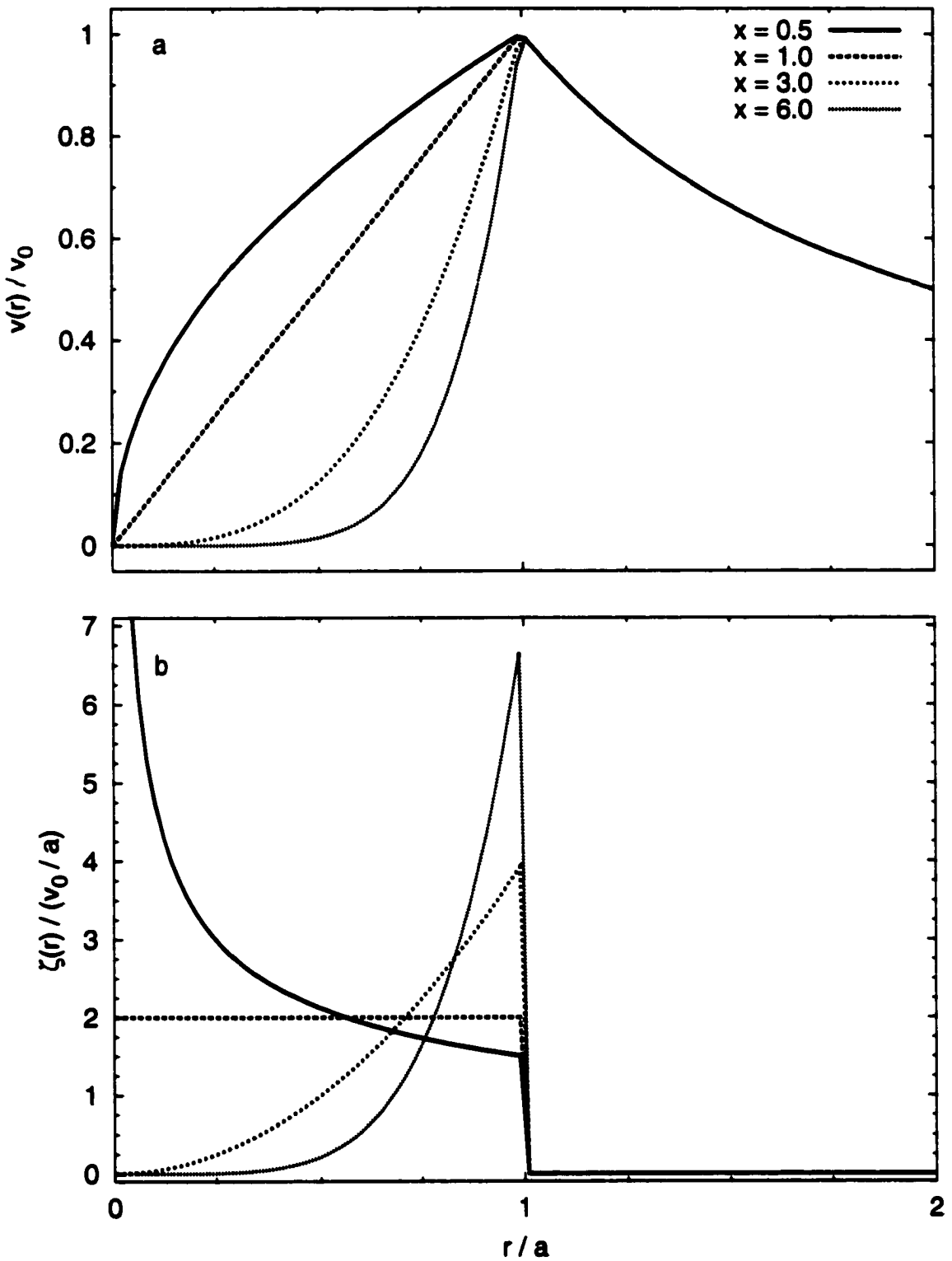

Figure 2.1: (a) Idealized tangential wind given by Eq. (2.1) and vorticity given by Eq. (2.2) describing the association between "U-shaped" wind profiles and annular rings of enhanced vorticity.

Reproduced with permission of the copyright owner. Further reproduction prohibited without permission.

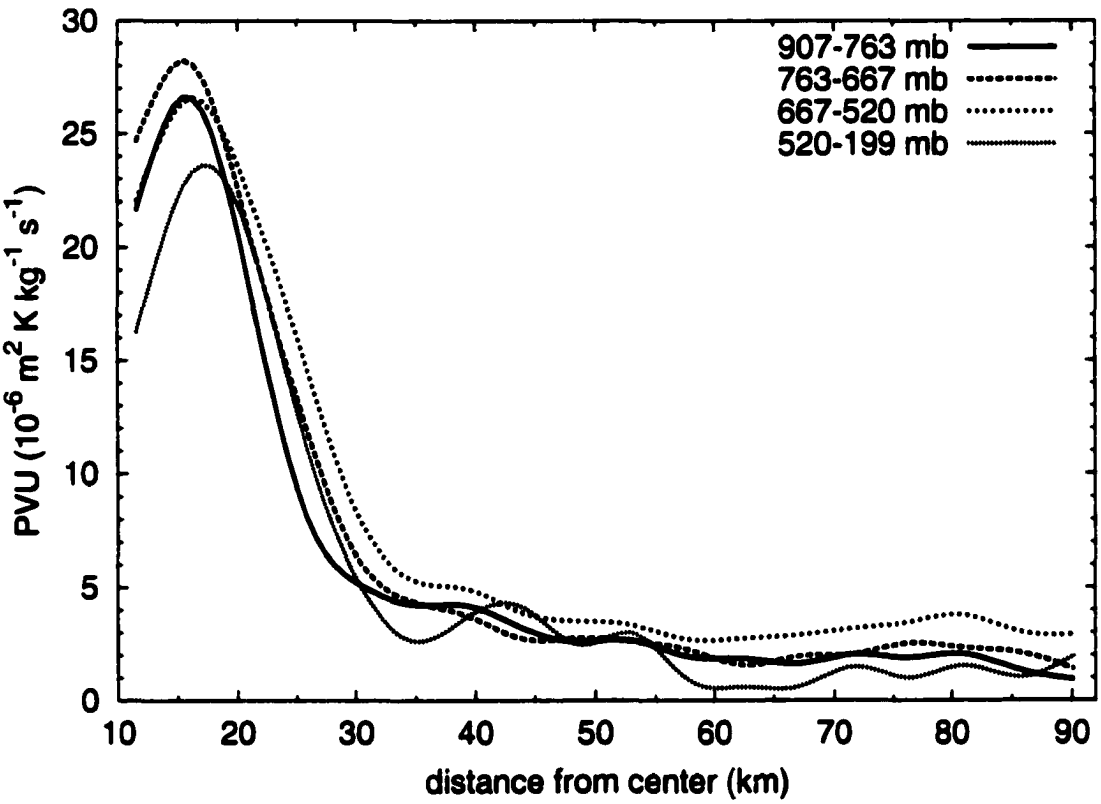

Figure 2.2: Potential vorticity in PV Units (10^{-6} m^2 K kg^{-1} s^{-1}) calculated using flight-level data in Hurricane Hilda on 1 October 1964. The data consists of smoothed azimuthally averaged fields of temperature and tangential wind obtained over a 6.5 hour period at 5 different flight levels (907, 763, 667, 520, and 199 mb). The average PV in each of the 4 layers is shown. Data limitations do not allow for calculations inside $r = 10$ km.

Reproduced with permission of the copyright owner. Further reproduction prohibited without permission.

Figure 2.3: Hurricane Andrew making landfall in Florida. (a) Low-level reflectivity obtained at 0835 UTC on 24 August 1992 from the National Weather Service WSR-57 radar. The data was recorded and processed by the NOAA Hurricane Research Division. The "+" symbol indicates the location of the radar at the National Hurricane Center. The annular ring of high reflectivity (dBZ) is associated with the eyewall while the central region of low reflectivity identifies the eye. The WSR-57 radar was partially demolished by high winds shortly after this image was recorded (Image courtesy of NOAA Hurricane Research Division). (b) 700 mb flight-level tangential wind (dashed) and relative vorticity (solid). The wind data was obtained during an outbound radial pass of an Air Force WC-130 "Hurricane Hunter" aircraft during the time 0806–0831 UTC on 24 August. Elevated vorticity in the region of the eyewall with weaker vorticity in the eye result in an annular ring or "hollow tower" structure.

Reproduced with permission of the copyright owner. Further reproduction prohibited without permission.

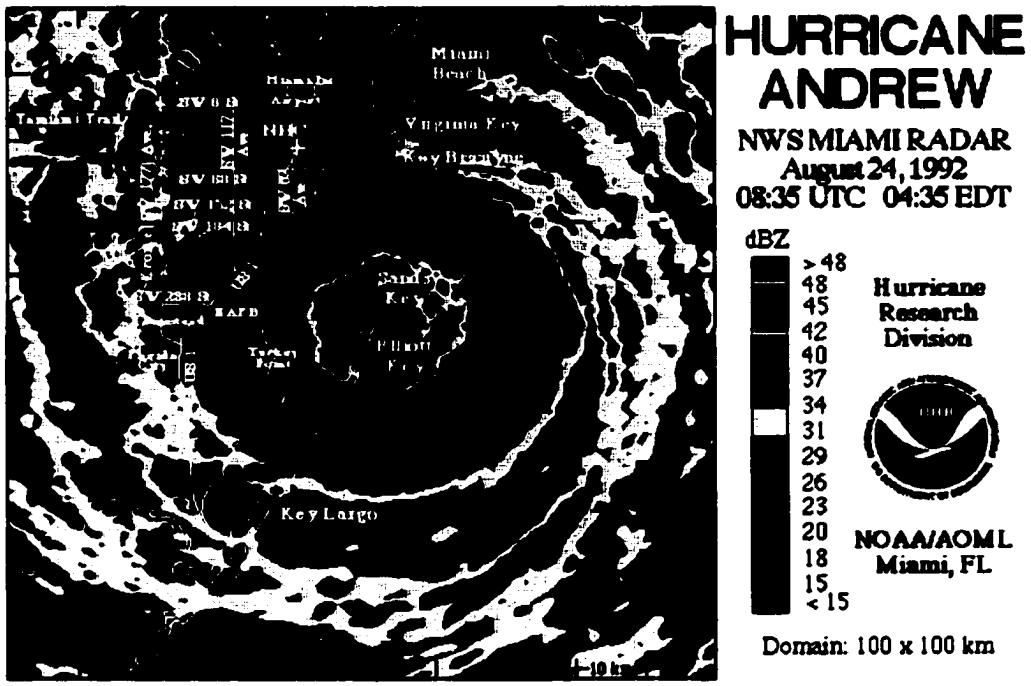

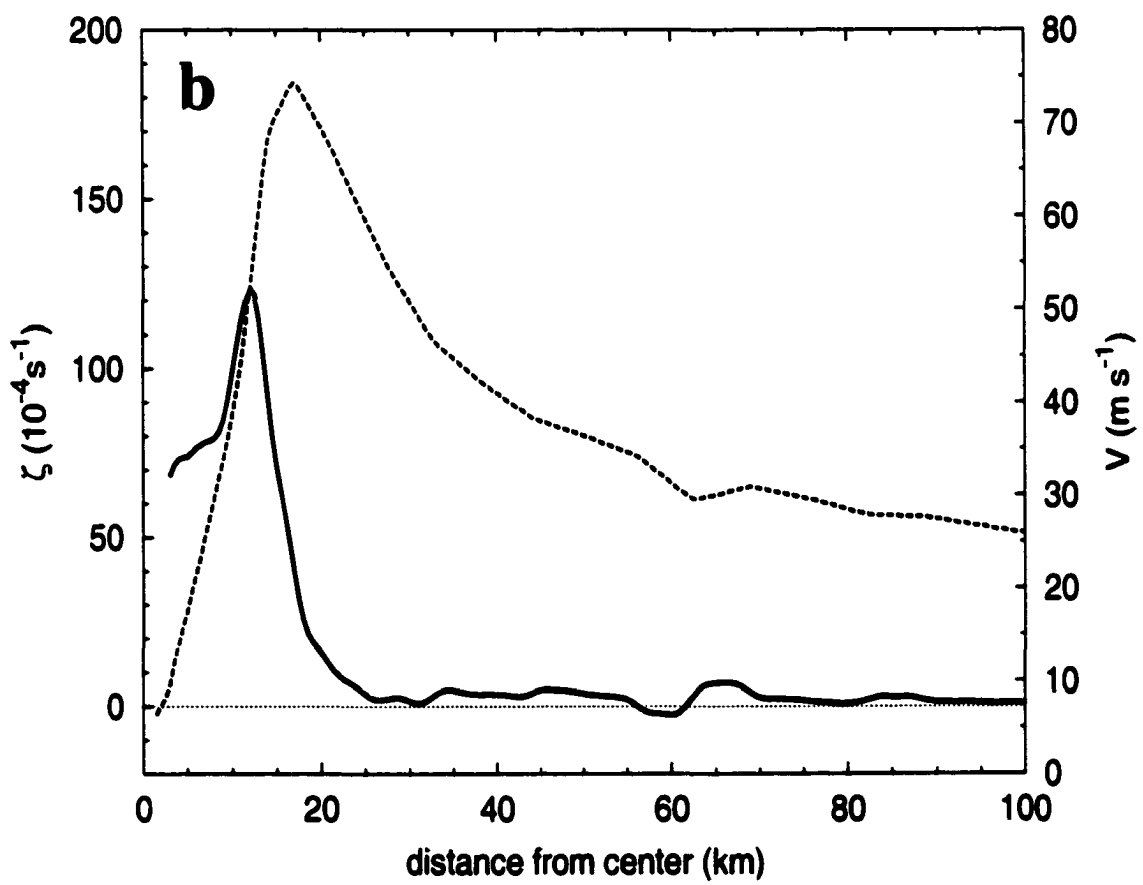

Figure 2.3: See caption on previous page.

Reproduced with permission of the copyright owner. Further reproduction prohibited without permission.

Chapter 3

EVOLUTION OF AN UNSTABLE PRIMARY EYEWALL

Then, disaster. Thick dark clouds suddenly envelop the aircraft. A titanic fist of wind, three times the force of gravity, smashes us. I am thrown into the computer console, bounce off, and for one terrifying instant find myself looking DOWN at a precipitous angle at Sean across the aisle from me.

A second massive jolt rocks the aircraft. Gear loosened by the previous turbulence flies about the inside the aircraft, bouncing off walls, ceiling, and crew members. Next to Terry Schricker, our 200-pound life raft breaks loose and hurtles into the ceiling. Neil Rain fends off screwdrivers, wrenches, and his airborne toolbox with his arms. The locked drawers in the galley rip open, and a cooler loaded with soft drink cans explodes into the air, showering Alan Goldstein with ice and 12-ounce cans. Hugh Willoughby watches as invisible fingers pry loose his portable computer from its mounting, and hurl it into the ceiling, ripping a gash in the tough ceiling fabric. At the radar station, Peter Dodge shields himself and the Barbados reporter from two flying briefcases. Next to them, Bob Burpee grabs two airborne boxes of computer tapes, but has no more hands to grab a third box of tapes that smashes against the ceiling, sending the tapes caroming through the cabin.

A third terrific blow, almost six times the force of gravity, staggers the airplane. Clip boards, flight bags, and headsets sail past my head as I am hurled into the console. Terrible thundering crashing sounds boom through the cabin; I hear crew members crying out. I scream inwardly. "This is what it feels like to die in battle", I think. We are going down. The final moments of the five hurricane hunter missions that never returned must have been like this.

The aircraft lurches out of control into a hard right bank. We plunge towards the ocean, our number three engine in flames. Debris hangs from the number four engine.

The turbulence suddenly stops. The clouds part. The darkness lifts. We fall into the eye of Hurricane Hugo.

From "Hunting Hugo" by Dr. Jeffrey M. Masters describing an encounter with massive wind shear while entering the eye of Hurricane Hugo (1989) in a NOAA WP-3D aircraft (Used with permission).

Reproduced with permission of the copyright owner. Further reproduction prohibited without permission.

3.1 Linear stability analysis of the three-region model

The cyclonic shear zone associated with a hurricane eyewall can be envisaged as an annular ring of uniformly high vorticity, with large radial vorticity gradients on its edges. On the inner edge of the annular ring the vorticity increases with radius, while on the outer edge the vorticity decreases with radius. In terms of vortex Rossby wave theory, waves on the inner edge of the annular ring will prograde relative to the flow there, while waves on the outer edge will retrograde relative to the flow there. It is possible for these two counterpropagating (relative to the tangential flow in their vicinity) waves to have the same angular velocity relative to the earth, that is, to be phase locked. If the locked phase is favorable, each wave will make the other grow, and barotropic instability will result. This effect is described in detail in Schubert et al. (1999) and can be understood as a special case of the of the four-region model, which is discussed in Appendix A. The main result of that analysis is the eigenvalue problem (A.9). For the case of an unstable primary eyewall, the four-region model reduces to the three-region model by assuming $\zeta_3 = 0$. A schematic of the three-region model considered in this chapter is shown in Fig. 3.1. In this case, the eigenvalue problem (A.9) reduces to

$$\begin{pmatrix} m\bar{\omega}_1 + \frac{1}{2}(\zeta_2 - \zeta_1) & \frac{1}{2}(\zeta_2 - \zeta_1)(r_1/r_2)^m \\ -\frac{1}{2}\zeta_2 (r_1/r_2)^m & m\bar{\omega}_2 - \frac{1}{2}\zeta_2 \end{pmatrix} \begin{pmatrix} \Psi_1 \\ \Psi_2 \end{pmatrix} = \nu \begin{pmatrix} \Psi_1 \\ \Psi_2 \end{pmatrix}, \tag{3.1}$$

where m is the azimuthal wavenumber, ν is the complex frequency, r_1, r_2 are the inner and outer radii of the annular ring, $\bar{\omega}_1, \bar{\omega}_2$ are the basic state angular velocities at r_1 and r_2, ζ_1, ζ_2 are the uniform vorticities of the central eye region and annular eyewall region, and Ψ_1, Ψ_2 are complex constants. The eigenvalues of (3.1) are given by

$$\nu = \tfrac{1}{2}(\nu_1 + \nu_2) \pm \tfrac{1}{2}\left[(\nu_1 - \nu_2)^2 - \zeta_2(\zeta_2 - \zeta_1)(r_1/r_2)^{2m}\right]^{1/2}, \tag{3.2}$$

where $\nu_1 = m\bar{\omega}_1 + \frac{1}{2}(\zeta_2 - \zeta_1)$ and $\nu_2 = m\bar{\omega}_2 - \frac{1}{2}\zeta_2$ are the pure (noninteracting) vorticity wave frequencies at the inner and outer interfaces. One can verify from (3.2) that ν must be real for $m = 1, 2$. This implies the vorticity field will remain

Reproduced with permission of the copyright owner. Further reproduction prohibited without permission.

exponentially stable to these disturbance patterns. The remaining wavenumbers can, however, produce frequencies with nonzero imaginary parts.

Following Schubert et al. (1999), it is convenient to minimize the number of adjustable parameters in (3.2). To write (3.2) in a different form we first define the average vorticity over the region $0 \leq r \leq r_2$ as $\zeta_{av} = \zeta_1\delta^2 + \zeta_2(1-\delta^2)$, where $\delta = r_1/r_2$. Then, defining $\gamma = \zeta_1/\zeta_{av}$ as the ratio of the inner-region vorticity to the average vorticity, we can express ζ_1 and ζ_2 in terms of $\zeta_{av}, \delta, \gamma$ and write (3.2) as

$$\begin{aligned}\frac{\nu}{\zeta_{av}} &= \tfrac{1}{4}\Big\{m + (m-1)\gamma \\ &\quad \pm\Big[\Big(m - (m-1)\gamma - 2\Big(\frac{1-\gamma\delta^2}{1-\delta^2}\Big)\Big)^2 \\ &\quad +4\Big(\frac{1-\gamma\delta^2}{1-\delta^2}\Big)\Big(\gamma - \frac{1-\gamma\delta^2}{1-\delta^2}\Big)\delta^{2m}\Big]^{\frac{1}{2}}\Big\}. \qquad (3.3)\end{aligned}$$

Using (3.3) we can calculate the dimensionless complex frequency ν/ζ_{av} as a function of the disturbance azimuthal wavenumber m and the two basic state flow parameters δ and γ. The imaginary part of ν/ζ_{av}, denoted by ν_i/ζ_{av}, is a dimensionless measure of the growth rate. Isolines of ν_i/ζ_{av} as a function of δ and γ for $m = 3, 4, \ldots, 8$ are shown in Fig. 3.2. Note that all basic states with $\gamma < 1$ satisfy the Rayleigh necessary condition for instability but that most of the region $\gamma < 1, \delta < \frac{1}{2}$ is in fact stable. Clearly, thinner annular regions (larger values of r_1/r_2) should produce the highest growth rates but at much higher azimuthal wavenumbers. Note also the overlap in the unstable regions of the γ-δ plane for different azimuthal wavenumbers. For example, the lower right area of the γ-δ plane is unstable to all the azimuthal wavenumbers $m = 3, 4, \ldots, 8$. We can collapse the six panels in Fig. 3.2 into a single diagram if, for each point in the γ-δ plane, we choose the largest growth rate of the six wavenumbers $m = 3, 4, \ldots, 8$. This results in Fig. 3.3, which shows clearly the preference for higher wavenumbers as the annular ring becomes thinner. Note that a contracting ring of fixed radial width becomes increasingly stable as δ becomes smaller. Another noteworthy, albeit somewhat counterintuitive, feature of Fig. 3.3 is that a stable vortex may become unstable if the central vorticity ζ_1 increases. For

Reproduced with permission of the copyright owner. Further reproduction prohibited without permission.

example, a vortex with $\delta = 0.5$ is stable provided that $\gamma = 0$, i.e. $\zeta_1 = 0$. Any increase in the central vorticity would introduce a wavenumber 3 instability. Of course, if the central vorticity is increased to the point where $\zeta_1 = \zeta_2$, the resulting vortex is a Rankine vortex and is assured to be exponentially stable by Rayleigh's theorem since the associated radial vorticity gradient never changes sign.

The analysis above is based on a piecewise uniform idealization of smooth vortices with continuous vorticity profiles. Comparisons of results obtained with (3.3) with results of stability analyses performed on continuous vorticity profiles were favorable for the vortex used by Schubert et al. (1999) and are also found to be good for the vortices used in chapters 6 and 7 of the present work. However, other choices of vortices may not compare as favorably. For example, consider a small intense hurricane such as Hurricane Andrew (1992) whose piecewise uniform idealization could be described by choosing $r_1 = 16$ km, $r_2 = 20$ km, $\zeta_1 = 45 \times 10^{-4}$ s^{-1}, $\zeta_2 = 98.57 \times 10^{-4}$ s^{-1}, and $\zeta_3 = 0$. In this case, $\delta = 0.8$, $\gamma = 0.7$, and $\zeta_{av} = 64.29 \times 10^{-4}$ s^{-1}. This profile and its continuous analogue are shown in Fig. 3.4. Applying an eigensolver (courtesy of M. T. Montgomery and discussed in Reasor et al. (1999)) to the continuous profile and comparing the results with those obtained using (3.3) for the idealized profile, we find poor agreement. The results are shown in Fig. 3.5 and demonstrate that (3.3) predicts a maximum growthrate at wavenumber 7 versus a predicted wavenumber 4 maximum for the corresponding continuous profile. The left axis of Fig. 3.5 displays growth rates and the right axis shows e-folding times. The comparison is again quite poor, with Eq. (3.3) predicting a minimum e-folding time of 26 minutes compared to a minimum e-folding time of 48 minutes for the continuous analogue.

The nonlinear evolution of the continuous profile shown in Fig. 3.4 is the subject of the following section.

Reproduced with permission of the copyright owner. Further reproduction prohibited without permission.

3.2 Relaxation to a monopole

We now perform a direct numerical integration of an initially unstable vorticity field using a pseudospectral numerical model in a barotropic framework. As the initial condition, we use a continuous axisymmetric "hollow tower" vorticity field. Details of the model and general form of the initial conditions are found in Appendix B. As shown in Table B.1, the model domain for this experiment is 200 km × 200 km and the maximum Fourier mode kept in the psedospectral code is 170. This results in an effective resolution of 1.18 km. For this experiment, we choose $\{r_1, r_2, d_1, d_2\}$ $= \{16, 20, 2, 2\}$ km and $\{\zeta_1, \zeta_2, \zeta_3\} = \{43, 97, -2\} \times 10^{-4}$ s^{-1} for the adjustable parameters of (B.5). Initial profiles of the vorticity, tangential wind, angular velocity, and pressure are shown by the solid black curves in Fig. 3.7 (the other curves will be discussed later) and describe an intense vortex with maximum tangential wind of 60 m s^{-1} at $r = 20$ km. As discussed in Schubert et al. (1999), the pressure was diagnosed in Fourier space using

$$\frac{1}{\rho}\nabla^2 p = f\nabla^2\psi - 2\left[\left(\frac{\partial^2\psi}{\partial x \partial y}\right)^2 - \frac{\partial^2\psi}{\partial x^2}\frac{\partial^2\psi}{\partial y^2}\right],$$

where $\rho = 1.13$ kg m^{-3} and $f = 5 \times 10^{-5}$ s^{-1}.

The results of this experiment are shown in Fig. 3.6 in the form of two dimensional vorticity maps. Near the start of the experiment, the prograding vortex Rossby waves along the inner edge of the ring ($14 \leq r \leq 18$ km) are embedded in a local angular velocity $\omega \approx 21 \times 10^{-4}$ s^{-1} while the retrograding waves along the outer edge of the ring ($18 \leq r \leq 22$ km) are embedded in stronger angular velocity $\omega \approx 29 \times 10^{-4}$ s^{-1} (Fig. 3.7 c). As the waves along each edge phase lock, they help each other to grow and at $t = 2$ h, the ring is visibly distorted. As the wave amplitude increases, the local differential rotation (i.e., $\partial\omega/\partial r$) further distorts the resulting asymmetries and wavebreaking occurs.

In this experiment, the wavebreaking occurs first along the outer ring edge. This

Reproduced with permission of the copyright owner. Further reproduction prohibited without permission.

is in contrast to the numerical results of Schubert et al. (1999) and Hidalgo (1999, Fig. 4.11) where wavebreaking occurred first along the inner ring edge. The reason for this difference might be explained by considering differences in shear in the (axisymmetric) initial conditions of the three experiments. The shear S is related to the differential rotation by $S = r\frac{\partial \omega}{\partial r} = \zeta - 2\omega$. For the experiment shown in Fig. 3.6, the maximum shear along the inner edge of the ring $|S| \approx 42 \times 10^{-4}$ s^{-1} is less than the maximum shear along the outer edge $|S| \approx 54 \times 10^{-4}$ s^{-1}. For the experiment of Schubert et al. (1999), the shear along the inner edge of the ring $|S| \approx 21 \times 10^{-4}$ s^{-1} is greater than the shear along the outer edge $|S| \approx 16 \times 10^{-4}$ s^{-1}. For the experiment of Hidalgo (1999), the shear is again greatest along the inner ring edge. Montgomery and Kallenbach (1997) demonstrated that the outward propagation of vortex Rossby wave packets within a region of negative basic state vorticity gradient ($\frac{d\bar{\zeta}}{dr} < 0$) is slowed by the presence of local shear which decreases the radial group velocity of the packet by increasing its radial wavenumber. In an asymptotic sense, the shear eventually dominates and radial propagation ceases at some "stagnation radius" which is inversely related to the local shear. Thus for the initial conditions for the experiment of Fig. 3.6, the outward radial propagation of the wave disturbances may be suppressed by the larger shear along the outer edge of the ring.

At $t = 3$ h, the breaking waves along the outer ring edge have taken the form of trailing spirals and the wavenumber 4 instability is evident along the inner ring edge. The strong differential rotation along the outer ring edge keeps the trailing spirals from moving significantly outwards and the vortex as a whole maintains a nearly circular shape of fairly constant size. This is again in contrast to the results of Schubert et al. (1999) and Hidalgo (1999) where the weaker shear along the outer ring edge allows the trailing spirals to move appreciably outwards before axisymmetrizing. This results in a significant broadening of the vortex as a whole.

Although in the present experiment the outer ring edge approximately maintains its original size and shape, the inner edge becomes increasingly distorted and at $t = 5.5$

Reproduced with permission of the copyright owner. Further reproduction prohibited without permission.

h, coherent structures have formed and begin to migrate into the central eye region. These coherent structures might be described as "mesovortices" and appear to be similar in structure, location, and evolution to mesovortices observed in Hurricane Hugo 1989 (Black and Marks, 1991) and Hurricane Andrew 1992 (Willoughby, 1996). When $t = 6$ h, a distinct mesovortex, orbiting cyclonically in the central region (eye), can be seen to the right (east) of the vortex center. As it orbits, it interacts with the coherent structures still embedded in the ring (eyewall) and as the eyewall vorticity collapses inward, intricate merger processes dominate. At $t = 12$ h, almost all of the strongest vorticity has consolidated into one structure orbiting near 5 km from the center of the domain and during the remaining 12 hours of the experiment, nearly complete axisymmetrization towards a monopole occurs. The maximum vorticity within the domain remains fairly robust during the mixing process and at $t = 24$ h, the vorticity near the center is roughly 89×10^{-4} s^{-1}, which is approximately an 8% reduction of the maximum vorticity initially in the ring.

The evolution of the symmetric part of the flow is shown by the dashed colored lines in Fig. 3.7 for $t = 6, 12, 18$, and 24 h. Averages were calculated relative to the domain center. At $t = 6$ h, the mean vorticity has spread inwards and slightly outwards and at $t = 12$ h, the peak average vorticity is found inside $r = 5$ km. At $t = 18$ h, the vorticity profile is monotonic. The evolution of the mean tangential wind shows a corresponding transition from a concave upwards to a concave downwards profile while the maximum wind decreases from 60 m s^{-1} to 50 m s^{-1}. Although the maximum wind decreases, the pressure profile (Fig. 3.7 d) shows a 5 mb reduction of the central pressure. This is due to the spin-up of the eye by the inward turbulent transport of angular momentum from the eyewall. From the perspective of hurricane intensification, a 5 mb change of central pressure over 12–24 hours is not significant. However, as will be further discussed in chapter 8, an association exists between a spin-up of the eye and factors which induce warming there. Increased warming in the eye can create a much more substantial lowering of the central pressure.

Reproduced with permission of the copyright owner. Further reproduction prohibited without permission.

For comparison with the results of Schubert et al. (1999), the evolution of the integral quantities given by (B.3) and (B.4) in Appendix B is shown in Fig. 3.8. As the vorticity gradients are steepened during the vigorous mixing phase ($t = 3$ h to $t = 8$ h), the palinstrophy increases and achieves a maximum at $t = 7.5$ h which is 278% of its initial value. As the palinstrophy increases, the enstrophy cascades to smaller scales and is lost to diffusion as it enters the viscous subrange associated with the specified value of the eddy viscosity coefficient ν in (B.1). As the palinstrophy decreases after $t = 12$ h, the enstrophy cascade rate also decreases. The initial enstrophy is reduced by 22% in the first 12 hours and an additional 5% over the following 12 hours. The kinetic energy evolution demonstrates a steady but slow decay and the final value after 24 hours is 99.1% of the initial value. The significant loss of enstrophy concurrent with the near conservation of energy is an example of the selective decay hypothesis (e.g., Matthaeus and Montgomery 1980).

Although the results of Fig. 3.8 are qualitatively similar to those of Schubert et al. (1999), the palinstrophy increase and the loss of enstrophy in our experiment are substantially less than theirs since their initial conditions result in greater and more prolonged mixing. For our experiment, the coherent structures which form from the ring are better able to maintain themselves against mixing with weaker vorticity. Thus the vorticity near the center at $t = 24$ h is comprised mostly, but not entirely, of vorticity which was originally in the ring, while the equilibrated vorticity in the experiment of Schubert et al. (1999) is comprised of a broader range of vorticity values. This is evident in their Fig. 4 which shows that the maximum vorticity in the equilibrated state is 79% of the initial maximum vorticity in their ring, compared with a decrease of 8% in our experiment.

In the following section, we introduce a method for quantifying these differences.

Reproduced with permission of the copyright owner. Further reproduction prohibited without permission.

3.3 Maximum entropy prediction

The direct numerical integration shown in Fig. 3.6 illustrates how the barotropic instability process can produce vorticity patterns of increasing intricacy. In the spectral method, the production of finer and finer scales in vorticity is arrested by the model resolution and by the diffusion processes operating near the resolution limit. While it is tempting to run spectral models at higher and higher resolution in order to follow vorticity structures to finer and finer scales, such costly pursuits do not necessarily produce fundamental dynamical advances. A statistical mechanics approach can be more useful. Such an approach has recently been developed by Miller (1990), Robert (1991), Robert and Sommeria (1991, 1992), Sommeria et al. (1991), Miller et al. (1992), Whitaker and Turkington (1994), Chavanis and Sommeria (1996), and Turkington and Whitaker (1996). Here we present a simple version of this maximum entropy argument. The following is a generalized two dimensional formulation of the description found in Schubert et al. (1999).

Working in a cylindrical coordinate system (r, ϕ), we assume that the initial state consists of L patches of constant vorticity $\hat{\zeta}_\ell$ with areas $\mathcal{A}_\ell$, $\ell = 1, \ldots, L$ contained within a disk of radius a. To begin the argument let us suppose that, after the vorticity field has become intricately stretched and folded, we sample the vorticity at N points within a small neighborhood of (r, ϕ). Let n_ℓ denote the number of sampled points at which the vorticity value $\hat{\zeta}_\ell$ is found. Then $\rho_\ell(r, \phi) = n_\ell / N$ denotes the probability, at point (r, ϕ), of finding the vorticity $\hat{\zeta}_\ell$. The number of possible arrangements having n_1 points with vorticity $\hat{\zeta}_1$, n_2 points with vorticity $\hat{\zeta}_2$, etc., is the multiplicity function W, which is given by

$$W = \frac{N!}{n_1! n_2! \cdots n_L!}.$$

The logarithm of the multiplicity function is $\ln W = \ln N! - \sum_{\ell=1}^{L} \ln n_\ell!$. Using the Stirling approximation (e.g., $\ln N! \approx N \ln N - N$ for large N), we obtain $\ln W \approx N \ln N - \sum_{\ell=1}^{L} n_\ell \ln n_\ell = -\sum_{\ell=1}^{L} n_\ell \ln(n_\ell / N)$, where we have used $\sum_{\ell=1}^{L} n_\ell = N$. We

Reproduced with permission of the copyright owner. Further reproduction prohibited without permission.

conclude that

$$\lim_{N\to\infty}\left(\frac{1}{N}\ln W\right) = -\sum_{\ell=1}^{L}\rho_\ell \ln \rho_\ell.$$

Considered as a function of $(\rho_1,\ldots,\rho_L)$ for $\rho_\ell \geq 0$ and with $\sum_{\ell=1}^{L}\rho_\ell = 1$ the function $-\sum_{\ell=1}^{L}\rho_\ell \ln \rho_\ell$ has its maximum value of $\ln L$ at $\rho_1 = \rho_2 = \cdots = \rho_L = 1/L$. In other words the multiplicity of microstates is a maximum when N/L of the sampled points in the neighborhood of (r,ϕ) have vorticity $\hat{\zeta}_1$, N/L have vorticity $\hat{\zeta}_2$, etc; this constitutes a well-mixed state.

We now define the Boltzmann mixing entropy $S[\rho_1(r,\phi),\ldots,\rho_L(r,\phi)]$ as

$$S[\rho_1(r,\phi),\ldots,\rho_L(r,\phi)] = -\int_0^a\int_0^{2\pi}\left(\sum_{\ell=1}^{L}\rho_\ell(r,\phi)\ln\rho_\ell(r,\phi)\right) r\,dr\,d\phi. \tag{3.4}$$

The functional $S[\rho_1(r,\phi),\ldots,\rho_L(r,\phi)]$ measures the loss of information in going from the fine grain (microscopic) view to the coarse grain (macroscopic) view. To find the most probable macroscopic state, we must find the particular set of functions $\rho_\ell(r,\phi)$, $\ell = 1,\ldots,L$, which maximize $S[\rho_1(r,\phi),\ldots,\rho_L(r,\phi)]$ subject to all the integral constraints associated with the inviscid vorticity dynamics in a cylindrical domain. In other words, the variational problem is to find the expectation functions $\rho_\ell(r,\phi)$ by maximizing (3.4) subject to the circulation constraints, the energy constraint, and the angular momentum constraint. Since $\hat{\zeta}_\ell$ are fixed constants, conservation of circulation associated with each of the L vorticity levels can be expressed by

$$\int_0^a\int_0^{2\pi}\rho_\ell(r,\phi)r\,dr\,d\phi = \mathcal{A}_\ell, \qquad \ell = 1,2,\ldots,L. \tag{3.5}$$

Using $u = -\frac{\partial\psi}{r\partial\phi}$, $v = \frac{\partial\psi}{\partial r}$, and $\zeta = \frac{\partial(rv)}{r\partial r} - \frac{\partial u}{r\partial\phi}$, the energy constraint

$$\tfrac{1}{2}\int_0^a\int_0^{2\pi}(u^2+v^2)r\,dr\,d\phi = \mathcal{E},$$

may be written, after integrating by parts, as

$$-\tfrac{1}{2}\int_0^a\int_0^{2\pi}\psi\zeta r\,dr\,d\phi = \mathcal{E},$$

Reproduced with permission of the copyright owner. Further reproduction prohibited without permission.

where we have imposed the Dirichlet boundary condition $\psi(a,\phi) = 0$. Noting that $\zeta(r,\phi) = \sum_{\ell=1}^{L} \hat{\zeta}_\ell \rho_\ell(r,\phi)$, the energy constraint may be written as

$$-\tfrac{1}{2}\int_0^a \int_0^{2\pi} \psi \left(\sum_{\ell=1}^{L} \hat{\zeta}_\ell \rho_\ell \right) r dr d\phi = \mathcal{E}. \tag{3.6}$$

The angular momentum constraint

$$\int_0^a \int_0^{2\pi} rv dr d\phi = \mathcal{M},$$

may be written, after integration by parts, as

$$\tfrac{1}{2}\int_0^a \int_0^{2\pi} (a^2 - r^2) \left(\sum_{\ell=1}^{L} \hat{\zeta}_\ell \rho_\ell \right) r dr d\phi = \mathcal{M}, \tag{3.7}$$

where we have used Stoke's theorem

$$\int_0^a \int_0^{2\pi} \zeta r dr d\phi = a \int_0^{2\pi} v(a,\phi) d\phi.$$

The angular momentum constraint (3.7) may be restated in a more compact form by introducing an angular impulse $\frac{1}{2}r^2\zeta = -rv + \frac{\partial}{r\partial r}(\frac{1}{2}r^2 rv) - \frac{\partial}{r\partial\phi}(\frac{1}{2}r^2 u)$ which is related to the angular momentum plus a divergence $\nabla \cdot (\frac{1}{2}r^2 v, -\frac{1}{2}r^2 u)$. The divergence, when integrated over the disk, is proportional to the circulation. Since both total circulation and angular momentum are conserved, (3.7) may be written in an equivalent form as

$$\int_0^a \int_0^{2\pi} r^2 \left(\sum_{\ell=1}^{L} \hat{\zeta}_\ell \rho_\ell \right) r dr d\phi = \mathcal{I}, \tag{3.8}$$

where $\mathcal{I}$ is the impulse.

Introducing the Lagrange multipliers α_ℓ, β, γ, the variational problem is

$$\begin{aligned} 0 &= \delta S - \sum_{\ell=1}^{L} \alpha_\ell \delta \mathcal{A}_\ell - \gamma \delta \mathcal{I} - \beta \delta \mathcal{E} \\ &= \delta \int_0^a \int_0^{2\pi} \sum_{\ell=1}^{L} \left(-\rho_\ell \ln \rho_\ell - \alpha_\ell \rho_\ell + \tfrac{1}{2}\beta \psi \hat{\zeta}_\ell \rho_\ell - \gamma r^2 \hat{\zeta}_\ell \rho_\ell \right) r dr d\phi \\ &= \int_0^a \int_0^{2\pi} \sum_{\ell=1}^{L} \left\{ \left[-1 - \ln \rho_\ell - \alpha_\ell + \hat{\zeta}_\ell \left(\beta\psi - \gamma r^2 \right) \right] \delta \rho_\ell \right\} r dr d\phi. \end{aligned} \tag{3.9}$$

Reproduced with permission of the copyright owner. Further reproduction prohibited without permission.

For arbitrary variations $\delta\rho_\ell$, we obtain

$$1 + \ln \rho_\ell = -\alpha_\ell + \hat{\zeta}_\ell \left(\beta\psi - \gamma r^2\right), \qquad \ell = 1, 2, \ldots, L. \tag{3.10}$$

The solution to the variational problem must satisfy an additional constraint, which we here make implicit. Assume that the solution to the variational problem is given by $\rho_\ell^*(r,\phi)$ and consider a function $\lambda(r,\phi)$ such that $\rho_\ell^*(r,\phi) = \lambda(r,\phi)\rho_\ell(r,\phi)$. The solution must satisfy the normalization condition $\sum_{\ell=1}^{L} \rho_\ell^* = 1$ at every point (r,ϕ). We can then write $\sum_{\ell=1}^{L} \rho_\ell^* = \lambda(r,\phi) \sum_{\ell=1}^{L} \rho_\ell = 1$, and substitution of (3.10) gives $\lambda(r,\phi) = e/\sum_{\ell=1}^{L} \exp[-\alpha_\ell + \hat{\zeta}_\ell(\beta\psi - \gamma r^2)]$. The solution to the complete variational problem is then given by

$$\rho_\ell^*(r,\phi) = Z^{-1} \exp[-\alpha_\ell + \hat{\zeta}_\ell(\beta\psi - \gamma r^2)], \tag{3.11}$$

where the partition function Z is given by

$$Z(r,\phi) = \sum_{\ell=1}^{L} \exp[-\alpha_\ell + \hat{\zeta}_\ell(\beta\psi - \gamma r^2)]. \tag{3.12}$$

Using $\zeta(r,\phi) = \nabla^2\psi$, we obtain

$$\nabla^2\psi = Z^{-1} \sum_{\ell=1}^{L} \hat{\zeta}_\ell \exp[-\alpha_\ell + \hat{\zeta}_\ell(\beta\psi - \gamma r^2)], \tag{3.13}$$

which is a nonlinear partial differential equation for $\psi(r,\phi)$ with $L+2$ yet to be determined Lagrange multipliers $\alpha_\ell, \beta, \gamma$. The equations for $\alpha_\ell, \beta, \gamma$ are obtained by enforcing the constraints (3.5), (3.6), and (3.8). Thus, substituting (3.11) into (3.5) we obtain

$$\int_0^a \int_0^{2\pi} Z^{-1} \exp[-\alpha_\ell + \hat{\zeta}_\ell \left(\beta\psi - \gamma r^2\right)] r dr d\phi = \mathcal{A}_\ell, \qquad \ell = 1, 2, \ldots, L. \tag{3.14}$$

When (3.11) is used in the energy constraint (3.6), we obtain

$$-\tfrac{1}{2} \int_0^a \int_0^{2\pi} \psi Z^{-1} \left(\sum_{\ell=1}^{L} \hat{\zeta}_\ell \exp[-\alpha_\ell + \hat{\zeta}_\ell(\beta\psi - \gamma r^2)] \right) r dr d\phi = \mathcal{E}. \tag{3.15}$$

When (3.11) is used in the angular impulse constraint (3.8), we obtain

$$\int_0^a \int_0^{2\pi} r^2 Z^{-1} \left(\sum_{\ell=1}^{L} \hat{\zeta}_\ell \exp[-\alpha_\ell + \hat{\zeta}_\ell(\beta\psi - \gamma r^2)] \right) r dr d\phi = \mathcal{I}. \tag{3.16}$$

Reproduced with permission of the copyright owner. Further reproduction prohibited without permission.

In summary, the solution of the maximum entropy vortex problem involves solving the nonlinear system (3.11)–(3.16) for $\psi(r,\phi), \alpha_\ell, \beta, \gamma$, given the initial conditions $\hat{\zeta}_\ell, \mathcal{A}_\ell, \mathcal{E}, \mathcal{I}$. Analytical solutions of the system are not easily obtained, and numerical methods are generally required. The solutions presented below were obtained using an iterative method developed by Turkington and Whitaker (1996). A complete description of the method is presented in Appendix C.

We now apply the maximum entropy theory to an initial flow field which may be described by the three-region model. In this case, we have 3 vorticity levels and the problem is reduced to that of tertiary mixing. In order to approximate the initial conditions used in the numerical experiment of section 3.2, we choose $\hat{\zeta}_1 = 43 \times 10^{-4}$ s^{-1}, $\hat{\zeta}_2 = 97 \times 10^{-4}$ s^{-1}, and $\hat{\zeta}_3 = -2 \times 10^{-4}$ s^{-1}. The central vorticity $\hat{\zeta}_1$ is contained within a circle of radius 16 km, the vorticity in the ring $\hat{\zeta}_2$ is contained between 16 and 20 km, and the far field vorticity $\hat{\zeta}_3$ is found beyond 20 km to the disk boundary at $a = 100$ km. The initial values of the energy $\mathcal{E}$, angular impulse $\mathcal{I}$, and areas of each patch $\mathcal{A}_\ell$ can then be determined. Performing the iterative algorithm described in Appendix C, the equilibrated vorticity associated with the initial flow can be deduced. The results are shown in Fig. 3.9. The predicted final vorticity profile is axisymmetric and monotonic, with a maximum value of 62×10^{-4} s^{-1} at $r = 0$. The reduction in the maximum vorticity value from the initial condition to the final state is a consequence of the fundamental mixing processes occurring during the flow evolution. This emphasizes the fact that material conservation of vorticity on the macroscale is not a useful description of the flow evolution, even though material conservation of vorticity on the microscale is a useful description. When compared with the maximum vorticity value of 89×10^{-4} s^{-1} of the numerical integration at $t = 24$ h, the value predicted by the maximum entropy theory is too low, suggesting an overprediction of mixing, but some of this difference is likely due to the approximation of a continuous profile with a piecewise constant profile. All things considered, the maximum entropy prediction yields a reasonable solution in this case.

Reproduced with permission of the copyright owner. Further reproduction prohibited without permission.

The expectation functions[2] $\rho_1(r)$, $\rho_2(r)$, and $\rho_3(r)$, associated with the 3 vorticity levels $\hat{\zeta}_1$, $\hat{\zeta}_2$, and $\hat{\zeta}_3$ respectively, are shown in Fig. 3.9b. These profiles can be interpreted as follows. In the end-state, fluid particles originally in the annular ring (eyewall) have the highest probability ($\sim 45\%$) of ending up in the central (eye) region, while fluid particles originally in the eye have the highest probability ($\sim 47\%$) of ending up in the original region of the eyewall. Both $\rho_1(r)$ and $\rho_2(r)$ profiles are fairly flat and equal inside $r = 10$ km suggesting a well mixed state between the two vorticity values. Approximately 14% of the vorticity at $r = 0$ was originally outside the eyewall. Thus the maximum vorticity found at $r = 0$ in the predicted state is a mixture of vorticity which was originally in the eye ($\sim 41\%$), vorticity originally in the eyewall ($\sim 45\%$), and vorticity originally outside the eyewall ($\sim 14\%$). In contrast, the maximum entropy prediction for an initial state based on the initial condition of Schubert et al. (1999) shows the vorticity at $r = 0$ consisting of 8% eye vorticity, 64% eyewall vorticity, and 28% far field vorticity. Thus for their example, there is a higher probability of finding air which was originally outside the eyewall than finding air which was originally inside the annular ring. In this sense, the vortex has been "turned inside-out." Such intense mixing is the typical fate of highly unstable initial vortices with very low central vorticity.

[2]For notational ease, we hereafter omit the "*" and refer to the solution set as ρ_ℓ.

Reproduced with permission of the copyright owner. Further reproduction prohibited without permission.

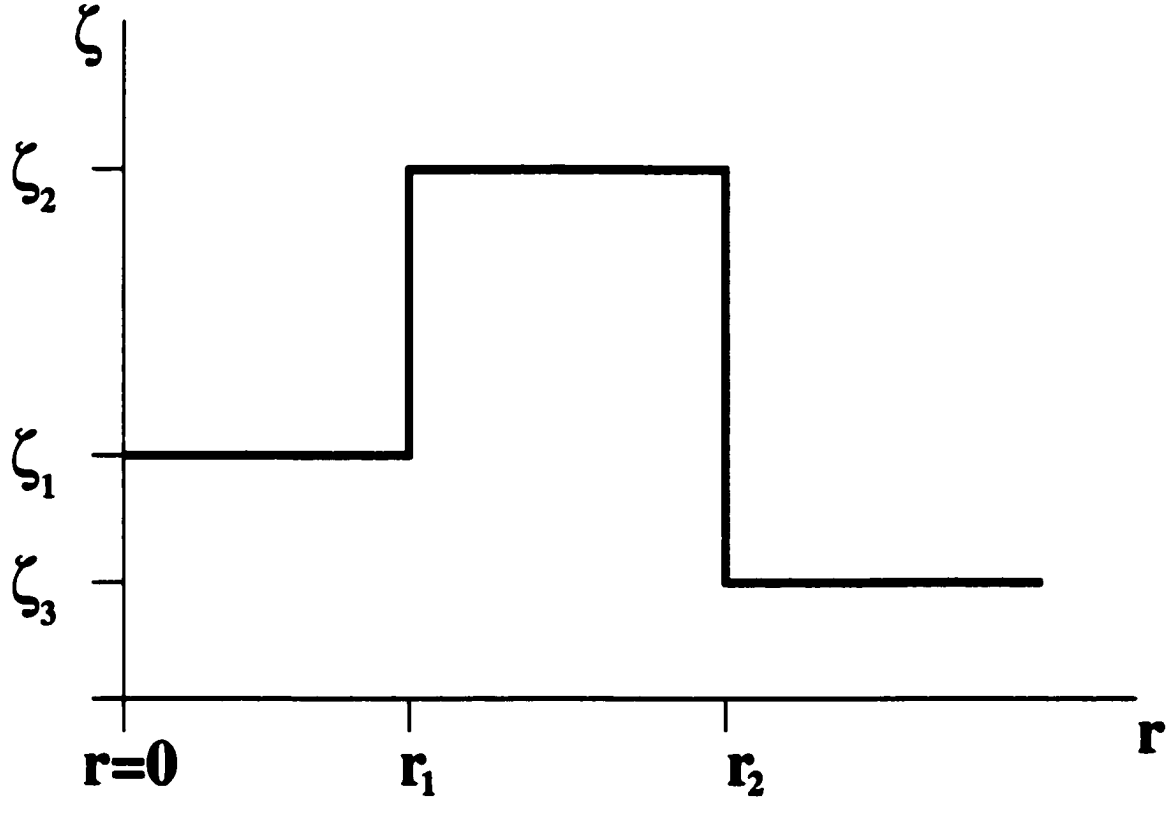

Figure 3.1: Schematic of the idealized piecewise uniform three-region vorticity model. The eye is a region of relatively weak vorticity ζ_1, the eyewall is represented by an annular ring of enhanced vorticity ζ_2, and the far field is nearly irrotational.

Reproduced with permission of the copyright owner. Further reproduction prohibited without permission.

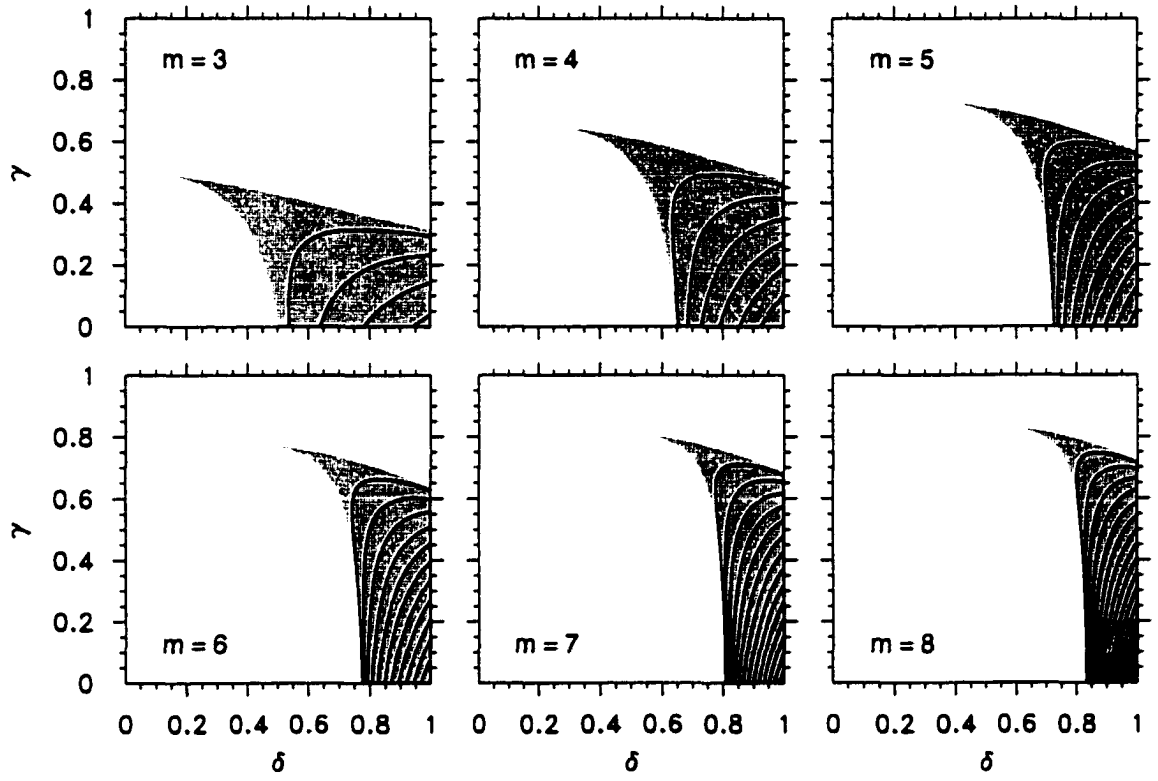

Figure 3.2: Isolines of the dimensionless growth rate ν_i/ζ_{av}, computed from Eq. (3.3), as a function of δ and γ for azimuthal wavenumbers $m = 3, 4, \ldots, 8$. The parameter γ is the ratio of the inner region basic state vorticity to the average basic state vorticity inside r_2. Positive growth rates occur only in the shaded regions. The displayed isolines are $\nu_i/\zeta_{av} = 0.1, 0.2, 0.3, \ldots$ with the largest growth rates occurring in the lower right corner of each figure (from Schubert et al. 1999).

Reproduced with permission of the copyright owner. Further reproduction prohibited without permission.

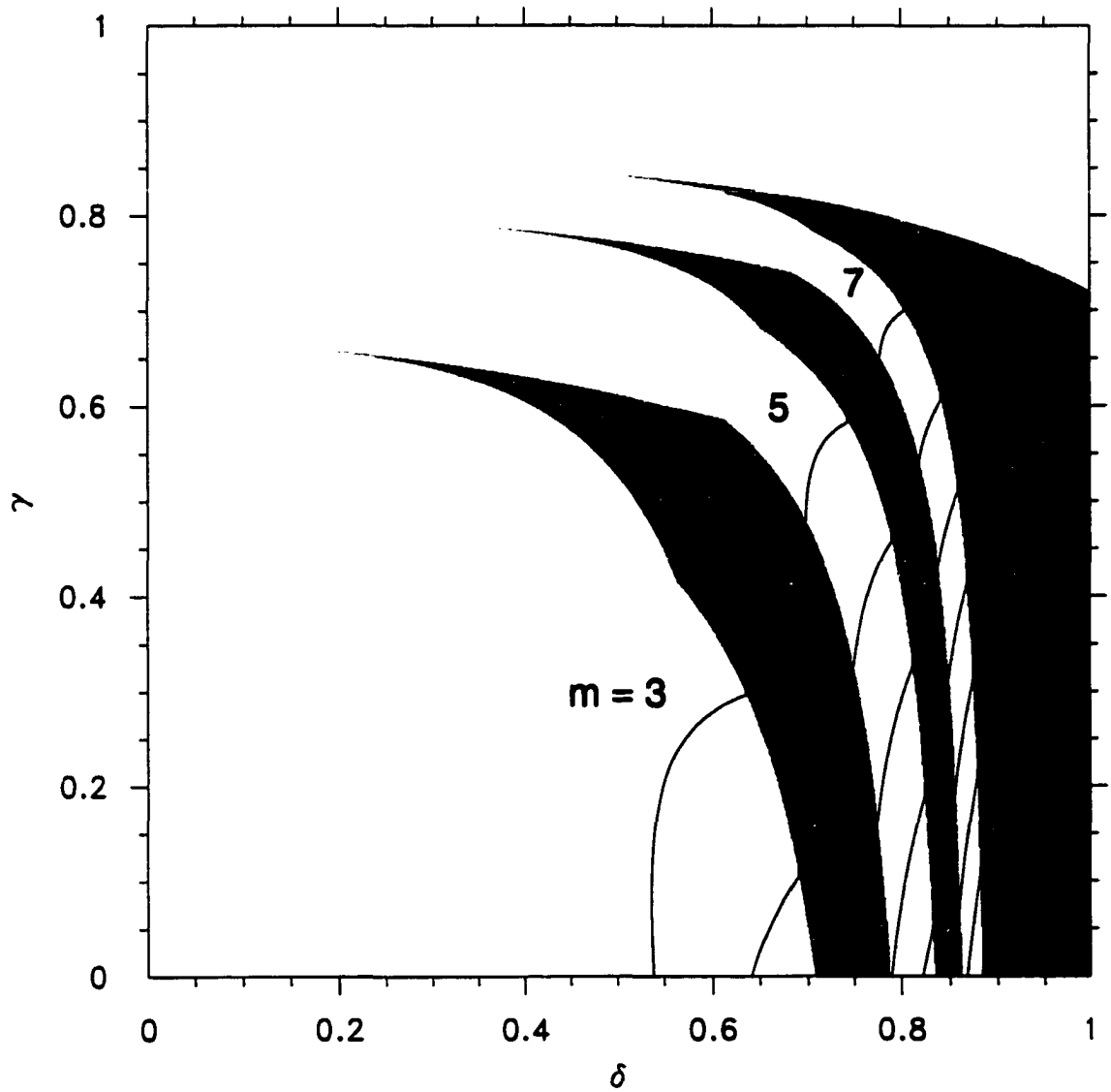

Figure 3.3: Isolines of the maximum dimensionless growth rate ν_i/ζ_{av} among the azimuthal wavenumbers $m = 3, 4, \ldots, 8$. The displayed isolines are the same as in Fig. 3.2, and again the largest growth rates occur in the lower right corner of the figure. Shading indicates the wavenumber associated with the maximum dimensionless growth rate at each point (from Schubert et al. 1999).

Reproduced with permission of the copyright owner. Further reproduction prohibited without permission.

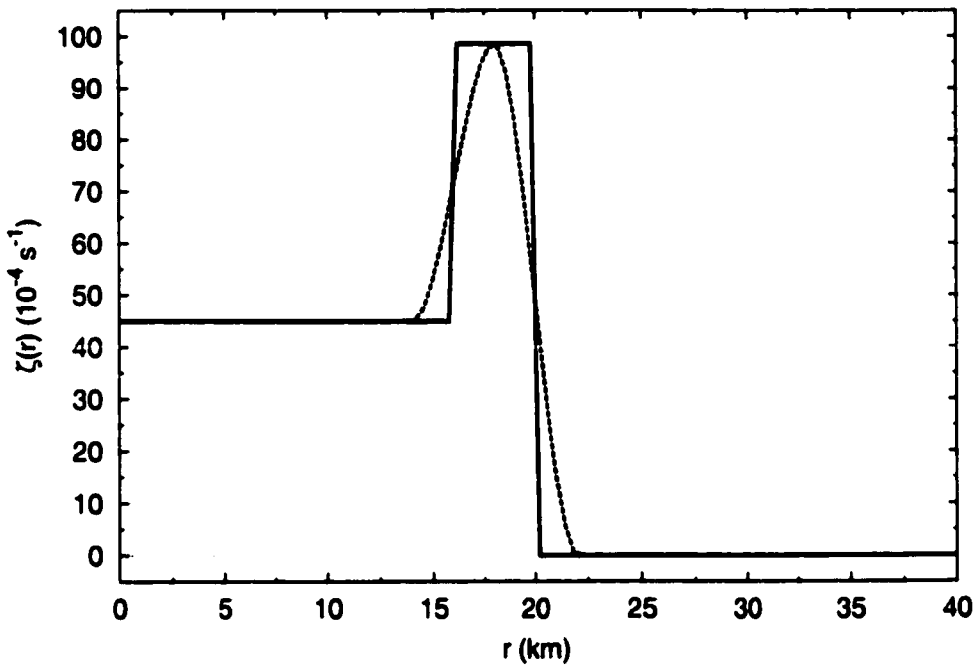

Figure 3.4: Piecewise uniform vorticity profile (solid) and its continuous analogue (dashed) for the case of a small intense hurricane-like vortex with a radially thin eyewall.

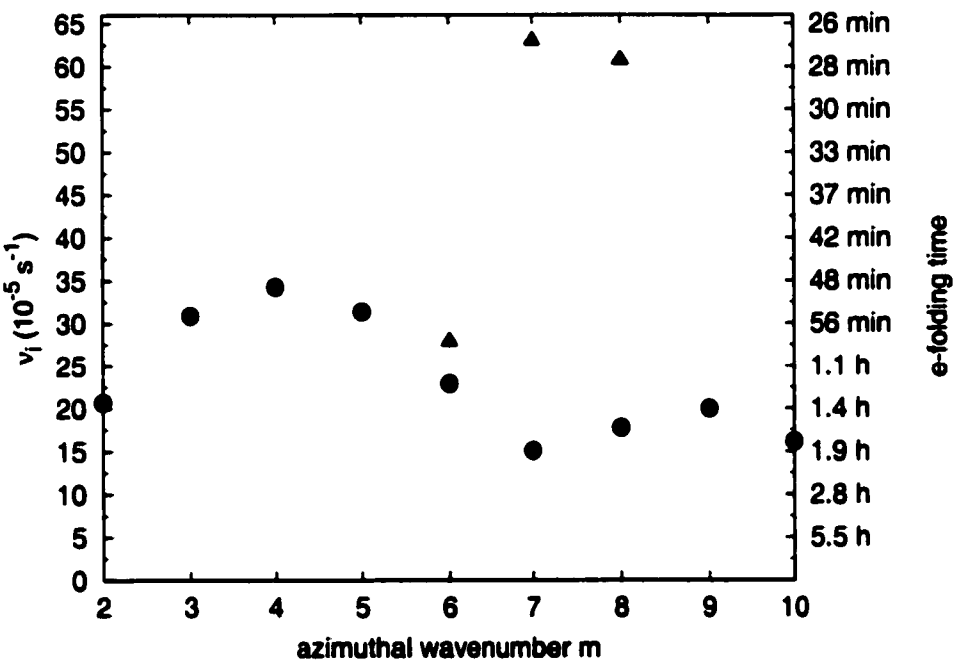

Figure 3.5: Instability growth rates and e-folding times for the case of the piecewise uniform idealization (triangles) and its continuous analogue (circles) shown in Fig. 3.4.

Reproduced with permission of the copyright owner. Further reproduction prohibited without permission.

Figure 3.6: Vorticity contour plots for the annular ring experiment. The model domain is 200 km × 200 km but only the inner 55 km × 55 km is shown. The contours begin at 7×10^{-4} s^{-1} and are incremented by 14×10^{-4} s^{-1}. Values along the label bar are in units of 10^{-4} s^{-1}. Warmer colors are associated with higher values of vorticity. Model run time in hours is shown on each plot. (a) $t = 0$ h to 3 h.

Reproduced with permission of the copyright owner. Further reproduction prohibited without permission.

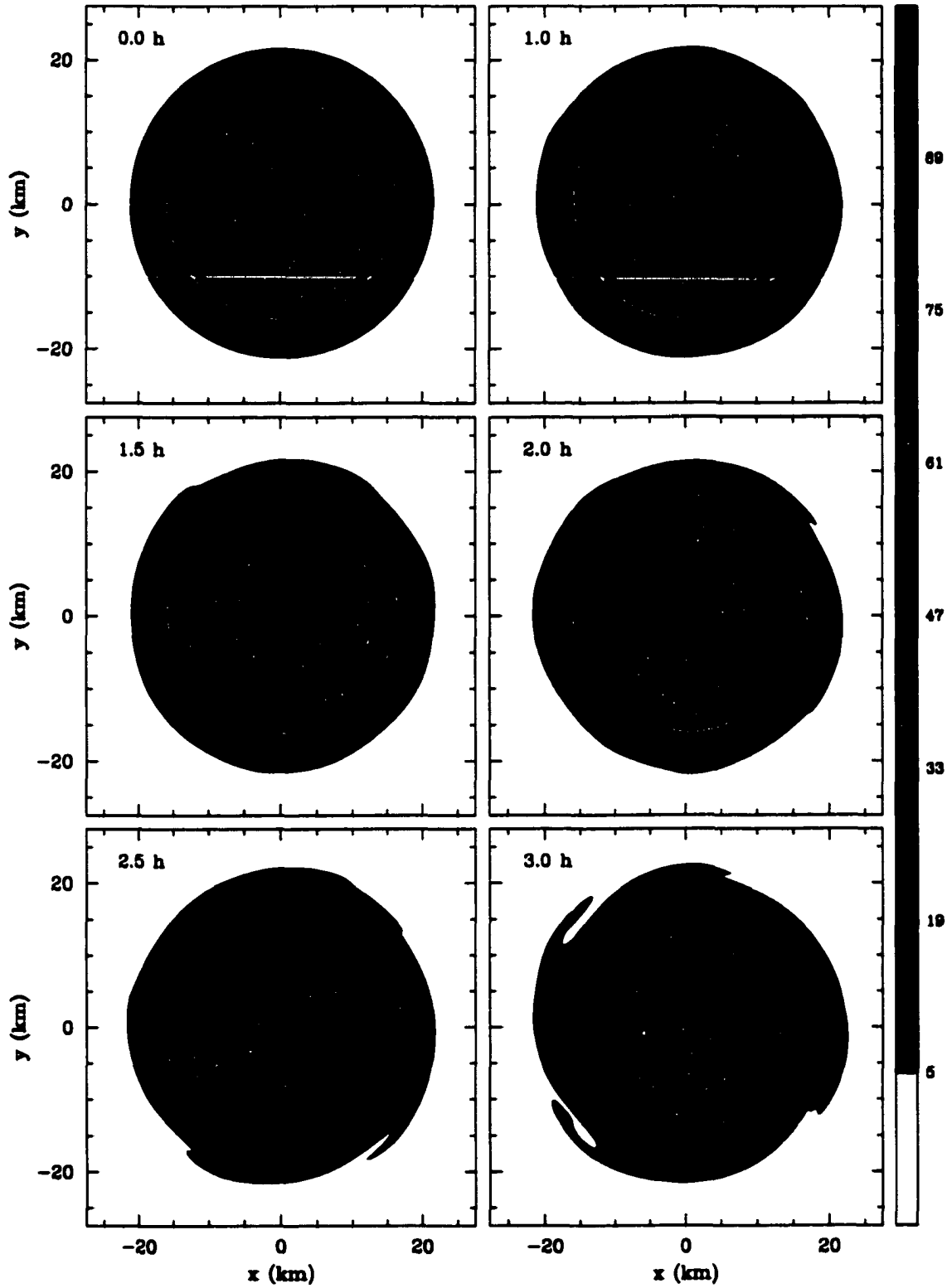

Figure 3.6: (a) See caption on previous page.

Reproduced with permission of the copyright owner. Further reproduction prohibited without permission.

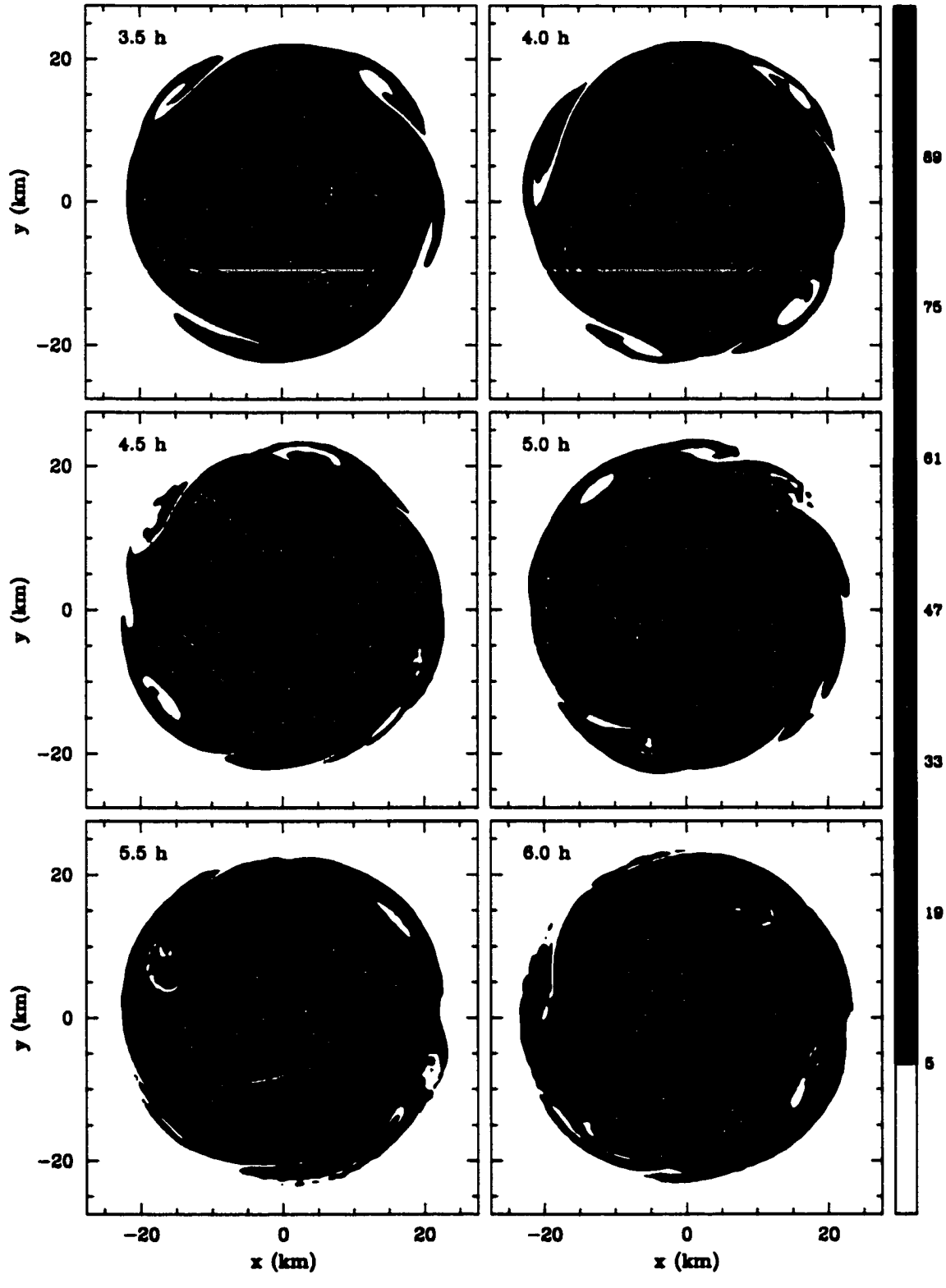

Figure 3.6: (*Continued*) (b) Vorticity from $t = 3.5$ h to 6 h.

Reproduced with permission of the copyright owner. Further reproduction prohibited without permission.

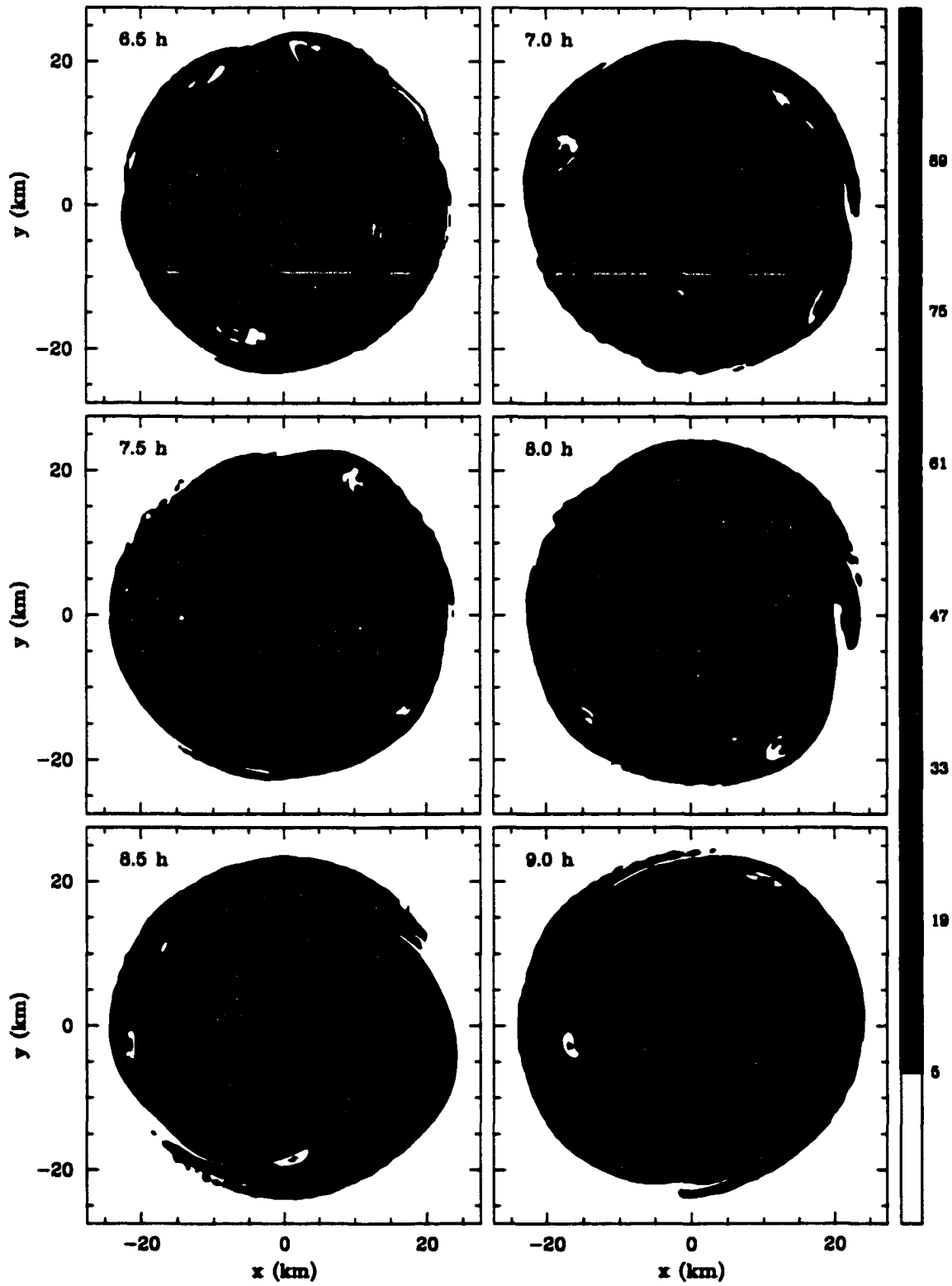

Figure 3.6: (*Continued*) (c) Vorticity from $t = 6.5$ h to 9 h.

Reproduced with permission of the copyright owner. Further reproduction prohibited without permission.

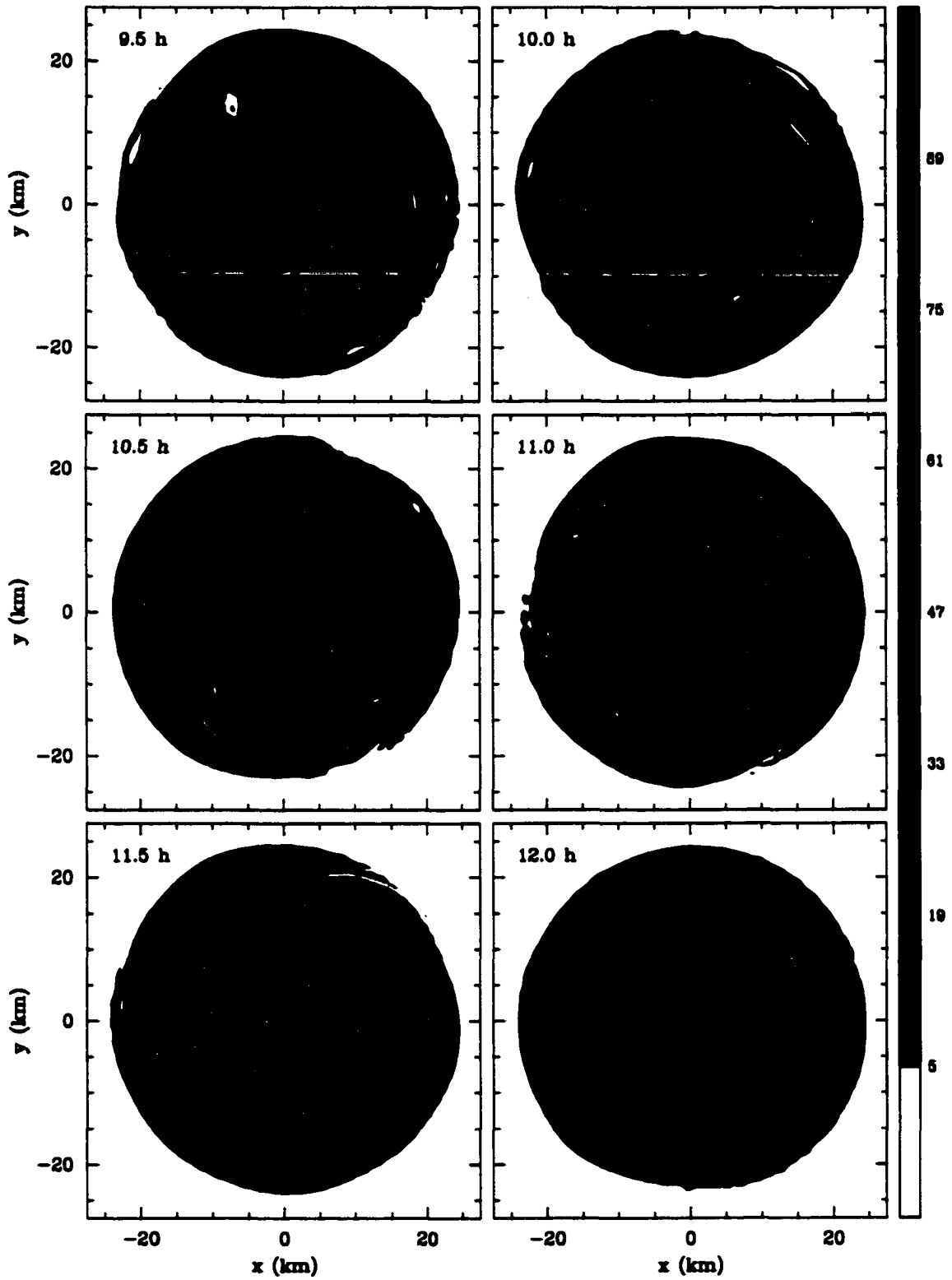

Figure 3.6: (*Continued*) (d) Vorticity from $t = 9.5$ h to 12 h.

Reproduced with permission of the copyright owner. Further reproduction prohibited without permission.

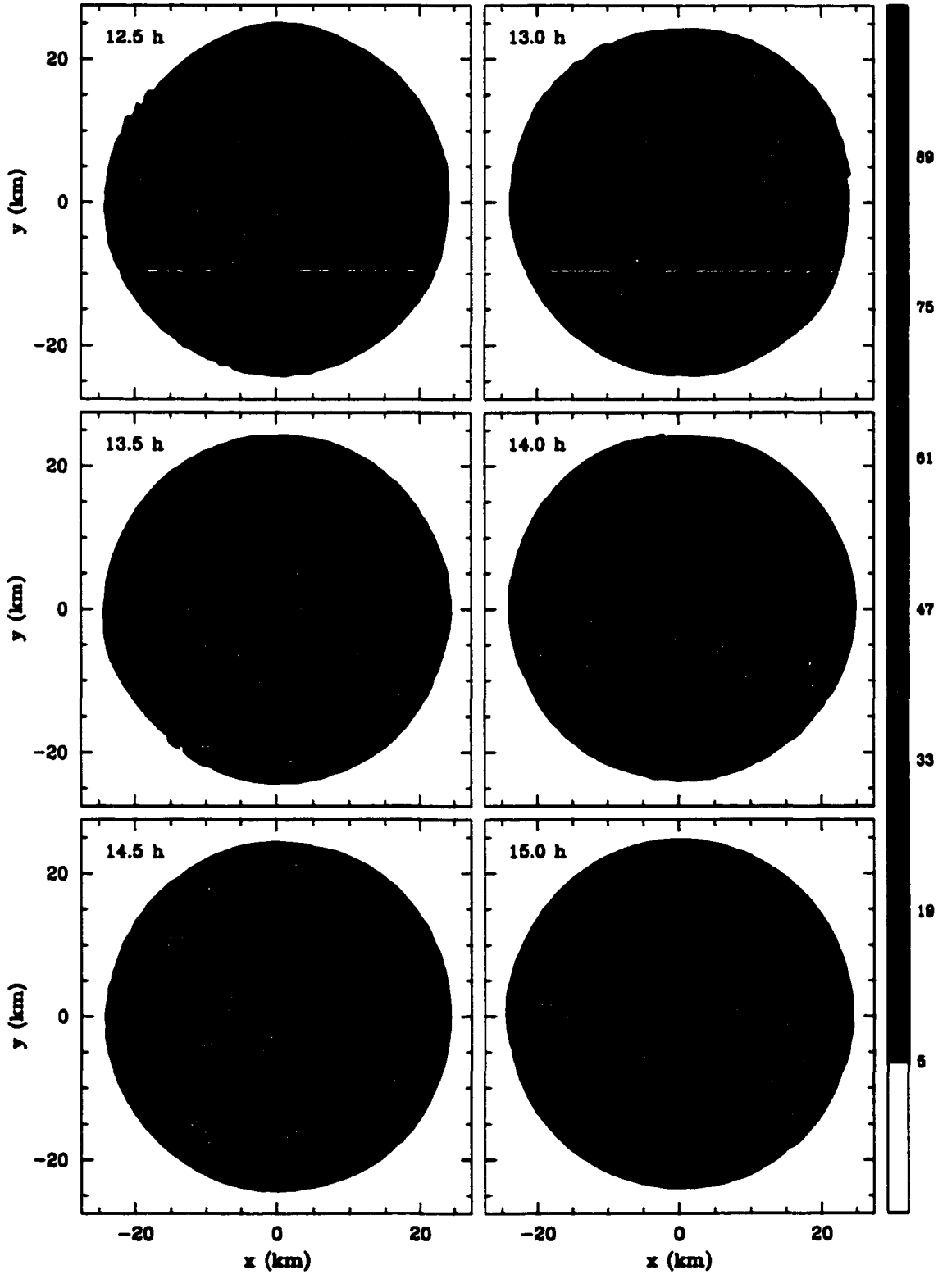

Figure 3.6: (*Continued*) (e) Vorticity from $t = 12.5$ h to 15 h.

Reproduced with permission of the copyright owner. Further reproduction prohibited without permission.

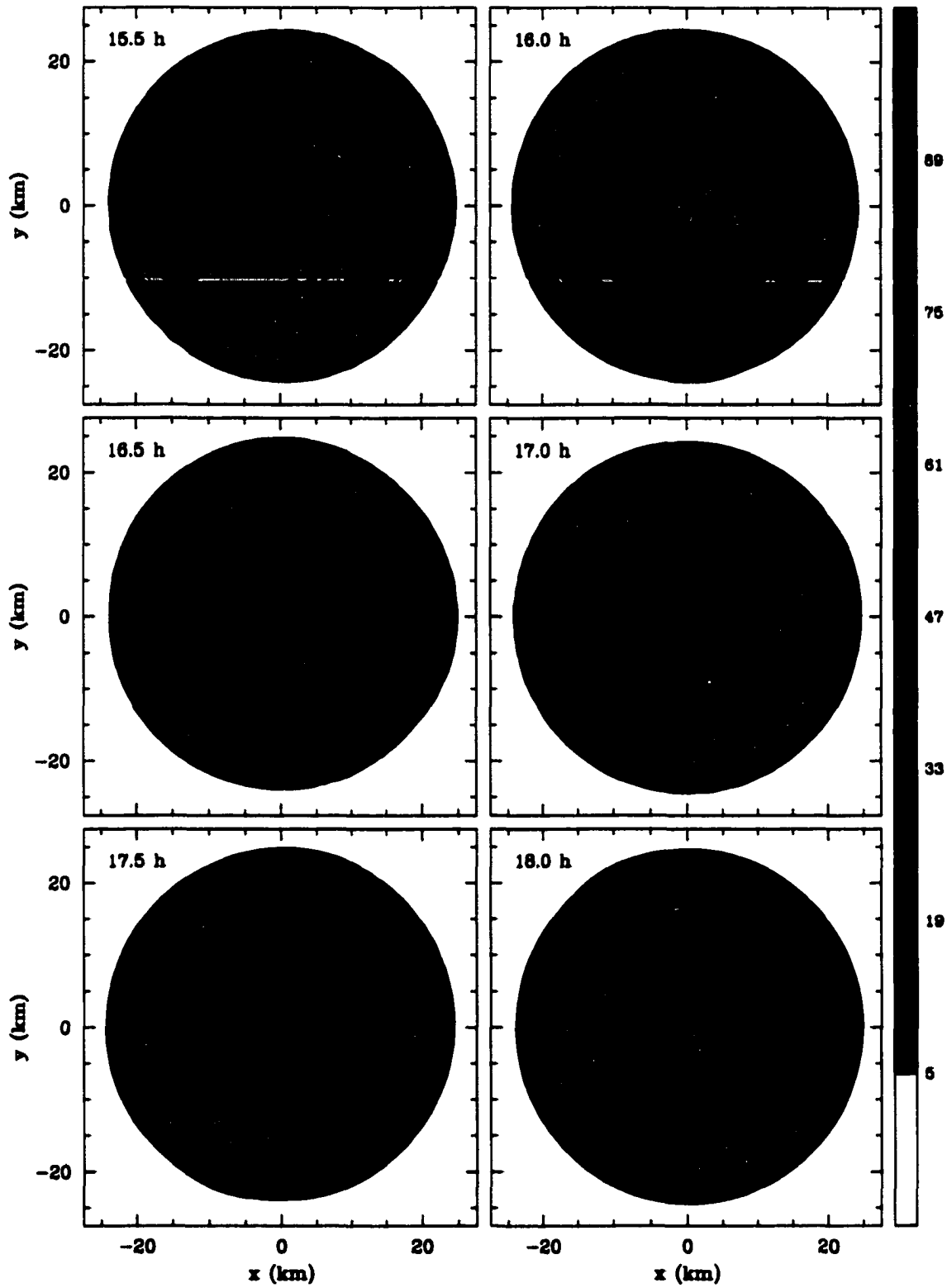

Figure 3.6: (*Continued*) (f) Vorticity from $t = 15.5$ h to 18 h.

Reproduced with permission of the copyright owner. Further reproduction prohibited without permission.

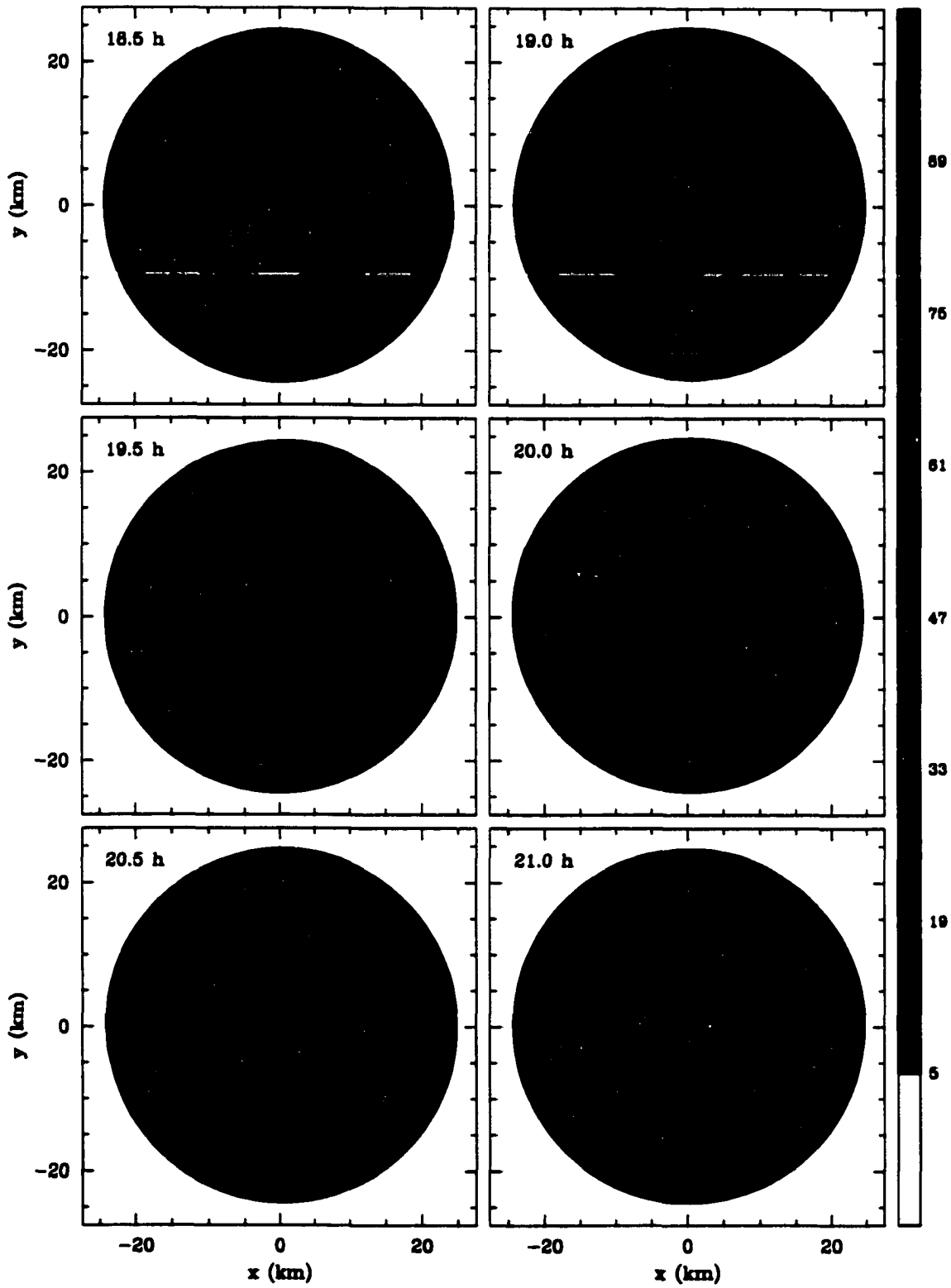

Figure 3.6: (*Continued*) (g) Vorticity from $t = 18.5$ h to 21 h.

Reproduced with permission of the copyright owner. Further reproduction prohibited without permission.

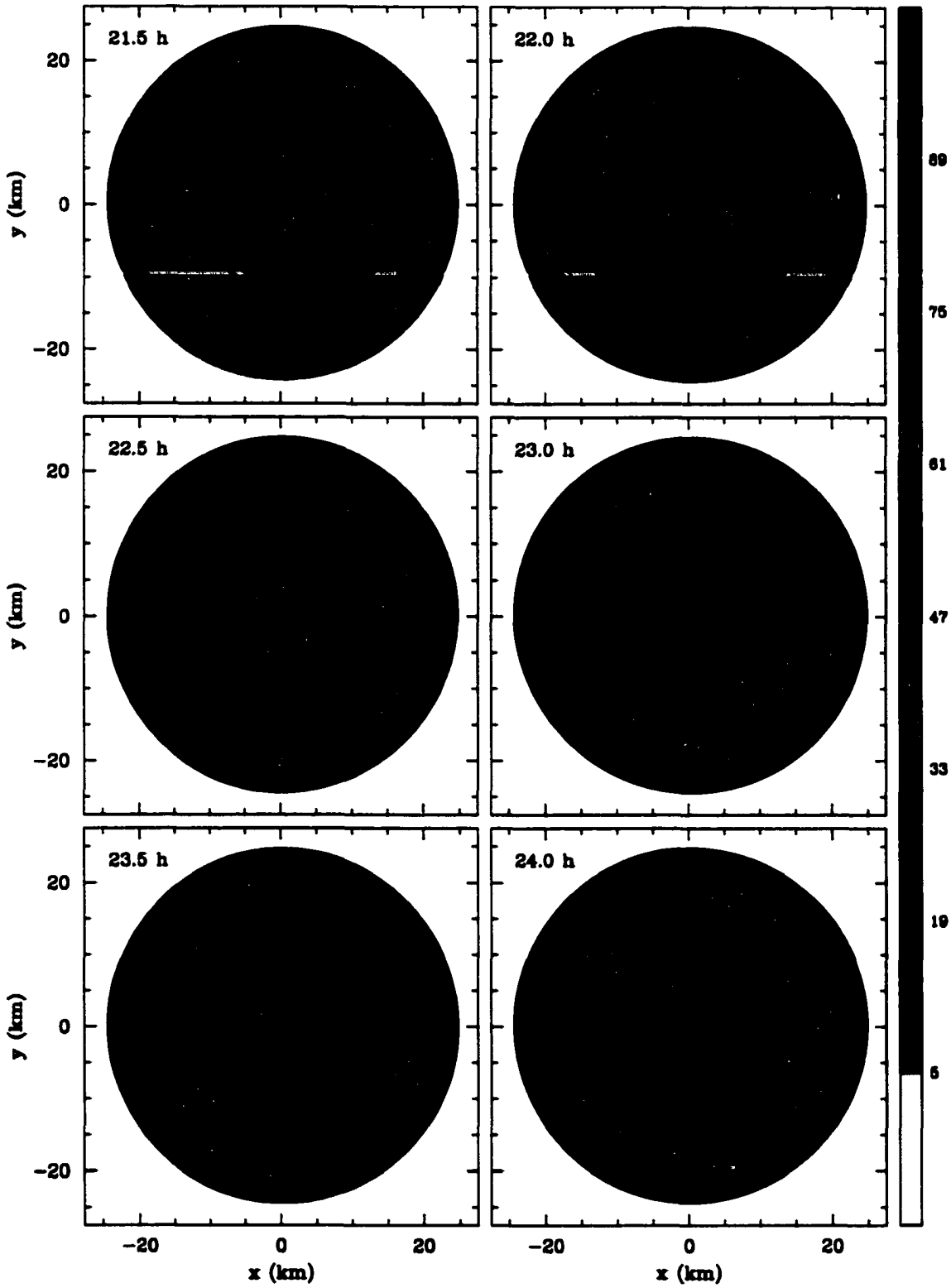

Figure 3.6: (*Continued*) (h) Vorticity from $t = 21.5$ h to 24 h.

Reproduced with permission of the copyright owner. Further reproduction prohibited without permission.

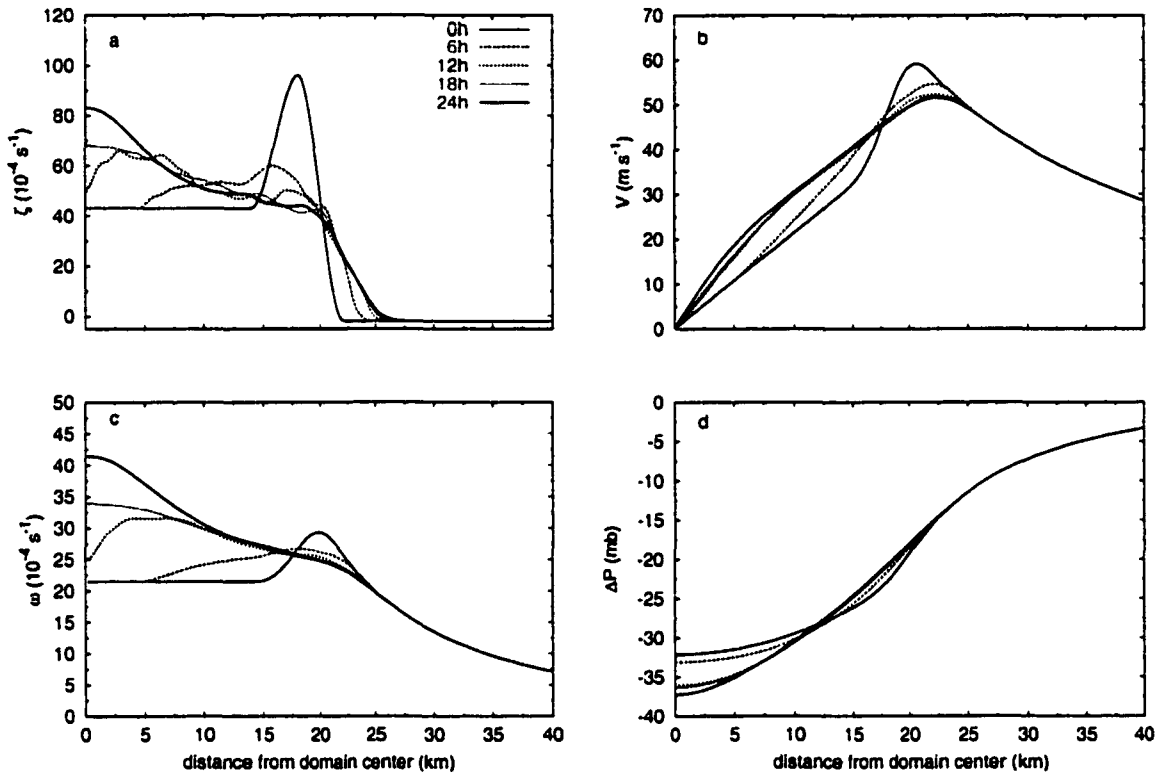

Figure 3.7: (a) Azimuthal mean vorticity, (b) tangential velocity, (c) angular velocity, and (d) pressure deviation for the experiment shown in Fig. 3.6 at the selected times $t = 0$ (thin solid black), 6 h (green long dash), 12 h (blue medium dash), 18 h (fuschia short dash), and 24 h (thick solid red). Averages were computed with respect to distance from the domain center. The pressure deviation Δp is fixed at zero at $r = 100$ km.

Reproduced with permission of the copyright owner. Further reproduction prohibited without permission.

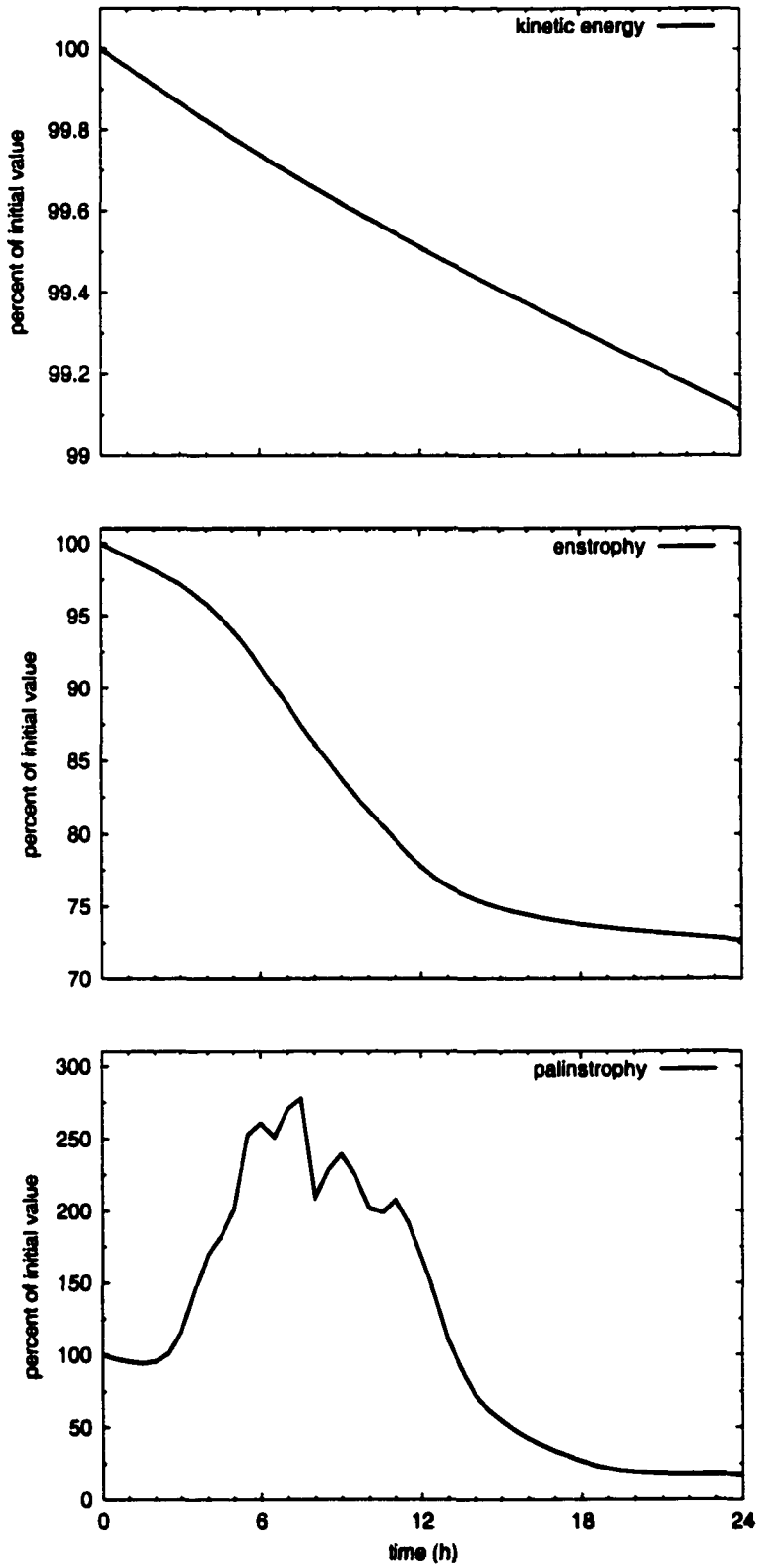

Figure 3.8: Time evolution of globally integrated kinetic energy ($\mathcal{E}$), enstrophy ($\mathcal{Z}$), and palinstrophy ($\mathcal{P}$), normalized by their initial values, for the experiment shown in Fig. 3.6.

Reproduced with permission of the copyright owner. Further reproduction prohibited without permission.

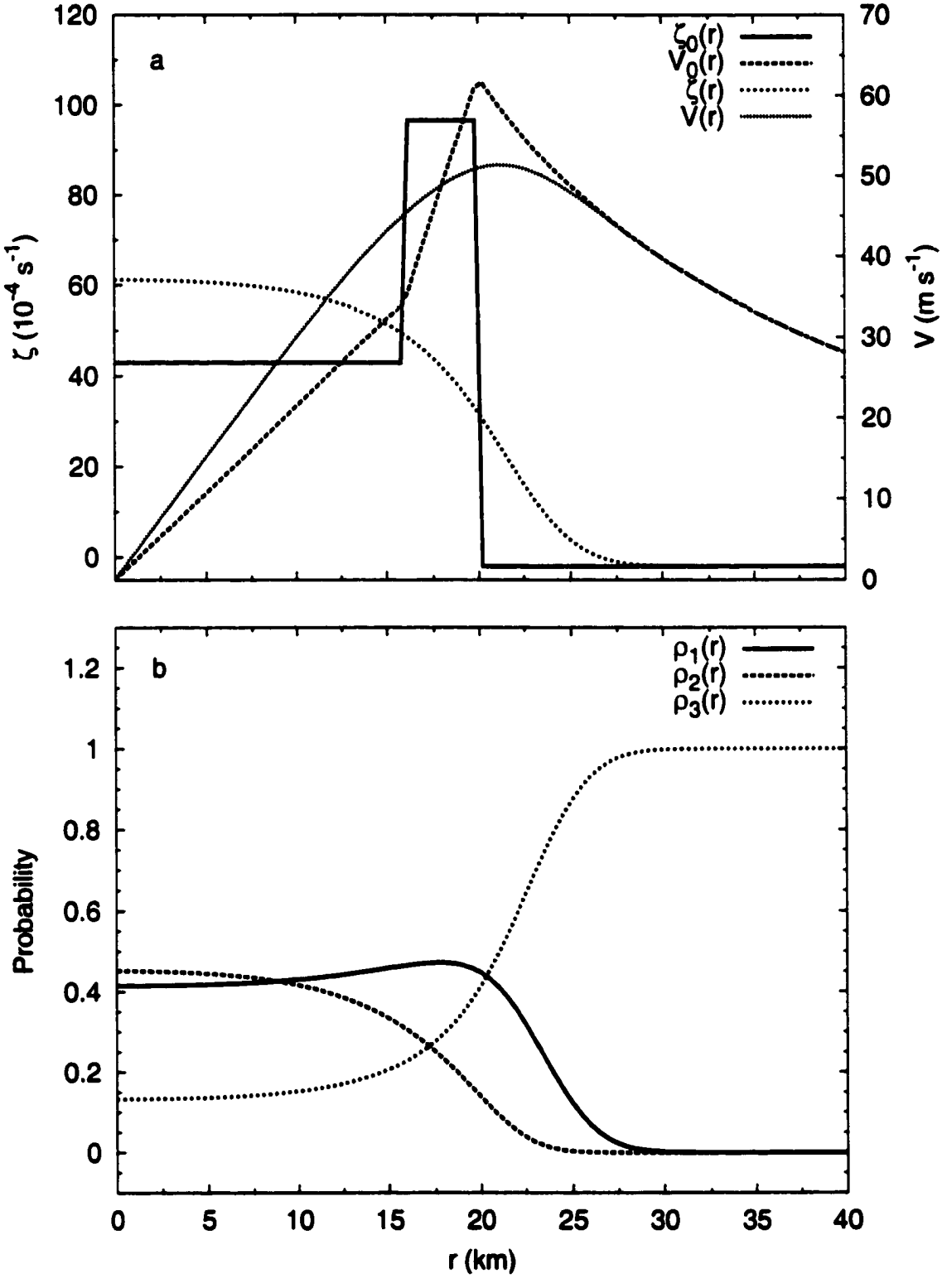

Figure 3.9: Maximum entropy predictions for the three-region model analogy to the initial condition of the annular ring experiment. (a) Initial vorticity $\zeta_0(r)$ and tangential wind $v_0(r)$, and equilibrated vorticity $\zeta(r)$ and tangential wind $v(r)$ predicted by the maximum entropy theory. (b) Expectation functions.

Reproduced with permission of the copyright owner. Further reproduction prohibited without permission.

Chapter 4

OBSERVATIONAL EVIDENCE FOR TURBULENT EXCHANGE BETWEEN THE HURRICANE EYE AND EYEWALL

The results of Chapter 3 provoke some questions, two of which are addressed here. Can we find observational verification that this process of turbulent exchange actually occurs in hurricanes, and if so, does the barotropic model adequately capture the observed physics? The most effective observational verification would come in the form of spatially and temporally detailed PV maps of the hurricane near-core region, but such maps are not currently available. As an alternative, we will employ one-dimensional flight-level data as a first step towards capturing the typical flow evolution of the hurricane eyewall and eye. Comparisons of the observed evolution with the numerical results of Chapter 3 will be discussed.

As demonstrated in Chapter 2, the diabatic heating within the eyewall elevates the local PV and sets the stage for the development of barotropic instability. This raises interesting questions about the observed presence of hollow tower PV configurations in hurricanes. If we imagine that the production of PV in the eyewall is constantly serving to destabilize the flow there, while horizontal PV rearrangement is constantly serving to remove the instability through nonlinear mixing, then the physics may be described as a battle between two *ongoing* processes. Since eyewall PV production is likely to be greater during an intensification phase and weaker during a non-intensifying phase, which process dominates may be expected to depend on the hurricane's rate of intensity change. In this case, we may expect to find highly

Reproduced with permission of the copyright owner. Further reproduction prohibited without permission.

elevated eyewall PV in intensifying hurricanes and quasi-monotonic PV profiles in non-intensifying hurricanes.

An alternative consideration is that during intensification, diabatic forcing in the eyewall may act to locally stabilize the flow. Andrews (1984) demonstrated that topographically induced flows in a nondivergent barotropic model can be stabilized by the topography itself. Although external forcing by topography is quantitatively different from diabatic forcing which is internal (i.e., contained within the flow), qualitative similarities may exist. Nolan (1999) and Nolan and Farrell (1999) demonstrated that stretching and radial inflow within and near the eyewall can decrease the growth rates of an unstable flow, although this effect may be slight. It could be surmised then, that if the forcing is greater during intensification, hollow tower structures may be more prevalent during intensification.

The question of how nonconservative effects might stabilize flows in the hurricane near-core is fundamental question, but we leave it here as an open question. Regardless of whether the flow is constantly being adjusted by nonlinear mixing processes or is in fact being stabilized by nonconservative effects, we can hypothesize the following: during intensification of a hurricane, the material increase of PV within the eyewall dominates and the mean radial profile of PV is that of a hollow tower. During non-intensifying phases, nonlinear asymmetric PV rearrangement dominates and the PV profile tends to be monotonic.

4.1 Data and methodology

The work presented here utilizes flight-level wind data from the National Oceanic and Atmospheric Administration (NOAA) Hurricane Research Division (HRD) archive of aircraft observations collected over 20 years (1977-1996) from 44 Atlantic and Eastern Pacific hurricanes. The data were collected by two NOAA WP-3D research aircraft and the Air Force 53rd Weather Reconaissance fleet of WC-130 aircraft. A formal

Reproduced with permission of the copyright owner. Further reproduction prohibited without permission.

description of the data processing and WP-3D instrumentation is found in Jorgensen (1984). Instrumentation onboard the WC-130 aircraft is nearly identical to that of the WP-3D aircraft but the data recording frequency is 0.1 Hz on the WC-130 versus 1.0 Hz on the WP-3D. The accuracies of the horizontal winds (tangential and radial) are $\pm$ 1.0 m s^{-1} and $\pm$2.0 m s^{-1} for the WP-3D and WC-130 aircraft respectively (OFCM 1993). The database consists of storm-relative observations of the three-dimensional wind field in cylindrical coordinates[3], temperature, dewpoint, geopotential height, and the aircraft location given in latitude and longitude, partitioned into radial legs. A radial leg is defined as either an inbound flight path toward the storm center, or an outbound path away from the storm center. Data within each radial leg is distributed into 0.5 km average bins. The radial legs used in this study were flown along the 850, 700, 600, and 500 hPa constant pressure surfaces.

For our purposes, we analyzed only the observed flight-level tangential winds, from which relative vorticity profiles were deduced. The one-dimensional nature of the data constrained our results to be approximate since only radial variations could be considered. Thus we are resigned to neglect contributions to the vorticity from asymmetric and vertical variations in the flow. Understanding this limitation, the vertical component of the relative vorticity associated with the swirling flow v in a polar coordinate system translating with the hurricane center is given by

$$\zeta(r,\phi) = \frac{v(r,\phi)}{r} + \frac{\partial v(r,\phi)}{\partial r}. \tag{4.1}$$

Noting that ϕ is roughly fixed along any radial leg, application of (4.1) to the flight-level data was performed using the difference formula, $\zeta(\bar{r}_i,\phi) = \bar{v}_i/\bar{r}_i + (v_{i+1} - v_i)/(r_{i+1} - r_i)$ where $\bar{r}_i = (r_i + r_{i+1})/2$ and $\bar{v}_i = (v_i + v_{i+1})/2$ and the subscripts refer to bin position. All vorticity profiles displayed in this chapter were smoothed using a 7 point filter with weights (1/15)(1,2,3,3,3,2,1), which effectively removes oscillations with wavelengths less than 5.5 km.

[3]Observations taken by the WC-130 aircraft include only horizontal winds.

Reproduced with permission of the copyright owner. Further reproduction prohibited without permission.

In the near-core region of hurricanes, where the curvature term v/r is always positive, the vorticity tends to achieve its maximum just inside the RMW where the shear term $\partial v/\partial r$ changes sign from negative to positive (as one moves inwards). Thus, if we wish to avoid smoothing out significant vorticity maxima, each vorticity profile from a given set of radial legs can be arranged with respect to distance from the RMW for that leg and the adjusted set can then be averaged with respect to distance from the RMW. This type of averaging has the desired effect of identifying (and accentuating) the presence of sharp peaks in the eyewall vorticity, but can also have the possibly undesirable effect of artificially masking the asymmetric nature of the peaks. For example, vorticity profiles may be sharply peaked in the eyewall but the eyewall may be far from circular. Recognizing the limitations of our averaging method, but also the unfeasibility of displaying each of the large number of radial legs within the data set, we choose to apply the averaging method and then validate the results with representative individual radial legs.

4.2 Results

4.2.1 Averages by sortie

In order to approximate the temporal evolution of a hurricane's vorticity profile, we construct averaged profiles associated with sequential aircraft sorties. A sortie consists of a set of sequential inbound and outbound radial legs associated with one particular aircraft. The number of radial legs contained in the sorties analyzed in this study range from 4 to 16. Information regarding the mean rate of intensity change during each sortie was deduced from the best-track post analysis database maintained by the Tropical Prediction Center in Miami, Florida. As a case study, we apply the averaging analysis to Hurricane Andrew (1992). This choice is somewhat arbitrary and is based on good temporal data coverage.

During the period 22–23 August 1992, Hurricane Andrew steadily intensified from a

Reproduced with permission of the copyright owner. Further reproduction prohibited without permission.

tropical storm to a category 4 hurricane with sustained winds of 135 kt and central pressure of 922 hPa. Between 18 UTC 23 August and 18 UTC 24 August, Andrew underwent a concentric eyewall cycle as it passed over the Bahamas resulting in a period of weakening (Willoughby and Black 1996). With the exception of a short period of re-intensification while making landfall over Homestead, Florida, Andrew continued to weaken over land. After re-emerging over the Gulf of Mexico between 12 and 18 UTC 24 August, Andrew again strengthened and remained a category 4 hurricane until making a second landfall in Louisiana on 26 August where it quickly weakened to a category 1 hurricane. The evolution of Andrew's central pressure and maximum winds is shown in Fig. 4.1. Air Force reconnaissance sorties which were continuously flown into Andrew are denoted by the black squares in Fig. 4.1 and are described in Table 4.1. All sorties were flown at 700 hPa. The averaged vorticity profiles during each sortie are shown in Fig. 4.2. During sorties 1–3, while Andrew steadily intensified, the eyewall vorticity became increasingly peaked. Although sortie 4 was flown while Andrew was beginning to weaken, the cumulative effects of the previous intensification result in the most dramatically peaked profile of all 7 sorties shown. Equally striking is the transformation between sorties 4 and 5. During sortie 5, intensification had been halted for 12 hours and the averaged vorticity relaxed to a monotonic profile.

It should be noted that the sortie averaged RMW calculated from the flight-level data increased from 11 km during sortie 4 to 21 km during sortie 5 (Table 4.1). This raises questions regarding how an expanding eyewall could affect the averaged vorticity profiles regardless of the presence of asymmetric eddy transport of vorticity to the center. For example, the evolution of eyewall vorticity, deduced from tangential winds in gradient balance with a decreasing radial pressure gradient, would exhibit a decrease in its maximum. This could also result in a more monotonic vorticity profile. To address this, we construct tangential wind profiles for sorties 4 and 5 using the same averaging method applied to the vorticity profiles. These are shown in Fig. 4.3.

Reproduced with permission of the copyright owner. Further reproduction prohibited without permission.

Recalling the average RMW for each sortie, it is evident that the tangential wind near the center of Andrew has increased from 9 m s^{-1} to 20 m s^{-1} between the two sorties. This spin-up of the tangential wind in the eye is not congruent with eyewall expansion alone and suggests an inward transport of angular momentum.

Further evidence that a transformation from a peaked to an approximately monotonic vorticity profile is not requisitely linked to an eyewall expansion can be found by analyzing hurricanes which do not exhibit an increase in RMW during the transformation. Examples of this are found in Hurricanes Hortense (1996), Elena (1985), and Diana (1984). Representative sortie-averaged vorticity profiles for these storms are described in Table 4.2 and shown in Fig. 4.4. In each case, cessation of intensification corresponds to a relaxation to a nearly monotonic profile with no appreciable change in the average location of the RMW.

The evolution of intensity in Andrew was influenced by the occurrence of a concentric eyewall cycle and several encroachments onto land. Analyses of hurricanes experiencing intensity change not associated with concentric eyewall cycles or land effects yielded similar results. The fundamental results shown for Andrew were found to be generic and the causal circumstances for intensity change do not appear to play any significant role in our results.

4.2.2 Example of vorticity evolution with no averaging

To validate the results of section 4.2.1, we now display individual radial profiles from within representative sorties. We choose sorties 4 and 5 in Hurricane Andrew and sorties 1, 2, and 3 in Hurricane Diana. This choice is based on the dramatic nature of their vorticity profile transitions shown in Fig. 4.2 and Fig. 4.4. Profiles of tangential wind and vorticity in Andrew are shown in Fig. 4.5. During sortie 4 (Fig. 4.5a), as Andrew has just ended a long period of rapid intensification, the vorticity is generally sharply peaked within the eyewall (just inside the RMW), while the vorticity in the

Reproduced with permission of the copyright owner. Further reproduction prohibited without permission.

eye and outside the eyewall is relatively depressed. The enhanced eyewall vorticity is thin, in the sense of its radial extent, which suggests that the reversal in sign of the vorticity gradient could support phaselocking of counterpropagating vortex Rossby waves as described in chapter 3. If such an instability were present, we might expect the vorticity to undergo a turbulent rearrangement towards a more monotonic state. This appears to occur during sortie 5 (Fig. 4.5b–c) where many of the vorticity profiles suggest that the vorticity across the eye and eyewall has become more uniform.

It is important to point out here, that due to instrumentation problems, the data available during sortie 5 is of a lesser resolution than the data of sortie 4 (Powell et al. 1996). This is apparent in the smoothed nature of Fig. 4.5b–c and may cause our results to be less convincing, since it is possible that such smoothing could remove significant peaks in the vorticity profiles. The following results using uncompromised data from Hurricane Diana, however, are shown to be consistent with our results from Andrew.

The evolution of tangential wind and vorticity in Hurricane Diana is shown in Fig. 4.6. Around 1130 UTC 11 September (top panel of Fig. 4.6a), Diana had been intensifying from a minimal category 1 to a category 3 hurricane during the previous 24 hours and continued to intensify over the next 12 hours (middle panel of Fig. 4.6a to top panel of Fig. 4.6d), becoming a category 4 hurricane around 0000 UTC 12 September (middle panel of Fig. 4.6d). During this period of intensification, the vorticity in the eyewall is sharply peaked and much higher than the vorticity in the eye. An extreme example of this is found in the top panel of Fig. 4.6c where the tangential winds increase from 17 m s^{-1} at 10 km radius to 55 m s^{-1} at 12 km radius. The near discontinuity of this flow may support the hypothesis that the dynamics of the eyewall are frontogenetic (Emanuel 1997).

After 0000 UTC 12 September, as Diana approached the east coast of the Carolinas, and just prior to executing a loop in its track, Diana rapidly weakened, and became

Reproduced with permission of the copyright owner. Further reproduction prohibited without permission.

a category 2 hurricane in the next 6 hours. In just 1 hour after the cessation of intensification, the vorticity profiles changed dramatically (bottom panel of Fig. 4.6d) and in the next hour, the vorticity profiles became nearly monotonic (top panel of Fig. 4.6e) and remained so for the next 8 hours. An interesting feature which seems to coincide with the transition of the vorticity from peaked to monotonic profiles, is the transition from a smoother to a more "noisy" profile. This would be expected under our hypothesis since turbulent rearrangement of unstable vorticity fields would be accompanied by the presence of vorticity filamentation within the eye and eyewall. This will be discussed further in section 4.2.4.

4.2.3 Averages by intensity change

To take better advantage of the complete flight-level data set, we now consider an analogous but slightly different averaging method than that of section 4.2.1. Using the data at a particular flight-level from all category 3, 4, and 5 hurricanes, we categorize each radial leg according to whether the hurricane was intensifying or not intensifying at the time the radial leg was flown (Table 4.3). Intensification is defined as an increase in the best-track maximum sustained wind greater than 10 knots over the 12 hour period centered on the time the radial leg was flown. There is little sensitivity of our results to the choice of 10 knots and very similar results are obtained in the range 5–15 knots. Similarly, there is little sensitivity between time intervals of 12 hours and less than 12 hours. Differences do emerge however if the interval is much greater than 12 hours. This is expected since intensity trends typically occur on time scales near 12 hours so that a 24 hour time interval for example tends to contain both intensification and non-intensification processes.

The averaged vorticity profiles for each flight level are shown in Fig. 4.7. During intensification, the vorticity in the eyewall exhibits a statistically significant peaked maximum at all levels[4]. For non-intensifying hurricanes, the average flow within the

[4]Attention should be given to the shape of the profiles here. Since the averages at any given level

Reproduced with permission of the copyright owner. Further reproduction prohibited without permission.

eye is close to solid-body rotation although the vorticity does increase slightly with radius. It is interesting to note that this slight increase of vorticity with radius is described by Emanuel (1997) as a theoretical requirement for steady state since the inward turbulent transfer of angular momentum must constantly act to balance the loss of angular momentum to the sea surface.

4.2.4 Comparison with numerical results

We now compare our observational results with those of the numerical experiment of Fig. 3.6. To do this, we can imagine an aircraft flying across the model domain. If the imaginary aircraft has a cruising speed similar to the actual aircraft described in section 4.1, i.e. $\sim$ 130 m s^{-1}, then a 40 km wide subdomain would be traversed in about 5 minutes of flight time. Thus a simple cross section of the inner model domain, at a fixed time, should well imitate an aircraft radial leg. We arbitrarily choose west to east cross sections from $x = 0$ to $x = 40$ km along the $y = 0$ line, and we will confine our comparisons to the observations of Hurricane Diana shown in Fig. 4.6. As a general representation of the vorticity evolution in Diana, we consider two time periods. The first time period is 1742–1800 UTC 11 September (inbound leg of the middle panel of Fig. 4.6c) and represents the flow shortly after intensification has ceased. The second time period is $\sim 7-8$ hours later during 0102–0123 UTC 12 September (inbound leg of the bottom panel of Fig. 4.6d). The vorticity profiles for each time period are shown in Fig. 4.8a.

The observed vorticity in Diana during the earlier time period demonstrates the peaked nature of the eyewall vorticity and the profile tends to follow a fairly smooth transition from the weaker vorticity outside the eyewall, to the strongest vorticity within the eyewall, and to the weaker vorticity in the eye. In contrast, the profiles during the later time period are much less peaked. The vorticity in the eyewall region

contain data from varying combinations of category 3, 4, and 5 hurricanes, comparisons between levels of the actual vorticity values has little meaning.

Reproduced with permission of the copyright owner. Further reproduction prohibited without permission.

is much weaker while the vorticity near the center of the eye ($r < 5$ km) has increased substantially. The vorticity just outside the eyewall ($15 < r < 20$ km) has also experienced a substantial increase. In a rough sense, the vorticity profile across the eye and eyewall has become broader and flatter. In a finer sense however, the profile has become more "noisy" and exhibits a much more oscillatory structure inside $r = 20$ km.

Cross sections of the model vorticity (for the experiment of chapter 3) at $t = 0$ and $t = 12$ h are shown in Fig. 4.8b and bear a striking resemblance to the Diana results. At $t = 12$ h, the mixing process has resulted in a vorticity field comprised of coherent "blobs" embedded in a background of thin filaments. The eyewall vorticity is weaker, the eye vorticity is stronger, and the vorticity just outside the eyewall has increased. Again, in a coarse sense, the profiles have become broader and weaker while in a finer sense, the filaments result in a much noisier profile.

Reproduced with permission of the copyright owner. Further reproduction prohibited without permission.

Table 4.1: Description of sequential sorties flown into Hurricane Andrew, including the date and time period, and number of radial legs for each sortie. The mean RMW (km) for each sortie is calculated from the radial leg flight-level data while the central pressure (hPa) and intensity change is deduced from the best-track. I = Intensifying, N = Non-intensifying.

Sortie Number	Date	Time (UTC)	Number of Legs	$\overline{\text{RMW}}$	MSLP	Intensity Change
1	22 August	1500-1800	4	15.6	972	I
2	23 August	0000-0600	10	15.9	955	I
3		1200-1800	10	13.0	926	I
4		2000-2400	6	11.1	928	N
5	24 August	0200-1100	12	21.3	939	N
6		1400-2400	13	17.8	946	N
7	25 August	0600-1400	12	23.1	946	N
8		1700-2400	10	26.4	939	N
9	26 August	0100-0900	16	26.0	954	N

Table 4.2: Similar to Table 4.1 but for representative sorties in Hurricanes Hortense (1996), Elena (1985), and Diana (1984).

Storm	Sortie Number	Date	Time (UTC)	Number of Legs	$\overline{\text{RMW}}$	MSLP	Intensity Change
Hortense	1	12 Sep	1600-2400	9	15.5	941	I
	2	13 Sep	0500-1300	9	15.2	944	N
Elena	1	1 Sep	1300-2100	14	25.1	956	I
	2	2 Sep	0100-0800	12	27.3	956	N
Diana	1	11 Sep	1100-1800	16	15.8	956	I
	2		2100-0300	10	16.5	951	N
	3	12 Sep	0500-1100	14	17.0	965	N

Reproduced with permission of the copyright owner. Further reproduction prohibited without permission.

Table 4.3: Inventory by flight-level of the number of radial legs used to construct Fig. 4.7.

	850 hPa	700 hPa	600 hPa	500 hPa	Total
Intensifying	67	53	13	15	160
Non-Intensifying	67	559	126	52	810

Reproduced with permission of the copyright owner. Further reproduction prohibited without permission.

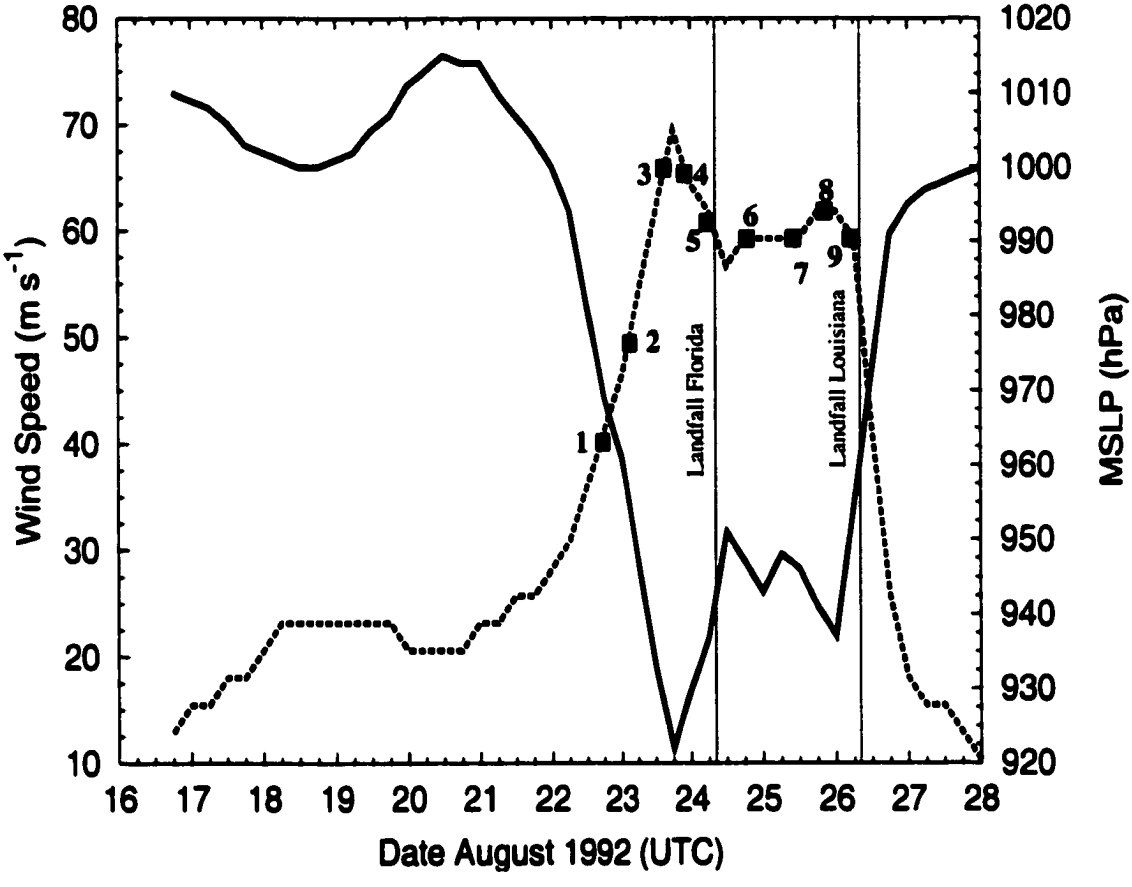

Figure 4.1: Evolution of the best track wind speed (dashed line) and central pressure (solid line) in Hurricane Andrew during the period 16–28 August 1992. Numbered black squares denote mean times of the nine individual aircraft sorties shown in Table 4.1.

Reproduced with permission of the copyright owner. Further reproduction prohibited without permission.

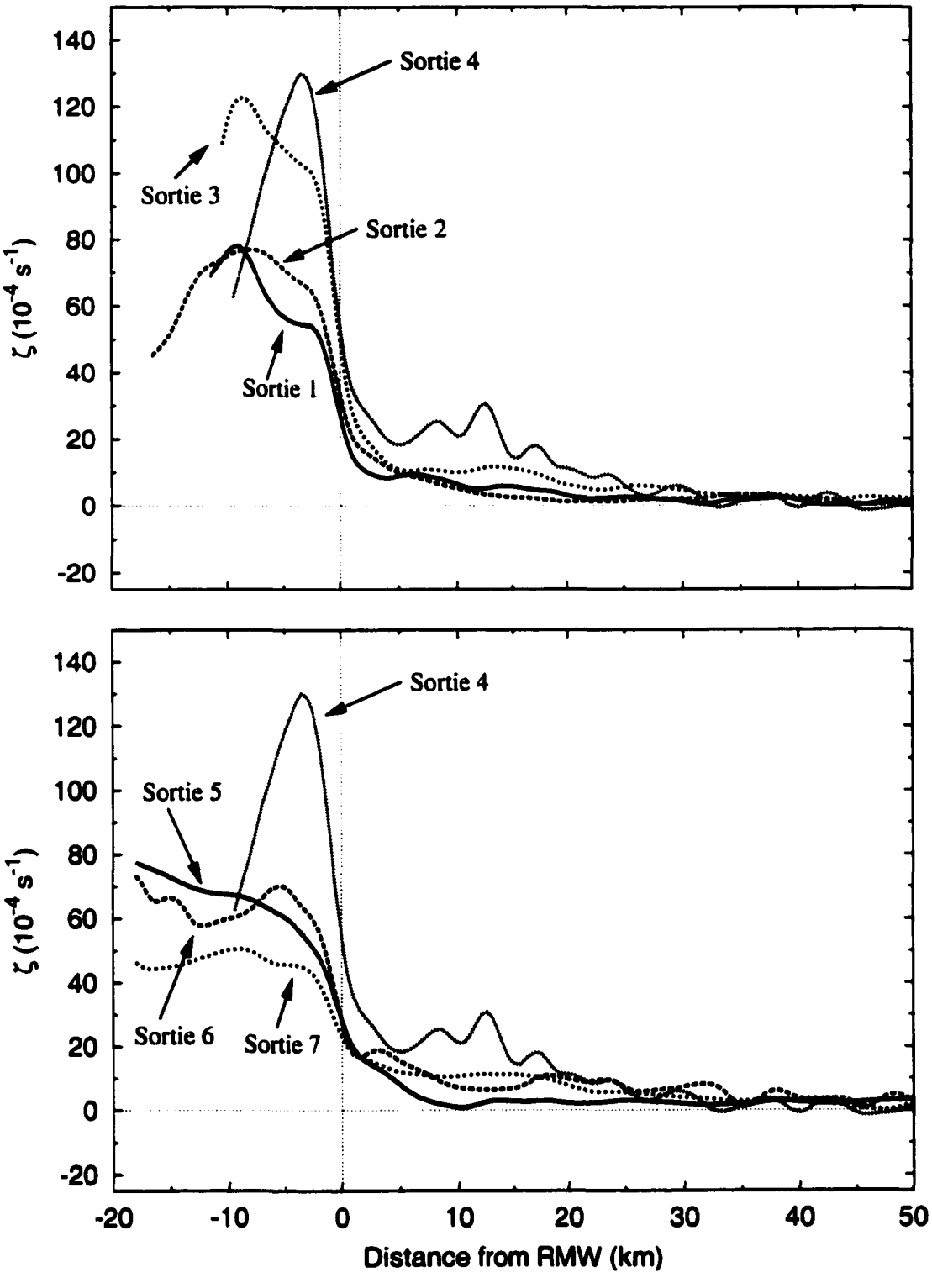

Figure 4.2: Averaged vorticity profiles for sorties 1–7 in Hurricane Andrew. Averages were computed with respect to distance from the RMW. Negative distances are inside the RMW. All sorties were flown at 700 hPa.

Reproduced with permission of the copyright owner. Further reproduction prohibited without permission.

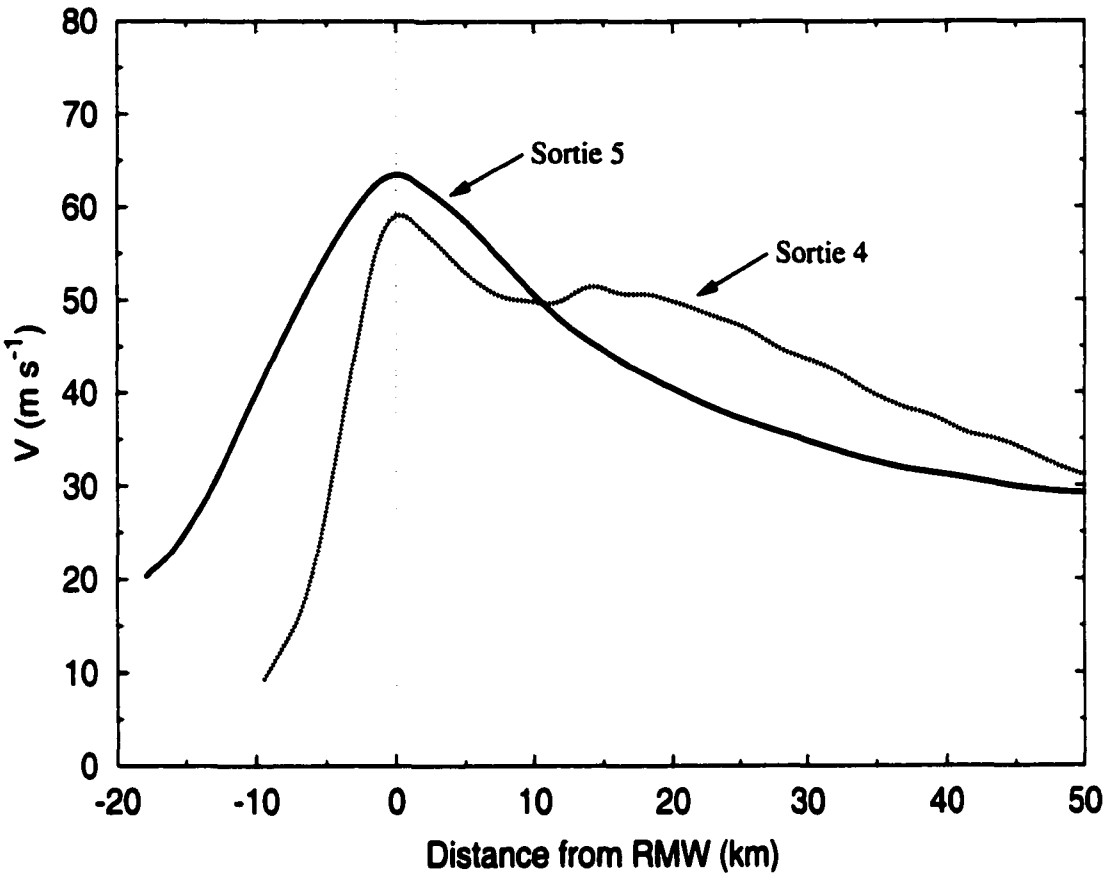

Figure 4.3: Averaged tangential wind profiles for sorties 4 and 5 in Hurricane Andrew. The mean RMW is 11.1 km during sortie 4 and 21.3 km during sortie 5. The winds near the eye center have increased from 9 m s^{-1} to 20 m s^{-1} during the transition of the vorticity to a monotonic profile.

Reproduced with permission of the copyright owner. Further reproduction prohibited without permission.

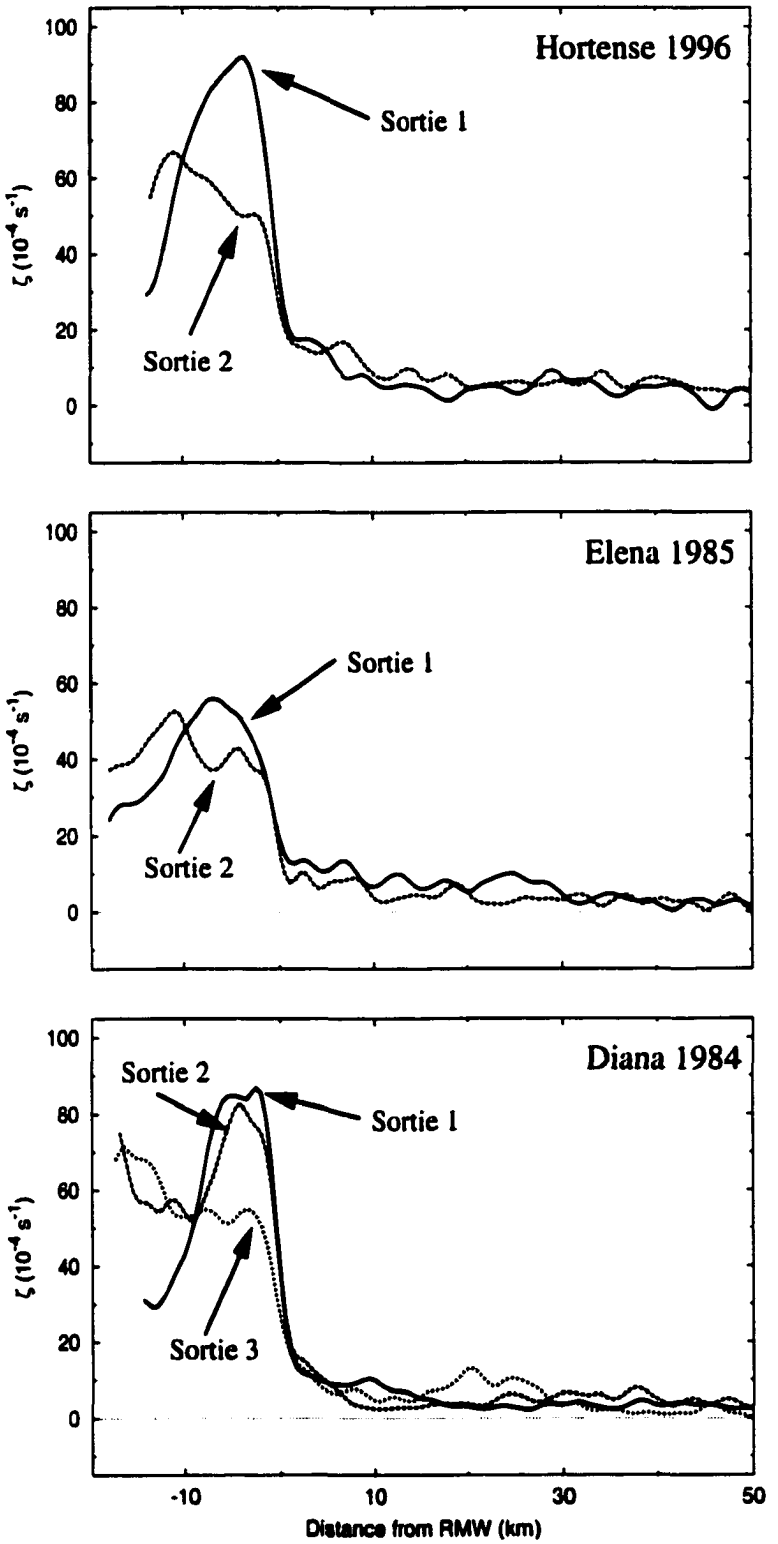

Figure 4.4: Representative sortie averaged vorticity profiles for Hurricanes Hortense (1996), Elena (1985), and Diana (1984) during transitions from peaked (during intensification) to nearly monotonic (after intensification has ceased) profiles. The transitions are similar to those of Hurricane Andrew but are not associated with an appreciable change in RMW.

Reproduced with permission of the copyright owner. Further reproduction prohibited without permission.

Figure 4.5: Sequential individual radial leg profiles of flight-level relative vorticity (solid line) and tangential wind (dashed line) within Hurricane Andrew (1992) during aircraft sorties 4 and 5. Each panel displays two radial legs, one inbound and one outbound, and the aircraft direction of flight is from left to right. The time period of each penetration is at upper right. (a) All 6 radial legs within sortie 4.

Reproduced with permission of the copyright owner. Further reproduction prohibited without permission.

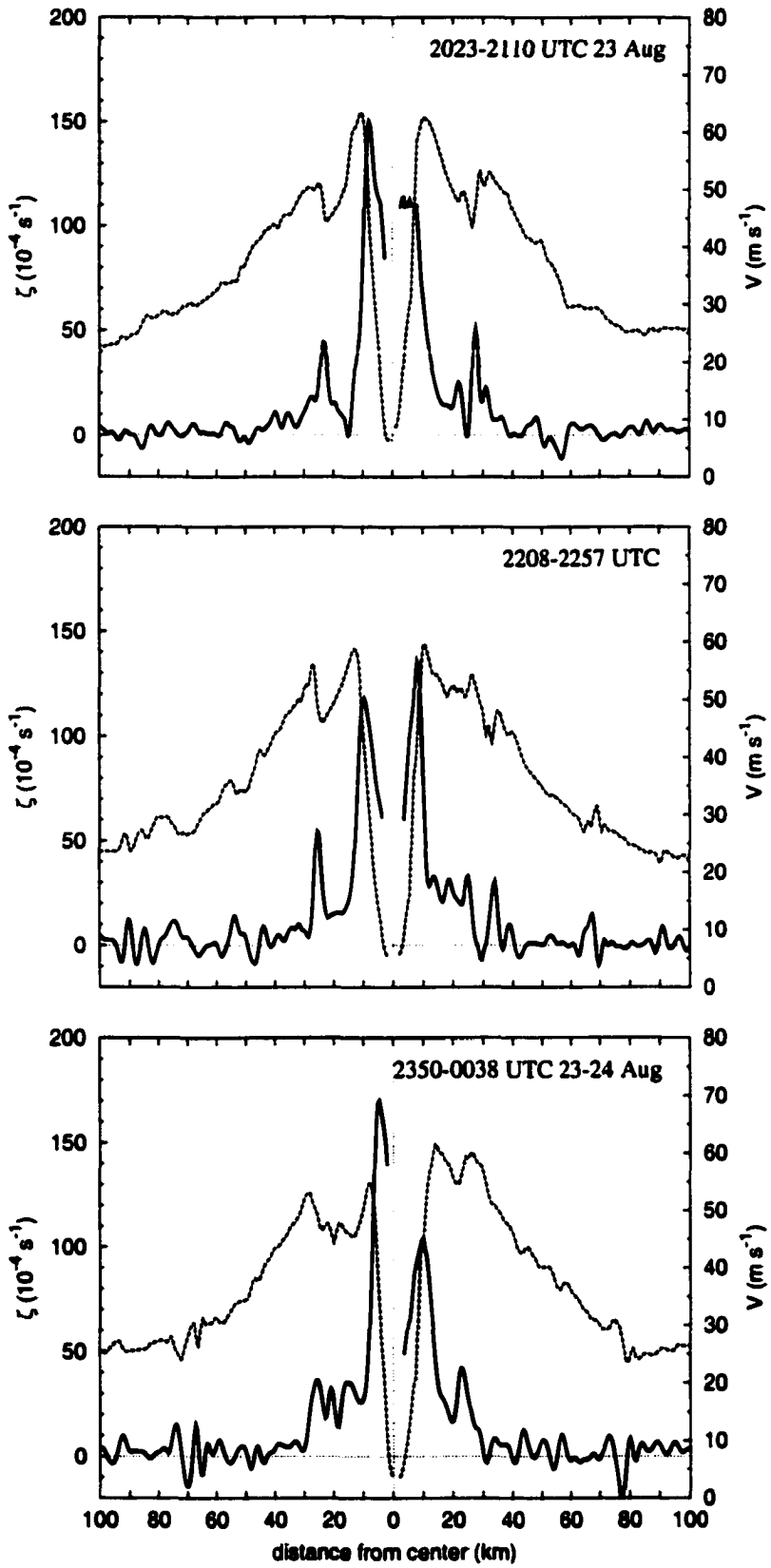

Figure 4.5: (a) See caption on previous page.

Reproduced with permission of the copyright owner. Further reproduction prohibited without permission.

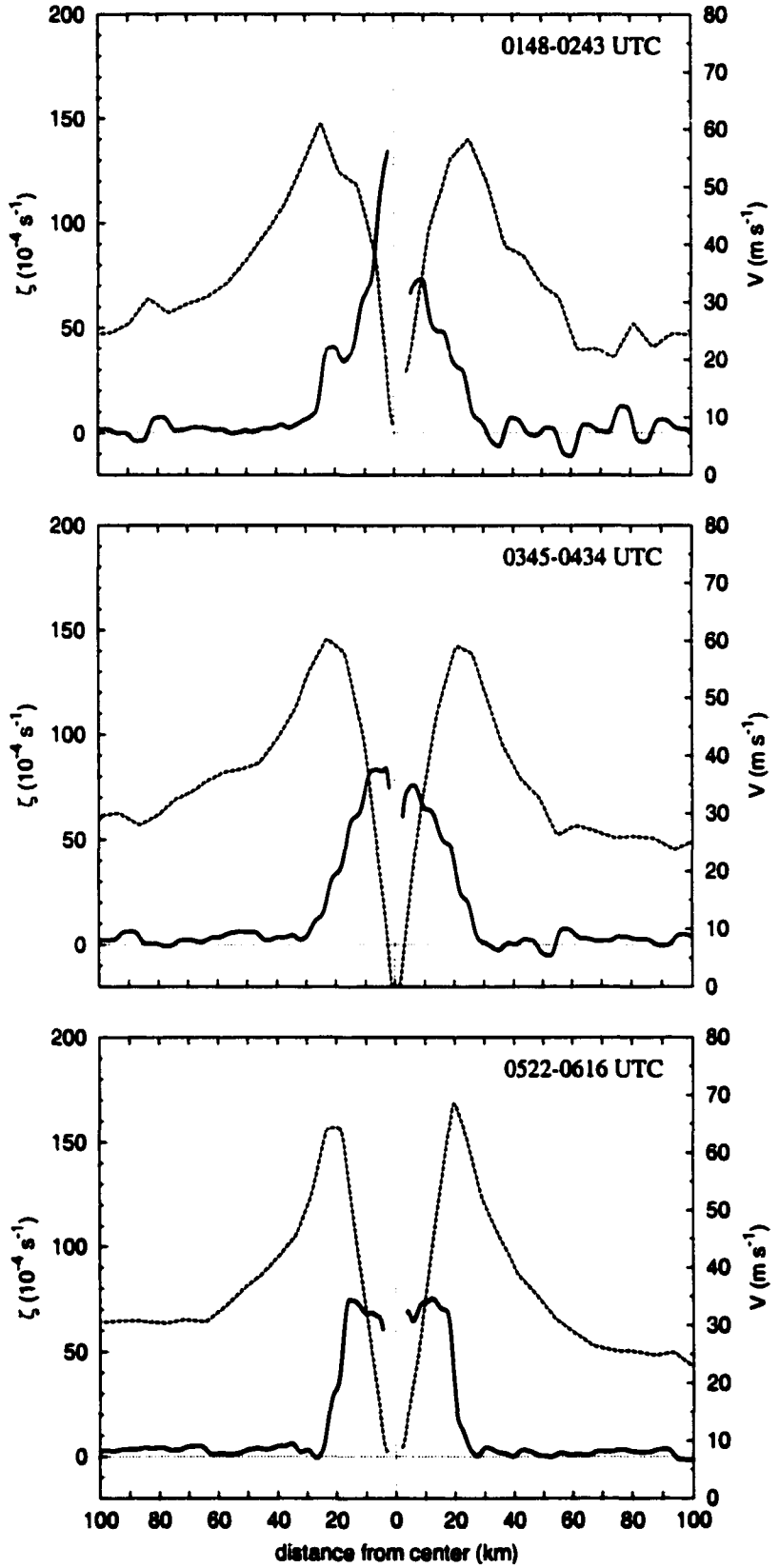

Figure 4.5: (*Continued*) (b) First 6 legs of sortie 5.

Reproduced with permission of the copyright owner. Further reproduction prohibited without permission.

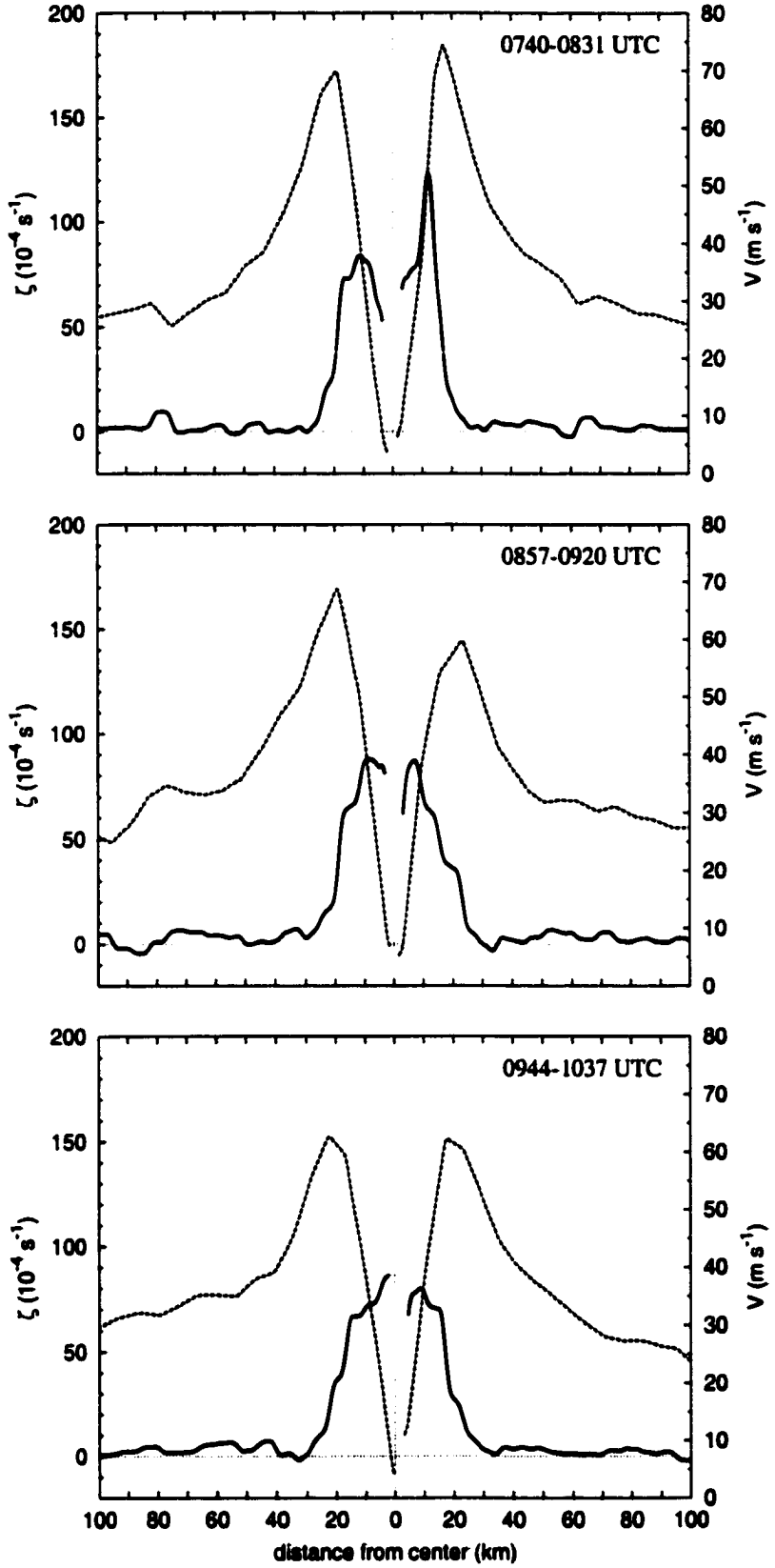

Figure 4.5: (*Continued*) (c) Last 6 legs of sortie 5.

Reproduced with permission of the copyright owner. Further reproduction prohibited without permission.

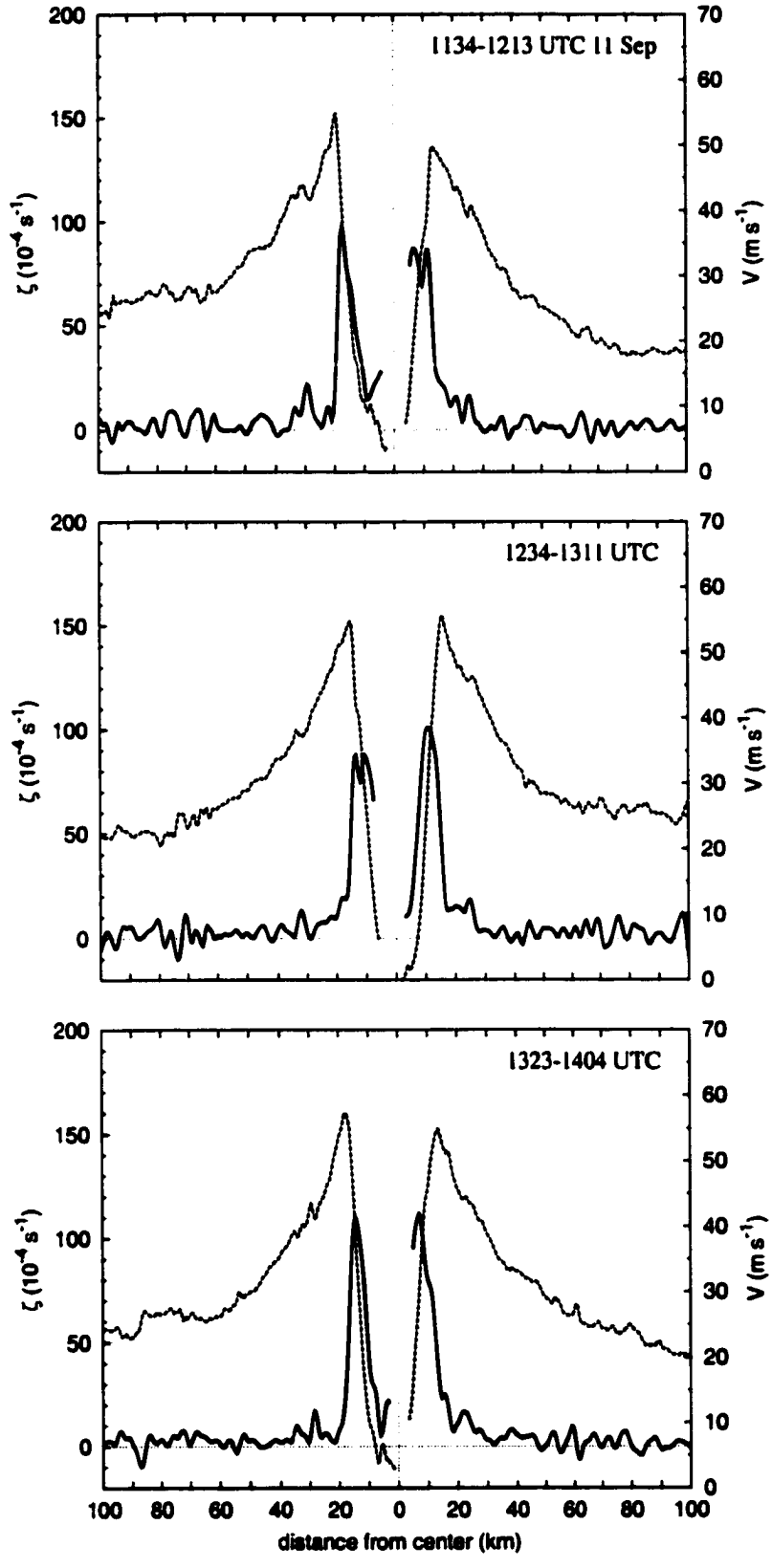

Figure 4.6: Similar to Fig. 4.5, but for Hurricane Diana (1984) during sorties 1, 2, and 3. Flight levels were along the 850 hPa surface. (a) First 6 legs of sortie 1.

Reproduced with permission of the copyright owner. Further reproduction prohibited without permission.

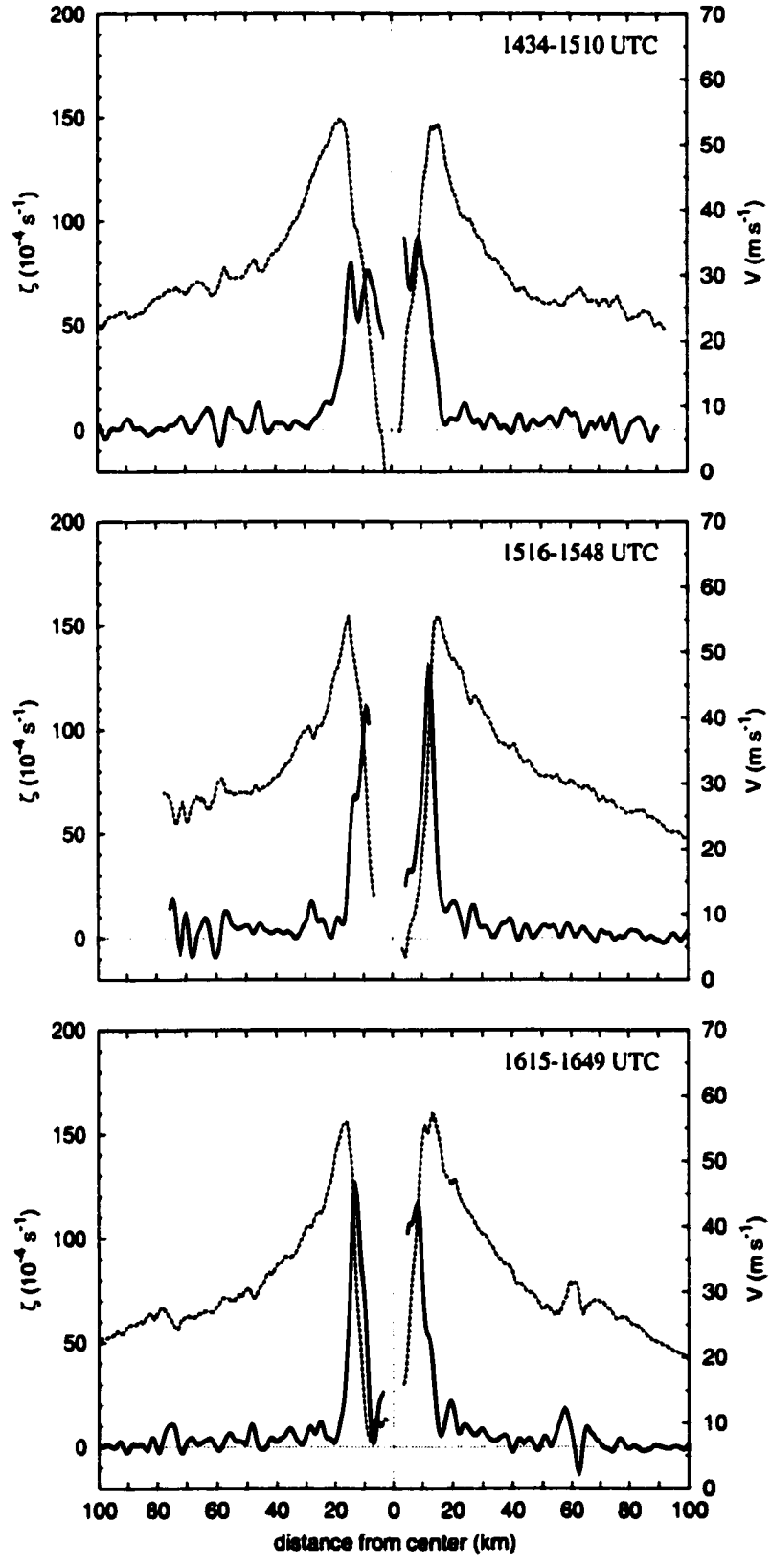

Figure 4.6: (*Continued*) (b) Legs 7–12 of sortie 1.

Reproduced with permission of the copyright owner. Further reproduction prohibited without permission.

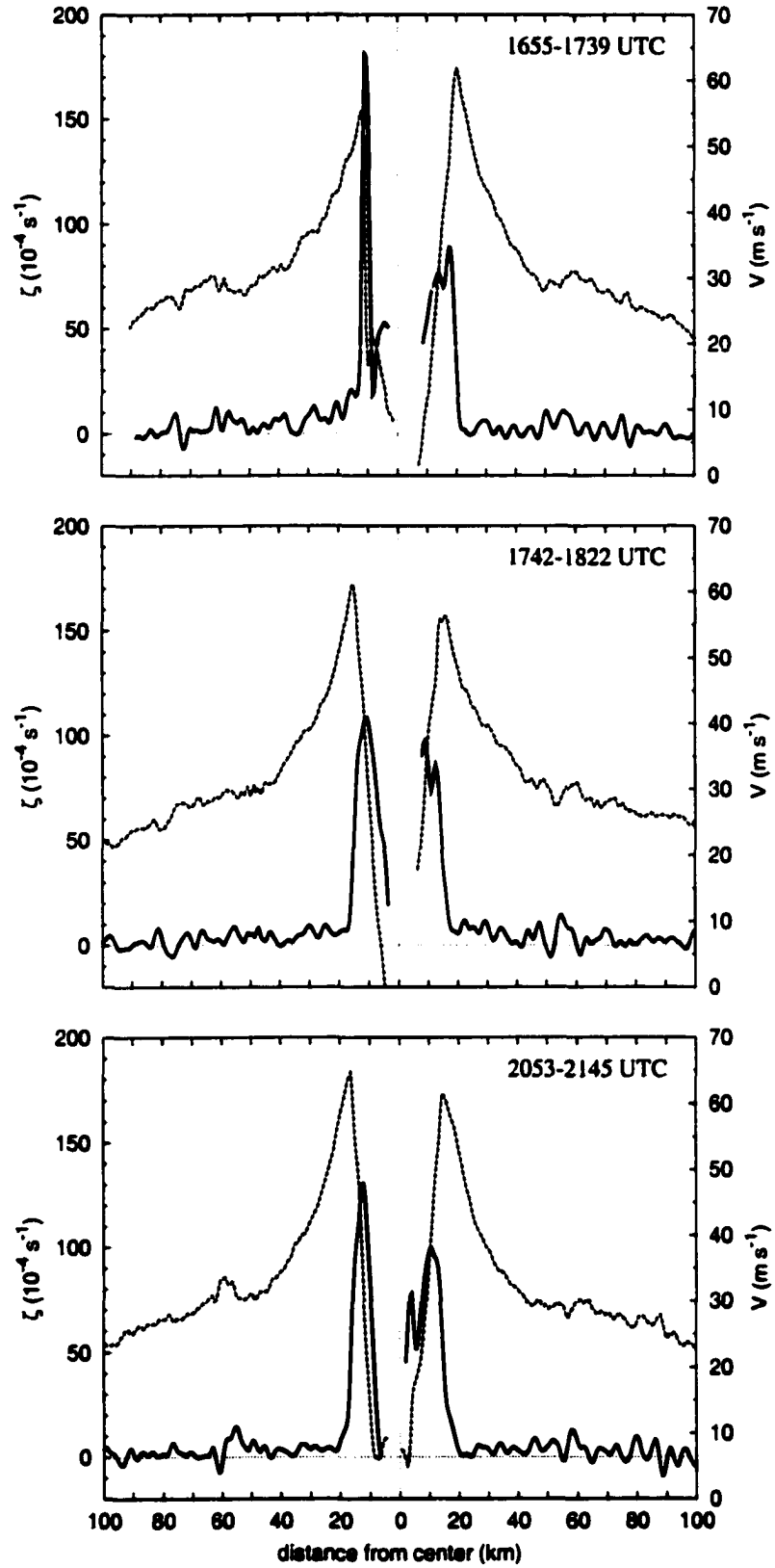

Figure 4.6: (*Continued*) (c) Last 4 legs of sortie 1 and first 2 legs of sortie 2.

Reproduced with permission of the copyright owner. Further reproduction prohibited without permission.

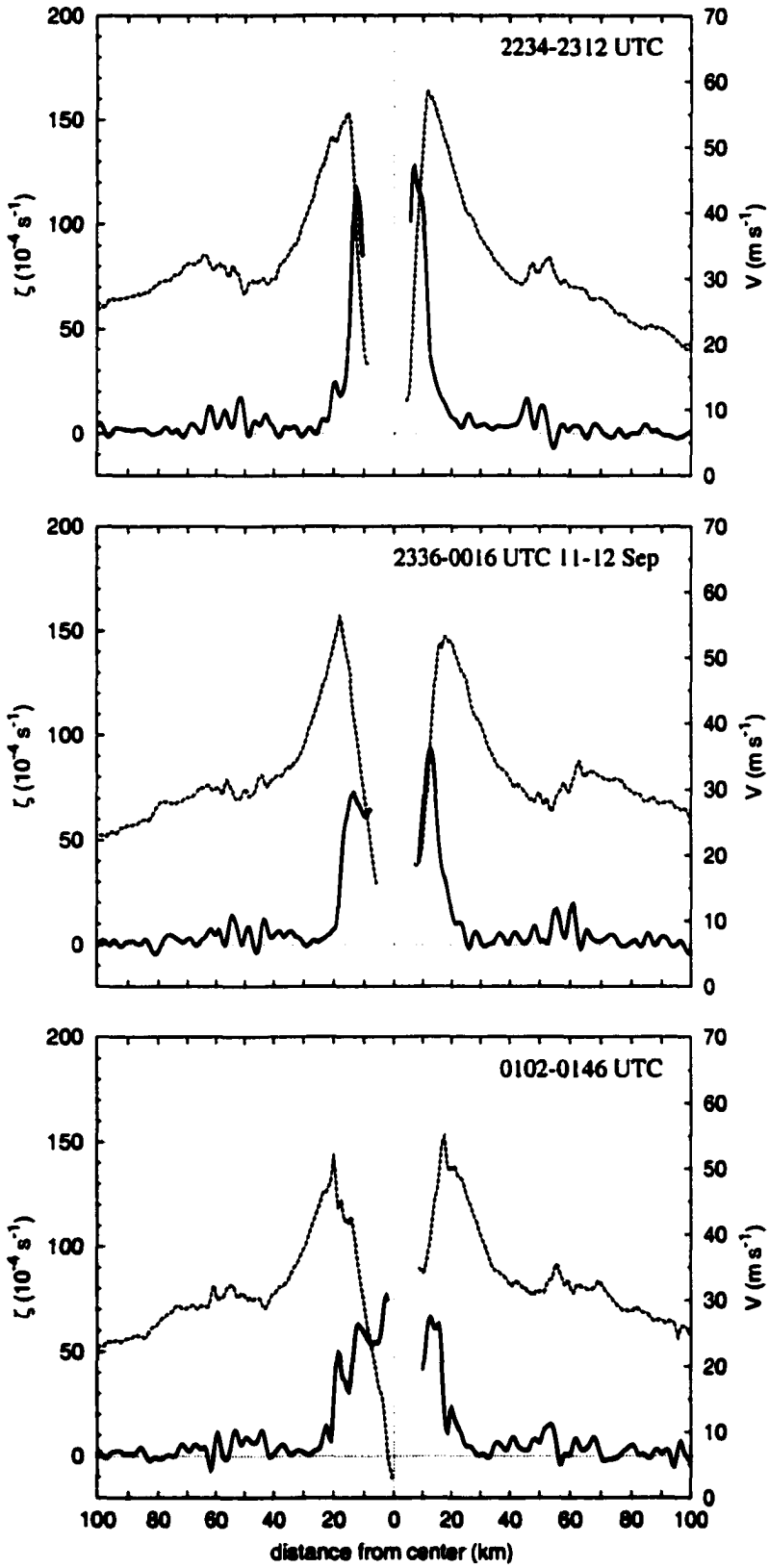

Figure 4.6: (*Continued*) (d) Legs 3–8 of sortie 2.

Reproduced with permission of the copyright owner. Further reproduction prohibited without permission.

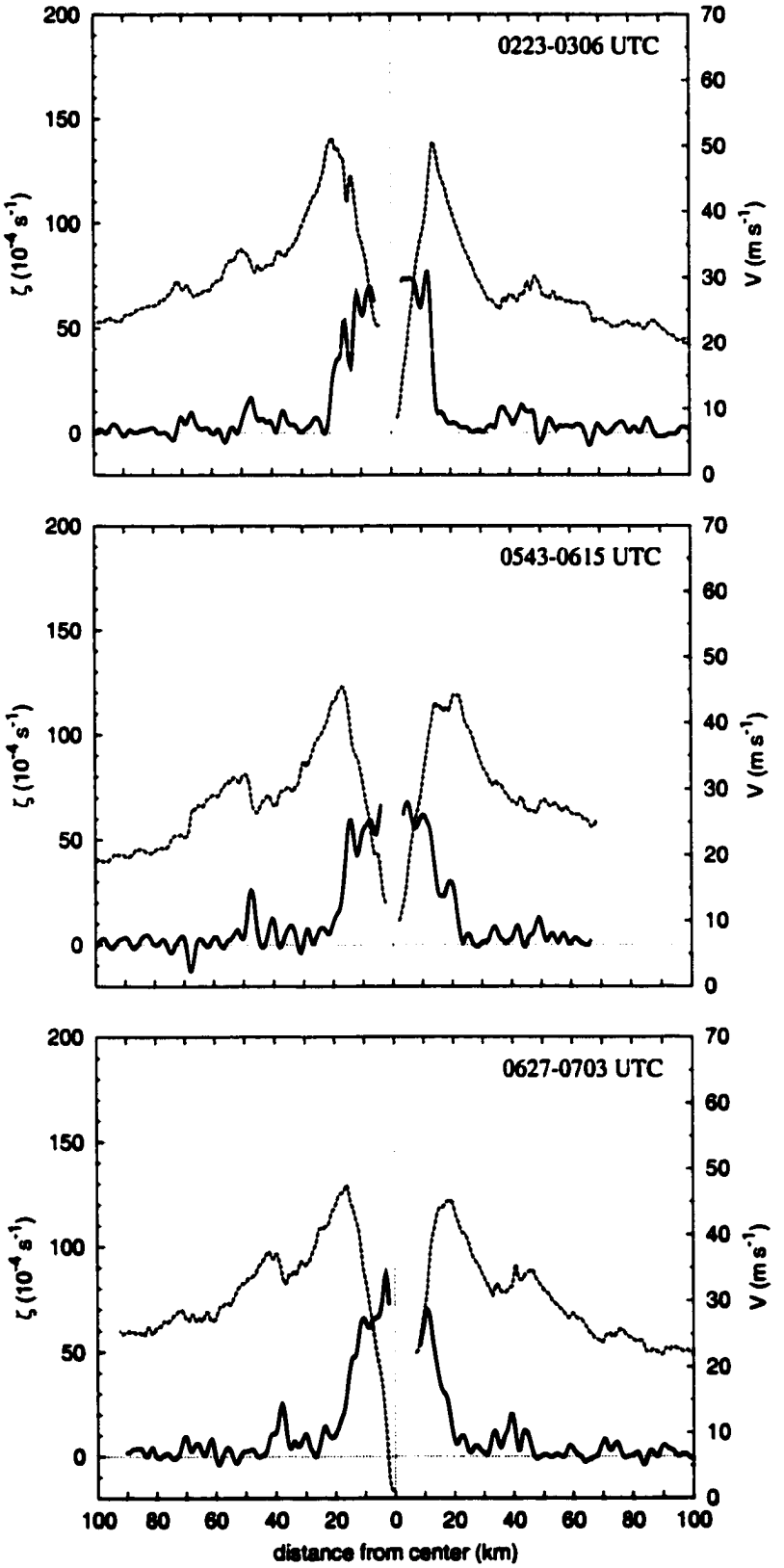

Figure 4.6: (*Continued*) (e) Last 2 legs of sortie 2 and first 4 legs of sortie 3.

Reproduced with permission of the copyright owner. Further reproduction prohibited without permission.

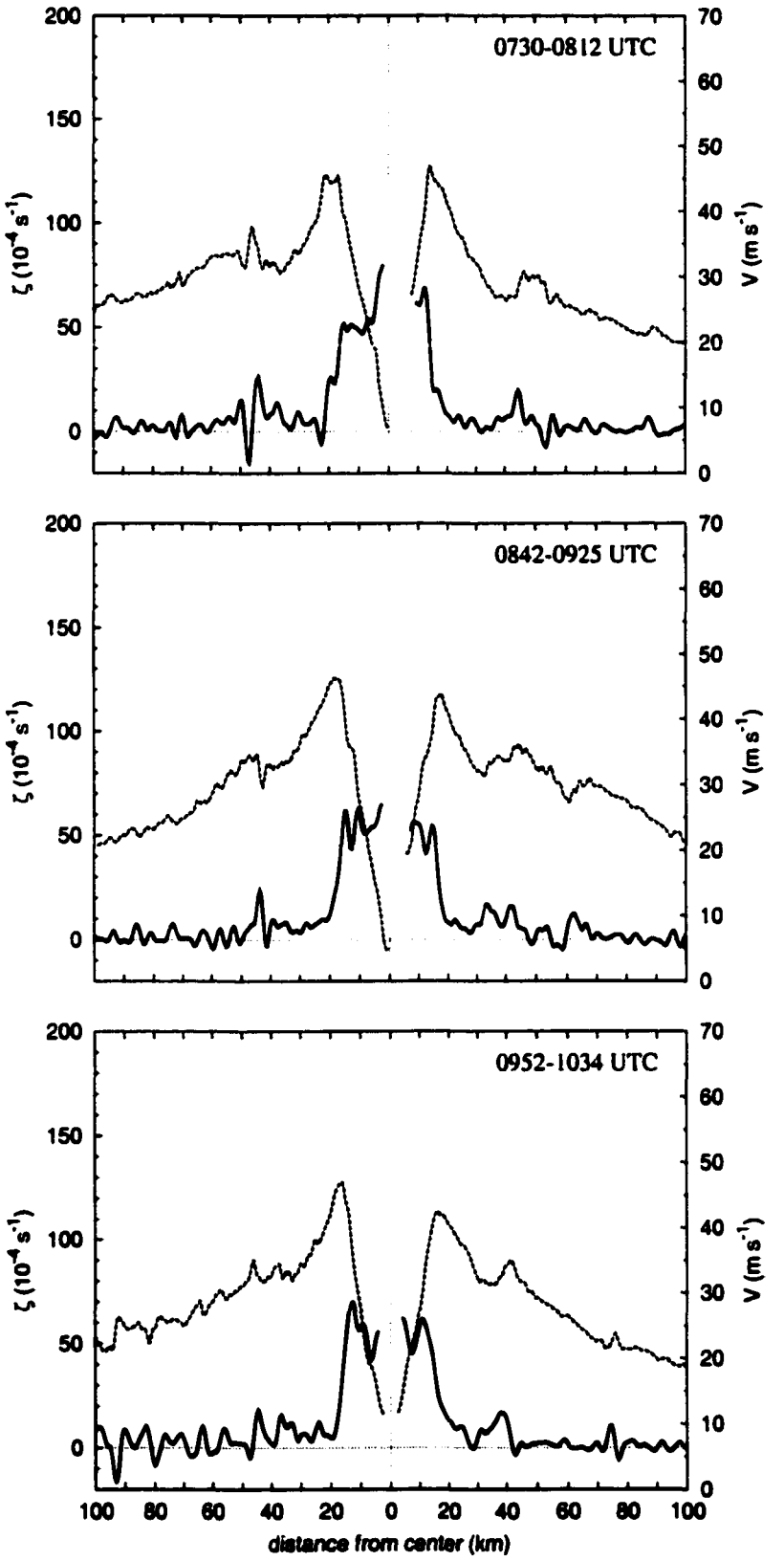

Figure 4.6: (*Continued*) (f) Legs 5–10 of sortie 3.

Reproduced with permission of the copyright owner. Further reproduction prohibited without permission.

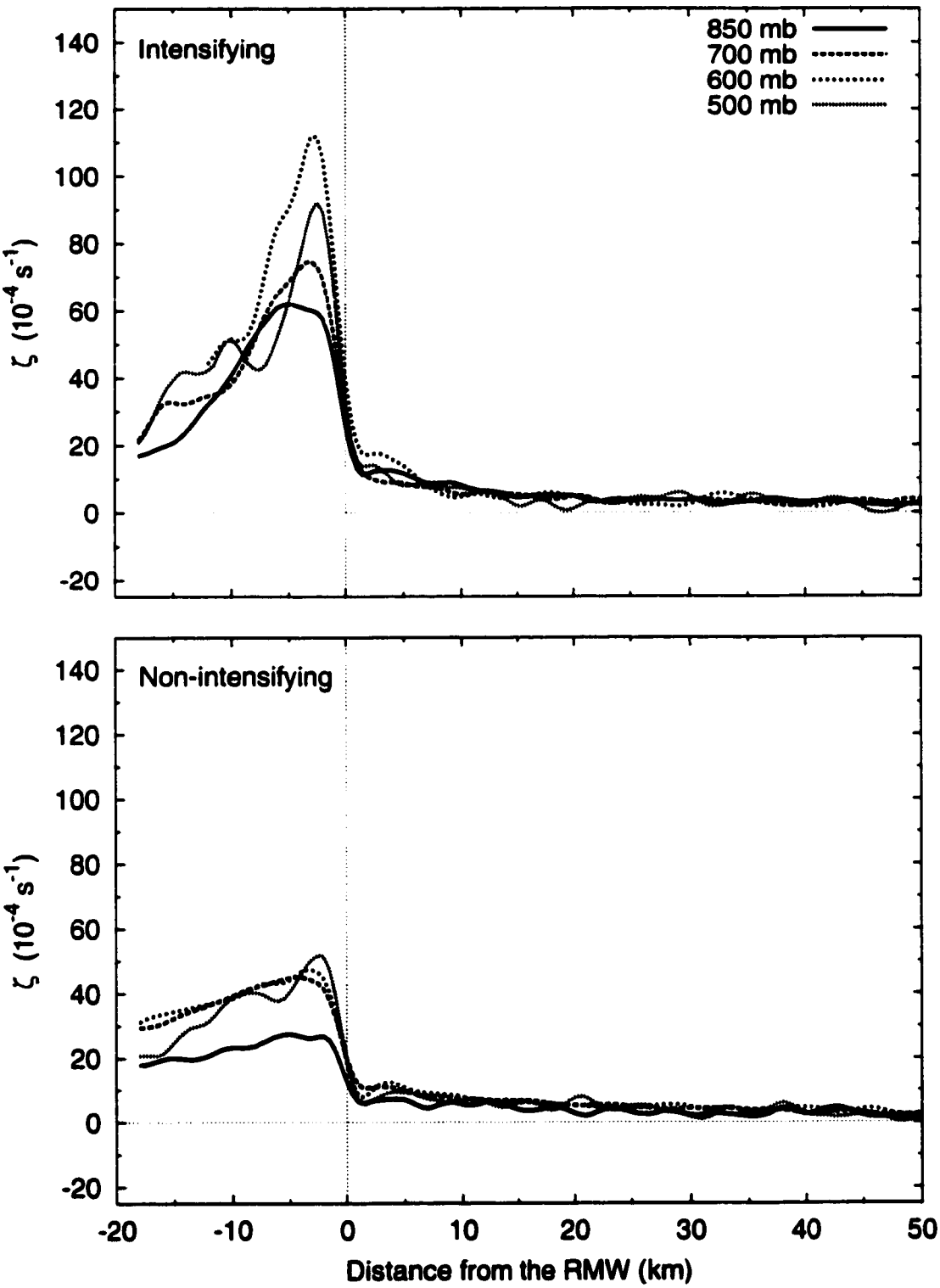

Figure 4.7: Averaged vorticity profiles for four different flight-levels for the case of intensifying and non-intensifying category 3, 4, and 5 hurricanes. Each profile represents contributions from different hurricanes. During periods of non-intensification, the averaged vorticity in the eye represents nearly solid body rotation.

Reproduced with permission of the copyright owner. Further reproduction prohibited without permission.

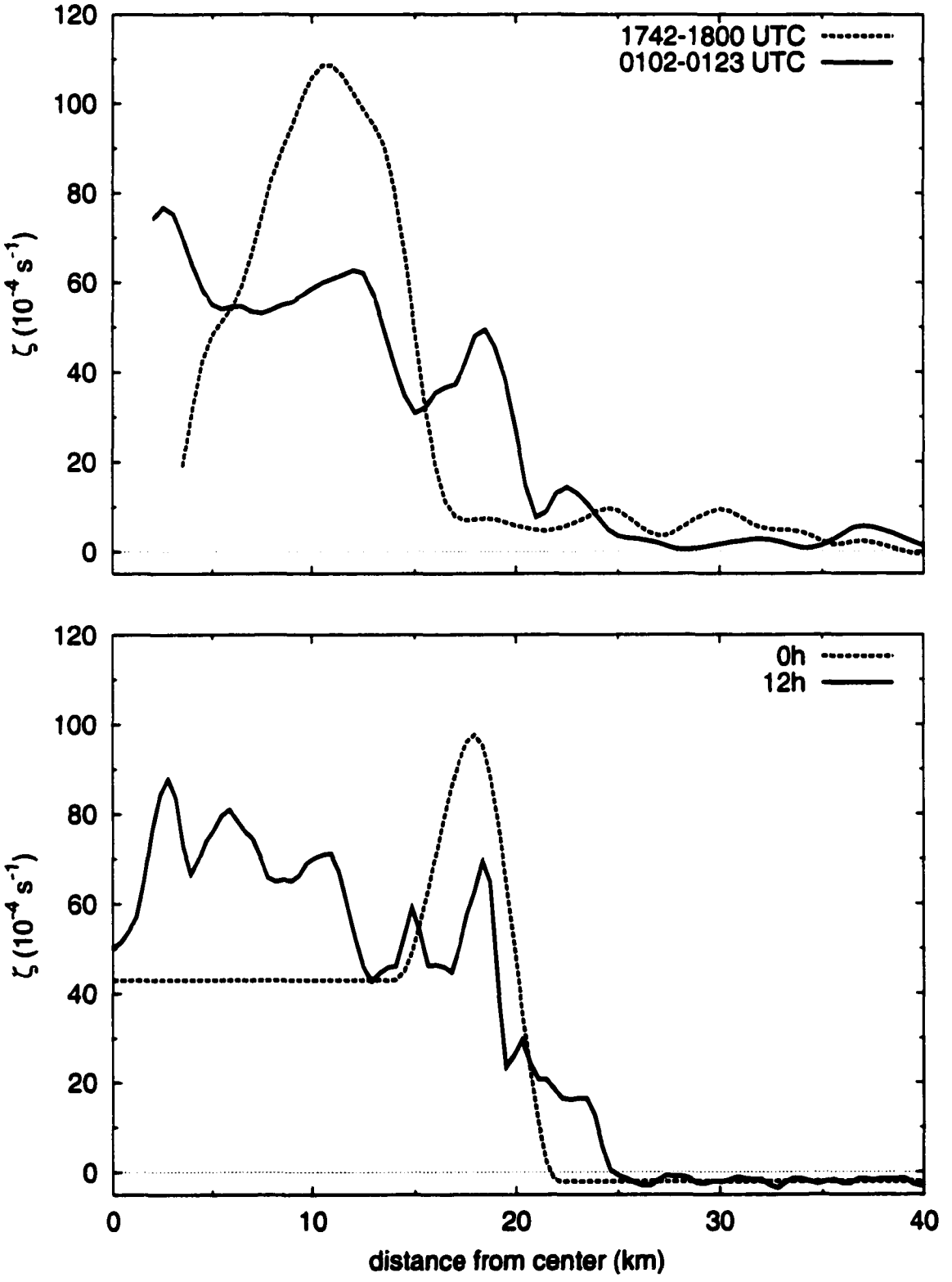

Figure 4.8: (a) Radial leg flight-level vorticity in Hurricane Diana shortly after intensification had ceased (dashed) and 7–8 hours later (solid). (b) Unsmoothed cross sections of model vorticity at $t = 0$ and $t = 12$ h.

Reproduced with permission of the copyright owner. Further reproduction prohibited without permission.

Chapter 5

PARAMETERIZATION OF THE MIXING PROCESS IN AN AXISYMMETRIC MODEL

Motivated by observed flow fields in hurricanes, chapter 3 considered the stability and nonlinear evolution of unforced hollow tower vorticity structures. In chapter 4, it was shown that annular rings of high vorticity are generated during intensification but are eradicated when intensification stops. During prolonged periods of intensification, the vorticity in the eyewall appears to approach a vortex sheet. This is especially evident in Fig. 4.6 which shows a substantial narrowing and strengthening of the eyewall vorticity in Hurricane Diana during intensification. Another well documented case of a hurricane's flow field evolving towards a vortex sheet is that of Hurricane Hugo (1989) where analyses of flight-level data (Black and Marks 1991) showed tangential winds which changed from 85 m s^{-1} to 20 m s^{-1} during less than 10 seconds of flight time. For the WP-3D aircraft, 10 seconds of flight time corresponds to less than 2 km of distance travelled. This dramatic feature was located near the inner edge of the eyewall and was co-located with the inner edge of the main updraft. The tendency of the eyewall flow towards a discontinuity suggests that the eyewall is frontogenetic. Chapter 3 offers a mechanism whereby high Reynolds number geophysical flows can combat the formation of such discontinuities. When this mechanism is suppressed, as is the case in axisymmetric models which exclude asymmetric processes, another mechanism must be introduced (see e.g., Emanuel 1997, Fig. 6a). As mentioned briefly in chapter 1, axisymmetric models must incorporate some type of diffusion as a parameterization of asymmetric horizontal mixing processes and the resulting cascade

Reproduced with permission of the copyright owner. Further reproduction prohibited without permission.

to the subgrid scale. The diffusion applied to maintain the numerical convergence of these models is generally large ($\nu > 10^3$ m^2 s^{-1}) when compared with the diffusion applied in the numerical experiments of this work ($\nu \approx 10^1$ m^2 s^{-1}). Such large diffusion essentially moves the flow simulations to much lower Reynold's numbers and consequently, the selective decay hypothesis discussed in section 3.2 is no longer well justified. Considering axisymmetric flows which evolve purely through diffusive processes at high viscosity, Hack (1980) demonstrated that the loss of kinetic energy to diffusion alone can be very large when the vortex is small. For example, his initial vortex with a RMW of 20 km would lose half of its initial kinetic energy in less than a day when $\nu = 10^3$ m^2 s^{-1}.

We now consider the effect that diffusion may have on a flow which is initially characterized by an annular ring of enhanced vorticity embedded in relatively weak vorticity by introducing the problem of viscous nondivergent axisymmetric flow described by

$$\frac{\partial v}{\partial t} = \nu \left[\frac{\partial}{r \partial r} \left(r \frac{\partial v}{\partial r} \right) - \frac{v}{r^2} \right], \tag{5.1}$$

or equivalently,

$$\frac{\partial \zeta}{\partial t} = \nu \frac{\partial}{r \partial r} \left(r \frac{\partial \zeta}{\partial r} \right), \tag{5.2}$$

where

$$\zeta = \frac{\partial (rv)}{r \partial r}. \tag{5.3}$$

As the initial condition for (5.1) or (5.2), consider the tangential wind profile given by

$$\frac{v(r)}{v_0} = \begin{cases} 0 & 0 \leq r < a, \\ a/r & a \leq r < \infty, \end{cases} \tag{5.4}$$

where v_0 is the maximum wind $v(a, 0)$. Equation (5.4) describes a circular vortex "sheet" at $r = a$. In order to study the time evolution of this initial condition, we introduce the order m Hankel transform pair

$$\begin{aligned} \chi(r,t) &= \int_0^\infty \hat{\chi}(k,t) J_m(kr) k dk, \\ \hat{\chi}(k,t) &= \int_0^\infty \chi(r,t) J_m(kr) r dr, \end{aligned} \tag{5.5}$$

Reproduced with permission of the copyright owner. Further reproduction prohibited without permission.

where $\chi(r,t)$ is some arbitrary function. Applying the order zero transform to (5.2) and integrating by parts, we obtain

$$\hat{\zeta}(k,t) = \hat{\zeta}(k,0)\exp(-\nu t k^2), \tag{5.6}$$

and then

$$\zeta(r,t) = \int_0^\infty \hat{\zeta}(k,0)\exp(-\nu t k^2) J_0(kr) k dk, \tag{5.7}$$

where

$$\hat{\zeta}(k,0) = \int_0^\infty \zeta(r,0) J_0(kr) r dr. \tag{5.8}$$

Noting that $\zeta(r,0) = 0$ everywhere except $r = a$ we can use (5.3) to rewrite (5.8) as

$$\begin{aligned}
\hat{\zeta}(k,0) &= \lim_{\epsilon\to 0}\int_{a-\epsilon}^{a+\epsilon} \frac{d}{dr}[rv(r,0)] J_0(kr) dr \\
&= \lim_{\epsilon\to 0}\{J_0(ka)[(a+\epsilon)v(a+\epsilon,0) - (a-\epsilon)v(a-\epsilon,0)]\} \\
&= a v_0 J_0(ka).
\end{aligned} \tag{5.9}$$

Substituting (5.9) into (5.7) gives

$$\begin{aligned}
\zeta(r,t) &= a v_0 \int_0^\infty J_0(ka)\exp(-\nu t k^2) J_0(kr) k dk \\
&= \frac{a v_0}{2\nu t}\exp\left[\frac{-(r^2+a^2)}{4\nu t}\right] I_0\left(\frac{ar}{2\nu t}\right),
\end{aligned} \tag{5.10}$$

where I_0 is the modified Bessel function of order zero (see Gradshteyn and Ryzhik, 1994, 5$^{\text{th}}$ Ed., pg. 739; 6.633; no. 2). Defining a dimensionless time $\tau = \nu t/a^2$, we can write (5.10) as

$$\frac{\zeta(r,t)}{v_0/a} = \frac{1}{2\tau}\exp\left[\frac{-(r^2/a^2+1)}{4\tau}\right] I_0\left(\frac{r/a}{2\tau}\right). \tag{5.11}$$

To deduce an expression for $v(r,t)$ we may proceed in two ways, first by numerical integration of (5.11), or second as follows. Applying the order one transform to (5.1) and solving, we have $\hat{v}(k,t) = \hat{v}(k,0)\exp(-\nu t k^2)$. Transforming the initial condition (5.4) gives $\hat{v}(k,0) = a v_0 J_0(ka)/k$ and then

$$v(r,t) = a v_0 \int_0^\infty J_0(ka)\exp(-\nu t k^2) J_1(kr) dk, \tag{5.12}$$

Reproduced with permission of the copyright owner. Further reproduction prohibited without permission.

which may be integrated (Gradshteyn and Ryzhik, 1994, 5th Ed., pg. 739; 6.633; no. 1) to obtain

$$\frac{v(r,t)}{v_0} = \frac{r/a}{4\tau} \sum_{m=0}^{\infty} \frac{1}{m!} \left(-\frac{1}{4\tau}\right)^m {}_2F_1\left(-m,-m;2;r^2/a^2\right), \tag{5.13}$$

where ${}_2F_1$ is the Gaussian hypergeometric function.

Radial profiles of nondimensional tangential wind, angular velocity, and vorticity are shown in Fig. 5.1 for different values of nondimensional time τ. For a vortex with $a = 30$ km and $\nu = 10^3$ m^2 s^{-1}, $\tau = 0.004$ represents one hour. When $\nu = 10^4$ m^2 s^{-1}, $\tau = 0.004$ represents one tenth of an hour (6 minutes). For a vortex with $a = 20$ km, such as the initial condition used in the experiment of section 3.2, and $\nu = 10^3$ m^2 s^{-1}, $\tau = 0.004$ represents 27 minutes. For the choice $\nu = 15$ m^2 s^{-1} used in the nonlinear mixing experiment of section 3.2, $\tau = 0.004$ represents ~ 30 hours.

At $\tau = 0$, all the vorticity is concentrated at $r = a$ and the flow is discontinuous there. When $\tau = 0.008$, the outward and inward directed diffusive flux has smoothed the profiles, eliminating the discontinuity. The maximum vorticity initially at $r = a$ has decreased and moved inwards, while the adjacent vorticity inside and outside $r = a$ has increased. The maximum wind has decreased and has moved radially outward while the wind inside $r = a$ has increased. As τ increases, the vorticity around $r = a$ continues to decrease, the central vorticity continues to increase, the winds become increasingly less U-shaped, and the angular velocity evolves toward a nearly solid body rotation. Eventually the vorticity profile becomes monotonic and all diffusive flux is directed outwards.

Setting $r = 0$ in (5.11) we can plot the evolution of the vorticity at the vortex center. This is shown in Fig. 5.2. The central flow remains approximately irrotational until $\tau \approx 0.03$, after which the central vorticity increases until it achieves its maximum at $\tau = 0.25$. When $\tau = 0.25$, the central vorticity is given by $\zeta(0, 0.25) = 2v_0/(ae)$. When compared with the results shown in Fig. 3.7a for the numerical experiment

Reproduced with permission of the copyright owner. Further reproduction prohibited without permission.

of chapter 3, or when compared with the numerical results of Schubert et al. (1999) using a larger vortex with a more depressed central vorticity, this value is far too low. For example, if we imagine the profile in Fig. 5.1c, at $\tau = 0.008$, as the initial condition for the barotropic model used in chapter 3, the central vorticity in the quasi-equilibrated state would be expected to be significantly higher. Thus, a purely diffusive evolution of an annular ring does not well represent the process where coherent vorticity structures can be transported from the ring to the vortex center while remaining relatively unmixed in the process.

When $\tau > 0.25$ the central vorticity decreases as all the diffusive flux is then directed outward. Note that the increase of the central vorticity (Fig. 5.2) due to the inward flux when $\tau < 0.25$, is much more rapid than the "slow diffusive spin down" which occurs later. In this sense, the diffusion is more efficient at eradicating an annular ring than a monopole.

In summary, by suppressing any asymmetric mechanism which might oppose the diabatic production of highly unstable annular rings, axisymmetric models must introduce an *artificial* mechanism, generally in the form of large diffusion. When applied to an initial flow associated with an annular ring of enhanced vorticity, the annular ring is diffused away and the inward directed part of the flux spins up the central region of the vortex. In a coarse sense then, the evolution of the vorticity given by (5.11) is similar to the evolution of unstable initial conditions using the nonlinear vorticity equation (B.1) with much smaller ν. The loss of energy associated with flows evolving with large ν however, is generally unrealistic when describing the high Reynold's number flow of an actual hurricane. Additionally, the asymmetric nonlinear transport process of an unstable annular ring evolving to a monopole is not accurately parameterized by the process of diffusive transport and can result in unrealistic values of the central vorticity.

Reproduced with permission of the copyright owner. Further reproduction prohibited without permission.

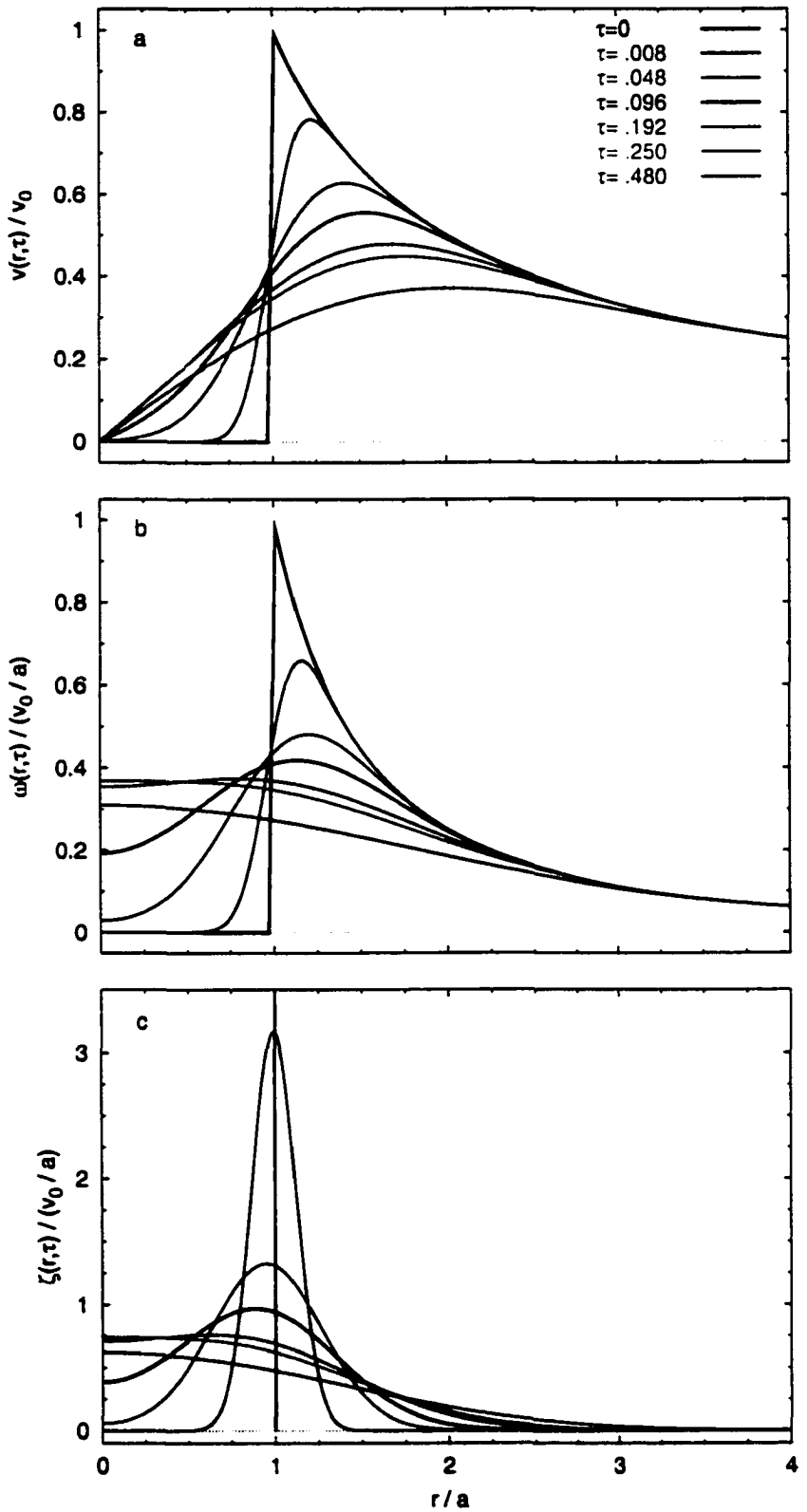

Figure 5.1: Evolution of the nondimensional (a) tangential wind, (b) angular velocity, and (c) vorticity based on the solution to the diffusion equation given by (5.11) for chosen values of nondimensional time $\tau = \nu t/a^2$. For a vortex with $a = 30$ km and $\nu = 10^3$ m^2 s^{-1}, $\tau = .004$ represents 1 hour.

Reproduced with permission of the copyright owner. Further reproduction prohibited without permission.

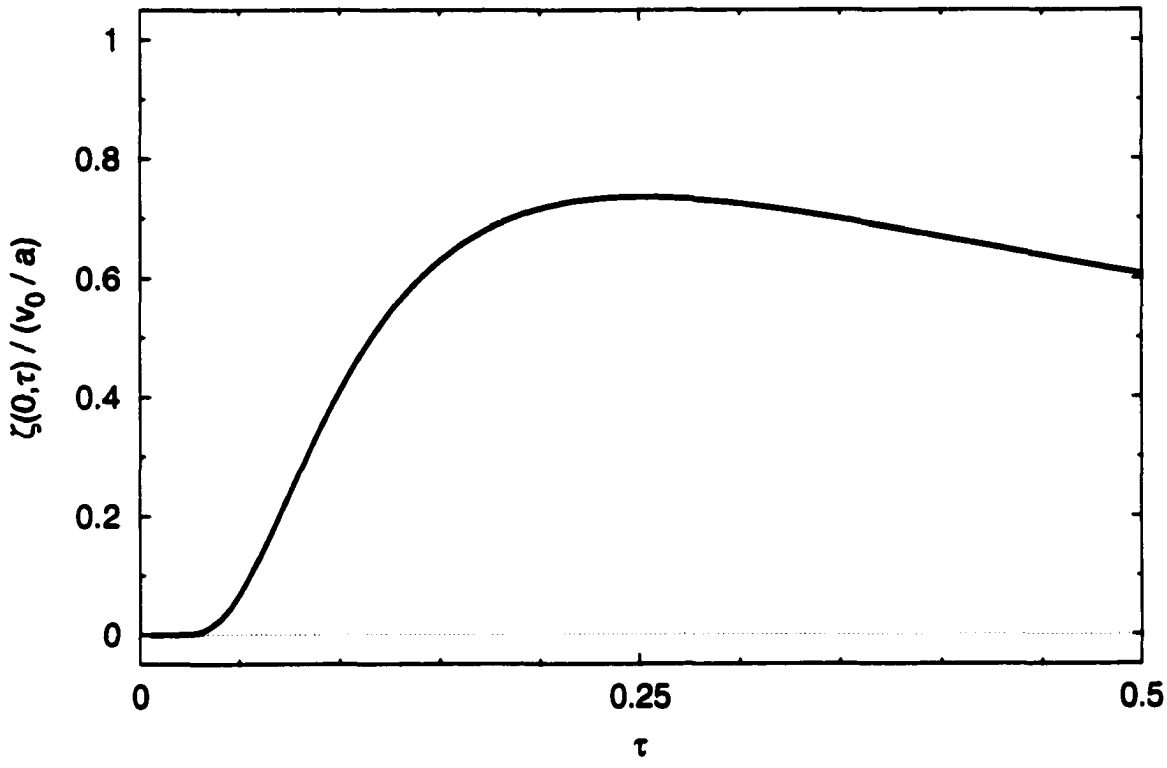

Figure 5.2: Evolution of nondimensional vorticity at $r = 0$ as a function of nondimensional time τ.

Reproduced with permission of the copyright owner. Further reproduction prohibited without permission.

Chapter 6

EVOLUTION OF AN UNSTABLE SECONDARY EYEWALL

> Hurricanes don't stay this way very long..... what's happening is there's a (second) ring of slightly stronger winds forming around the eye that we see on radar. *Hugh Willoughby* on 13 September, 1988 describing why Hurricane Gilbert was expected to weaken. On the following day, the ring of slightly stronger winds had become one of the most dramatic secondary eyewalls ever observed.

During the period 11–17 September 1988, Hurricane Gilbert moved westward across the Caribbean Sea, over the tip of the Yucatan Peninsula and across the Gulf of Mexico, making landfall just south of Brownsville, Texas. After passing directly over Jamaica on 12 September, Gilbert intensified rapidly and at 2152 UTC on 13 September reached a minimum sea level pressure of 888 mb, the lowest yet recorded in the Atlantic basin (Willoughby et al. 1989). Approximately 12 h later, when its central pressure was 892 mb, the horizontal structure of the radar reflectivity and the radial profiles of tangential wind and angular velocity were as shown in Fig. 6.1. At this time the storm had concentric eyewalls. The inner eyewall was between 8 and 20 km radius and the outer eyewall between 55 and 100 km radius, with a 35 km echo-free gap (or moat) between the inner and outer eyewalls. The inner tangential wind maximum was 66–69 ms^{-1} at 10 km radius, while the outer tangential wind maximum was 49–52 ms^{-1} at 61–67 km radius.

Echo-free moats such as the one shown in Fig. 6.1 are often found in intense storms, even when no well-defined outer eyewall is present. In general, echo-free moats are regions of strong differential rotation. For example, in the Gilbert case, the circuit

Reproduced with permission of the copyright owner. Further reproduction prohibited without permission.

time (i.e., the time required to traverse a complete circle) for a parcel at a radius of 10 km, with tangential wind 68 ms^{-1}, is 15.4 minutes, while the circuit time for a parcel at a radius of 50 km, with tangential wind 30 ms^{-1}, is 175 minutes. In other words, the parcel at 10 km radius completes 11 circuits in the time the parcel at 50 km radius completes one circuit. Under such strong differential rotation, small asymmetric regions of enhanced potential vorticity are rapidly filamented to small radial scales (Carr and Williams 1989; Sutyrin 1989; Smith and Montgomery 1995) as they symmetrize. Thus, the moat is typically a region of active potential enstrophy cascade to small scales. In contrast, the region just inside the secondary wind maximum has weak differential rotation. For example, the circuit time for a parcel at 61 km radius, with tangential wind 52 ms^{-1}, is 123 minutes, compared to the previously computed 175 minutes at 50 km radius. Hence, the region between 50 and 61 km is characterized by weak differential rotation and can be considered a local haven against the ravages of potential enstrophy cascade to small scales. Similarly, the updraft cores within the primary eyewall are typically embedded in the local minimum of differential rotation which lies just inside the radius of maximum wind. This is evident in Fig. 6.1c which shows a flattening of the angular velocity profile inside of the wind maximum.

The tendency for convection to be suppressed in the moat region is often attributed to mesoscale subsidence between two regions of strong upward motion. Dodge et al. (1999) found that the moat of Hurricane Gilbert consisted of stratiform precipitation with weak (less than 1 m s^{-1}) downward motion below the bright band observed near 5 km height, and weak upward motion above. An additional mechanism for suppressed convection in the moat may be strong differential rotation. For example, imagine a circular 5 km diameter cloud updraft which lies between 15 km and 20 km radius from the hurricane center. For the Gilbert wind field, the inner edge of this updraft would be advected azimuthally 140 degrees in 10 minutes, while the outer edge is advected 70 degrees in 10 minutes. Since a parcel rising at 5 ms^{-1} ascends

Reproduced with permission of the copyright owner. Further reproduction prohibited without permission.

only 3 km in this 10 minute interval, one could imagine that ordinary cumulonimbus convection embedded in such a flow would be inhibited from persisting as the convection becomes increasingly susceptible to entrainment.

Concentric eyewall structures and tangential wind profiles like those shown in Fig. 6.1 raise interesting questions about the dynamic stability of hurricane flows. The answers to such questions require studies using a hierarchy of dynamical models, the simplest of which is the nondivergent barotropic model. In such a model, Hurricane Gilbert might be idealized as an axisymmetric flow field with four distinct regions of vorticity: an inner region ($r < r_1 \approx 10$ km) of very high vorticity $\zeta_1 \approx 159 \times 10^{-4}$ s^{-1}; a moat region ($r_1 < r < r_2 \approx 55$ km) of relatively low vorticity $\zeta_2 \approx 5 \times 10^{-4}$ s^{-1}; an annular ring ($r_2 < r < r_3 \approx 100$ km) of elevated vorticity $\zeta_3 \approx 27 \times 10^{-4}$ s^{-1}; and the far field ($r > r_3$) nearly irrotational flow. A schematic of such a four-region model is shown in Fig. 6.2. The assumption of a monotonic profile near the vortex center removes the possibility for primary eyewall instabilities which were the focus of chapter 3. In this idealization, vorticity gradients and associated vortex Rossby waves are concentrated at the radii r_1, r_2, r_3. In this case, there are two types of instabilities, as the vortex Rossby wave on the positive radial vorticity gradient at r_2 can interact with either of the vortex Rossby waves on the negative radial vorticity gradients at r_1 and r_3.

In the first type of instability (called type 1), the dominant interactions occur between the Rossby edge waves associated with r_2 and r_3. The central vorticity does not play a direct role in this instability, in the sense that the vorticity wave at r_1 is dynamically inactive. However, the central vorticity does induce a differential rotation between r_2 and r_3, and this differential rotation can help suppress the instability across the ring (Dritschel 1989). Type 1 instability leads to a roll-up of the annular ring and the formation of coherent vorticity structures. Once roll-up has occured, the flow evolution is described by a collection of vortex merger events in which the central vortex is victorious (Melander et al. 1987b; Dritschel and Waugh 1992) in the sense that the vorticity within the central vortex remains largely unchanged while

Reproduced with permission of the copyright owner. Further reproduction prohibited without permission.

the relatively weak coherent vortices become rapidly filamented and axisymmetrized by the differential rotation imposed across the moat by the intense central vortex. The result is a widening of the annular ring of elevated vorticity, and a weakening but ultimate maintenance of the secondary wind maximum. This type of evolution is discussed in the present chapter.

In the second type of instability (called type 2), the dominant interactions occur between the edge waves associated with r_1 and r_2, that is, across the moat. In this case, type 1 instabilities are largely or completely suppressed by the presence of the central vortex. Type 2 instability leads to a rearrangement of the low vorticity of the moat. One possible nonlinear outcome of this instability is the production of a vortex tripole in which the low vorticity of the moat pools into two satellites of an elliptically deformed central vortex, with the whole structure rotating cyclonically. This type of evolution will be discussed in chapter 7.

6.1 Point vortex approximation

In section 3.1, the linear stability of an annular ring of enhanced vorticity was discussed. The presence of a region of high vorticity at the center of the ring complicates this picture in two ways. First, the edge of the central region can also support waves, which might interact with waves along the other two edges if they are close enough. Secondly, even if the annular ring is far enough away from the central region that the waves along the edge of the central region do not significantly interact, the central region of high vorticity can induce an axisymmetric differential rotation across the annular ring and thereby stabilize the ring. Both of these effects can be understood as special cases of a four-region model, which is discussed in Appendix A. In order to understand the stabilizing effect of differential rotation across the annular ring we consider the special case where $\zeta_2 = 0$, and where $r_1 \to 0$ and $\zeta_1 \to \infty$ in such a way that $\pi r_1^2 \zeta_1 = 2\pi r_1^2 \bar{\omega}_1 \to C$, where C is a specified constant circulation associated with

Reproduced with permission of the copyright owner. Further reproduction prohibited without permission.

the central point vortex. In this special case the axisymmetric basic state angular velocity $\bar{\omega}(r)$ given by (A.3) reduces to

$$\bar{\omega}(r) = \frac{C}{2\pi r^2} + \tfrac{1}{2}\zeta_3 \begin{cases} 0 & 0 \le r \le r_2, \\ 1 - (r_2/r)^2 & r_2 \le r \le r_3, \\ (r_3/r)^2 - (r_2/r)^2 & r_3 \le r < \infty, \end{cases} \tag{6.1}$$

and the corresponding basic state relative vorticity $\bar{\zeta}(r)$ given by (A.4) reduces to

$$\bar{\zeta}(r) = \frac{d(r^2\bar{\omega})}{r dr} = \begin{cases} 0 & 0 < r < r_2, \\ \zeta_3 & r_2 < r < r_3, \\ 0 & r_3 < r < \infty, \end{cases} \tag{6.2}$$

where r_2, r_3 are specified radii and ζ_3 a specified vorticity level. This is the idealization studied by Dritschel (1989). The eigenvalue problem (A.9) reduces to

$$\begin{pmatrix} m\bar{\omega}_2 + \frac{1}{2}\zeta_3 & \frac{1}{2}\zeta_3 (r_2/r_3)^m \\ -\frac{1}{2}\zeta_3 (r_2/r_3)^m & m\bar{\omega}_3 - \frac{1}{2}\zeta_3 \end{pmatrix} \begin{pmatrix} \Psi_2 \\ \Psi_3 \end{pmatrix} = \nu \begin{pmatrix} \Psi_2 \\ \Psi_3 \end{pmatrix}. \tag{6.3}$$

The system (6.3) can be regarded as a concise mathematical description of the interaction between two counterpropagating vortex Rossby edge waves along r_2 and r_3 and influenced by the central vortex. The upper right matrix element in (6.3) gives the effect of the vorticity anomaly pattern at r_3 on the behavior of the interface at r_2, while the lower left matrix element in (6.3) gives the effect of the vorticity anomaly pattern at r_2 on the behavior of the interface at r_3. Note that the effect of these interactions decays with increasing wavenumber and decreasing values of the ratio r_2/r_3. If these off-diagonal interactions were not present, the vortex Rossby edge waves at r_2 would propagate with angular velocity $\bar{\omega}_2 + \zeta_3/(2m)$ and the vortex Rossby edge waves at r_3 would propagate with angular velocity $\bar{\omega}_3 - \zeta_3/(2m)$. In other words, for $\zeta_3 > 0$, the inner waves would propagate counterclockwise relative to the basic state flow at $r = r_2$, while the outer waves would propagate clockwise relative to the basic state flow at $r = r_3$. As we shall see below, with the off-diagonal interactions included and with a basic flow satisfying $\bar{\omega}_2 < \bar{\omega}_3$, the waves can phase lock, and instability is possible. Note that the effects of the central point vortex enter through $\bar{\omega}_2$ and $\bar{\omega}_3$. The effect of a strong central vortex is to make $\bar{\omega}_2 > \bar{\omega}_3$, which disrupts the ability of the two waves to phase lock. This is shown schematically in Fig. 6.3 which

Reproduced with permission of the copyright owner. Further reproduction prohibited without permission.

demonstrates how the differential rotation across the annular ring can be reduced or reversed by the presence of a central vortex. To quantify the effects of the central point vortex on the stability of the annular ring, let us now examine the formula for the eigenvalues ν.

The eigenvalues of (6.3), normalized by ζ_3, are given by

$$\frac{\nu}{\zeta_3} = \tfrac{1}{2}m\left(\frac{\bar{\omega}_2+\bar{\omega}_3}{\zeta_3}\right) \pm \tfrac{1}{2}\left\{\left[1+m\left(\frac{\bar{\omega}_2-\bar{\omega}_3}{\zeta_3}\right)\right]^2 - \left(\frac{r_2}{r_3}\right)^{2m}\right\}^{\frac{1}{2}}. \qquad (6.4)$$

In order to more easily interpret the eigenvalue relation (6.4), it is convenient to reduce the number of adjustable parameters to two. We first define $\delta = r_2/r_3$ as a measure of the width of the annular ring of vorticity and $\Gamma = C/[\zeta_3\pi(r_3^2 - r_2^2)]$ as the ratio of the central point vortex circulation to the circulation of the secondary eyewall. According to (6.4), stability will occur when the term in braces is positive, so that stability is guaranteed if $1 + m(\bar{\omega}_2 - \bar{\omega}_3)/\zeta_3 > \delta^m$ for integer m satisfying $1 \leq m < \infty$. Expressing $\bar{\omega}_2/\zeta_3$ and $\bar{\omega}_3/\zeta_3$ in terms of Γ and δ, this inequality becomes $\Gamma > [\delta^2/(1-\delta^2)][1 - (2/m)(1-\delta^m)/(1-\delta^2)]$ for $1 \leq m < \infty$. For $m = 1$, the inequality is $\Gamma > -[\delta/(1+\delta)]^2$, while for $m = 2$ it is $\Gamma > 0$. We shall restrict our attention to $\Gamma > 0$, so that both wavenumbers one and two will be exponentially stable. Now, since $1-(2/m)(1-\delta^m)/(1-\delta^2) \to 1$ as $m \to \infty$ and is always less than unity, our sufficient condition for stability is

$$\Gamma > \frac{\delta^2}{1-\delta^2}. \qquad (6.5)$$

The region of the Γ-δ plane satisfying (6.5) lies above the dashed lines in Fig. 6.4. A physical interpretation of the sufficient condition for stability (6.5) is related to Fjørtoft's theorem (Montgomery and Shapiro 1995) and is as follows. Returning to the inequality $1+m(\bar{\omega}_2-\bar{\omega}_3)/\zeta_3 > \delta^m$, we note that, since the right hand side of (6.5) is less than unity and the left hand side is greater than unity if $(\bar{\omega}_2 - \bar{\omega}_3)/\zeta_3 > 0$, stability is assured if $\bar{\omega}_2 > \bar{\omega}_3$ (for $\zeta_3 > 0$). Since, in the absence of coupling, the waves on the inner edge of the annular ring prograde relative to the flow in its vicinity,

Reproduced with permission of the copyright owner. Further reproduction prohibited without permission.

and since the waves on the outer edge retrograde relative to the flow in its vicinity, a larger basic state angular velocity on the inner edge ($\bar{\omega}_2 > \bar{\omega}_3$) will prevent the waves from phase locking, satisfying a sufficient condition for stability.

Wavenumbers larger than two can produce frequencies with nonzero imaginary parts. Expressing $\bar{\omega}_2/\zeta_3$ and $\bar{\omega}_3/\zeta_3$ in terms of δ and Γ as $\bar{\omega}_2/\zeta_3 = \frac{1}{2}\Gamma(\delta^{-2} - 1)$ and $\bar{\omega}_3/\zeta_3 = \frac{1}{2}(\Gamma + 1)(1 - \delta^2)$, and then using these in (6.4), we can calculate the dimensionless complex frequency ν/ζ_3 as a function of the disturbance azimuthal wavenumber m and the two basic state flow parameters δ and Γ. The imaginary part of ν/ζ_3, denoted by ν_i/ζ_3, is a dimensionless measure of the growth rate. Isolines of ν_i/ζ_3 as a function of δ and Γ for $m = 3, 4, \ldots, 8$ are shown in Fig. 6.4. Note that all basic states, no matter what the value of Γ, satisfy the Rayleigh necessary condition for instability but that most of the region shown in Fig. 6.4 is in fact stable. Clearly, thinner annular regions (larger values of r_2/r_3) should produce the highest growth rates but at much higher azimuthal wavenumbers. Note also the overlap in the unstable regions of the Γ-δ plane for different azimuthal wavenumbers. For example, the lower right area of the Γ-δ plane is unstable to all the azimuthal wavenumbers $m = 3, 4, \ldots, 8$. We can combine the six panels in Fig. 6.4 with the remaining growth rate plots for $m = 3, 4, \ldots, 16$ and collapse them into a single diagram if, for each point in the Γ-δ plane, we choose the largest growth rate of the fourteen wavenumbers. This results in Fig. 6.5.

To estimate the growth rates expected in a secondary eyewall mixing problem, consider the case $\delta \approx 0.84$ and $\Gamma \approx 0.45$, which are suggested by the Hurricane Gilbert data shown in Fig. 6.1 (but for the special case of $\zeta_2 = 0$). Then, from the isolines drawn on Fig. 6.5, we obtain $\nu_i \approx 0.12\zeta_3$ for $m = 8$. Using $\zeta_3 \approx 2.8 \times 10^{-3}$ s^{-1}, we obtain an e–folding time $\nu_i^{-1} \approx 50$ minutes.

Reproduced with permission of the copyright owner. Further reproduction prohibited without permission.

6.2 Type 1 instability in the presence of a central vortex: Maintenance of a secondary wind maximum

An initial condition which simulates an annular ring of high PV with concentrated vorticity at its center may be imposed by choosing $\zeta_1 \gg \zeta_3 > \zeta_2$ and $r_1 \ll r_2$ in (B.6) in Appendix B. In this way, wave interactions between the ring and the central vortex are minimized and the ring 'feels' the presence of the central vortex only through the angular velocity field. For this experiment, the numerical integration is performed under the initial condition $\{r_1, r_2, r_3, r_4\} = \{9.5, 52.5, 62.5, 120.0\}$ km, $\{d_1, d_2, d_3, d_4\} = \{2.5, 2.5, 2.5, 15.0\}$ km, and $\{\zeta_1, \zeta_2, \zeta_3, \zeta_4, \zeta_5\} = \{159.18, 5.18, 27.18, 2.18, -0.82\} \times 10^{-4}$ s^{-1}. The associated tangential wind profile is analogous to an observed profile from a single NOAA WP-3D radial flight leg into Hurricane Gilbert during 1012 to 1029 UTC 14 September 1988 (as shown in Fig. 6.1c). Radial profiles of the symmetric part of the initial vorticity, tangential wind, and angular velocity fields are shown by the thin solid lines in Fig. 6.7. The maximum wind of 69 ms^{-1} is found near 10 km while a secondary maximum of 47 ms^{-1}, associated with the ring of enhanced vorticity, is evident near 64 km. The prograding vortex Rossby waves along the inner edge of the ring ($50 \leq r \leq 55$ km) are embedded in a local angular velocity of approximately 5.6×10^{-4} s^{-1} while the retrograding waves along the outer edge of the ring ($60 \leq r \leq 65$ km) are embedded in a stronger local angular velocity of approximately 7.3×10^{-4} s^{-1}. Although the presence of the central vortex reduces the differential rotation across the annular ring by about 30% when compared to the differential rotation with the central vortex removed, it is not enough to eliminate all instabilities. A piecewise uniform vorticity profile as described by the four-region model of Appendix A and which imitates the smooth initial vorticity profile of Fig. 6.7 is found to be unstable in wavenumbers seven through ten, with the maximum growth rate occuring in wavenumber nine with an associated e-folding time of 67 minutes. Application of the eigensolver for continuous vorticity profiles introduced in section 3.1, to the smooth initial profile of

Reproduced with permission of the copyright owner. Further reproduction prohibited without permission.

Fig. 6.7a yields similar results. The comparison is shown in Appendix A (Fig. A.1) and demonstrates very good agreement in the predicted maximum growth rate and most unstable wavenumber.

Results of this experiment are shown in Fig. 6.6 in the form of vorticity maps plotted every hour over a 24h period. The growth of the wavenumber nine maximum instability becomes evident within 4 h and by $t = 6$ h the ring has undergone a nearly complete 'roll-up' into nine coherent structures. The differential rotation induced by the central vortex advects the inner edges of the coherent structures more rapidly than the outer edges so that at $t = 8$ h, the structures have become cyclonically stretched around the vortex, while trailing spirals have formed as vorticity is stripped from their outer edges. At $t = 10$ h, the stretching has resulted in a banded structure with thin strips of enhanced vorticity being wrapped around the vortex. Leading spirals, which have been stripped from the inner edges of the bands, have propagated inwards into regions of intense differential rotation (and active enstrophy cascade). At $t = 12$ h, the moat has been maintained although its outer radius has contracted to 35 km from its initial value of 60 km. Outside $r = 35$ km, the vorticity of the strips is sufficiently strong to maintain the strips against the vortex induced differential rotation. Inside $r = 35$ km, the strips can no longer maintain themselves and they are rapidly filamented to small scales where they are lost to diffusion. Thus for these initial conditions, $r = 35$ km represents a barrier to inward mixing. Also evident at this time, particularly in the two eastern quadrants of the vortex, are secondary instabilities across individual strips of vorticity. These instabilities occur as the strips become too thin to be stabilized by the vortex and are most pronounced at larger radii where the vortex induced differential rotation is weak. We see then that the presence of a central vortex influences the flow evolution in two somewhat disparate ways. In the region of the moat, coherent vorticity structures are filamented and lost to diffusion while at larger radii (but still inside $r = 80$ km), the vortex helps to maintain the vorticity by inhibiting secondary instabilities within the thin strips. At

Reproduced with permission of the copyright owner. Further reproduction prohibited without permission.

$t = 15$ h, the instabilities across the strips have rolled up into miniature vortices and during the remainder of the evolution to $t = 24$ h, these vortices undergo mixing and merger processes, relaxing the flow towards axisymmetry. Further time integration past $t = 24$ h results in little appreciable change other than a slow diffusive spindown.

The colored lines of Fig. 6.7 show the evolution of the vorticity, tangential velocity, and angular velocity. The profiles represent azimuthal averages taken with respect to distance from the minimum streamfunction[5]. At $t = 6$ h, the annular ring has become broader and weaker and its maximum vorticity has moved inwards. The tangential wind profile shows a weakening of the secondary maximum while the flow inside of the ring has strengthened, smoothing out the initially steep gradient between 52 km and 62 km. The angular velocity evolution exhibits a lessening of the differential rotation across the ring. At $t = 12$ h, the symmetric part of the flow has relaxed to a nearly steady state. The vorticity in the ring has further broadened and weakened but the secondary maximum and its associated gradient reversal have persisted. Similarly, the tangential wind maintains a significant secondary maximum with the flow increasing from 30 ms^{-1} at 35 km to 42 ms^{-1} at 73 km. The angular velocity has become monotonic, eliminating the positive differential rotation across the ring. Thus the symmetric part of the flow has become stable in the context of the four-region model, and little change is noted during the next 12 h. This characteristic of the flow may offer insight into the observed longevity of hurricane secondary eyewalls.

The results of the above experiment are based on an initial condition which imitates a profile observed during a *single* radial flight leg into Hurricane Gilbert on 14 September 1988. Black and Willoughby (1992) calculated *azimuthal mean* tangential wind profiles in Hurricane Gilbert based on aircraft observations at the beginning and end of the 14 September sortie. In the context of the four-region model, the mean profile at the beginning was found to be slightly unstable (or nearly neutral) to wavenumber

[5]Although the centroid of vorticity on an f-plane is invariant, asymmetries formed during the evolution cause the location of the minimum streamfunction to oscillate.

Reproduced with permission of the copyright owner. Further reproduction prohibited without permission.

10, with an e-folding time of 6 hours, and wavenumber 11 with an e-folding time of 13 hours. A numerical experiment (not shown) using the mean profile as an initial condition demonstrated a slow growth of the wavenumber 10 instability but wave-mean flow interactions appeared to be sufficient to stabilize the flow by *slightly* altering the gradients along the ring edges. The mean profile calculated by Black and Willoughby (1992) based on observations at the end of the sortie was found to be stable. Thus, the results of the experiment shown in Fig. 6.6 are useful in describing how an unstable secondary eyewall can evolve to a stable secondary eyewall, but these results are likely an *exaggeration* of the actual evolution of a hurricane's secondary eyewall. It is possible that mixing associated with an unstable secondary eyewall is just enough to maintain a near-neutral flow.

For comparison with the experiment shown in Fig. 6.6, a numerical simulation is now performed with the central vortex removed, so that $\zeta_1 = \zeta_2 = 5.18 \times 10^{-4} s^{-1}$ and all other parameters in (B.6) remain essentially unchanged. Radial profiles of the initial vorticity, tangential wind, and angular velocity fields are shown by the solid lines in Fig. 6.9. The differential rotation across the ring is greater than the previous example ($\omega \approx 3.1 \times 10^{-4}$ s^{-1} when $50 \leq r \leq 55$ km and $\omega \approx 5.3 \times 10^{-4}$ s^{-1} when $60 \leq r \leq 65$ km) and a linear analysis using (3.3) demonstrates that the maximum growth rate has shifted from wavenumber nine to six while the e-folding time has decreased from 67 to 48 minutes. The evolution is again displayed in the form of vorticity maps in Fig. 6.8.

At $t = 4$ h, the wavenumber six maximum instability has amplified and a roll-up of the annular ring has occured. The presence of the wavenumber seven instability, whose growth rate is 96% of the maximum instability, is evident in the northern quadrant. At $t = 8$ h, six well formed elliptical vortices have emerged. Weak vorticity from outside of the ring is beginning to carve into the central region of the vortex while stronger vorticity from the center is ejected outwards in the form of trailing spirals. After this time, intricate vortex merger and mixing processes dominate the evolution

Reproduced with permission of the copyright owner. Further reproduction prohibited without permission.

so that at $t = 16$ h, five vortices remain and at $t = 24$ h, only three remain. Without the presence of a dominant central vortex, each coherent structure imposes a similar flow across the others. There is no clear victor in the merger process and high vorticity can mix to the center. At $t = 54$ h, the vorticity has nearly relaxed to a monotonic distribution which satisfies the Rayleigh sufficient condition for stability. This is in marked contrast to the behavior in the presence of a central vortex, where the mixing results in a monotonic angular velocity distribution which satisfies Fjørtoft's, but not Rayleigh's, sufficient condition for stability across the ring.

6.3 Maximum entropy prediction

In section 3.3, we introduced a statistical mechanics approach for predicting the end state of an initially unstable flow, and applied the method to the three-region model. In that case, the end state was predicted correctly to be a monopole. However, the results of the numerical experiment shown in Fig. 6.6 demonstrate a quasi-equilibrated state which is not a monopole and which still satisfies Rayleigh's necessary condition for instability. Can the maximum entropy theory predict such an end state?

We now apply the maximum entropy theory to an initial flow field which may be described by the four-region model, in which case we have 4 vorticity levels. In order to approximate the initial conditions used in the numerical experiment of Fig. 6.6, we choose $\hat{\zeta}_1 = 160 \times 10^{-4}$ s^{-1}, $\hat{\zeta}_2 = 6 \times 10^{-4}$ s^{-1}, $\hat{\zeta}_3 = 28 \times 10^{-4}$ s^{-1}, and $\hat{\zeta}_4 = 0$. The central vorticity $\hat{\zeta}_1$ is contained within a circle of radius 9.5 km, the vorticity in the moat $\hat{\zeta}_2$ is contained between 9.5 km and 52.5 km, the vorticity in the ring $\hat{\zeta}_3$ is contained between 52.5 km and 62.5 km, and the far field vorticity $\hat{\zeta}_4$ is found beyond 62.5 km to the disk boundary at $a = 300$ km. The initial values of the energy $\mathcal{E}$, angular impulse $\mathcal{I}$, and areas of each patch $\mathcal{A}_\ell$ can then be determined. Performing the iterative algorithm described in Appendix C, the equilibrated vorticity associated with the initial flow can be deduced. The results are shown in Fig. 6.10.

Reproduced with permission of the copyright owner. Further reproduction prohibited without permission.

Similar to the predicted end state of section 3.3 for the case of an annular ring with no vortex at its center, the predicted final vorticity profile is axisymmetric and *monotonic*. The vorticity initially at $r = 0$ has been reduced by almost 75% and the maximum wind has been reduced to a value below 50 m s^{-1}. The expectation functions $\rho_1(r)$, $\rho_2(r)$, $\rho_3(r)$, and $\rho_4(r)$, associated with the 4 vorticity levels, are shown in Fig. 6.10b and depict a much more well mixed state than the results of the numerical experiment would suggest. At $r = 0$, most of the vorticity is comprised of vorticity initially found in the ring and there are roughly equal contributions from vorticity initially found in the central vortex, moat and far field. In this case, the maximum entropy theory does not seem to recognize the processes by which the central vortex is protected from mixing with outside fluid by the intense differential rotation around it.

Reproduced with permission of the copyright owner. Further reproduction prohibited without permission.

Figure 6.1: Hurricane Gilbert on 14 September 1988. (a) Reflectivity obtained at 1010 UTC from radar onboard a NOAA WP–3D research aircraft. The image spans 240 km × 240 km with tick marks every 24 km. Near the image center, the primary eyewall is identified by a nearly annular ring of high reflectivity with a radial width of 8 km to 20 km. The secondary eyewall is associated with the encircling ring of high reflectivity located around 60 km from the hurricane center. The relatively clear region inside the primary eyewall is the eye and the clear region between the primary and secondary eyewalls is the moat. The flight track of the aircraft is shown by the white lines. Flight-level winds are shown by the wind barbs along the flight track (Image courtesy of NOAA Hurricane Research Division). (b) Composite radar reflectivity spanning the time 0959–1025 UTC. The domain is 360 km × 360 km, with tick marks every 36 km. The primary eyewall and concentric secondary eyewall are apparent as two dark rings. The line through the center is the north–south part of the flight track (From Samsury and Zipser 1995). (c) Flight-level tangential wind (solid) and angular velocity (dashed) profiles along the southern outbound leg of the flight track during the time 1012–1030 UTC.

Reproduced with permission of the copyright owner. Further reproduction prohibited without permission.

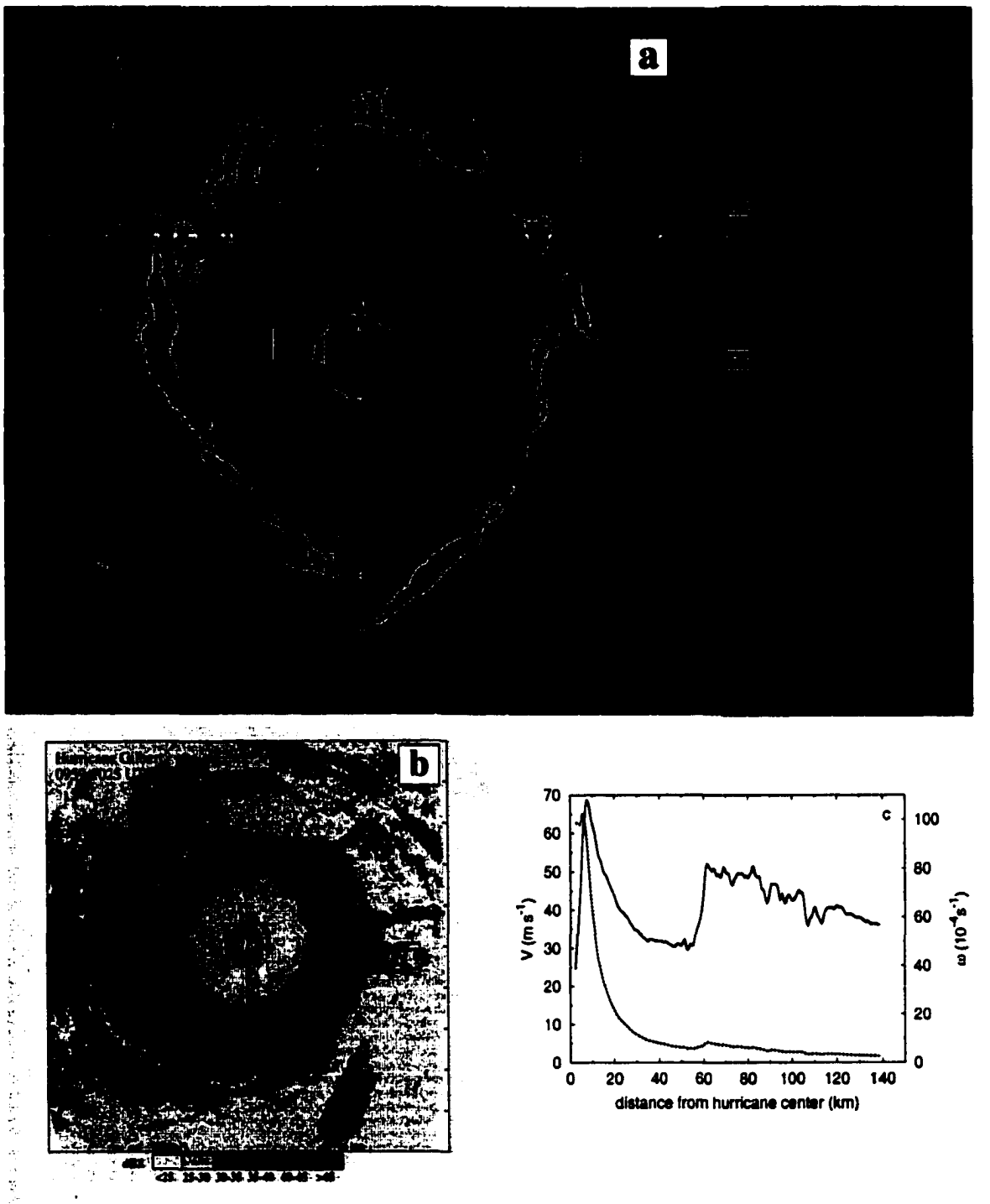

Figure 6.1: See caption on previous page.

Reproduced with permission of the copyright owner. Further reproduction prohibited without permission.

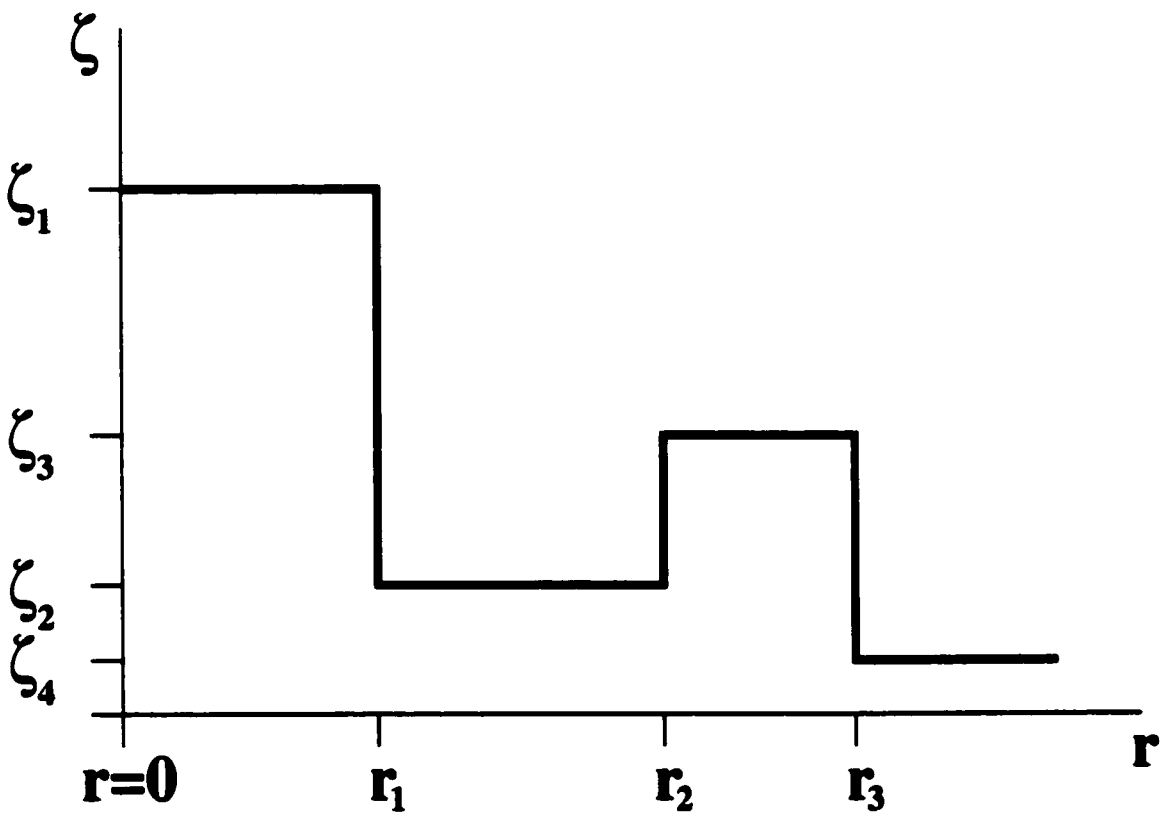

Figure 6.2: Schematic of the idealized piecewise uniform four-region vorticity model. The central vortex has strong vorticity ζ_1, the moat has relatively weak vorticity ζ_2, the secondary ring has enhanced vorticity ζ_3, and the far-field is nearly irrotational.

Reproduced with permission of the copyright owner. Further reproduction prohibited without permission.

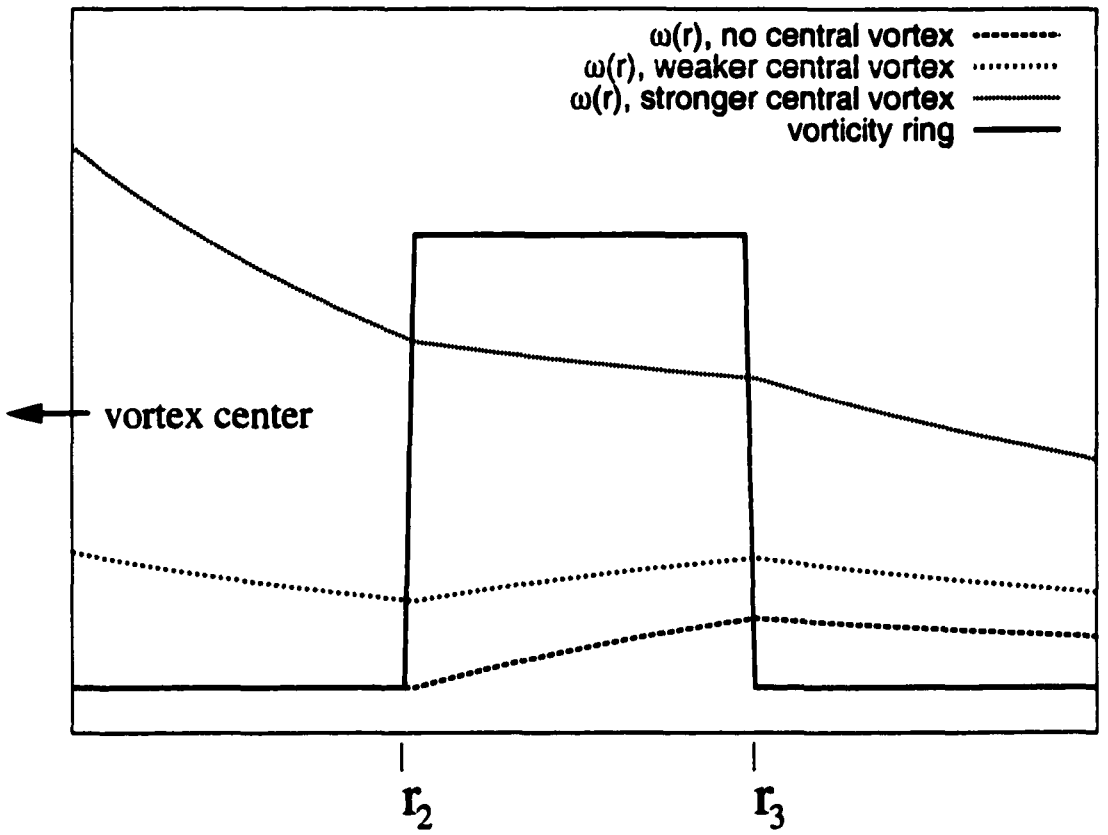

Figure 6.3: Schematic showing the effect of a central vortex on the differential rotation (shear) across an annular ring of enhanced vorticity spanning $r_2 \leq r \leq r_3$. When no central vortex is present, the shear is positive and entirely self-induced by the ring. When a central vortex is present, an adverse shear is introduced which counters the ring-induced shear. If the central vortex is strong enough relative to the ring (or close enough to the ring), the shear can be reversed (i.e. $\omega(r_2) > \omega(r_3)$) and the ring is then assured to be exponentially stable.

Reproduced with permission of the copyright owner. Further reproduction prohibited without permission.

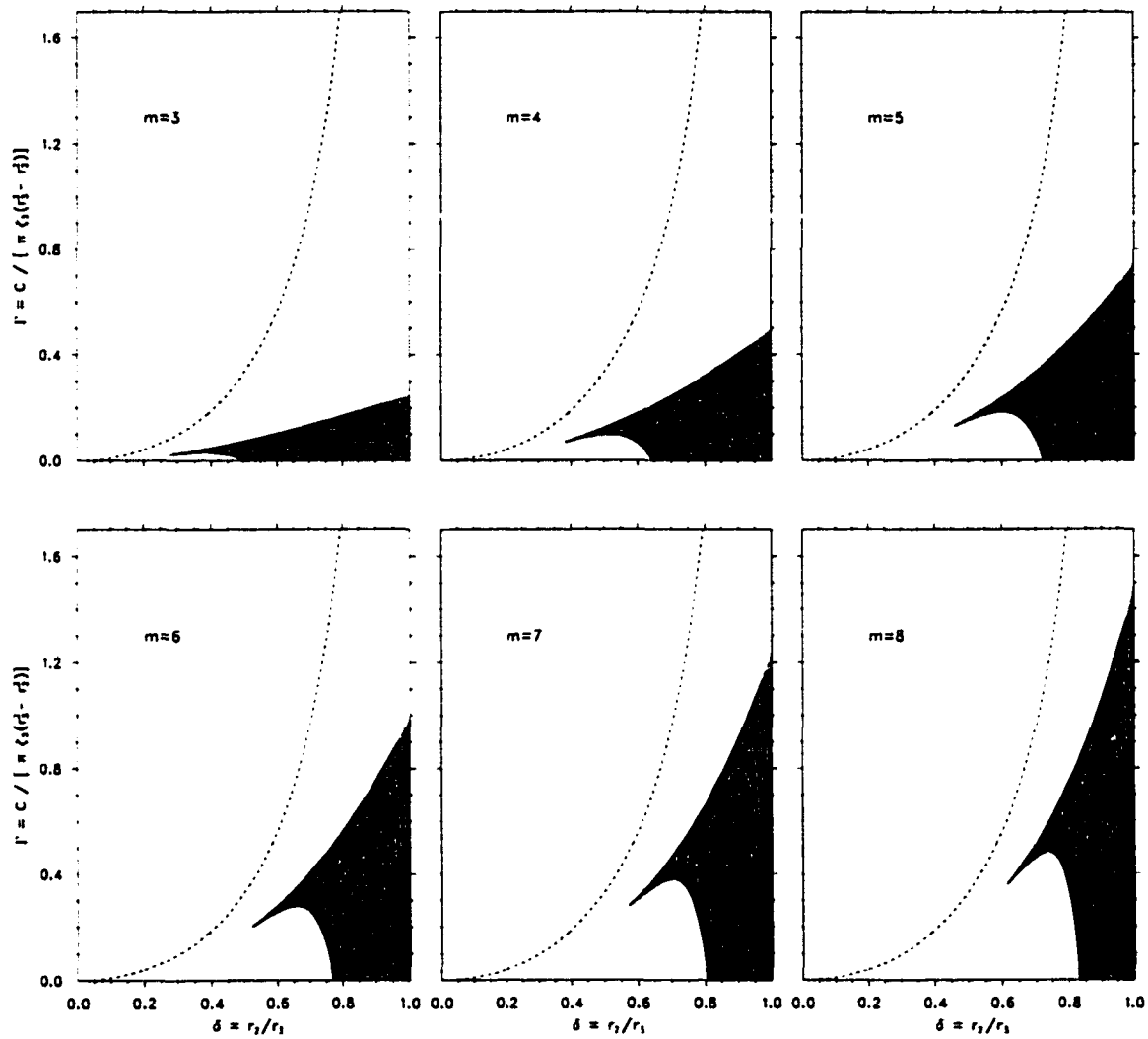

Figure 6.4: Isolines of the dimensionless growth rate ν_i/ζ_3, computed from Eq. (6.4), as a function of $\delta = r_2/r_3$ and $\Gamma = C/[\zeta_3\pi(r_3^2 - r_2^2)]$ for tangential wavenumbers $m = 3, 4, \ldots, 8$. The parameter Γ is the ratio of the circulation associated with the central point vortex to the circulation associated with the annular ring of elevated vorticity between r_2 and r_3. Non-zero growth rates occur only in the shaded regions. The isolines are $\nu_i/\zeta_3 = 0.01, 0.03, 0.05, \ldots$. The maximum growth rates increase and are found closer to $\delta = 1$ as m increases. The region above the dashed line satisfies the sufficient condition for stability given by Eq. (6.5).

Reproduced with permission of the copyright owner. Further reproduction prohibited without permission.

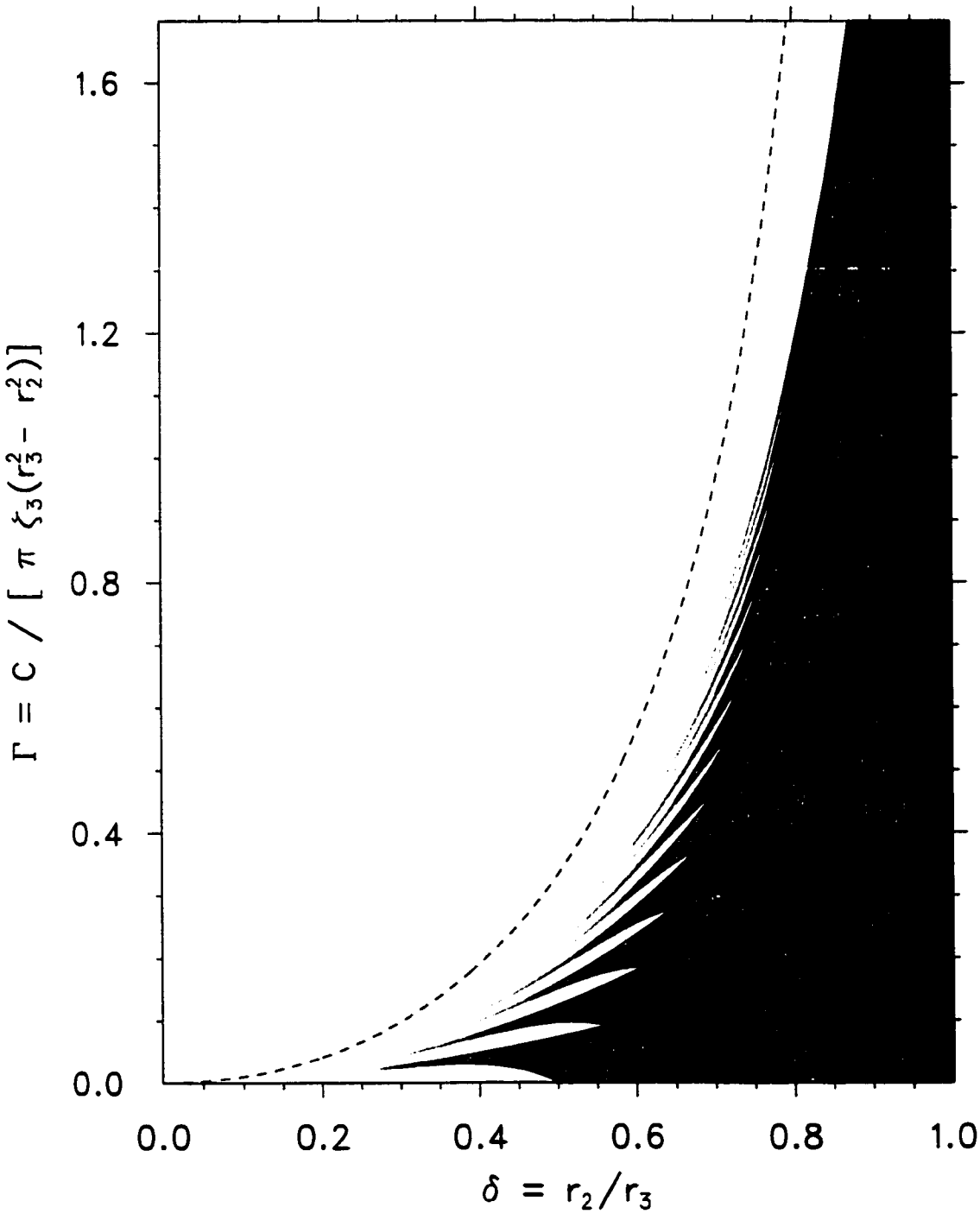

Figure 6.5: Isolines of the maximum dimensionless growth rate ν_i/ζ_3 among the azimuthal wavenumbers $m = 3, 4, \ldots, 16$ for type 1 instability. The isolines are the same as in Fig. 6.4. Shading indicates the wavenumber associated with the maximum dimensionless growth rate at each point.

Reproduced with permission of the copyright owner. Further reproduction prohibited without permission.

Figure 6.6: Vorticity contour plots for the type 1 instability experiment. The model domain is 600 km × 600 km but only the inner 190 km × 190 km is shown. Values along the label bar are in units of 10^{-4} s^{-1}. Warmer colors are associated with higher values of vorticity. Model run time in hours is shown on each plot. (a) $t = 0$ h to 6 h.

Reproduced with permission of the copyright owner. Further reproduction prohibited without permission.

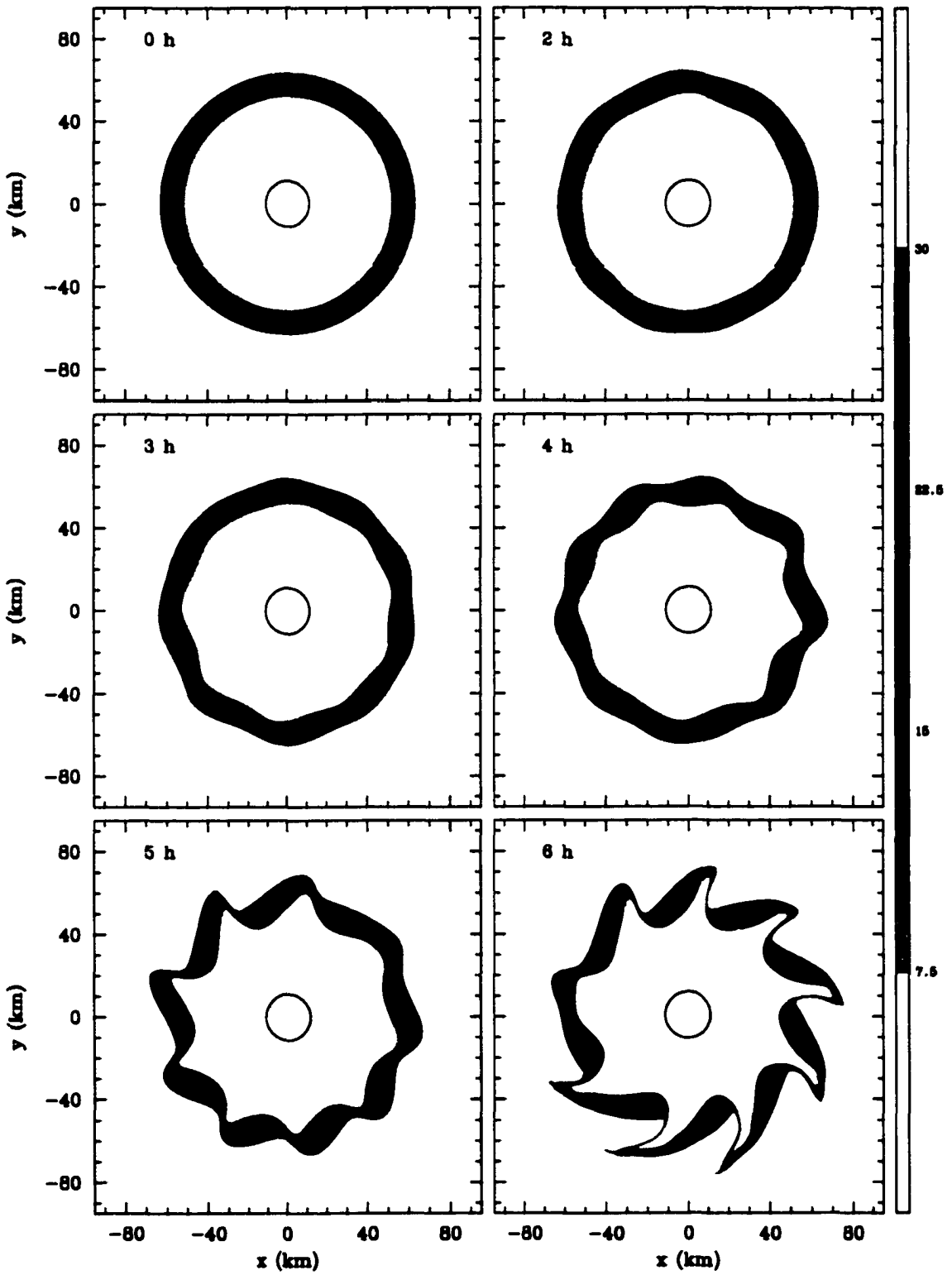

Figure 6.6: (a) See caption on previous page.

Reproduced with permission of the copyright owner. Further reproduction prohibited without permission.

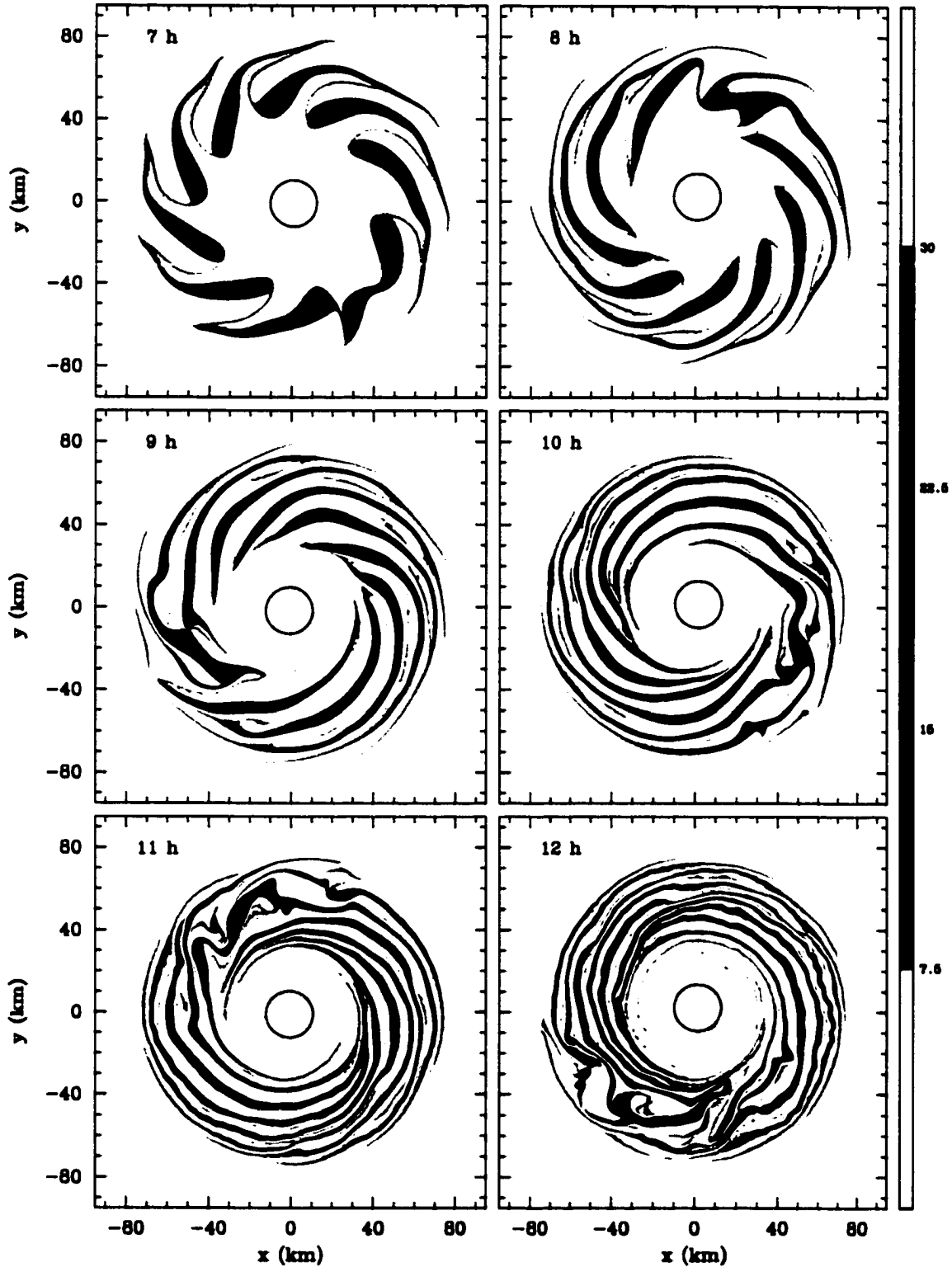

Figure 6.6: (*Continued*) (b) Vorticity from $t = 7$ h to 12 h.

Reproduced with permission of the copyright owner. Further reproduction prohibited without permission.

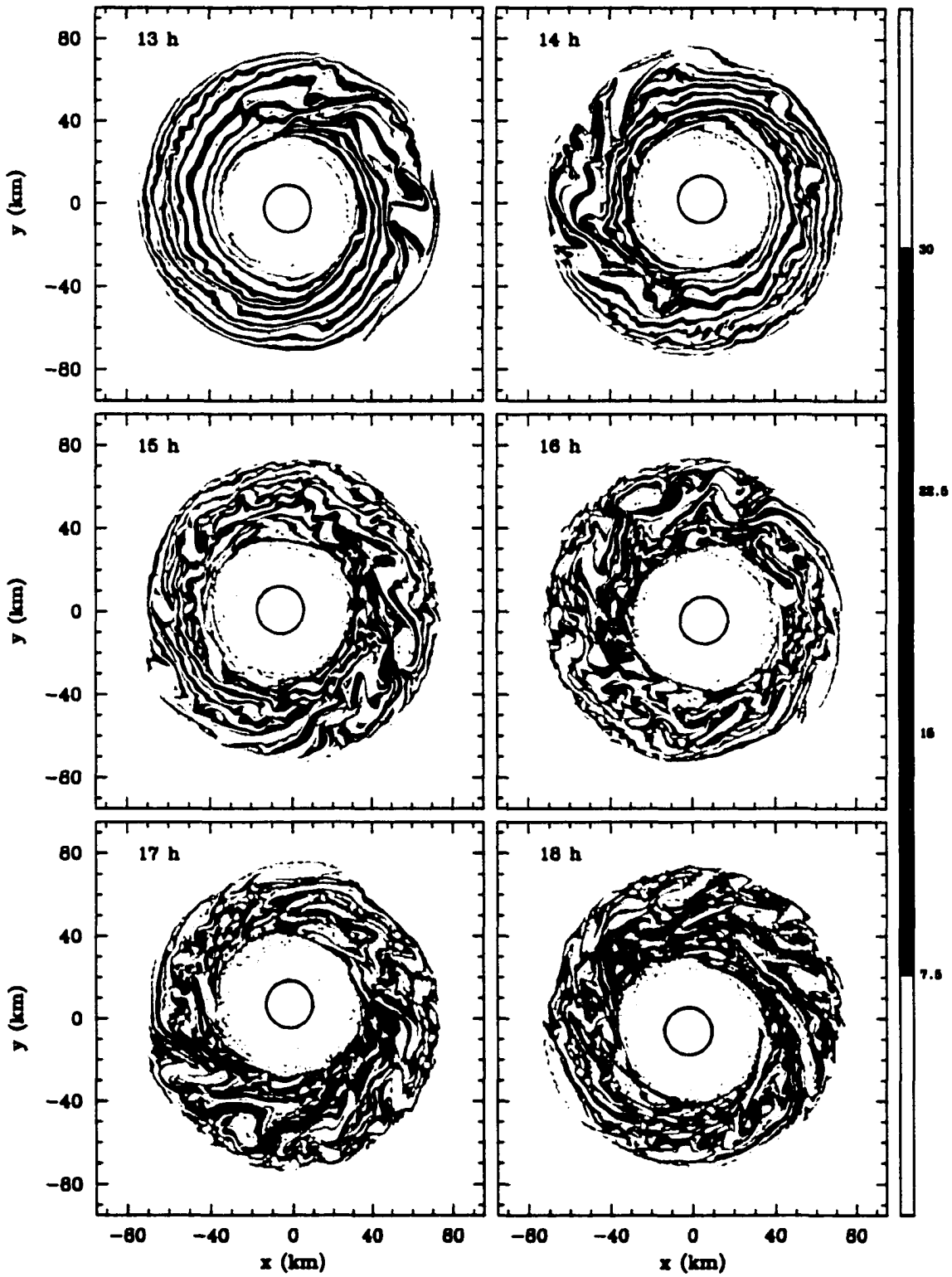

Figure 6.6: (*Continued*) (c) Vorticity from $t = 13$ h to 18 h.

Reproduced with permission of the copyright owner. Further reproduction prohibited without permission.

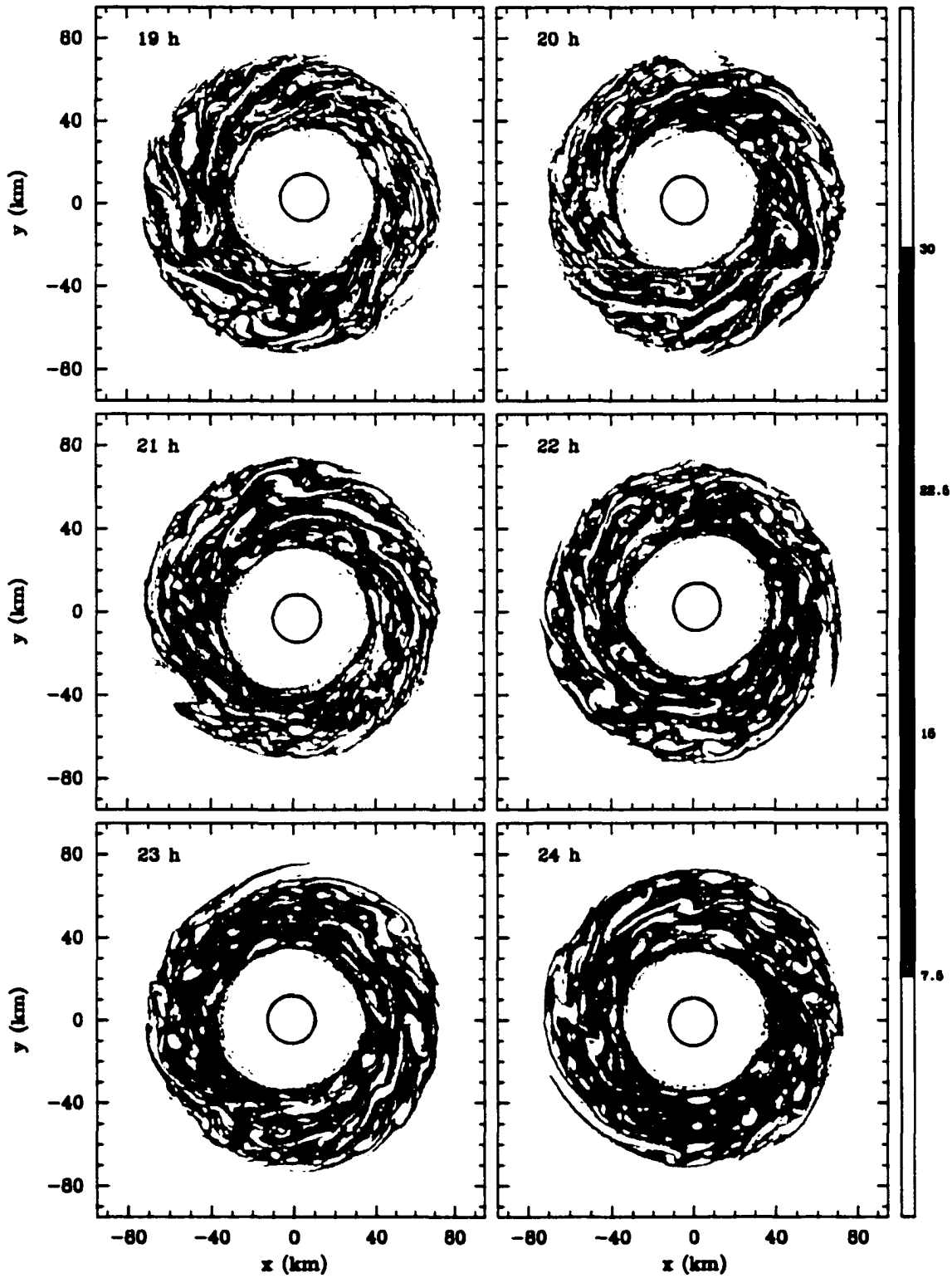

Figure 6.6: (*Continued*) (d) Vorticity from $t = 19$ h to 24 h.

Reproduced with permission of the copyright owner. Further reproduction prohibited without permission.

Figure 6.7: (a) Azimuthal mean vorticity, (b) tangential velocity, and (c) angular velocity for the experiment shown in Fig. 6.6 at the selected times $t = 0$ (thin solid black), 6 h (green long dash), 12 h (blue short dash), and 24 h (thick solid red). Averages were computed with respect to distance from the minimum streamfunction position. The maximum angular velocity is truncated in the image to highlight the region of the annular ring. Note the reversal of differential rotation across the ring between 6 h and 12 h.

Reproduced with permission of the copyright owner. Further reproduction prohibited without permission.

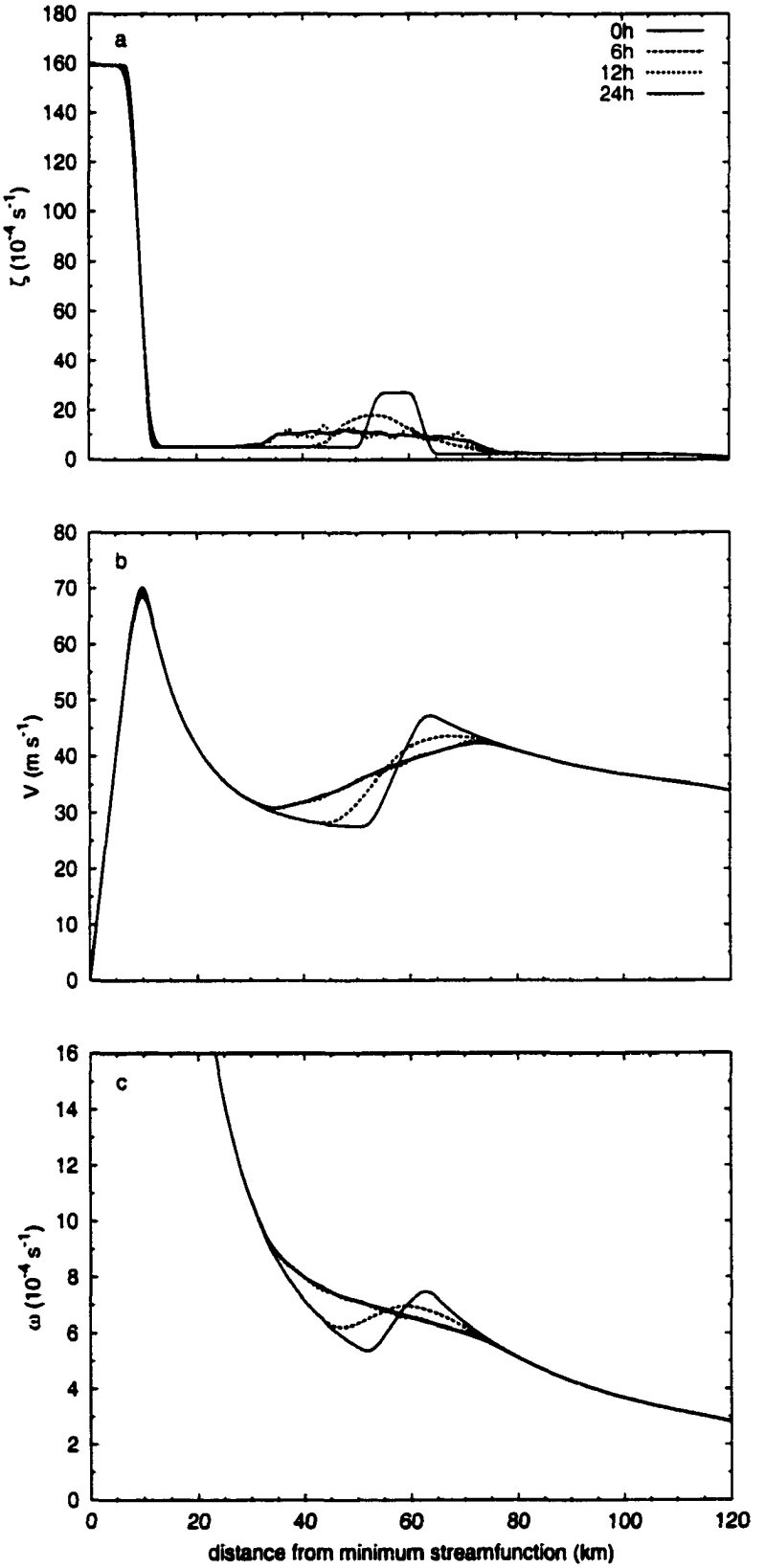

Figure 6.7: See caption on previous page.

Reproduced with permission of the copyright owner. Further reproduction prohibited without permission.

Figure 6.8: Vorticity contour plots. The initial field is similar to the type 1 instability experiment, but without the presence of the central vortex. The model domain is 600 km $\times$ 600 km but only the inner 230 km $\times$ 230 km is shown. The contours begin at 4×10^{-4} s^{-1} and are incremented by 4×10^{-4} s^{-1}. Values along the label bar are in units of 10^{-4} s^{-1}. Selected times are $t = 0, 4, 8, 16, 24$, and 54 h.

Reproduced with permission of the copyright owner. Further reproduction prohibited without permission.

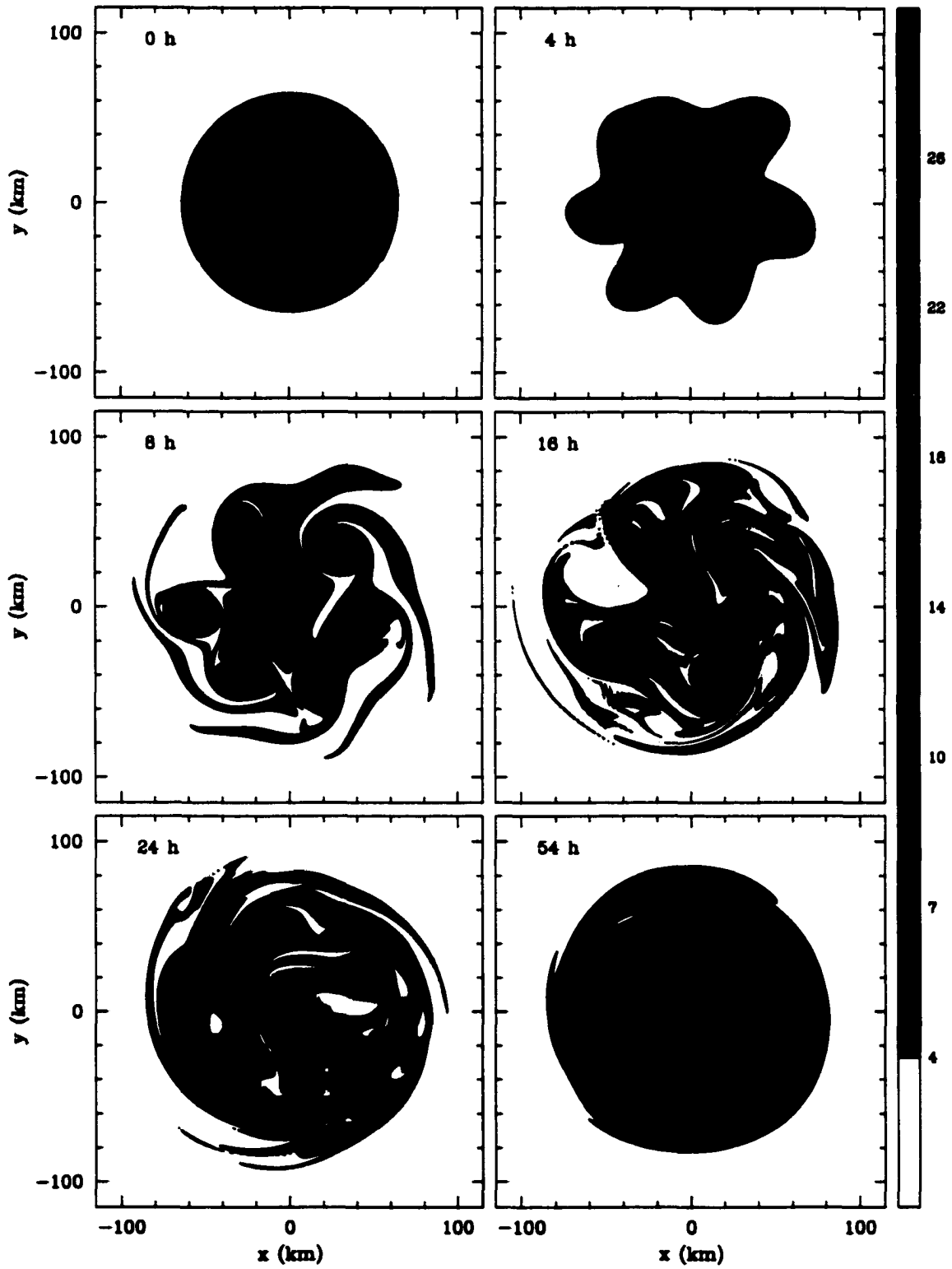

Figure 6.8: See caption on previous page.

Reproduced with permission of the copyright owner. Further reproduction prohibited without permission.

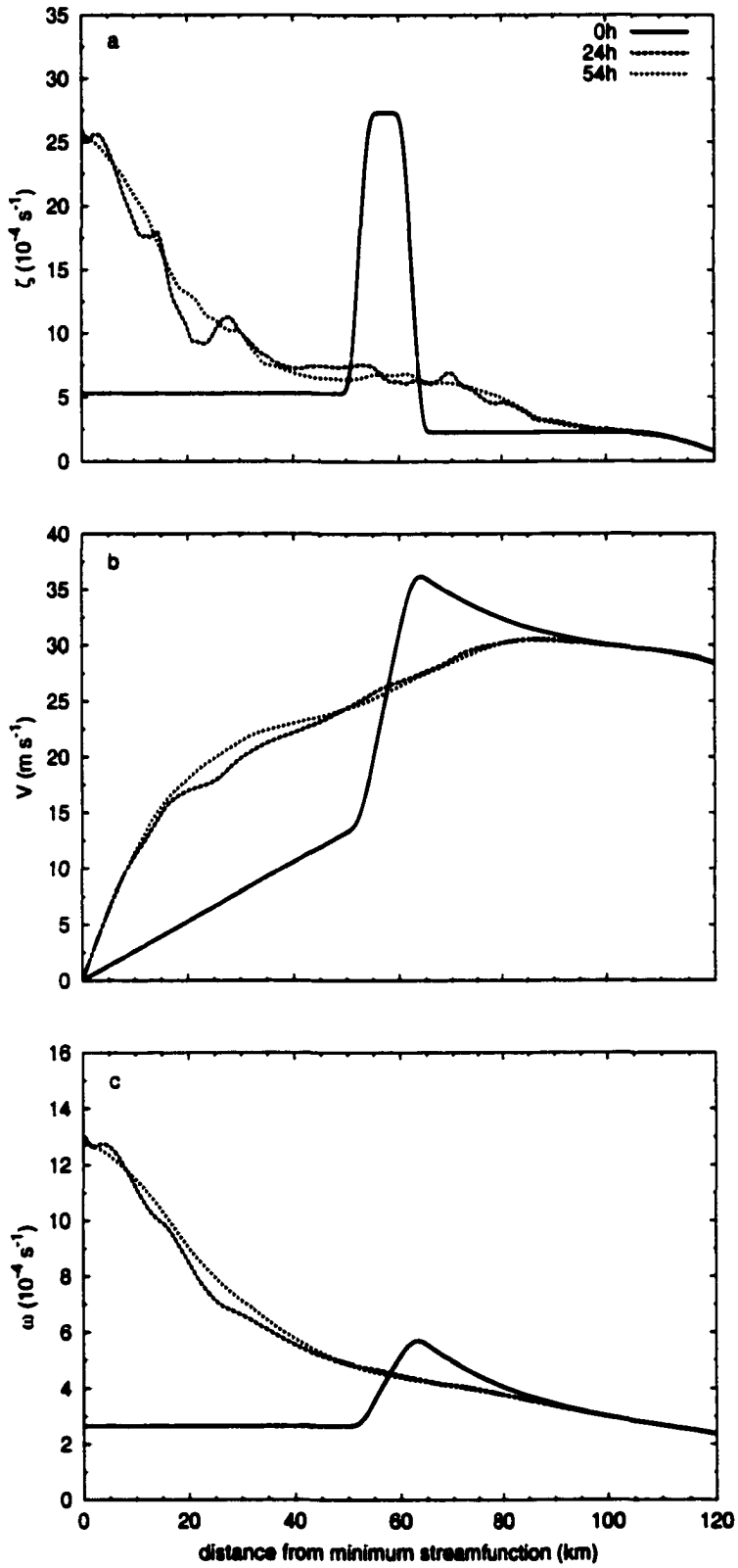

Figure 6.9: Similar to Fig. 6.7 but for the experiment with the central vortex removed shown in Fig. 6.8. The vorticity profile when $t = 54$ h is nearly monotonic.

Reproduced with permission of the copyright owner. Further reproduction prohibited without permission.

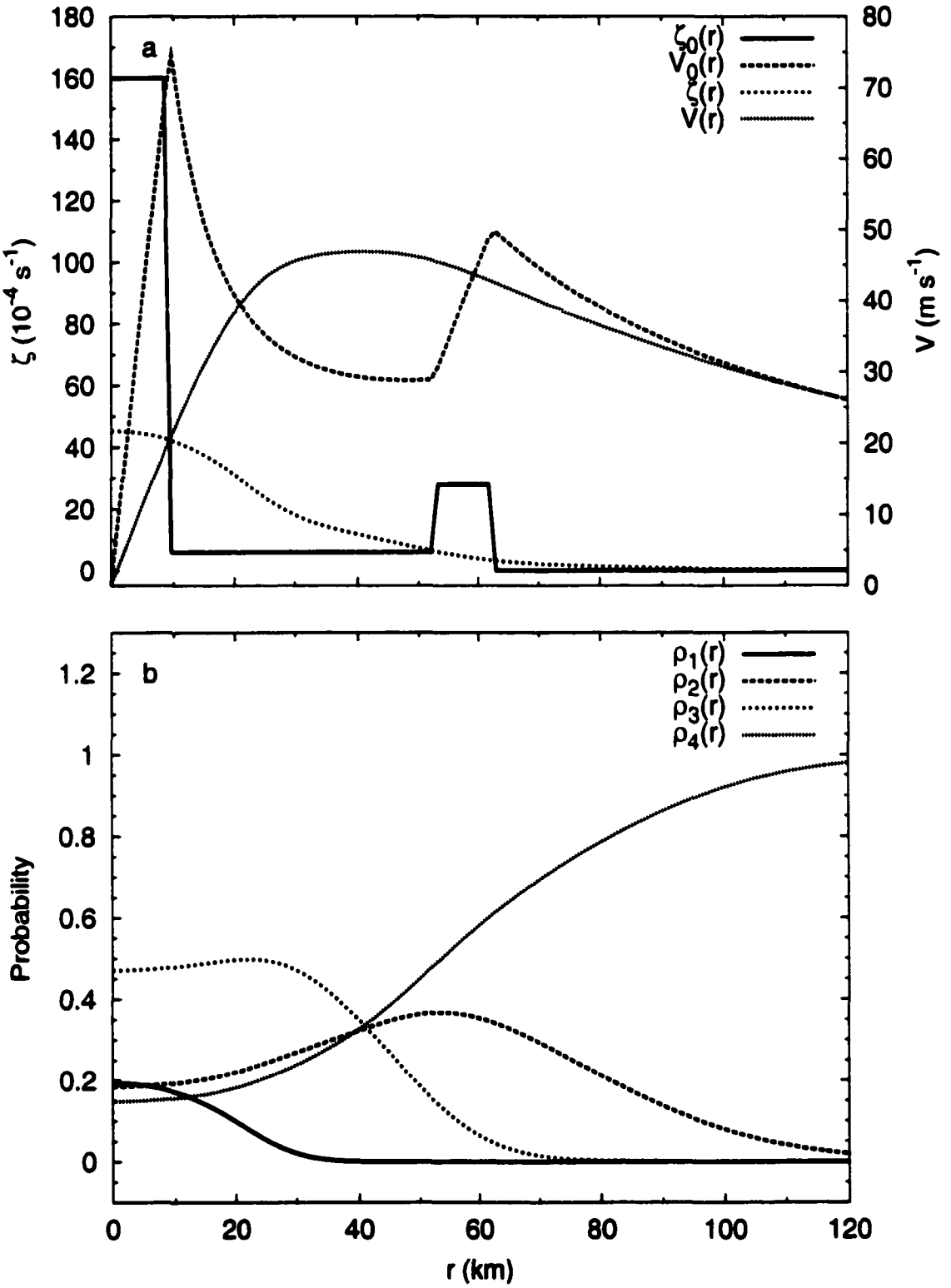

Figure 6.10: Maximum entropy predictions for the four-region model analogy to the initial condition of the secondary eyewall experiment. (a) Initial vorticity $\zeta_0(r)$ and tangential wind $v_0(r)$, and equilibrated vorticity $\zeta(r)$ and tangential wind $v(r)$ predicted by the maximum entropy theory. (b) Expectation functions.

Reproduced with permission of the copyright owner. Further reproduction prohibited without permission.

Chapter 7

FORMATION AND PERSISTENCE OF AN ELLIPTICAL CENTRAL VORTEX

Tropical cyclones sometimes have rotating elliptical eyes. Two outstanding examples were recently documented by Kuo et al. (1999) for the case of Typhoon Herb (1996), and by Reasor et al. (1999) for the case of Hurricane Olivia (1994). Typhoon Herb was observed using the WSR-88D radar on Wu-Feng mountain in Taiwan. The elliptical eye of Typhoon Herb had an aspect ratio (major axis/minor axis) of approximately 1.5. Two complete rotations of the elliptical eye, each with a period of 144 minutes, were observed as the typhoon approached the radar. Kuo et al. interpreted this elliptical eye in terms of the Kirchhoff vortex (Lamb 1932, page 232), an exact, stable (for aspect ratios less than 3) solution for two-dimensional incompressible flow having an elliptical patch of constant vorticity fluid surrounded by irrotational flow. Is the Kirchhoff vortex, with its discontinuous vorticity at the edge of the ellipse, a useful model of rotating elliptical eyes? Melander et al. (1987a) have shown that elliptical vortices with smooth transitions to the far field irrotational flow are not robust but tend to become axisymmetrized via an inviscid process in which a halo of vorticity filaments become wrapped around a more symmetric vortex core. Montgomery and Kallenbach (1997) further clarified the physics of this process for initially monopolar distributions of basic state vorticity, showing that axisymmetrization can be described as the radial and azimuthal dispersion of vortex Rossby waves that are progressively sheared by the differential rotation of the vortex winds. In this latter work, the dependence of the local wave frequency and stagnation radius on the radial

Reproduced with permission of the copyright owner. Further reproduction prohibited without permission.

vorticity gradient was made explicit. In other recent work, Koumoutsakos (1997) and Dritschel (1998) have shown that the extent to which a vortex axisymmetrizes is controlled by the steepness of the vortex edge, with very sharp initial vorticity distributions resulting in robust non-axisymmetric configurations. This could be anticipated by Kelvin's linear analysis for Rossby edge waves in which the asymmetries never axisymmetrize on a discontinuous basic state vorticity profile. If we now allow a sharp but smooth gradient, the local Wenzel-Kramers-Brillouin (WKB) theory of Montgomery and Kallenbach (1997) suggests radially trapped waves which axisymmetrize very slowly. The physics is generally a struggle between Rossby elasticity and radial shearing. Dritschel (1998, Figs. 6 and 7) gives an example of a robust, quasi-steady rotating elliptical pattern of vorticity with aspect ratio 1.6 in which approximately 40% of the vorticity drop from the center to the far field occurs discontinuously at the edge of the ellipse. A recent study by Montgomery and Enagonio (1998) further suggests that even in the absence of any discontinuity in a monotonic basic state vorticity profile, convectively generated vortex Rossby waves can modify the basic state and cause a reversal in radial vorticity profile. The sign change allows for the existence of a discrete neutral or weakly unstable vortex Rossby mode which may not decay.

Reasor et al. (1999) documented the elliptical eyewall of Hurricane Olivia using NOAA WP-3D airborne dual-Doppler radar data and flight level data and identified barotropic instability across the eyewall as a possible source for the observed wavenumber two asymmetry. During the observation period, the symmetric part of the vorticity consisted of an elevated annular region within the eyewall surrounding a depressed region within the eye. An associated smooth basic state vorticity profile was found to support instabilities with a maximum growth in wavenumber two. The observed wavenumber two vorticity asymmetry in the eyewall was hypothesized to be associated with the breakdown of an initially unstable ring of elevated vorticity as described by Schubert et al. (1999) and in chapter 3 of this study.

Reproduced with permission of the copyright owner. Further reproduction prohibited without permission.

An alternative interpretation of the elliptical patterns in Typhoon Herb and Hurricane Olivia is that their vorticity fields had evolved into structures resembling tripoles. Strictly speaking, a tripole is defined as a linear arrangement of three regions of distributed vorticity of alternate signs, with the whole configuration steadily rotating in the same sense as the vorticity of the elliptically-shaped central core. Tripoles have been the subject of several laboratory experiments (Kloosterziel and van Heijst 1991, van Heijst et al. 1991, Denoix et al. 1994) and numerical simulations ever since they were shown to emerge as coherent structures in forced two-dimensional turbulence simulations (Legras et al. 1988). In addition to their emergence as coherent structures in two-dimensional turbulence, tripoles can be produced in a variety of ways, some quite exotic from the point of view of tropical cyclone dynamics. For example, tripoles can be produced by the collision of two asymmetric dipoles (Larichev and Reznik 1983) or by the offset collision of two symmetric Lamb dipoles (Orlandi and van Heijst 1992). Rossi et al. (1997) applied a quadrupolar distortion to a monopolar Gaussian vorticity distribution and found that for a large enough distortion, relaxation to a tripole can occur, demonstrating that finite amplitude asymmetric perturbations applied to a stable monopole do not always relax to their axisymmetric base state. The generation mechanism of probable importance to tropical cyclone dynamics, however, is that associated with the barotropic instability of axisymmetric shielded or, more importantly, partially shielded[6] vortices (Gent and McWilliams 1986, Flierl 1988). Here we consider the central core of the vortex to be monotonic and hence eliminate possibly dominant instabilities which may occur across the eyewall, as investigated by Reasor et al. (1999).

[6]An annular ring of negative vorticity can "partially shield" the far-field flow from a central core of positive vorticity just as, for example, in the element Lithium (atomic number 3), the two electrons that occupy the inner, spherical $1s$-orbital "partially shield" the outermost electron from the +3 charge of the nucleus.

Reproduced with permission of the copyright owner. Further reproduction prohibited without permission.

7.1 Instability across the moat of a shielded vortex

A well-studied family of shielded monopoles has the angular velocity $\omega(r)$ given by

$$\omega(r) = \omega_0 \exp[-(r/b)^\alpha], \tag{7.1}$$

where ω_0 is the angular velocity at $r = 0$, b the size of the vortex, and α the steepness parameter, with $\alpha > 0$. The associated tangential wind $v(r) = r\omega(r)$ and vorticity $\zeta(r) = d(rv)/rdr$ are given by

$$v(r) = \omega_0 r \exp[-(r/b)^\alpha], \tag{7.2}$$

and

$$\zeta(r) = 2\omega_0 \left[1 - \tfrac{1}{2}\alpha(r/b)^\alpha\right] \exp[-(r/b)^\alpha]. \tag{7.3}$$

Plots of ω/ω_0, $v/(b\omega_0)$ and $\zeta/(2\omega_0)$ as functions of r/b for $\alpha = 2, 3, 4, 5, 6$ are shown in Fig. 7.1. The radius of maximum tangential wind occurs at $r/b = (1/\alpha)^{1/\alpha}$, and the vorticity reverses sign at $r/b = (2/\alpha)^{1/\alpha}$ and is a minimum at $r/b = (1+2/\alpha)^{1/\alpha}$. Note that for increasing α, the vorticity in the core becomes more uniform, the annulus of negative $\zeta/(2\omega_0)$ becomes thinner and the vorticity gradient at the edge of the core becomes steeper. The instability and nonlinear evolution of this particular initial vorticity profile has been studied by Carton and McWilliams (1989), Carton et al. (1989), Orlandi and van Heijst (1992), Carton and Legras (1994), Carnevale and Kloosterziel (1994). Carton and McWilliams (1989) showed that this vortex is linearly stable for $\alpha \lesssim 1.9$ and unstable for larger values of α. Carnevale and Kloosterziel (1994, Fig. 7) showed that wavenumber two remains the fastest growing wave until $\alpha \approx 6$, at which point wavenumber three becomes the fastest growing wave. Within the range $1.9 < \alpha < 6$, the wavenumber two instability can saturate as two distinct quasi-stable structures. Carton and Legras (1994) found that when $\alpha < 3.2$, saturation to a tripole occurs, while for $\alpha > 3.2$, two separating dipoles emerge. As α is increased, the nonlinear amplification of wavenumber two increasingly elongates

Reproduced with permission of the copyright owner. Further reproduction prohibited without permission.

the central monopole, and when $\alpha > 3.2$, the central monopole is elongated to the point where it breaks as the two dipoles separate.

Two experiments are now performed using initial vorticity profiles given by (7.3) with $b = 35$ km, and $\omega_0 = 1.85 \times 10^{-3}\text{s}^{-1}$. For the first experiment, $\alpha = 3$ and for the second, $\alpha = 4$.

When $\alpha = 3$, the wavenumber two maximum instability results in a rearrangement of the vorticity into a tripole (Fig. 7.2). During the early stages of the evolution, the central vorticity becomes highly elongated as the negative vorticity of the annulus is anticyclonically wrapped into two satellite vortices. The anticyclonic advection of the vorticity originally in the annulus is not due to the sign of the vorticity there, but is due to the arrangement of the positive vorticity being pulled from the central region. This will be discussed in greater detail in section 7.3. During the later stages, the aspect ratio (major axis / minor axis) of the elliptical central region has decreased to 1.7 with the satellite vortices found along the minor axis.

When $\alpha = 4$, the end result of the vorticity rearrangement is dramatically different. The wavenumber two maximum instability does not saturate as a tripole but results in the formation of two separating dipoles (Fig. 7.3). In the early part of the evolution, the negative vorticity within the moat is strong enough to elongate the central region into a strip and two pools of positive vorticity form within the strip near the two satellite vortices. The strip is eventually broken as the two dipoles propagate away from each other.

Since the radius of minimum vorticity is given by $r/b = (1 + 2/\alpha)^{1/\alpha}$, the evaluation of (7.3) at this radius yields the minimum vorticity $\zeta_{\text{min}} = -\omega_0 \alpha \exp[-(1 + 2/\alpha)]$, from which it is easily shown that $f + \zeta_{\text{min}} < 0$ when $2\omega_0/f > (2/\alpha)\exp(1 + 2/\alpha)$. Thus, the minimum absolute vorticity is negative when $2\omega_0/f > 7.39, 3.53, 2.24$ for $\alpha = 2, 3, 4$ respectively. Recognizing that tropical cyclones have values of central vorticity exceeding fifty times the Coriolis parameter (i.e., $2\omega_0/f > 50$), the use of

Reproduced with permission of the copyright owner. Further reproduction prohibited without permission.

(7.1)–(7.3) as an initial condition in a full primitive equation model would result in regions of unrealistic negative inertial stability, that is, regions with $(f + 2v/r)(f + \zeta) < 0$. These considerations make application of the well-studied family of shielded monopoles (7.1)–(7.3) to tropical cyclones highly questionable. In section 7.3, we will demonstrate that more realistic initial conditions, with positive vorticity in the moat, can also lead to the formation of tripoles.

7.2 Linear stability analysis of a partially shielded vortex

Returning to the four-region model of Appendix A, consider the special case $\zeta_1 > 0$, $\zeta_2 < 0$ and $\zeta_3 = 0$. The axisymmetric basic state angular velocity $\bar{\omega}(r)$ given by (A.3) then reduces to

$$\bar{\omega}(r) = \tfrac{1}{2}\begin{cases} \zeta_1 & 0 \le r \le r_1, \\ [\zeta_1 r_1^2 + \zeta_2(r^2 - r_1^2)]r^{-2} & r_1 \le r \le r_2, \\ [\zeta_1 r_1^2 + \zeta_2(r_2^2 - r_1^2)]r^{-2} & r_2 \le r < \infty, \end{cases} \tag{7}$$

and the corresponding basic state relative vorticity $\bar{\zeta}(r)$ given by (A.4) reduces to

$$\bar{\zeta}(r) = \frac{d(r^2\bar{\omega})}{r dr} = \begin{cases} \zeta_1 & 0 < r < r_1, \\ \zeta_2 & r_1 < r < r_2, \\ 0 & r_2 < r < \infty, \end{cases} \tag{7.5}$$

where r_1, r_2 are specified radii and ζ_1, ζ_2 specified vorticity levels. The eigenvalue problem (A.9) reduces to

$$\begin{pmatrix} m\bar{\omega}_1 + \frac{1}{2}(\zeta_2 - \zeta_1) & \frac{1}{2}(\zeta_2 - \zeta_1)(r_1/r_2)^m \\ -\frac{1}{2}\zeta_2(r_1/r_2)^m & m\bar{\omega}_2 - \frac{1}{2}\zeta_2 \end{pmatrix} \begin{pmatrix} \Psi_1 \\ \Psi_2 \end{pmatrix} = \nu \begin{pmatrix} \Psi_1 \\ \Psi_2 \end{pmatrix}. \tag{7.6}$$

Analogously to the discussion of sections 3.1 and 6.1, the system (7.6) describes the interaction between two counterpropagating vortex Rossby waves with the wave along the edge of the vortex ($r = r_1$) propagating counterclockwise relative to strong cyclonic flow and the wave along the outer edge of the moat ($r = r_2$) propagating clockwise relative to weaker flow. In this case, both the Rayleigh and Fjørtoft necessary conditions for instability are satisfied. The eigenvalues of (7.6), normalized by

Reproduced with permission of the copyright owner. Further reproduction prohibited without permission.

ζ_1, are given by

$$\begin{aligned}\frac{\nu}{\zeta_1} &= \tfrac{1}{4}\left\{m\left[1+\zeta_2/\zeta_1+(1-\zeta_2/\zeta_1)\,(r_1/r_2)^2\right]-1\right\} \\ &\pm \tfrac{1}{4}\Big\{\Big[m\,(1-\zeta_2/\zeta_1)\,\left(1-(r_1/r_2)^2\right)-(1-2(\zeta_2/\zeta_1))\Big]^2 \\ &+ 4(\zeta_2/\zeta_1)\,(1-\zeta_2/\zeta_1)\,(r_1/r_2)^{2m}\Big\}^{\frac{1}{2}}. \qquad (7.7)\end{aligned}$$

Fig. 7.4 shows isolines of the imaginary part of ν/ζ_1 as a function of r_1/r_2 and $-\zeta_2/\zeta_1$. Although all basic states satisfy both the Rayleigh and Fjørtoft necessary conditions for instability, much of the region shown in Fig. 7.4 is stable, and for any value of $-\zeta_2/\zeta_1$, instability can occur only when $r_1/r_2 \gtrsim 0.38$. An interesting feature observed in Fig. 7.4 is that a larger central vortex is more susceptible to instability across its moat. For example, the secondary eyewall in Hurricane Gilbert on 14 September would need to contract to a radius less than 17 km in order for type 2 instability to occur. For the case of a larger central vortex ($r_1 = 30$ km) surrounded by a secondary eyewall where $-\zeta_2/\zeta_1$ is the same as the Gilbert case, type 2 instability occurs when the inner edge of the secondary eyewall contracts to a radius of 55 km.

7.3 Type 2 instability across a moat of positive vorticity: Application to hurricanes

The wind structure of a hurricane is intimately tied to the convective field, with the convection tending to produce low level convergence and hence cyclonic vorticity in the area of a convective ring. When convection is concentrated near the inner edge of a ring of enhanced vorticity, a contraction of the ring may follow in response to nonconservative forcing (Shapiro and Willoughby 1982; Willoughby et al. 1982; Willoughby 1990a). As the ring contracts, the differential rotation imposed across the ring by the central vortex becomes greater and eventually reverses the self induced differential rotation of the ring. At this point, the ring is assured to have no type 1 instabilities. Further contraction however, brings the inner edge of the ring closer to the central vortex where type 2 instabilities between the ring and central vortex can

Reproduced with permission of the copyright owner. Further reproduction prohibited without permission.

take place. Recalling Fig. 7.4 and noting that during a contraction, r_1/r_2 increases from small values towards unity, we expect type 2 instabilities to appear first with a maximum growth rate in wavenumber two. The vorticity mixing associated with such an instability perturbs the vortex into a tripole and offers an explanation for the origin and persistence of elliptical eyewalls in hurricanes.

A numerical integration is now performed under the initial condition (B.6) with parameters $\{r_1, r_2, r_3, r_4\} = \{25, 40, 45, 67.5\}$ km, $\{d_1, d_2, d_3, d_4\} = \{2.5, 2.5, 2.5, 7.5\}$ km, and $\{\zeta_1, \zeta_2, \zeta_3, \zeta_4, \zeta_5\} = \{47.65, 1.15, 9.65, 1.15, -0.35\} \times 10^{-4}$ s^{-1} which simulate a large central vortex of uniform vorticity surrounded by a thin ring of enhanced vorticity located at $r = 42.5$ km or 1.7 times the radius of maximum wind. The symmetric part of the initial vorticity and tangential wind fields are shown by the solid lines in Fig. 7.6. The secondary ring has the effect of flattening the tangential wind near $r = 42$ km but no secondary wind maximum is present. The retrograding vorticity waves along the central vortex edge ($r \approx 25$ km) are embedded in relatively strong angular velocity of 23.5×10^{-4} s^{-1} while the prograding waves along the inner edge of the ring ($r \approx 40$ km) are embedded in weaker angular velocity of 10.1×10^{-4} s^{-1}. Near the outer edge of the ring ($r \approx 45$ km), the angular velocity is 8.8×10^{-4} s^{-1} suppressing type 1 instability. Solving (A.9) for this basic state reveals a sole wavenumber 2 instability whose growth rate has an e-folding time of 62 minutes. Results of this experiment are shown in Fig. 7.5.

At $t = 8$ h, the wavenumber two instability has become evident as the vortex and inner edge of the ring have been perturbed into ellipses. Asymmetries along the vortex are advected more quickly than those along the ring edge while the aspect ratios of the vortex and ring edge move further away from unity, so that at $t = 9$ h, the major vertices of the vortex have moved close enough to the ring to begin stripping vorticity from it. The tongues of vorticity being stripped from the ring are then pulled across the moat into regions of stronger rotation and are advected along the vortex edge. As the leading edges of the tongues approach the downstream major vertices of the

Reproduced with permission of the copyright owner. Further reproduction prohibited without permission.

vortex, the differential rotation becomes greater and by $t = 10.5$ h, the outer edges of the tongues have become trailing features. As the trailing edges approach the downstream major vertices, their inner edges are again swept cyclonically along the edge of the vortex. At $t = 12$ h, this repetitive process has resulted in two strips of vorticity, which originated from the ring edge, wound anticyclonically around two pools of low vorticity, which originally comprised the moat. The pools, or satellite vortices, lie along the minor axis of the elliptical central vortex. During its evolution, the central vortex takes on a variety of shapes most of which are elliptical patterns with aspect ratios (major axis / minor axis) ranging from 1.3 to 1.8, but which also include distinct trapezoidal patterns. This type of evolution may offer an additional mechanism for the formation of polygonal eyewalls (Schubert et al. 1999 and references therein). Near the end of the simulation, the semi-major (semi-minor) axis is ~ 60 km (~ 40 km) giving an aspect ratio of 1.5. Although the ellipticity of the central vortex is a fairly persistent feature, the tripole pattern becomes less easily identified when $t > 12$ h as the vorticity of the ring becomes increasingly mixed into the regions of the satellites.

The period of rotation of the tripole is approximately 89 minutes. The linear theory of Kelvin (Lamb 1932, pp. 230–231) applied to a wavenumber two asymmetry on a Rankine vortex with $V_{\max} = 58$ m s^{-1} at $r = 25$ km predicts a period of rotation of 90 minutes. The good agreement between Kelvin's theory and the model results suggest that the period of rotation of a tripole can be predicted well if treated as a Kirchhoff vortex and is then in good agreement with the results of Kuo et al. (1999). Polvani and Carton (1990) calculated the rotation rate of a point-vortex tripole using the formula

$$\Omega = \frac{1}{2\pi d^2}\left(\Gamma_1 + \frac{\Gamma_2}{2}\right) \tag{7.8}$$

where d is the distance from the centroid of the elliptical central vortex to the centroid of either satellite vortex and Γ_1, Γ_2 are the circulations of the central and satellite vortices. It is not clear how to accurately apply (7.8) to our numerical results since the

Reproduced with permission of the copyright owner. Further reproduction prohibited without permission.

calculation of Γ_2 requires quantification of how much vorticity from the ring has been wound around the low vorticity of the moat. We can however approximate a range of values between two extreme cases, one in which the satellite vortices contain only vorticity from the moat, and the other in which the satellite vortices have ingested all of the vorticity of the ring. At 24 hours the centroid of each satellite vortex is roughly 36 km from the centroid of the central vortex and we can assume that the circulation of the central vortex has remained nearly fixed so that $\Gamma_1 \approx 2.98\pi$ km^2 s^{-1}. If no vorticity from the ring was ingested by the satellite vortices, then their circulations are half the initial circulation of the moat, that is, $\Gamma_2 \approx 0.06\pi$ km^2 s^{-1}. If all of the ring vorticity was ingested by the satellite vortices, then their circulations are half the sum of the initial circulations of the moat and ring, that is, $\Gamma_2 \approx 0.26\pi$ km^2 s^{-1}. Using these values in (7.8) we obtain the range of rotation periods $87 \lesssim P \lesssim 90$ minutes, where $P = 2\pi/\Omega$. It is clear that in this case, where $\Gamma_1 \gg \Gamma_2$ there is little sensitivity to the choice of Γ_2 and the accuracy of (7.8) depends largely on the estimated value of d.

The evolution of the symmetric part of the flow (dashed lines in Fig. 7.6) shows a 26% reduction of the maximum vorticity in the ring during the initial stage of the tripole formation between $t = 7.5$ h and $t = 9$ h. This reduction smooths out the wind profile with the initial flat spot replaced with a more uniform slope. At $t = 24$ h, the vorticity has become nearly monotonic except for a small bump near $r = 50$ km where trailing spirals are present, and the tangential wind maximum has decreased from its initial value of 58 ms^{-1} to 52 ms^{-1}. During the early part of their observation of Hurricane Olivia, Reasor et al. (1999) identified a secondary 'bump' in the vorticity profile (and an associated secondary updraft maximum) near $r = 25$ km although it was found to be too weak to produce type 2 instability. Since the eyewall of Olivia was already observed to contain a wavenumber two asymmetry at this time, it is possible that the bump had already been weakened as a result of type 2 instability mixing but there is no conclusive evidence of this.

Reproduced with permission of the copyright owner. Further reproduction prohibited without permission.

Unlike the case of an initial shielded vortex in section 7.1, where wavenumber two instabilities can saturate as tripoles or dipole pairs, the emergence of a tripole in our numerical simulations appears to be an ubiquitous result of type 2 instability across a moat of reduced, but positive vorticity. Tripoles result from a variety of initial conditions which share the common feature of a depressed region of vorticity within the moat with higher vorticity outside. The initial width of the annular ring is unimportant to the early development of a tripole since the outer edge of the ring is dynamically inactive. The width of the ring does, however, play a role in the flow evolution at later times. To demonstrate this, we perform a numerical integration using the initial conditions $\{r_1, r_2, r_3, r_4\}$ = {12.5, 20.5, 62.5, 120} km, $\{d_1, d_2, d_3, d_4\}$ = {2.5, 2.5, 2.5, 15} km, and $\{\zeta_1, \zeta_2, \zeta_3, \zeta_4, \zeta_5\}$ = $\{119.4, 0.4, 11.4, 0.4, -0.6\} \times 10^{-4}$ s^{-1} which simulate a central vortex of uniform vorticity surrounded by a radially broad ring of enhanced vorticity. The symmetric part of the initial vorticity and tangential wind fields are shown by the solid lines in Fig. 7.8 and the results of this experiment are shown in Fig. 7.7. In this case, the formation of a tripole is followed by a relaxation to a nearly steady solid body rotation which is absent in the previous experiment. Most of the vorticity within the interior of the ring does not participate in the vorticity rearrangement, and the tripole pattern is more robust.

Reproduced with permission of the copyright owner. Further reproduction prohibited without permission.

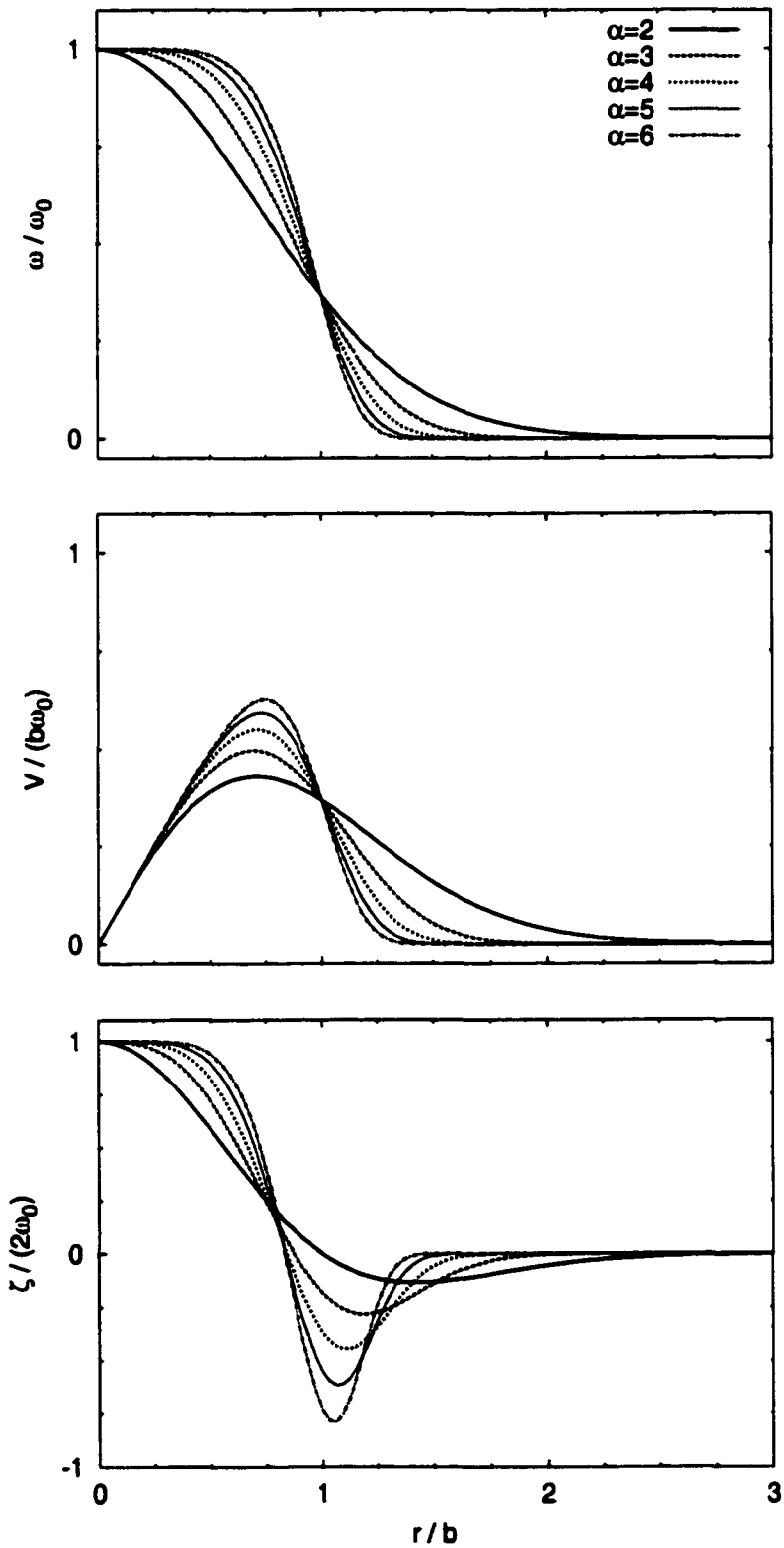

Figure 7.1: Profiles of dimensionless angular velocity, tangential wind, and vorticity for unstable shielded monopoles. The maximum growth is in $m = 2$ when $\alpha = 2, 3, 4, 5$ and $m = 3$ when $\alpha = 6$. The profile is stable when $\alpha \lesssim 1.9$.

Reproduced with permission of the copyright owner. Further reproduction prohibited without permission.

Figure 7.2: Vorticity contour plots for the shielded monopole experiment with $\alpha = 3$. The wavenumber two maximum instability saturates to a tripole. The model domain is 600 km $\times$ 600 km but only the inner 190 km $\times$ 190 km is shown. The contours begin at -7×10^{-4} s^{-1} and are incremented by 5×10^{-4} s^{-1}. Values along the label bar are in units of 10^{-4} s^{-1}. (a) $t = 0$ h to 12 h.

Reproduced with permission of the copyright owner. Further reproduction prohibited without permission.

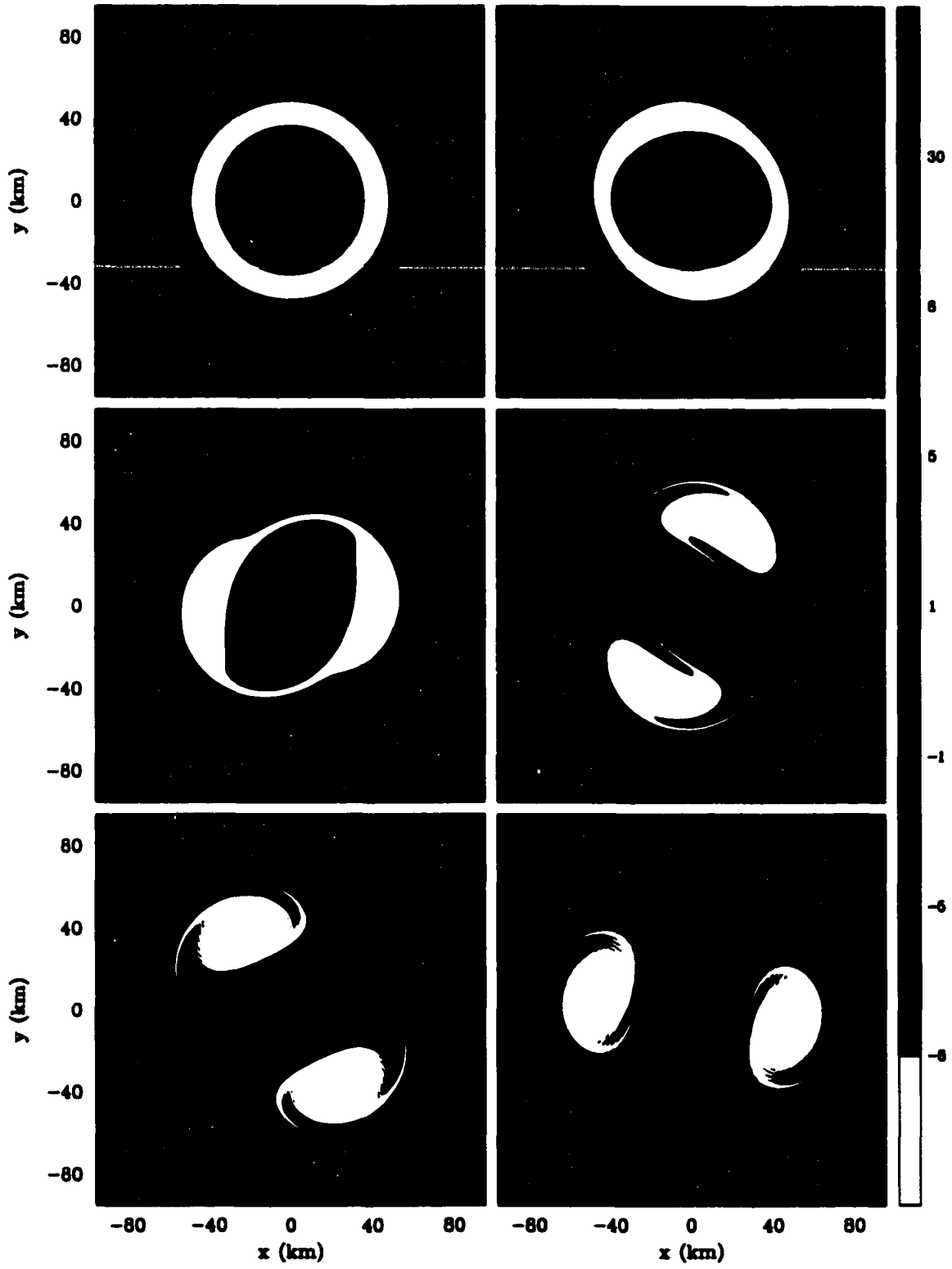

Figure 7.2: (a) See caption on previous page.

Reproduced with permission of the copyright owner. Further reproduction prohibited without permission.

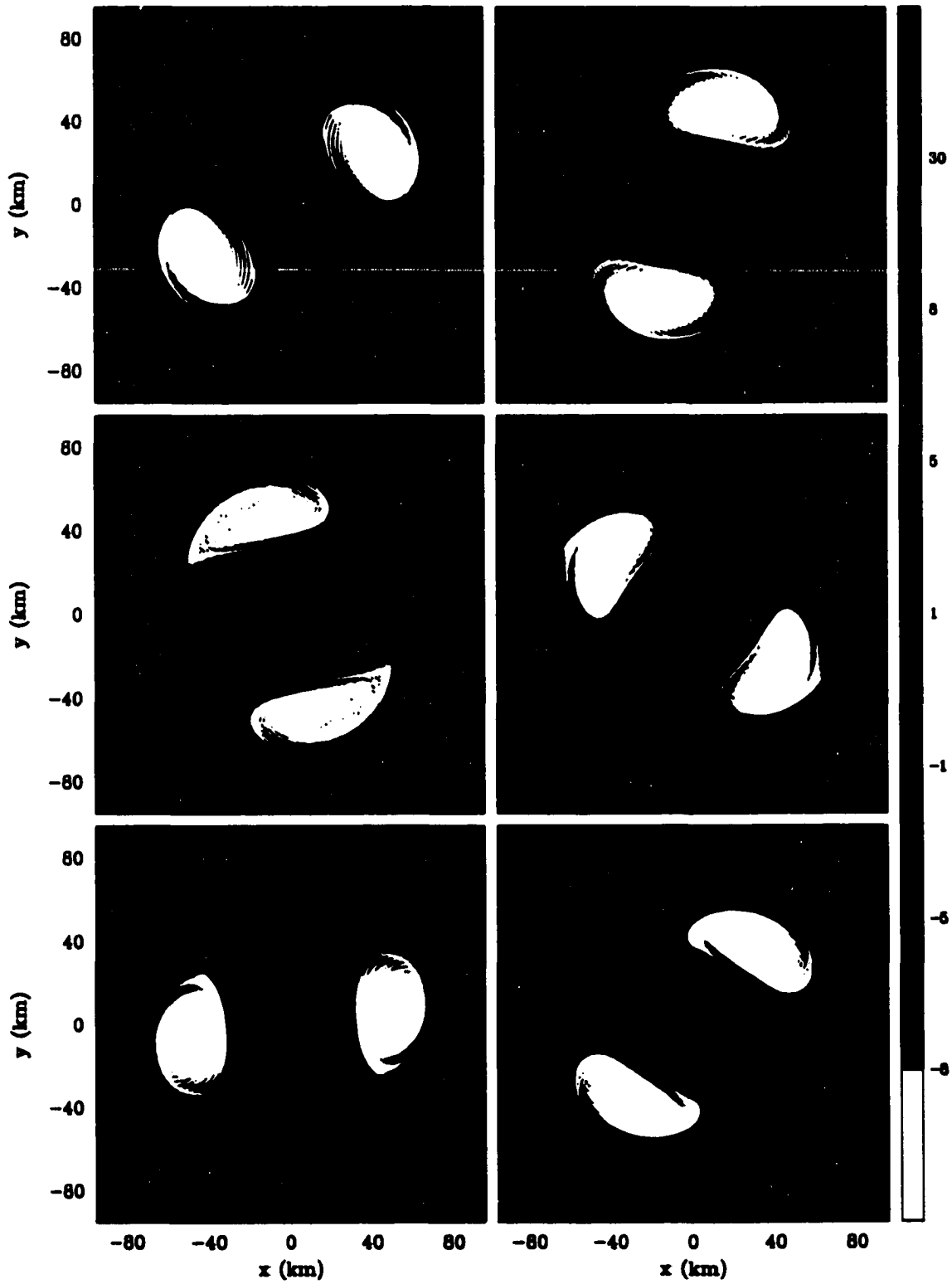

Figure 7.2: (*Continued*) (b) Vorticity from $t = 13$ h to 18 h.

Reproduced with permission of the copyright owner. Further reproduction prohibited without permission.

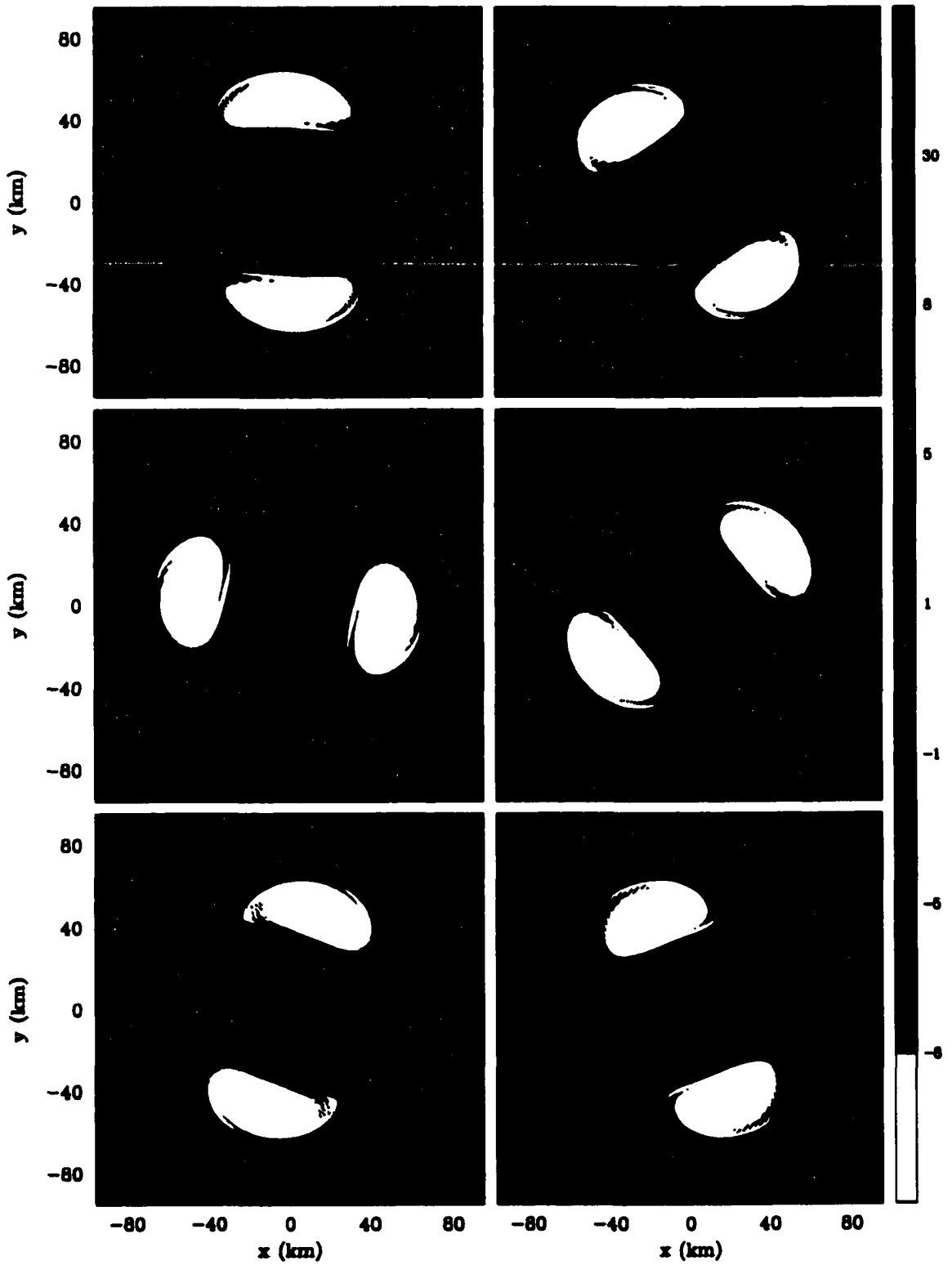

Figure 7.2: (*Continued*) (c) Vorticity from $t = 19$ h to 24 h.

Reproduced with permission of the copyright owner. Further reproduction prohibited without permission.

Figure 7.3: Vorticity contour plots for the shielded monopole experiment with $\alpha = 4$. The wavenumber two maximum instability saturates to two separating dipoles. The model domain is 600 km $\times$ 600 km and the domain shown is expanded as the dipoles translate away from the center. The contours begin at -20×10^{-4} s^{-1} and are incremented by 8×10^{-4} s^{-1}. Values along the label bar are in units of 10^{-4} s^{-1}. (a) $t = 0$ h to 6 h. The domain shown is 150 km $\times$ 150 km.

Reproduced with permission of the copyright owner. Further reproduction prohibited without permission.

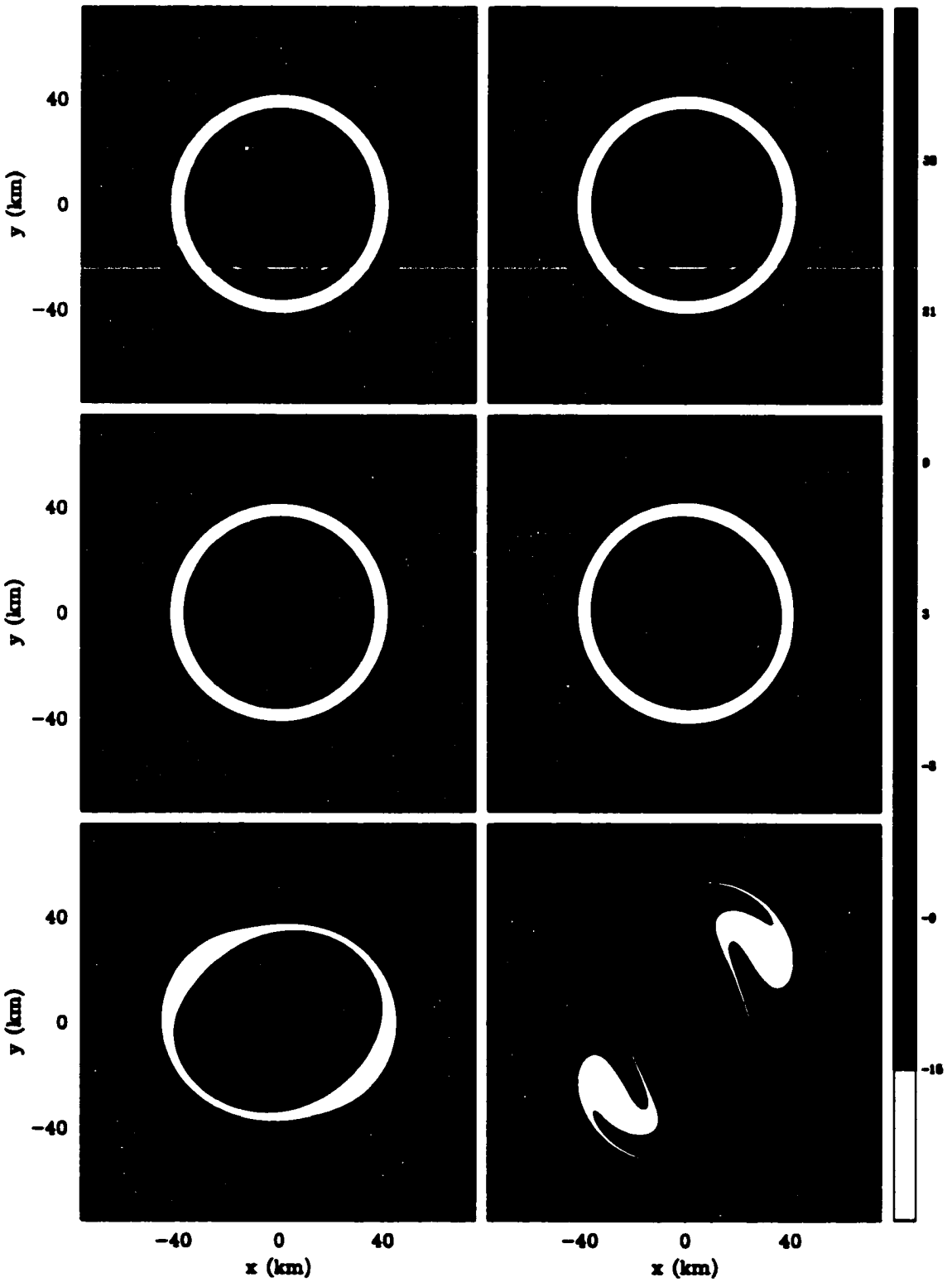

Figure 7.3: (a) See caption on previous page.

Reproduced with permission of the copyright owner. Further reproduction prohibited without permission.

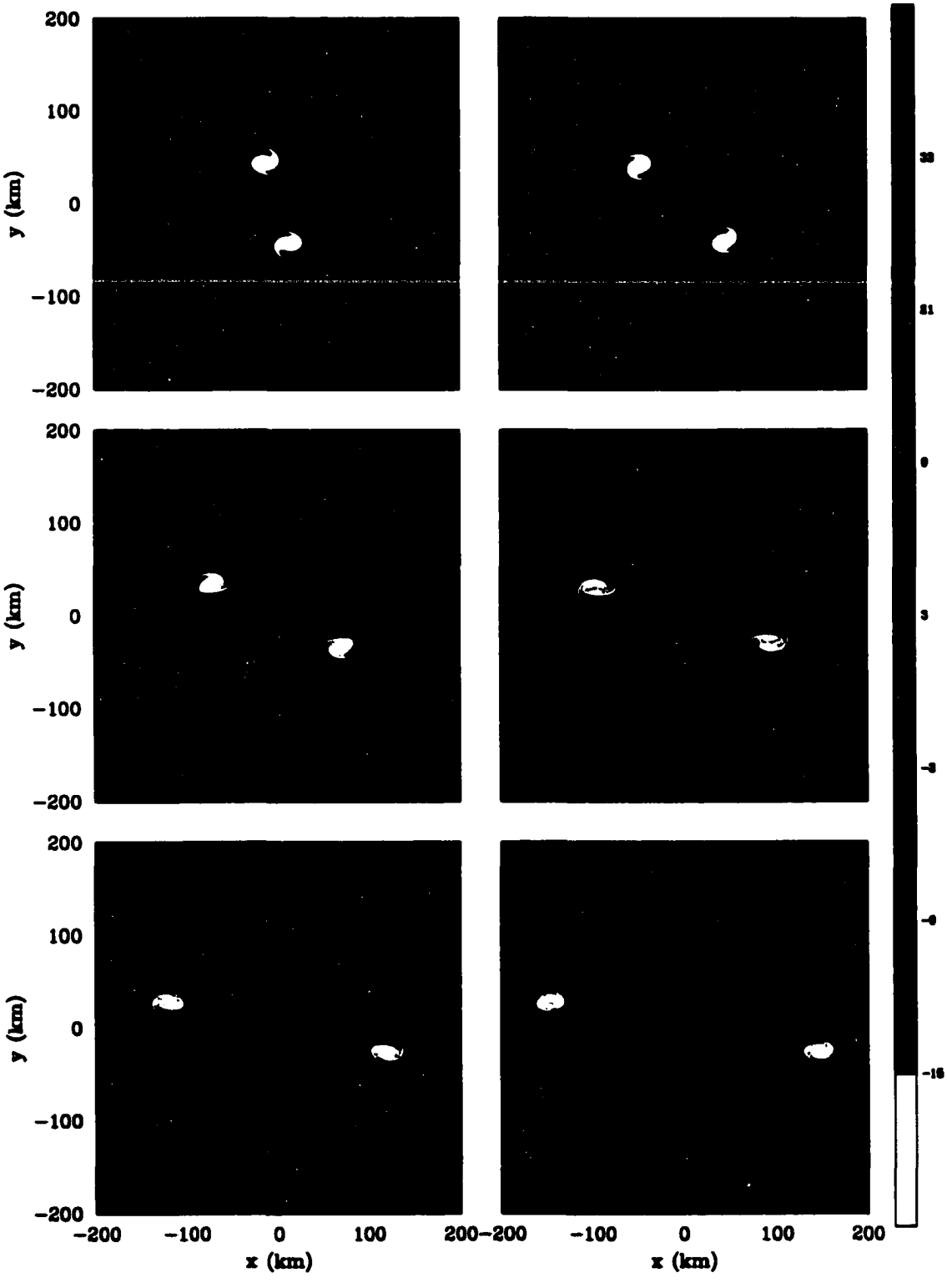

Figure 7.3: (*Continued*) (b) Vorticity from $t = 7$ h to 12 h. The domain shown is 400 km × 400 km.

Reproduced with permission of the copyright owner. Further reproduction prohibited without permission.

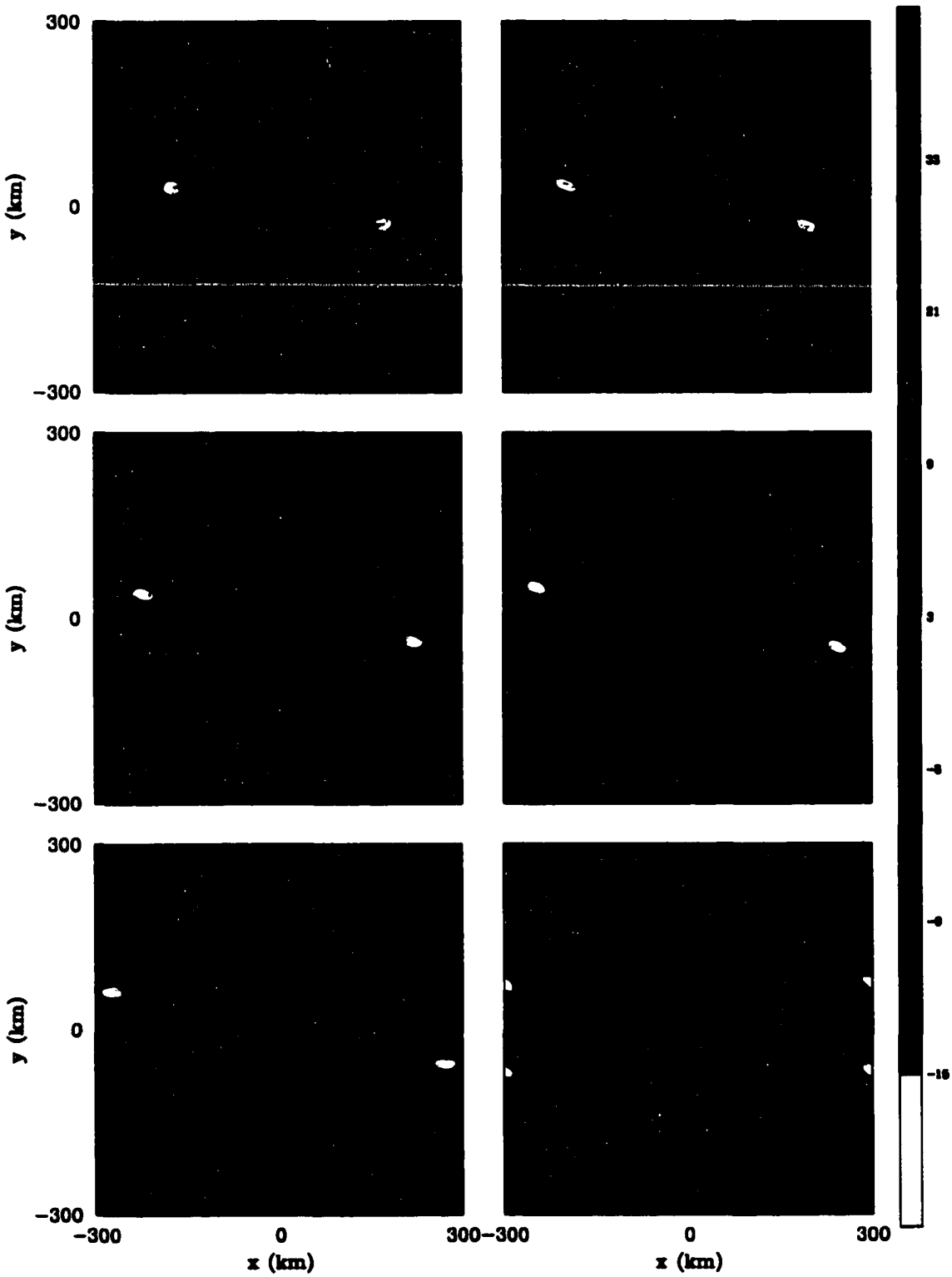

Figure 7.3: (*Continued*) (c) Vorticity from $t = 13$ h to 18 h. The entire domain is shown.

Reproduced with permission of the copyright owner. Further reproduction prohibited without permission.

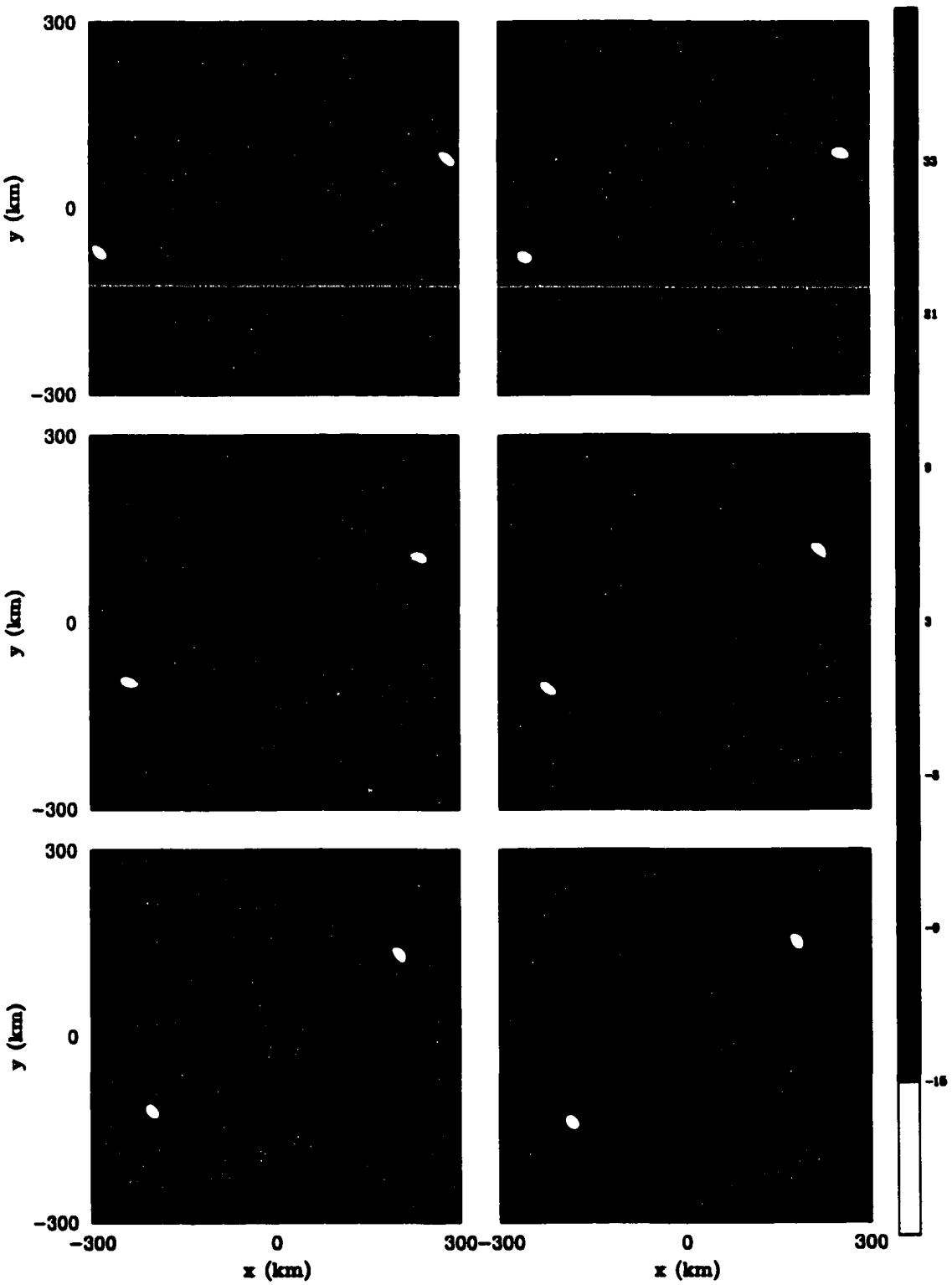

Figure 7.3: (*Continued*) (d) Vorticity from $t = 19$ h to 24 h. The entire domain is shown.

Reproduced with permission of the copyright owner. Further reproduction prohibited without permission.

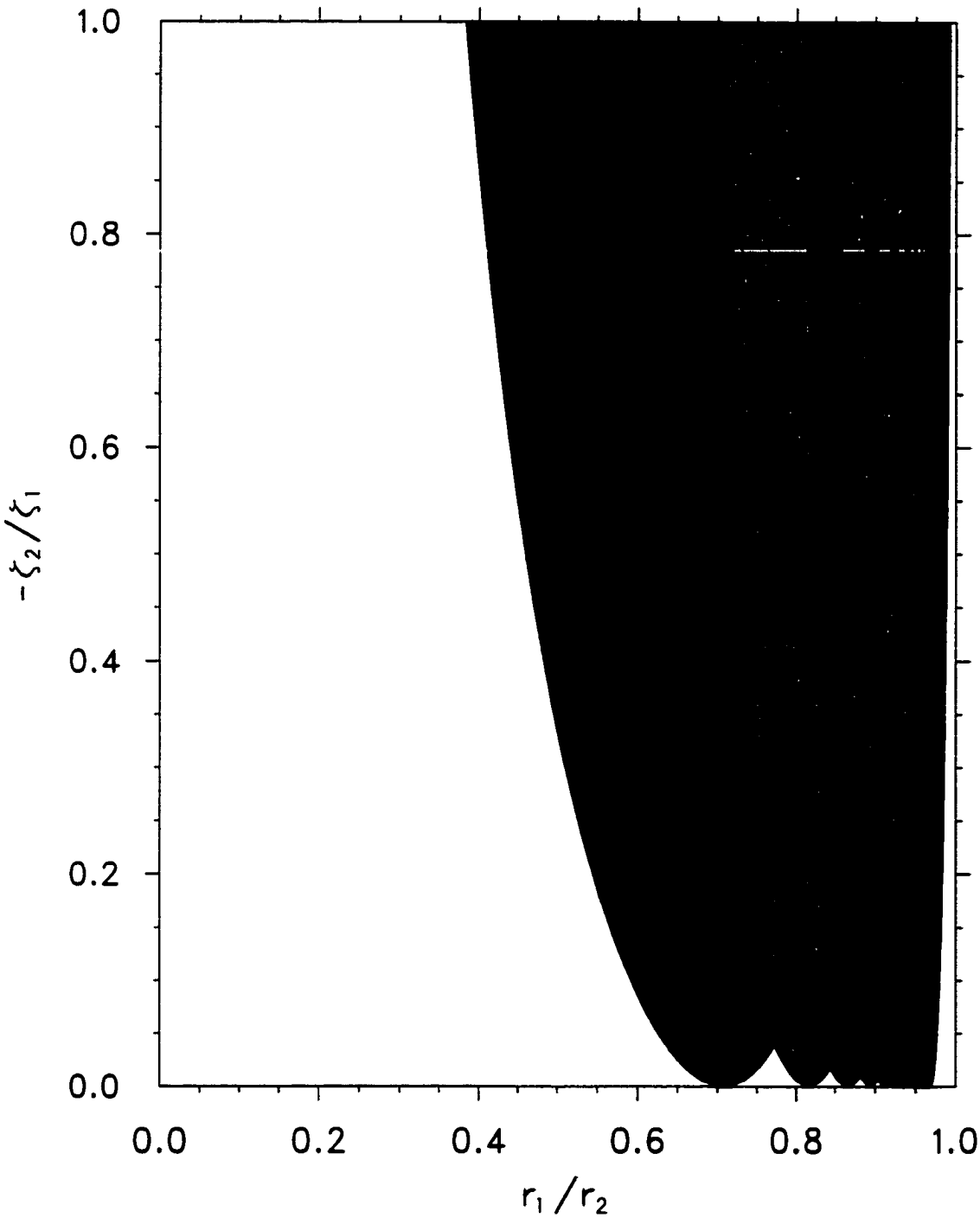

Figure 7.4: Isolines of the maximum dimensionless growth rate ν_i/ζ_1 among the azimuthal wavenumbers $m = 3, 4, \ldots, 16$ for instability of a partially shielded vortex. The isolines and shading are the same as in Fig. 6.5.

Reproduced with permission of the copyright owner. Further reproduction prohibited without permission.

Figure 7.5: Vorticity contour plots for the type 2 instability experiment using an initially narrow annular ring. The model domain is 600 km × 600 km but only the inner 130 km × 130 km is shown. Values along the label bar are in units of 10^{-4} s^{-1}. (a) $t = 0$ h to 9 h.

Reproduced with permission of the copyright owner. Further reproduction prohibited without permission.

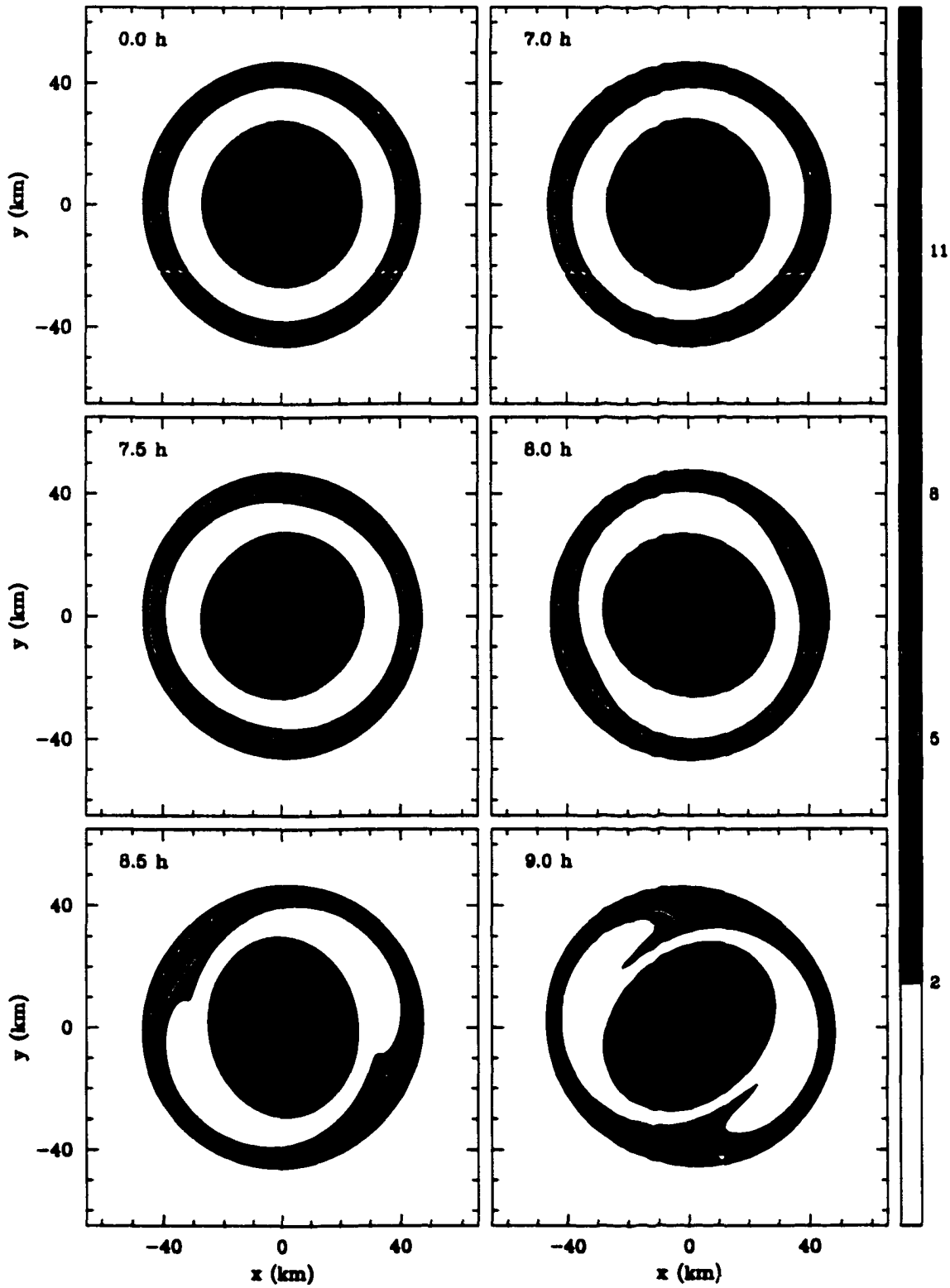

Figure 7.5: (a) See caption on previous page.

Reproduced with permission of the copyright owner. Further reproduction prohibited without permission.

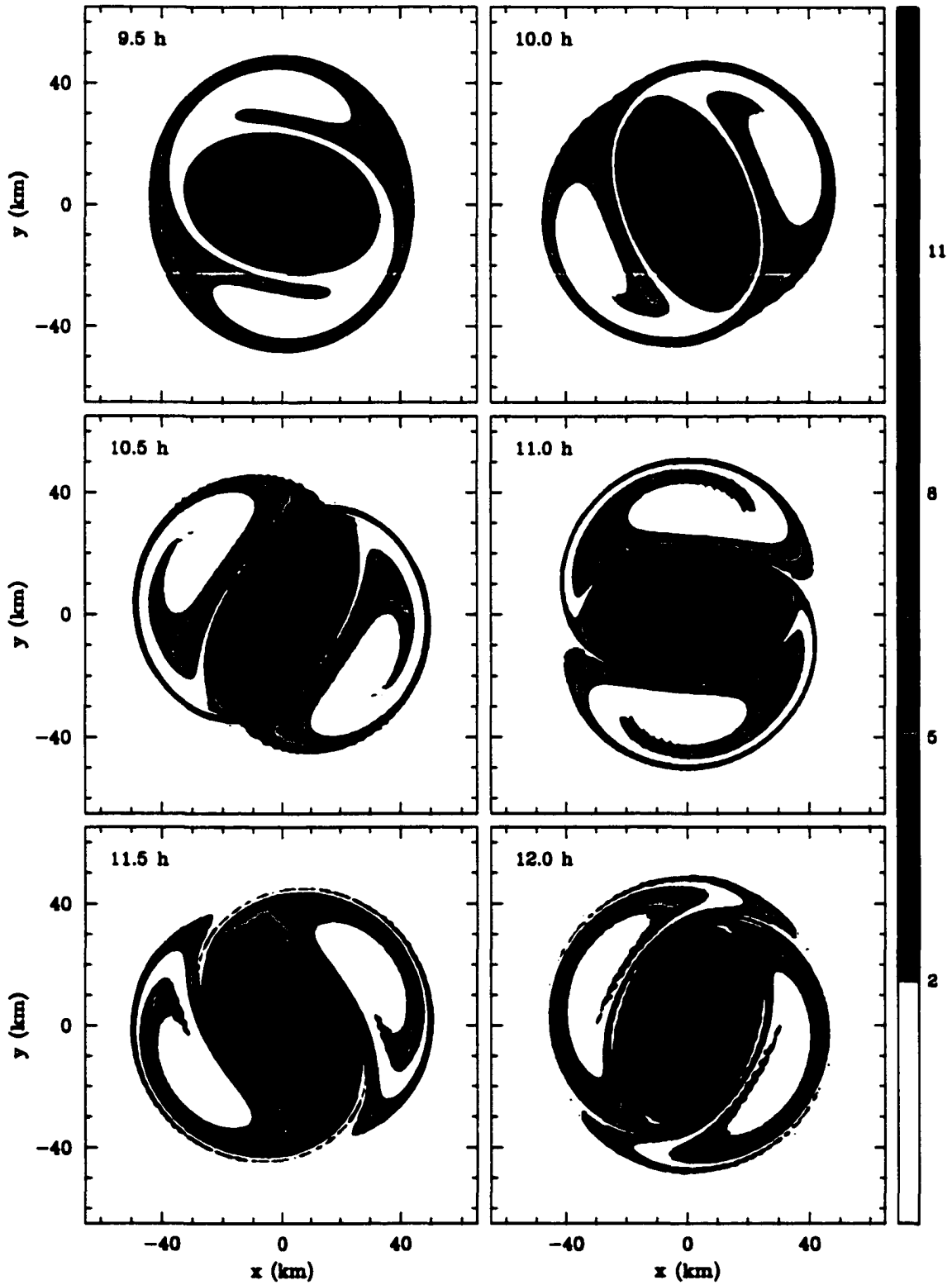

Figure 7.5: (*Continued*) (b) Vorticity from $t = 9.5$ h to 12 h.

Reproduced with permission of the copyright owner. Further reproduction prohibited without permission.

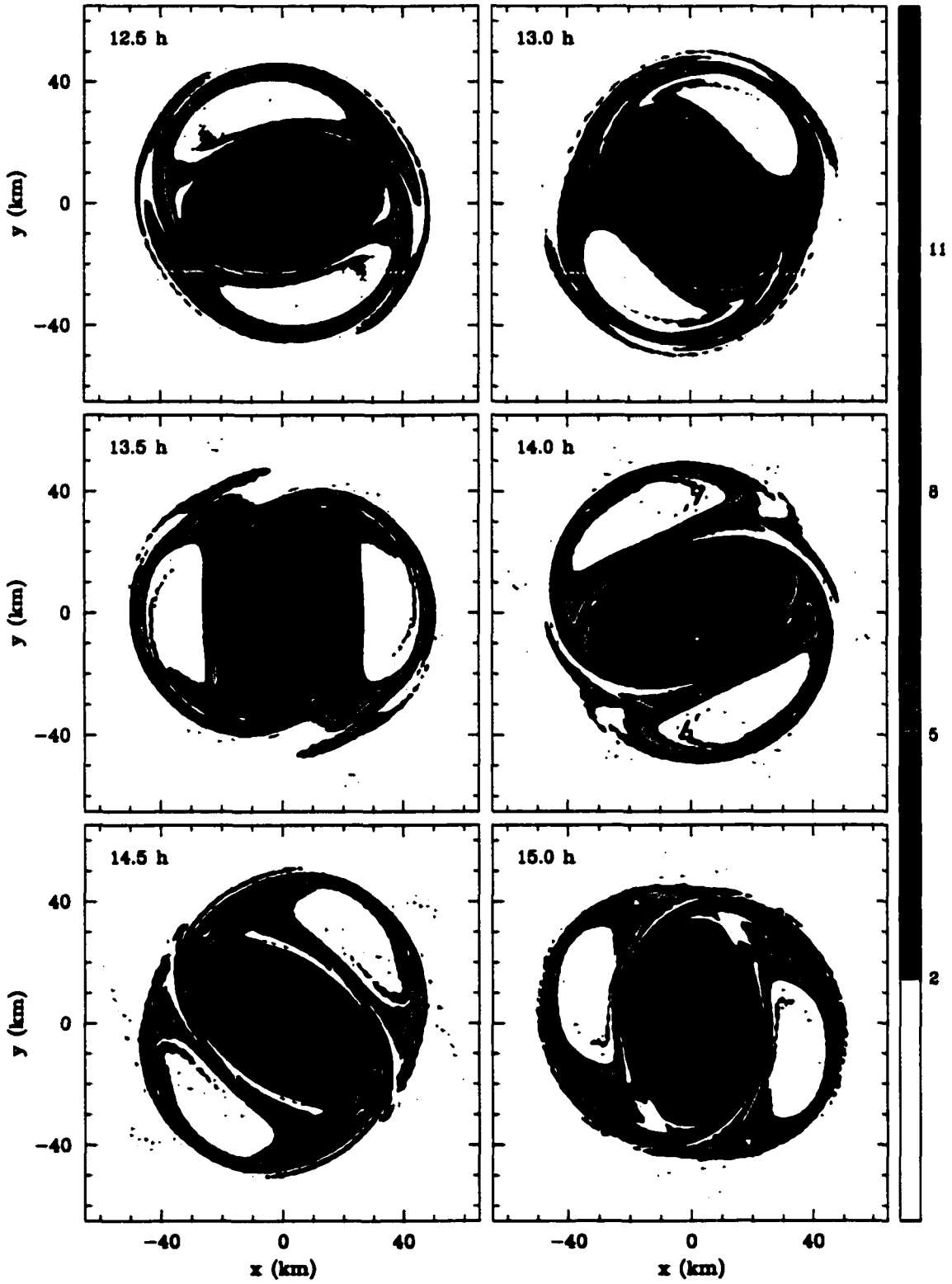

Figure 7.5: (*Continued*) (c) Vorticity from $t = 12.5$ h to 15 h.

Reproduced with permission of the copyright owner. Further reproduction prohibited without permission.

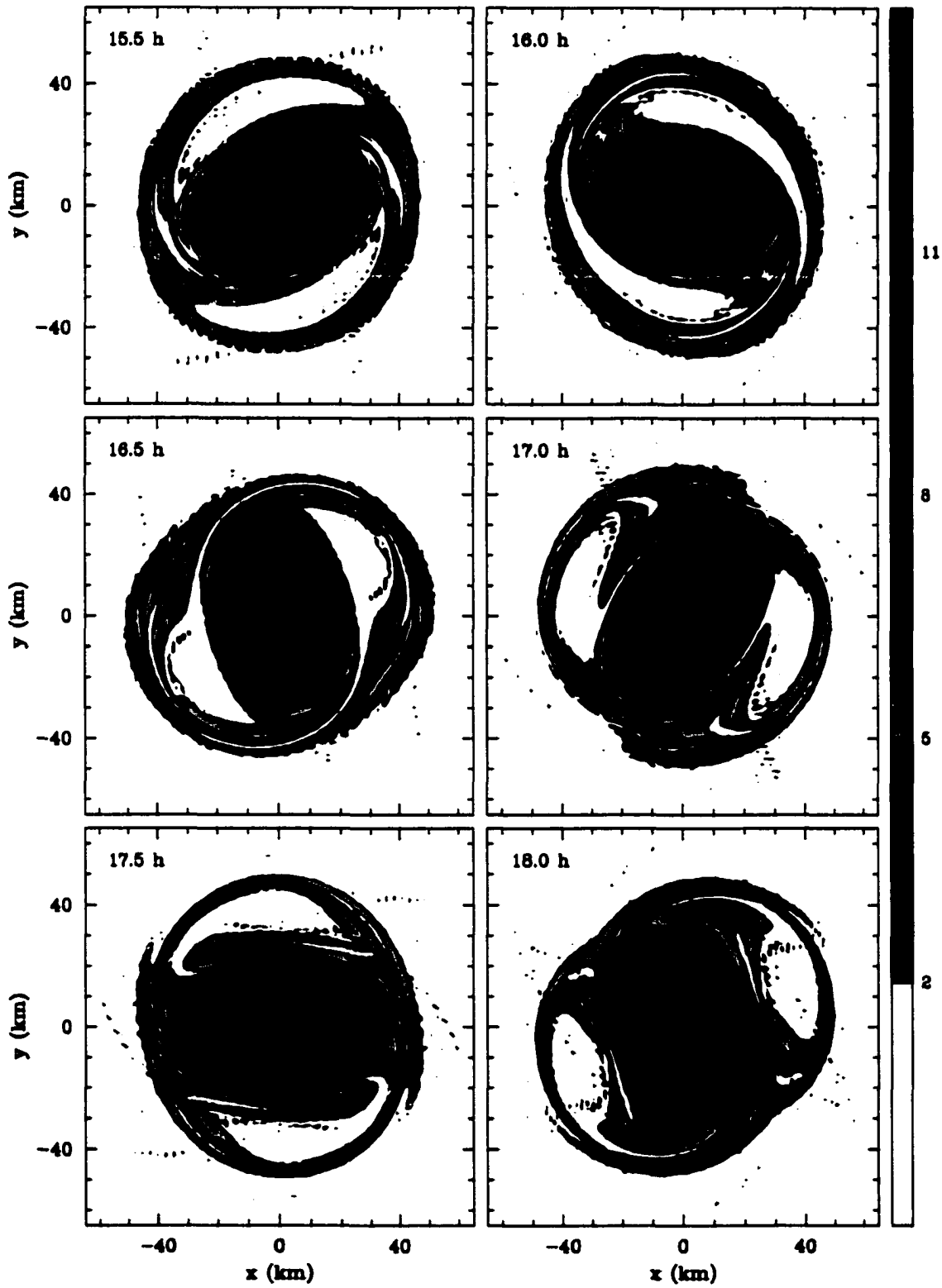

Figure 7.5: (*Continued*) (d) Vorticity from $t = 15.5$ h to 18 h.

Reproduced with permission of the copyright owner. Further reproduction prohibited without permission.

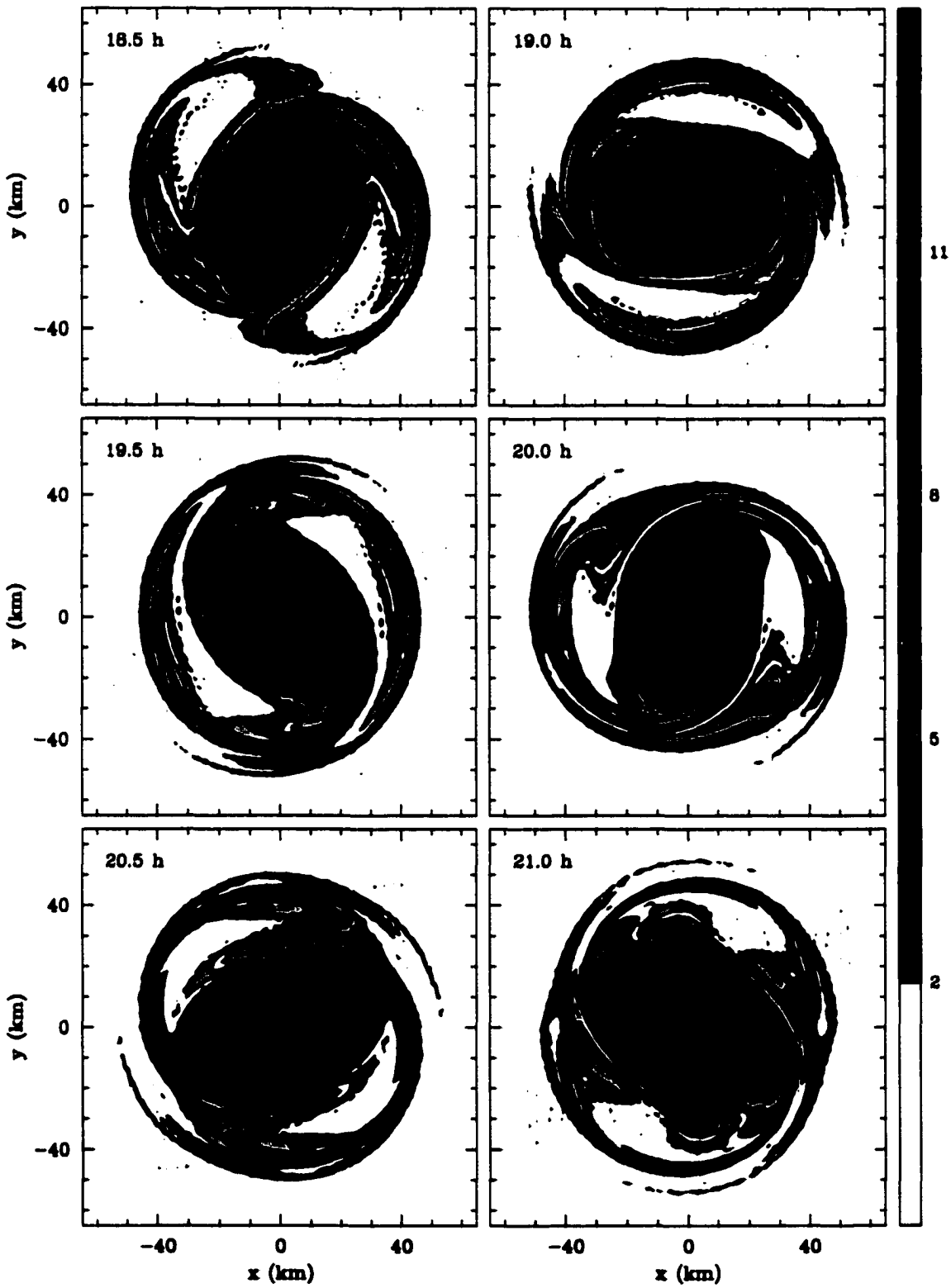

Figure 7.5: (*Continued*) (e) Vorticity from $t = 18.5$ h to 21 h.

Reproduced with permission of the copyright owner. Further reproduction prohibited without permission.

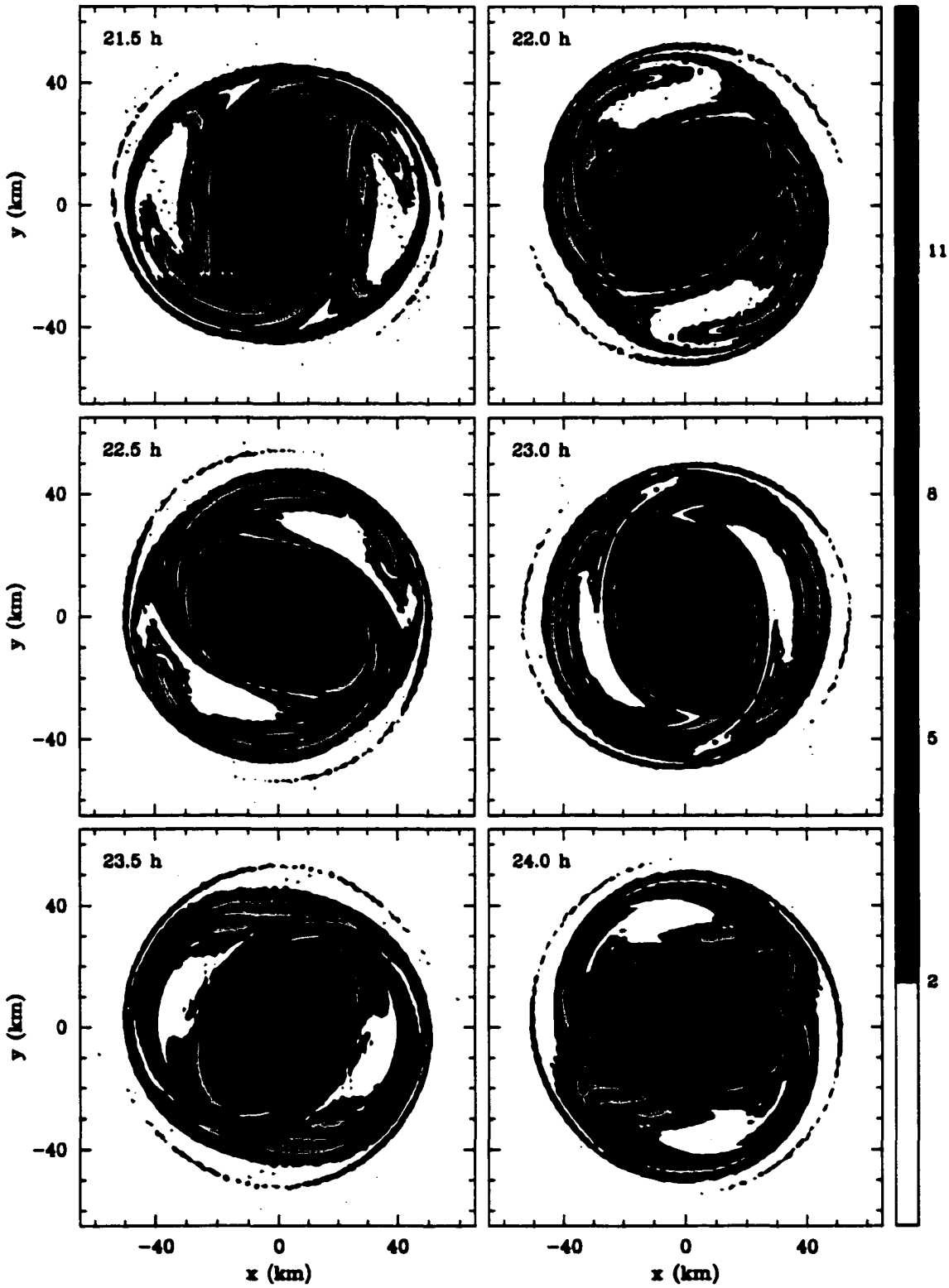

Figure 7.5: (*Continued*) (f) Vorticity from $t = 21.5$ h to 24 h.

Reproduced with permission of the copyright owner. Further reproduction prohibited without permission.

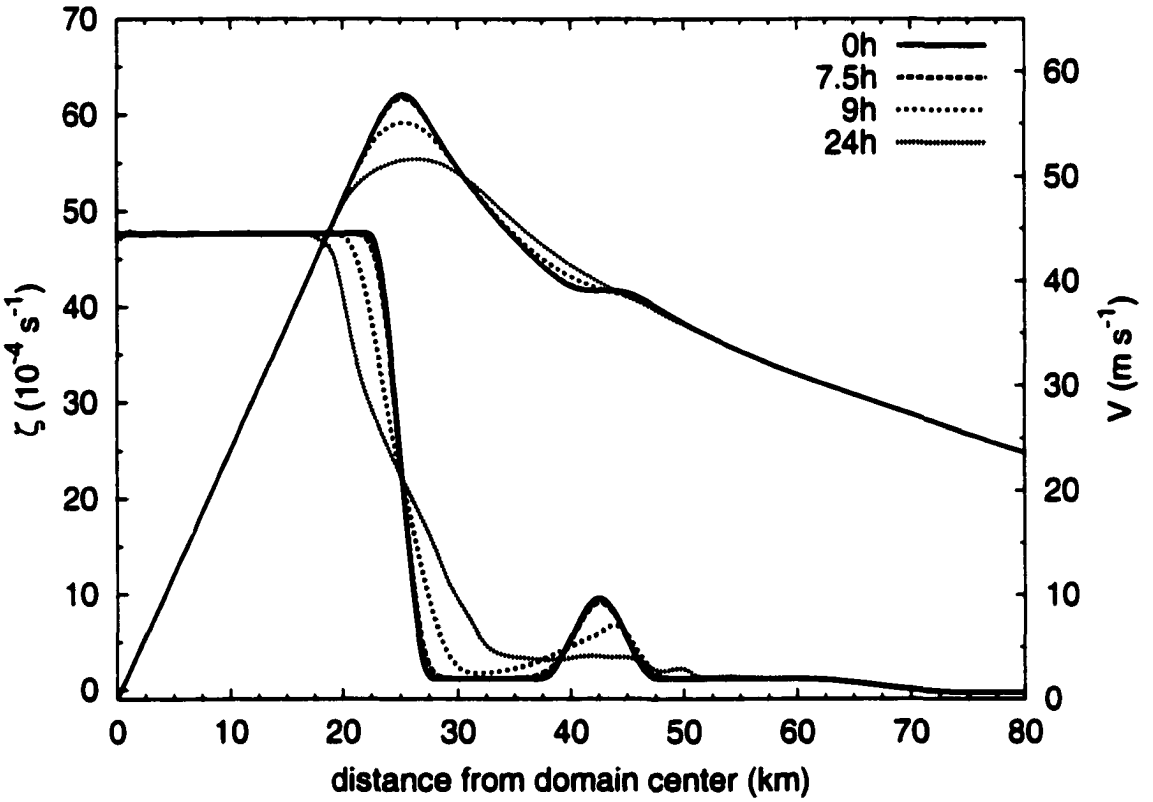

Figure 7.6: Azimuthal mean vorticity and tangential velocity for the experiment shown in Fig. 7.5 at the selected times $t = 0$ (solid), 7.5 h (long dash), 9 h (medium dash), and 24 h (short dash).

Reproduced with permission of the copyright owner. Further reproduction prohibited without permission.

Figure 7.7: Vorticity contour plots for the type 2 instability experiment using an initially wide annular ring. The model domain is 600 km × 600 km but only the inner 150 km × 150 km is shown. Values along the label bar are in units of 10^{-4} s^{-1}. (a) $t = 0$ h to 3 h.

Reproduced with permission of the copyright owner. Further reproduction prohibited without permission.

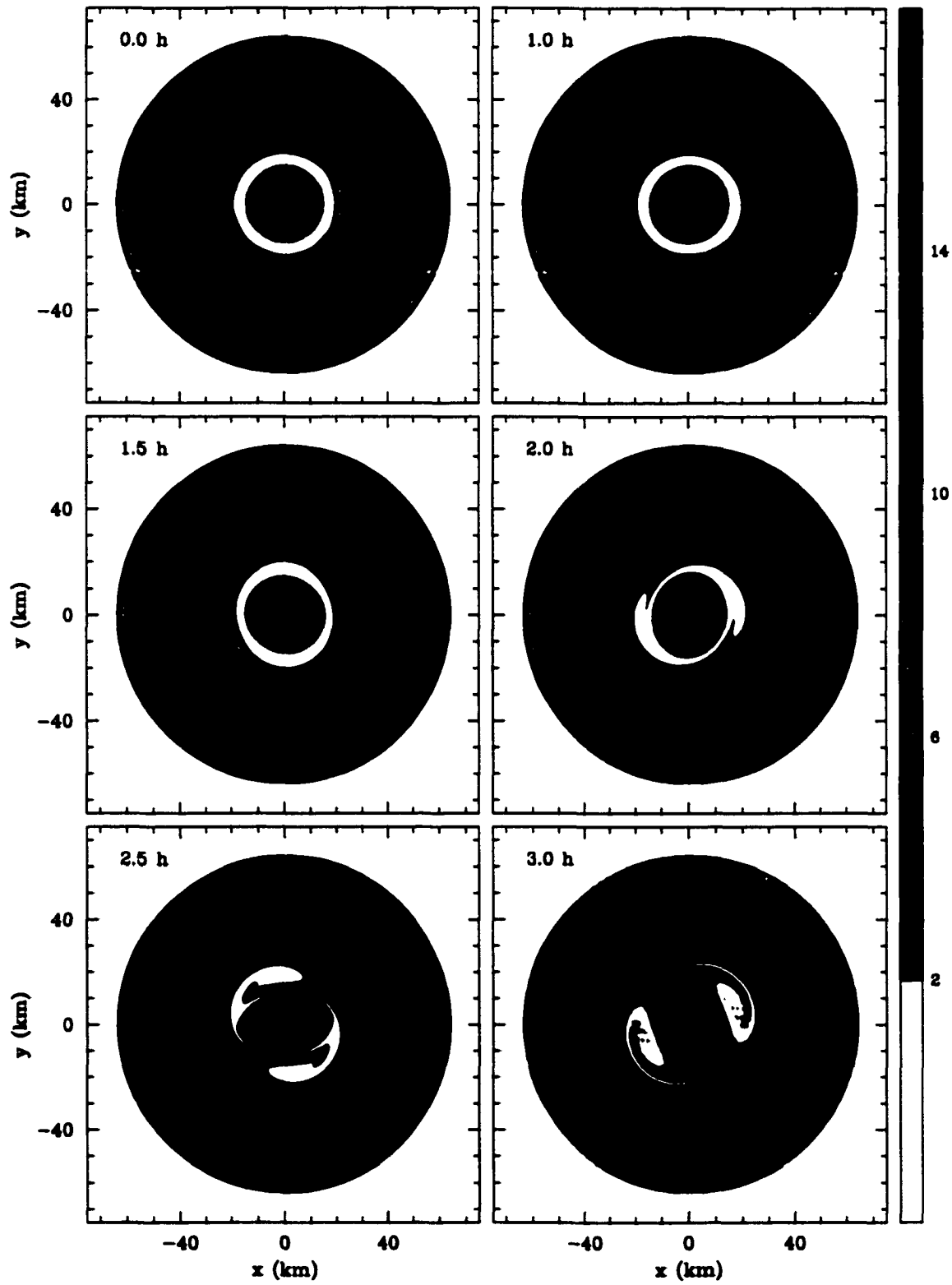

Figure 7.7: (a) See caption on previous page.

Reproduced with permission of the copyright owner. Further reproduction prohibited without permission.

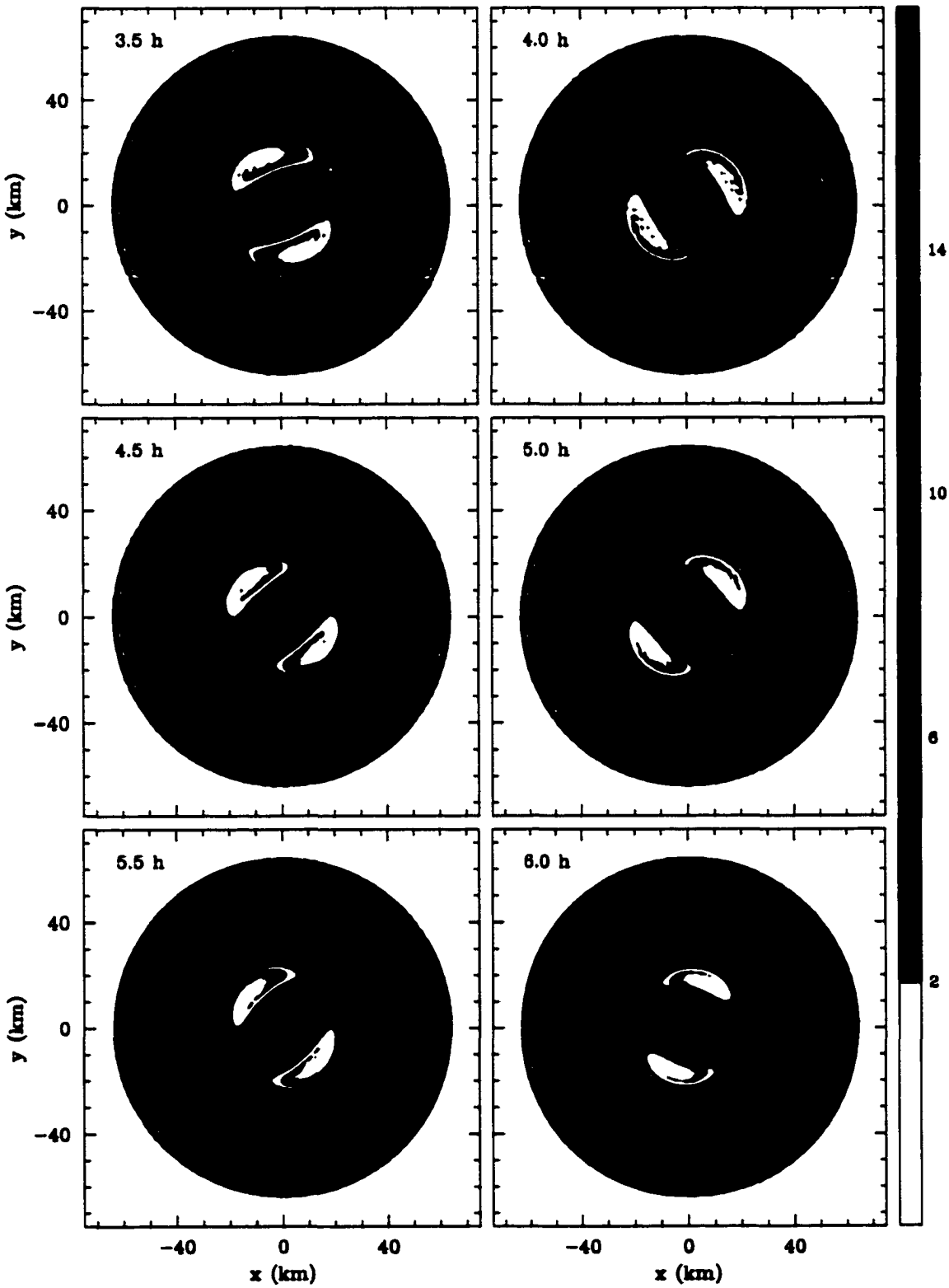

Figure 7.7: (*Continued*) (b) Vorticity from $t = 3.5$ h to 6 h.

Reproduced with permission of the copyright owner. Further reproduction prohibited without permission.

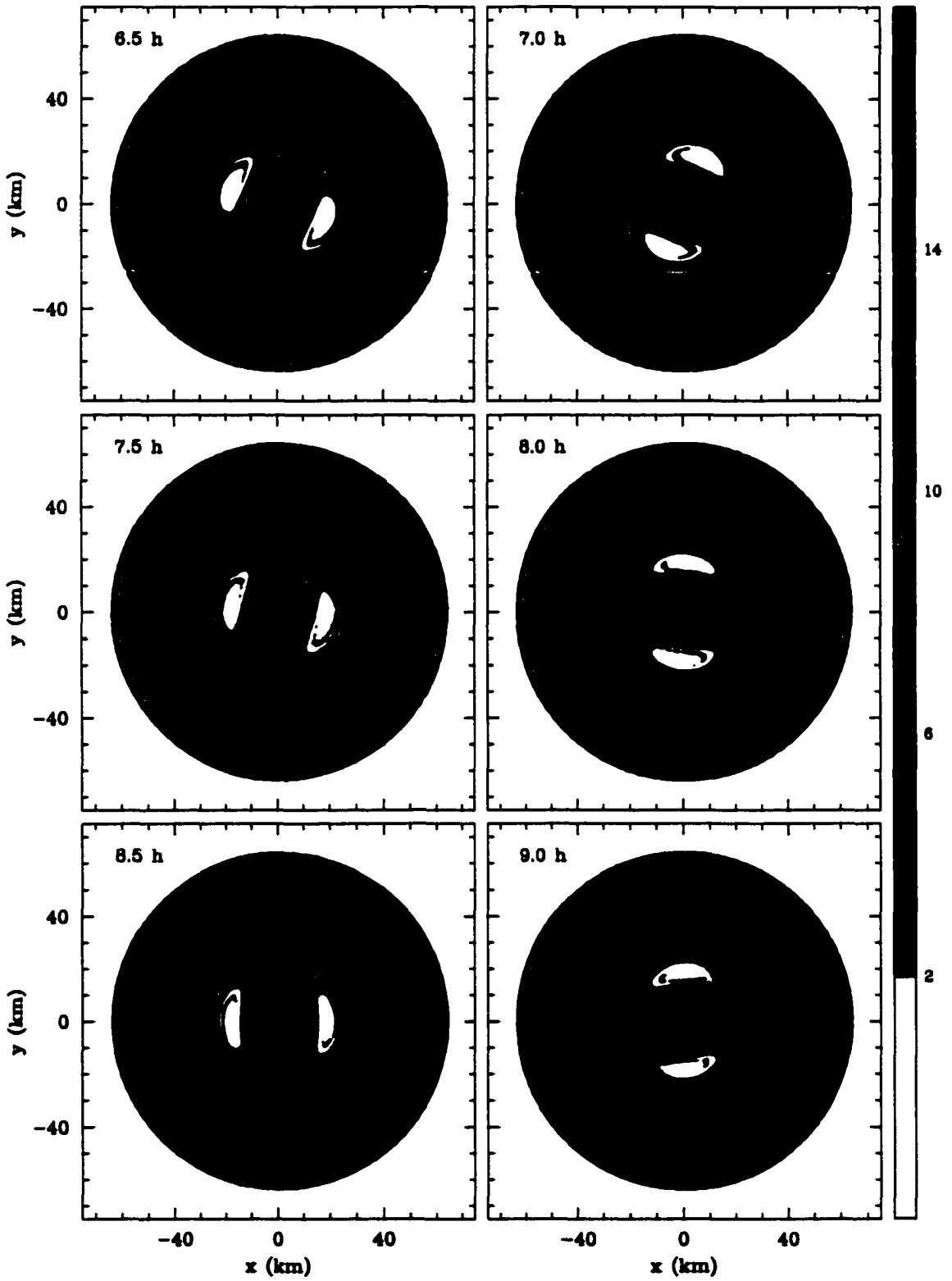

Figure 7.7: (*Continued*) (c) Vorticity from $t = 6.5$ h to 9 h.

Reproduced with permission of the copyright owner. Further reproduction prohibited without permission.

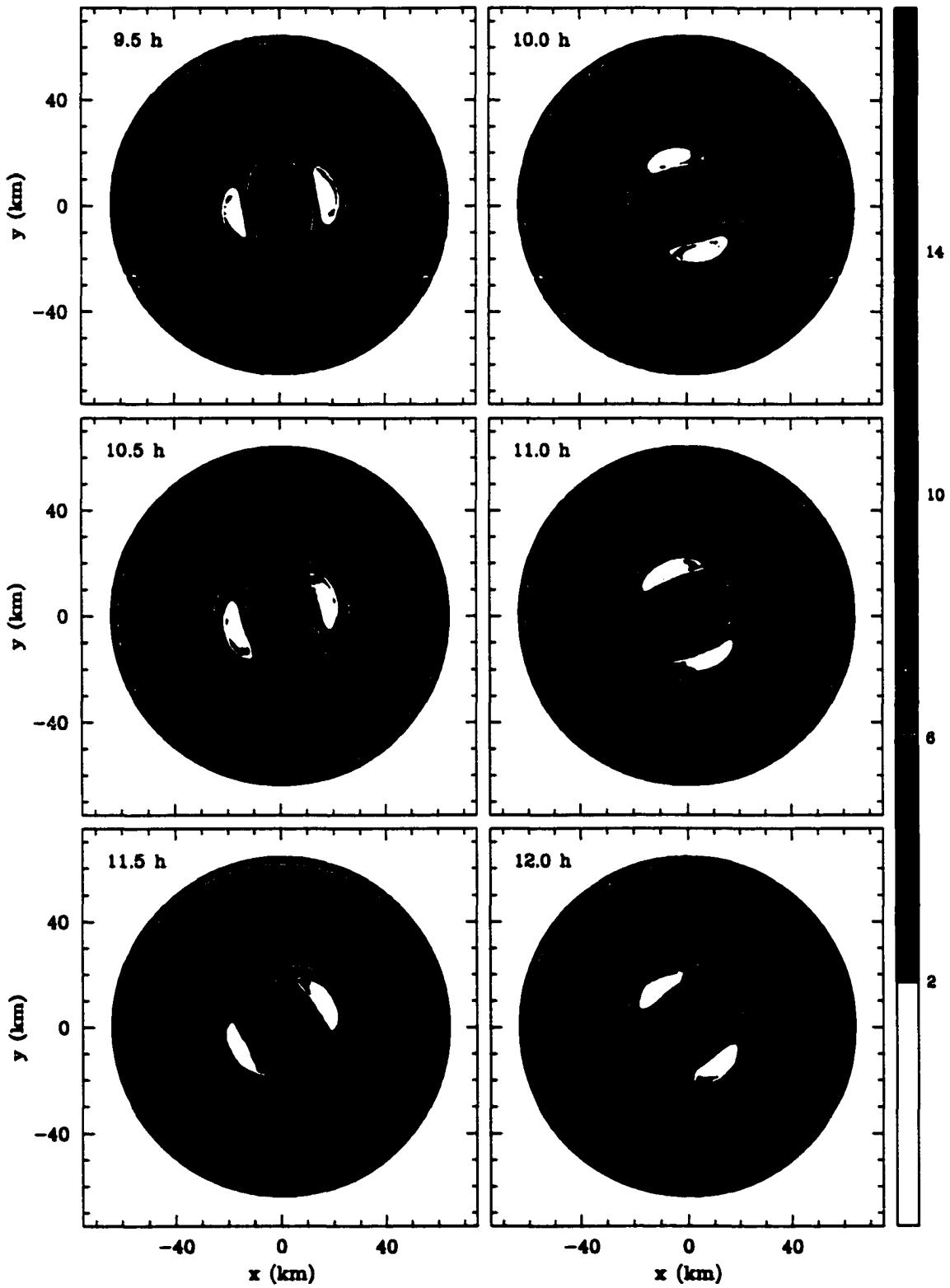

Figure 7.7: (*Continued*) (d) Vorticity from $t = 9.5$ h to 12 h.

Reproduced with permission of the copyright owner. Further reproduction prohibited without permission.

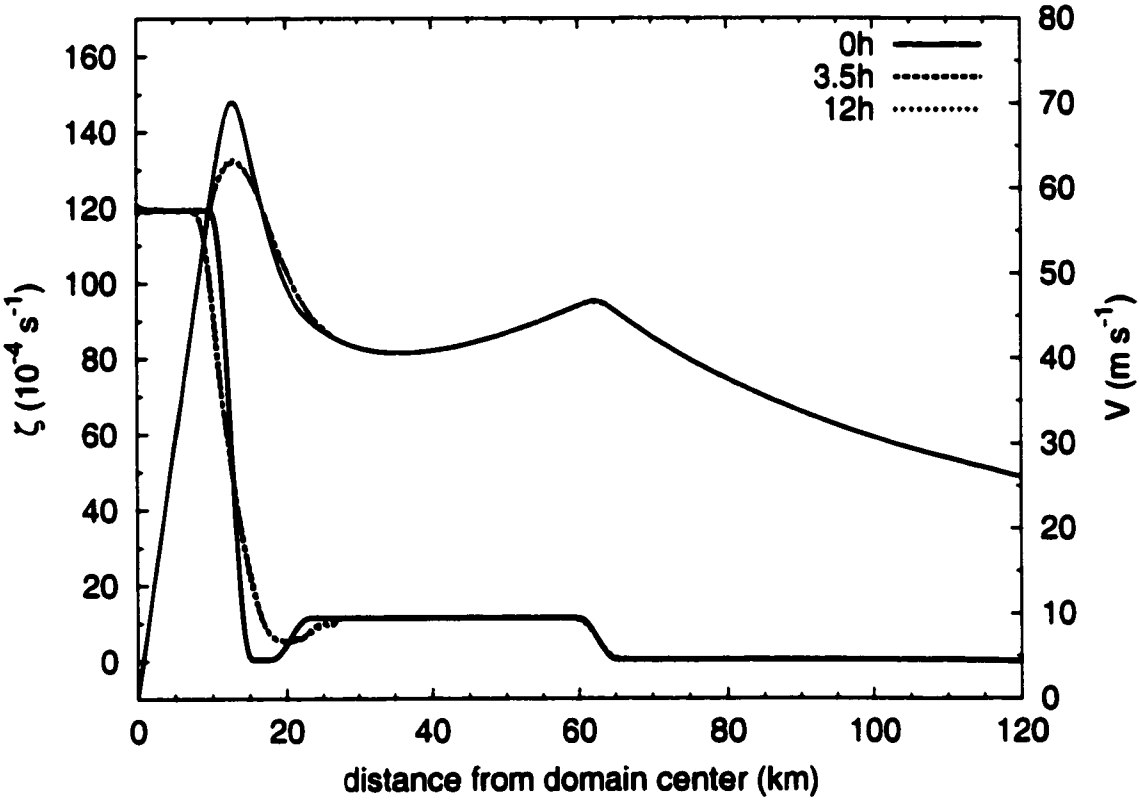

Figure 7.8: Azimuthal mean vorticity and tangential velocity for the experiment shown in Fig. 7.7 at the selected times $t = 0$ (solid), 3.5 h (long dash), and 12 h (short dash).

Reproduced with permission of the copyright owner. Further reproduction prohibited without permission.

Chapter 8

CONCLUDING REMARKS

The relative importance of conservative vorticity dynamics in a mature hurricane, compared with the non-conservative effects of friction and moist convection is an open question. Ideally, the hurricane should be simulated using a progression of numerical models of varying complexity. Working from the nonhydrostatic primitive equations to the nondivergent barotropic model, the implications of each simplification can be measured in terms of the question "what physics remain?", while progressing in the opposite sense, the question "what physics are introduced?" must be addressed. With more complex models, fundamental mechanisms may be obscured by the inclusion of additional but extraneous dynamics. With simpler models, there exists the danger that apparently dominant mechanisms would be completely overshadowed by the inclusion of additional physics. While recognizing the limitations, the present study was confined to the simple framework of the nondivergent barotropic model in an attempt to capture fundamental processes affecting a hurricane's primary and secondary eyewalls.

The dynamic stability of a primary eyewall was considered in the context of a three-region model where it was demonstrated that unstable annular rings of enhanced vorticity evolved to a stable state through nonlinear asymmetric mixing processes. During this transition, coherent structures emerged which bear strong resemblance to mesovortices occasionally observed in intense hurricanes. These coherent structures can transport relatively high (unmixed) vorticity to the vortex center. The

Reproduced with permission of the copyright owner. Further reproduction prohibited without permission.

mixing of enhanced vorticity originally in the annular ring (eyewall) into the central region (eye) caused the tangential wind in the eye to increase while the winds in the eyewall decreased, resulting in a tendency towards solid body rotation. A statistical mechanics approach was introduced which predicts equilibrated flows via solution of a variational problem which maximizes the entropy of the flow. The predictions of this method were shown to be reasonable in the context of unstable primary eyewalls.

Observational evidence was presented, using flight-level data, which demonstrated that during intensification, vorticity profiles tended to be sharply peaked within a hurricane's eyewall while the vorticity in the eye and outside of the eyewall remained relatively weak. When intensification ceased, the vorticity within the eye and eyewall relaxed towards a monotonic profile and coincided with a spin up of the swirling flow, and thus an increase in the angular momentum, throughout the hurricane eye. Our results were found to be generic and did not depend on the external or internal causal factors which brought about the cessation of intensification. Since a typical hurricane evolution includes intensifying and non-intensifying periods, mixing between the eye and eyewall is likely commonplace during its lifetime. Comparisons with numerical results using a nondivergent barotropic model suggest that our simple framework captures much of the relevant physics of this process.

In an attempt to identify a mechanism for subsidence in the eye, a number of studies have considered turbulent exchange between the hurricane eye and eyewall. Malkus (1958) and Kuo (1959) describe an "entrainment hypothesis" where the introduction of higher angular momentum eyewall air into the eye imposes a supergradient flow and thus an outward radial acceleration near the inner eyewall edge. The outward acceleration and resulting divergence is then argued as the mechanism for subsidence in the eye. The existence of such systematic supergradient flow has been the subject of debate (Gray and Shea 1973; Gray 1991; Willoughby 1990, 1991). Two recent and disparate studies by Emanuel (1997) and Willoughby (1998) reconsider the existence and implications of turbulent exchange between the eye and eyewall. Emanuel

Reproduced with permission of the copyright owner. Further reproduction prohibited without permission.

distinguishes between convectively and mechanically induced subsidence and argues that by itself, the former cannot account for an amplification of a hurricane's entropy field. The amplification necessary to achieve realistic intensification rates then must be realized by mechanically induced subsidence driven by turbulent flux of momentum into the eye. Alternatively, Willoughby defines the hurricane eye in terms of two distinct volumes of air separated by an inversion level which is observed to lie between 850 and 500 hPa. The air above the inversion is described as a closed volume in dynamic and thermodynamic isolation while the air below can freely interact with detrained air from the eyewall. Divergence resulting from outward flowing air below the inversion level is argued to drive the subsidence in the eye, while the volume of air above the inversion level remains fixed as its lower levels are pulled downward while the eye diameter decreases. The results of our chapter 4 do not support this hypothesis since the apparent turbulent transfer from the eyewall to the eye is observed to occur throughout the 850–500 hPa layer. It is not clear why turbulent exchange between the eyewall and eye, as discussed in the present study, would preferentially occur below the inversion level and be strongly inhibited above. The inversion level clearly represents a thermodynamic interface, but dynamic distinctions between the two volumes of air are not obvious.

An important question which remains to be answered and was briefly discussed in chapter 4, is whether the exchange between the eyewall and eye is an ongoing or episodic process. Emanuel (1997) suggests a "frontal collapse" theory in which the amplification of the swirling flow within the eyewall is frontogenetic and results in a rapid collapse and turbulent mixing of the inner edge of the eyewall into the eye. This theory would seem to favor the episodic nature of the mixing process but the time scale of this process may be much shorter than the apparent time scale suggested in our present work, that is, it may occur not once, but many times during intensification. If this is the case, the mixing could be better described as an ongoing process.

In chapter 5, we considered the effect of diffusion on an axisymmetric flow and demon-

Reproduced with permission of the copyright owner. Further reproduction prohibited without permission.

strated that in addition to removing unrealistic amounts of kinetic energy from the system, large values of diffusion will relax an initial annular ring of enhanced vorticity towards a monopole. However, the process whereby asymmetric mixing, described in chapter 3, allowed coherent structures to mix high vorticity to the vortex center was not well represented by diffusive processes. Consequently, axisymmetric models which incorporate diffusion to parameterize subgrid scale mixing may underpredict the flux of high angular momentum from the eyewall to the eye.

In order to capture the fundamental interaction between a hurricane's primary eyewall and surrounding regions of enhanced vorticity, a four-region model was introduced to simulate a monopolar central vortex surrounded by a region of low vorticity, or moat, which in turn is surrounded by an annular ring of enhanced vorticity. The moat was found to be a region of intense differential rotation and associated enstrophy cascade where cumulonimbus convection would have difficulty persisting. This offered an additional explanation beyond mesoscale subsidence for the relative absence of deep convection in the moat.

The four-region model provides a basic state which can support two instability types. In the first instability type, phase locking occurs between vortex Rossby waves propagating along the inner and outer edges of the annular ring. The central vortex is dynamically inactive but serves to induce a differential rotation across the ring. This has the effect of stabilizing the ring by opposing its self-induced differential rotation and inhibiting phase locking between the ring edges. In the case where the opposing differential rotation is insufficient to completely stabilize the ring, the vorticity of the ring mixes to form a broader and weaker ring. During this process, the central vortex imposes a barrier to inward mixing and inhibits rearrangement into a monopole. The flow relaxes to a quasi-steady state which satisfies the Fjørtoft sufficient condition for stability while still satisfying the Rayleigh necessary condition for instability. The stability of vorticity profiles associated with concentric eyewalls and secondary wind maxima was addressed by fitting the four-region model to a profile observed

Reproduced with permission of the copyright owner. Further reproduction prohibited without permission.

during a single radial flight leg into Hurricane Gilbert on 14 September 1988. The profile was found to support type 1 instability but relaxation to a quasi-steady state allowed a significant secondary wind maximum to persist. This result may offer insight into the observed longevity of secondary eyewalls. The statistical mechanics (maximum entropy) approach introduced in chapter 3 was found to poorly predict the equilibrated flows associated with type 1 instability. The predicted solution was monotonic (i.e., no secondary ring of enhanced vorticity was maintained) and the central vortex, which was virtually unchanged in the numerical evolution, was reduced considerably through mixing with much lower vorticity from the moat and far field regions. The maximum entropy theory did not recognize the processes by which an intense central vortex is protected from mixing by the differential rotation it induces around itself.

In the second instability type, the outer edge of the annulus had been rendered dynamically inactive by the vortex induced differential rotation, and interaction across the moat between the inner edge of the annular ring and the outer edge of the central vortex took place. This instability was most likely realized in azimuthal wavenumber two and the subsequent mixing resulted in the formation of a tripole. This mechanism offered one explanation for the origin and persistence of elliptical eyewalls, but the existence and significance of type 2 instabilities in tropical cyclones remains an open question. A remarkable aspect of type 2 instability is that a large and intense central vortex can be dramatically perturbed by apparently undramatic features of its near environment. For example, a thin ring of vorticity which is stabilized by its proximity to a hurricane's eyewall can persist but is barely discernable in the wind-field. If the ring strengthens or contracts to yield type 2 instability, the primary eyewall could be significantly rearranged. The observational signature of a tripolar structure would likely be identified by its satellite vortices but the weakness of the vorticity in the satellites would necessitate detailed maps of the hurricane's inner core. In the present state of data aquisition, these high resolution vorticity maps are not yet available.

Reproduced with permission of the copyright owner. Further reproduction prohibited without permission.

Qualitative scrutiny of airborne and land-based Doppler radar reflectivity hints at ongoing asymmetric processes in the inner core of hurricanes, as amplifying wavelike features along the interfaces between high and low reflectivity seem commonplace and mesovortices are sometimes observed. Such observations are limited however, since the lack of scatterers in the eye and moat do not allow for easy identification of features which may exist in the vorticity field but not in the reflectivity field. Thus any occurence of wavebreaking and turbulent exchange from a primary eyewall to the center of the eye or from a secondary eyewall to the moat is purely speculative. Experiments planned for the near future, where reflective material (chaff) is introduced into the inner core, will hopefully provide better insight into the nature of asymmetric mixing processes in the near-core of hurricanes.

Reproduced with permission of the copyright owner. Further reproduction prohibited without permission.

REFERENCES

Andrews, D. G., 1984: On the stability of forced non-zonal flows. *Quart. J. Roy. Meteor. Soc.*, **110**, 657-662.

Black, M. L., and H. E. Willoughby, 1992: The concentric eyewall cycle of Hurricane Gilbert. *Mon. Wea. Rev.*, **120**, 947-957.

Black, P. G., and F. D. Marks, 1991: The structure of an eyewall meso-vortex in Hurricane Hugo (1989). Proceedings of the 19th Conference on Hurricanes and Tropical Meteorology. Amer. Meteor. Soc. 579-582.

Carnevale, G. F., and R. C. Kloosterziel, 1994: Emergence and evolution of triangular vortices. *J. Fluid Mech.*, **259**, 305-331.

Carton, X. J., and B. Legras, 1994: The life-cycle of tripoles in two-dimensional incompressible flows. *J. Fluid Mech.*, **267**, 53-82.

——, G. R. Flierl and L. M. Polvani, 1989: The generation of tripoles from unstable axisymmetric isolated vortex structures. *Europhys. Lett.*, **9**, 339-344.

——, and J. C. McWilliams, 1989: Barotropic and baroclinic instabilities of axisymmetric vortices in a quasi-geostrophic model. In *Mesoscale/Synoptic Coherent Structures in Geophysical Turbulence* (ed. J. C. J. Nihoul and B. M. Jamart), pp. 339-344. Elsevier.

Carr, L. E. III, and R. T. Williams, 1989: Barotropic vortex stability to perturbations from axisymmetry. *J. Atmos. Sci.*, **46**, 3177-3191.

Reproduced with permission of the copyright owner. Further reproduction prohibited without permission.

Challa, M., and R. L. Pfeffer, 1992: The role of environmental asymmetries in Atlantic hurricane formation. *J. Atmos. Sci.*, **49**, 1051–1059.

Charney, J., and A. Eliassen, 1964: On the growth of the hurricane depression. *J. Atmos. Sci.*, **21**, 68–75.

Chavanis, P. H., and J. Sommeria, 1996: Classification of self-organized vortice s in two-dimensional turbulence: the case of a bounded domain. *J. Fluid Mech.*, **314**, 267–297.

Denoix, M.-A., J. Sommeria and A. Thess, 1994: Two-dimensional turbulence: The prediction of coherent structures by statistical mechanics. In *Progress in Turbulence Research* (ed. H. Branover and Y. Unger), pp. 88–107, AIAA.

Dodge, P., R. W. Burpee and F. D. Marks Jr., 1999: The kinematic structure of a hurricane with sea level pressure less than 900 mb. *Mon. Wea. Rev.*, **127**, 987–1004.

Dritschel, D. G., 1989: On the stabilization of a two-dimensional vortex strip by adverse shear. *J. Fluid Mech.*, **206**, 193–221.

——, and D. W. Waugh, 1992: Quantification of the inelastic interaction of unequal vortices in two-dimensional vortex dynamics. *Phys. Fluids A*, **4**, 1737–1744.

——, 1998: On the persistence of non-axisymmetric vortices in inviscid two-dimensional flows. *J. Fluid Mech.*, **371**, 141–155.

Eliassen, A., 1952: Slow thermally or frictionally controlled meridional circulation in a circular vortex. *Astrophys. Norv.*, **5(2)**, 60 pp.

Emanuel, K. A., 1997: Some aspects of hurricane inner-core dynamics and energetics. *J. Atmos. Sci.*, **54**, 1014–1026.

Flierl, G. R., 1988: On the instability of geostrophic vortices. *J. Fluid Mech.*, **197**, 349–388.

Reproduced with permission of the copyright owner. Further reproduction prohibited without permission.

Frank, W. M., 1977: The structure and energetics of the tropical cyclone, Paper I: Storm structure. *Mon. Wea. Rev.*, **105**, 1119–1135.

Gent, P. R., and J. C. McWilliams, 1986: The instability of barotropic circular vortices. *Geophys. Astrophys. Fluid Dyn.*, **35**, 209–233.

Gradshteyn, I. S., and I. M. Ryzhik, 1994: *Table of Integrals, Series, and Products*, 5th Ed. Academic Press, 1204 pp.

Gray, W. M., 1979: Hurricanes: Their formation, structure, and likely role in the tropical circulation. *Meteorology over the tropical oceans*, D. B. Shaw, Ed., Roy. Meteor. Soc., 155–218.

——, and D. J. Shea, 1973: The hurricane's inner core region. II. Thermal stability and dynamic characteristics. *J. Atmos. Sci.*, **30**, 1565–1576.

——, 1991: Comments on "Gradient Balance in Tropical Cyclones". *J. Atmos. Sci.*, **48**, 1201–1208.

Guinn, T. A., and W. H. Schubert, 1993: Hurricane spiral bands. *J. Atmos. Sci.*, **50**, 3380–3403.

Heijst, G. J. F. van, R. C. Kloosterziel and C. W. M. Williams, 1991: Laboratory experiments on the tripolar vortex in a rotating fluid. *J. Fluid Mech.*, **225**, 301–331.

Hidalgo, J. M., 1999: A semi-spectral numerical method for modeling the vorticity dynamics of the near-core region of hurricane-like vortices. M. S. Thesis, Dept. of Atmospheric Science, Colorado State University, 56 pp.

Jorgensen, D. P., 1984: Mesoscale and convective-scale characteristics of mature hurricanes. Part I: General observations by research aircraft. *J. Atmos. Sci.*, **41**, 1268–1285.

Reproduced with permission of the copyright owner. Further reproduction prohibited without permission.

Kloosterziel, R. C., and G. J. F. van Heijst, 1991: An experimental study of unstable barotropic vortices in a rotating fluid. *J. Fluid Mech.*, **223**, 1–24.

Koumoutsakos, P., 1997: Inviscid axisymmetrization of an elliptical vortex. *J. Comp. Phys.*, **138**, 821–857.

Kuo, H.-C., R. T. Williams and J.-H. Chen, 1999: A possible mechanism for the eye rotation of Typhoon Herb. *J. Atmos. Sci.*, **56**, 1659–1673.

Kuo, H.-L., 1959: Dynamics of convective vortices and eye formation. *The Atmosphere and Sea in Motion*, B. Bolin, Ed., Rockefeller Institute Press, 413–424.

Lamb, H., 1932: Hydrodynamics, Sixth Edition, Cambridge University Press, 738 pp.

Larichev, V. D., and G. M. Reznik, 1983: On collisions between two-dimensional solitary Rossby waves. *Oceanology*, **23**, 545–552.

Legras, B., P. Santangelo, and R. Benzi, 1988: High resolution numerical experiments for forced two-dimensional turbulence. *Europhys. Lett.*, **5**, 37–42.

Malkus, J. S., 1958: On the structure and maintenance of the mature hurricane eye. *J. Meteor.*, **15**, 337–349.

MacDonald, N. J., 1968: The evidence for the existence of Rossby-like waves in the hurricane vortex. *Tellus*, **XX**, 138–150.

Matthaeus, W. H., and D. Montgomery, 1980: Selective decay hypothesis at high mechanical and magnetic Reynolds numbers. *Annals New York Academy of Sciences*, **357**, 203–222

Melander, M. V., J. C. McWilliams, and N. J. Zabusky, 1987a: Axisymmetrization and vorticity-gradient intensification of an isolated two-dimensional vortex through filamentation. *J. Fluid Mech.*, **178**, 137–159.

Reproduced with permission of the copyright owner. Further reproduction prohibited without permission.

——, N. J. Zabusky, and J. C. McWilliams, 1987b: Asymmetric vortex merger in two dimensions: Which vortex is "victorious"? *Phys. Fluids*, **30**, 2610–2612.

Miller, J., 1990: Statistical mechanics of Euler equations in two dimensions. *Phys. Rev. Lett.*, **65**, 2137–2140.

——, P. B. Weichman, and M. C. Cross, 1992: Statistical mechanics, Euler's equations, and Jupiter's red spot. *Phys. Rev. A*, **45**, 2328–2359.

Möller, J. D., and R. K. Smith, 1994: The development of potential vorticity in a hurricane-like vortex. *Quart. J. Roy. Meteor. Soc.*, **120**, 1255–1265.

——, and M. T. Montgomery, 1999: Vortex Rossby waves and hurricane intensification in a barotropic model. *J. Atmos. Sci.*, **56**, 1674–1687.

Montgomery, M. T., and J. Enagonio, 1998: Tropical cyclogenesis via convectively forced vortex Rossby waves in a three-dimensional quasigeostrophic model. *J. Atmos. Sci.*, **55**, 3176–3207.

——, and R. J. Kallenbach, 1997: A theory for vortex Rossby-waves and its application to spiral bands and intensity changes in hurricanes. *Quart. J. Roy. Meteor. Soc.*, **123**, 435–465.

——, and L. J. Shapiro, 1995: Generalized Charney-Stern and Fjørtoft theorems for rapidly rotating vortices. *J. Atmos. Sci.*, **52**, 1829–1833.

——, and B. F. Farrell, 1993: Tropical cyclone formation. *J. Atmos. Sci.*, **50**, 285–310.

Nolan, D. S., 1999: Vortex stabilization in deformation fields. Proceedings of the 12^{th} Conference on Atmospheric and Oceanic Fluid Dynamics. Amer. Meteor. Soc. 290–293.

——, and B. F. Farrell, 1999: Generalized stability analyses of asymmetric disturbances in one- and two-celled vortices maintained by radial inflow. *J. Atmos. Sci.*, **56**, 1282–1307.

Reproduced with permission of the copyright owner. Further reproduction prohibited without permission.

OFCM, 1993: National hurricane operations plan. 125 pp. [Available from Office of the Federal Coordinator for Meteorological Services and Supporting Research, Suite 1500, 8455 Colesville Rd., Silver Spring, MD 20910.]

Ooyama, K., 1964: A dynamical model for the study of tropical cyclone development. *Geofis. Int.*, **4**, 187–198.

——, 1969: Numerical simulation of the life cycle of tropical cyclones. *J. Atmos. Sci.*, **26**, 3–40.

Orlandi, P., and G. J. F. van Heijst, 1992: Numerical simulations of tripolar vortices in 2d flow. *Fluid Dyn. Res.*, **9**, 179–206.

Polvani, L. M., and X. J. Carton, 1990: The tripole: A new coherent vortex structure of incompressible two-dimensional flows. *Geophys. Astrophys. Fluid Dynamics*, **51**, 87–102.

Powell, M. D., S. H. Houston, and T. A. Reinhold, 1996: Hurricane Andrew's landfall in South Florida. Part I: Standardizing measurements for documentation of surface wind fields. *Wea. Forecasting*, **11**, 304–328.

Reasor, P. D., M. T. Montgomery, F. D. Marks, and J. F. Gamache, 1999: Low-wavenumber structure and evolution of the hurricane inner core observed by airborne dual-Doppler radar. *Mon. Wea. Rev.*, **127**, in press.

Riehl, H., and J. S. Malkus, 1961: Some aspects of Hurricane Daisy, 1958. *Tellus*, **13**, 181–213.

Robert, R., 1991: A maximum-entropy principle for two-dimensional perfect fluid dynamics. *J. Stat. Phys.*, **65**, 531–551.

——, and J. Sommeria, 1991: Statistical equilibrium states for two-dimens ional flows. *J. Fluid Mech.*, **229**, 291–310.

Reproduced with permission of the copyright owner. Further reproduction prohibited without permission.

——, and J. Sommeria, 1992: Relaxation towards a statistical equilibrium state in two-dimensional perfect fluid dynamics. *Phys. Review Lett.*, **69**, 2776–2779.

Rossi, L. F., J. F. Lingevitch, and A. J. Bernoff, 1997: Quasi-steady monopole and tripole attractors for relaxing vortices. *Phys. Fluids*, **9**, 2329–2338.

Rotunno, R., and K. A. Emanuel, 1987: An air-sea interaction theory for tropical cyclones. Part II: Evolutionary study using a nonhydrostatic axisymmetric numerical model. *J. Atmos. Sci.*, **44**, 542–561.

Samsury, C. E., and E. J. Zipser, 1995: Secondary wind maxima in hurricanes: Airflow and relationship to rainbands. *Mon. Wea. Rev.*, **123**, 3502–3517.

Schubert, W. H., M. T. Montgomery, R. K. Taft, T. A. Guinn, S. R. Fulton, J. P. Kossin and J. P. Edwards, 1999: Polygonal eyewalls, asymmetric eye contraction, and potential vorticity mixing in hurricanes. *J. Atmos. Sci.*, **56**, 1197–1223.

Shapiro, L. J., and H. E. Willoughby, 1982: The response of balanced hurricanes to local sources of heat and momentum. *J. Atmos. Sci.*, **39**, 378–394.

——, and J. L. Franklin, 1999: Potential vorticity asymmetries and tropical cyclone motion. *Mon. Wea. Rev.*, **127**, 124–131.

Smith, G. B., and M. T. Montgomery, 1995: Vortex axisymmetrization: dependence on azimuthal wavenumber or asymmetric radial structure changes. *Quart. J. Roy. Meteor. Soc.*, **121**, 1615–1650.

Sommeria, J., C. Staquet and R. Robert, 1991: Final equilibrium state of a two-dimensional shear layer. *J. Fluid Mech.*, **233**, 661–689.

Sutyrin, G. G., 1989: Azimuthal waves and symmetrization of an intense vortex. *Sov. Phys. Dokl.*, **34**, 104–106.

Reproduced with permission of the copyright owner. Further reproduction prohibited without permission.

Turkington, B., and N. Whitaker, 1996: Statistical equilibrium computations of coherent structures in turbulent shear layers. *SIAM J. Sci. Comput.*, **17**, 1414–1433.

Whitaker, N., and B. Turkington, 1994: Maximum entropy states for rotating vortex patches. *Phys. Fluids*, **6**, 3963–3973.

Willoughby, H. E., J. A. Clos and M. G. Shoreibah, 1982: Concentric eyewalls, secondary wind maxima, and the evolution of the hurricane vortex. *J. Atmos. Sci.*, **39**, 395–411.

——, J. M. Masters and C. W. Landsea, 1989: A record minimum sea level pressure observed in Hurricane Gilbert. *Mon. Wea. Rev.*, **117**, 2824–2828.

——, 1990a: Temporal changes of the primary circulation in tropical cyclones. *J. Atmos. Sci.*, **47**, 242–264.

——, 1990b: Gradient balance in tropical cyclones. *J. Atmos. Sci.*, **47**, 265–274.

——, 1991: Reply to "Comments on Gradient balance in tropical cyclones". *J. Atmos. Sci.*, **48**, 1209–1212.

——, and P. G. Black, 1996: Hurricane Andrew in Florida: dynamics of a disaster. *Bull. Amer. Meteor. Soc.*, **77**, 543–549.

——, 1998: Tropical cyclone eye thermodynamics. *Mon. Wea. Rev.*, **126**, 3053–3067.

Reproduced with permission of the copyright owner. Further reproduction prohibited without permission.

Appendix A

LINEAR STABILITY ANALYSIS OF THE FOUR-REGION MODEL

Consider a circular basic state vortex whose angular velocity $\bar{\omega}(r)$ is a given function of radius r. Using cylindrical coordinates (r, ϕ), assume that the small amplitude perturbations of the streamfunction, $\psi'(r, \phi, t)$, are governed by the linearized barotropic nondivergent vorticity equation

$$\left(\frac{\partial}{\partial t} + \bar{\omega}\frac{\partial}{\partial \phi}\right)\nabla^2\psi' - \frac{\partial \psi'}{r\partial\phi}\frac{d\bar{\zeta}}{dr} = 0, \tag{A.1}$$

where $\bar{\zeta}(r) = d(r^2\bar{\omega})/rdr$ is the basic state relative vorticity, $(u', v') = (-\partial\psi'/r\partial\phi, \partial\psi'/\partial r)$ the perturbation radial and tangential components of velocity, and $\partial(rv')/r\partial r - \partial u'/r\partial\phi = \nabla^2\psi'$ the perturbation vorticity. Searching for modal solutions of the form $\psi'(r, \phi, t) = \hat{\psi}(r)e^{i(m\phi - \nu t)}$, where m is the azimuthal wavenumber and ν the complex frequency, we obtain from (A.1) the radial structure equation

$$(\nu - m\bar{\omega})\left[r\frac{d}{dr}\left(r\frac{d\hat{\psi}}{dr}\right) - m^2\hat{\psi}\right] + mr\frac{d\bar{\zeta}}{dr}\hat{\psi} = 0. \tag{A.2}$$

A useful idealization of an annular region of vorticity surrounding a central vortex is the piecewise constant four region model. In this model the axisymmetric basic state angular velocity $\bar{\omega}(r)$ is given by

$$\bar{\omega}(r) = \tfrac{1}{2}\begin{cases} \zeta_1 & 0 \le r \le r_1, \\ \zeta_2 - (\zeta_2 - \zeta_1)(r_1/r)^2 & r_1 \le r \le r_2, \\ \zeta_3 - (\zeta_2 - \zeta_1)(r_1/r)^2 - (\zeta_3 - \zeta_2)(r_2/r)^2 & r_2 \le r \le r_3, \\ \quad -(\zeta_2 - \zeta_1)(r_1/r)^2 - (\zeta_3 - \zeta_2)(r_2/r)^2 + \zeta_3(r_3/r)^2 & r_3 \le r < \infty, \end{cases} \tag{A.3}$$

Reproduced with permission of the copyright owner. Further reproduction prohibited without permission.

and the corresponding basic state relative vorticity by

$$\bar{\zeta}(r) = \frac{d(r^2\bar{\omega})}{rdr} = \begin{cases} \zeta_1 & 0 < r < r_1, \\ \zeta_2 & r_1 < r < r_2, \\ \zeta_3 & r_2 < r < r_3, \\ 0 & r_3 < r < \infty, \end{cases} \tag{A.4}$$

where r_1, r_2, r_3 are specified radii and $\zeta_1, \zeta_2, \zeta_3$ are specified vorticity levels.

Restricting study to the class of perturbations whose disturbance vorticity arises solely through radial displacement of the basic state vorticity, then the perturbation vorticity vanishes everywhere except near the edges of the constant vorticity regions, i.e., (A.1) reduces to $\nabla^2\psi' = 0$ for $r \neq r_1, r_2, r_3$, or equivalently, (A.2) reduces to

$$r\frac{d}{dr}\left(r\frac{d\hat{\psi}}{dr}\right) - m^2\hat{\psi} = 0 \qquad \text{for} \qquad r \neq r_1, r_2, r_3. \tag{A.5}$$

The general solution of (A.5) in the four regions separated by the radii r_1, r_2, r_3 can be constructed from different linear combinations of r^m and r^{-m} in each region. A physically revealing approach is to write the general solution of (A.5), valid in any of the four regions, as a linear combination of the basis functions $B_1^{(m)}(r)$, $B_2^{(m)}(r)$ and $B_3^{(m)}(r)$, defined by

$$B_1^{(m)}(r) = \begin{cases} (r/r_1)^m & 0 \leq r \leq r_1, \\ (r_1/r)^m & r_1 \leq r < \infty, \end{cases} \tag{A.6a}$$

$$B_2^{(m)}(r) = \begin{cases} (r/r_2)^m & 0 \leq r \leq r_2, \\ (r_2/r)^m & r_2 \leq r < \infty. \end{cases} \tag{A.6b}$$

$$B_3^{(m)}(r) = \begin{cases} (r/r_3)^m & 0 \leq r \leq r_3, \\ (r_3/r)^m & r_3 \leq r < \infty. \end{cases} \tag{A.6c}$$

The solution for $\hat{\psi}(r)$ is then

$$\hat{\psi}(r) = \Psi_1 B_1^{(m)}(r) + \Psi_2 B_2^{(m)}(r) + \Psi_3 B_3^{(m)}(r), \tag{A.7}$$

where Ψ_1, Ψ_2 and Ψ_3 are complex constants. Since $dB_1^{(m)}/dr$ is discontinuous at $r = r_1$, the solution associated with the constant Ψ_1 has vorticity anomalies concentrated at $r = r_1$ and the corresponding streamfunction decays away in both directions from $r = r_1$. Similarly, the solutions associated with the constants Ψ_2 and Ψ_3 have vorticity anomalies concentrated at $r = r_2$ and $r = r_3$, respectively.

Reproduced with permission of the copyright owner. Further reproduction prohibited without permission.

In order to relate Ψ_1, Ψ_2, Ψ_3, let us now integrate (A.2) over the narrow radial intervals centered at r_1, r_2, r_3 to obtain the jump (pressure continuity) conditions

$$\lim_{\epsilon \to 0} \left\{ (\nu - m\bar{\omega}_1) r_1 \left[\frac{d\hat{\psi}}{dr} \right]_{r_1-\epsilon}^{r_1+\epsilon} \right\} + (\zeta_2 - \zeta_1) m\hat{\psi}(r_1) = 0, \tag{A.8a}$$

$$\lim_{\epsilon \to 0} \left\{ (\nu - m\bar{\omega}_2) r_2 \left[\frac{d\hat{\psi}}{dr} \right]_{r_2-\epsilon}^{r_2+\epsilon} \right\} + (\zeta_3 - \zeta_2) m\hat{\psi}(r_2) = 0, \tag{A.8b}$$

$$\lim_{\epsilon \to 0} \left\{ (\nu - m\bar{\omega}_3) r_3 \left[\frac{d\hat{\psi}}{dr} \right]_{r_2-\epsilon}^{r_2+\epsilon} \right\} - \zeta_3 m\hat{\psi}(r_3) = 0, \tag{A.8c}$$

where $\bar{\omega}_1 = \bar{\omega}(r_1)$, $\bar{\omega}_2 = \bar{\omega}(r_2)$, and $\bar{\omega}_3 = \bar{\omega}(r_3)$. Substituting the solution (A.7) into the jump conditions (A.8) yields the matrix eigenvalue problem

$$\begin{pmatrix} m\bar{\omega}_1 + \frac{1}{2}(\zeta_2 - \zeta_1) & \frac{1}{2}(\zeta_2 - \zeta_1)(r_1/r_2)^m & \frac{1}{2}(\zeta_2 - \zeta_1)(r_1/r_3)^m \\ \frac{1}{2}(\zeta_3 - \zeta_2)(r_1/r_2)^m & m\bar{\omega}_2 + \frac{1}{2}(\zeta_3 - \zeta_2) & \frac{1}{2}(\zeta_3 - \zeta_2)(r_2/r_3)^m \\ -\frac{1}{2}\zeta_3 (r_1/r_3)^m & -\frac{1}{2}\zeta_3 (r_2/r_3)^m & m\bar{\omega}_3 - \frac{1}{2}\zeta_3 \end{pmatrix} \begin{pmatrix} \Psi_1 \\ \Psi_2 \\ \Psi_3 \end{pmatrix} = \nu \begin{pmatrix} \Psi_1 \\ \Psi_2 \\ \Psi_3 \end{pmatrix}. \tag{A.9}$$

Noting that for the basic state given by (A.3), $\bar{\omega}_1 = \frac{1}{2}\zeta_1$, $\bar{\omega}_2 = \frac{1}{2}[\zeta_2 - (\zeta_2 - \zeta_1)(r_1/r_2)^2]$ and $\bar{\omega}_3 = \frac{1}{2}[\zeta_3 - (\zeta_2 - \zeta_1)(r_1/r_3)^2 - (\zeta_3 - \zeta_2)(r_2/r_3)^2]$, we can solve the eigenvalue problem (A.9) once we have specified the parameters $m, r_1, r_2, r_3, \zeta_1, \zeta_2, \zeta_3$.

As an example, consider a four-region basic state described with the choice of parameters, $\{r_1, r_2, r_3\} = \{9.5, 52.5, 62.5\}$ km and $\{\zeta_1, \zeta_2, \zeta_3, \zeta_4\} = \{160, 6, 28, 3, 0\} \times 10^{-4}\ \mathrm{s}^{-1}$, which describes a small and intense central vortex surrounded by a secondary ring of enhanced vorticity. Applying (A.9) we find that this basic state is unstable in wavenumbers 7–10 with the maximum growth occuring in wavenumber 9. For comparison, we also consider a continuous analogue, which is similar to the profile shown by the thin solid line of Fig. 6.7a in chapter 6, and apply an eigensolver to it. The results of the linear analyses for the piecewise uniform and smooth basic states are shown in Fig. A.1 and demonstrate good agreement, particularly in the prediction of the wavenumber of maximum growth.

We can gain further insight into instabilities supported by the four-region model by reducing the number of adjustable parameters in (A.9). Assuming $\zeta_2 = 0$, then

Reproduced with permission of the copyright owner. Further reproduction prohibited without permission.

dividing the first row of (A.9) by $\frac{1}{2}\zeta_1$ and the second and third rows by $\frac{1}{2}\zeta_3$, we obtain

$$\begin{vmatrix} 1-m+2\left(\frac{\zeta_1}{\zeta_3}\right)^{-1}\left(\frac{\nu}{\zeta_3}\right) & \left(\frac{r_1}{r_2}\right)^m & \left(\frac{r_1}{r_3}\right)^m \\ \left(\frac{r_1}{r_2}\right)^m & 1+m\left(\frac{\zeta_1}{\zeta_3}\right)\left(\frac{r_1}{r_2}\right)^2-2\left(\frac{\nu}{\zeta_3}\right) & \left(\frac{r_2}{r_3}\right)^m \\ \left(\frac{r_1}{r_3}\right)^m & \left(\frac{r_2}{r_3}\right)^m & 1-m\left[1+\left(\frac{\zeta_1}{\zeta_3}\right)\left(\frac{r_1}{r_3}\right)^2-\left(\frac{r_2}{r_3}\right)^2\right]+2\left(\frac{\nu}{\zeta_3}\right) \end{vmatrix} = 0. \tag{A.10}$$

For given r_1/r_2, r_2/r_3 and ζ_1/ζ_3, the determinant (A.10) yields three values of the dimensionless frequency ν/ζ_3. Choosing the most unstable of these three roots, Fig. A.2 shows isolines of the imaginary part of ν/ζ_3 as a function of r_1/r_2 and r_2/r_3 for the case $\zeta_1/\zeta_3 = 5.7$. For this value of ζ_1/ζ_3, there are two distinct types of instability. Type 1 occurs for azimuthal wavenumbers $m = 3, 4, 5, \ldots$ when r_1 is small compared to r_2 and when r_2 is nearly as large as r_3 (the annular ring of elevated vorticity is narrow). Type 1 instability involves the interaction of vorticity waves at r_2 and r_3, i.e., across the ring of elevated vorticity. Type 2 instability occurs for azimuthal wavenumbers $m = 2, 3, 4, \ldots$ when r_1 is nearly as large as r_2 (the moat is narrow). Type 2 instability involves the interaction of vorticity waves at r_1 and r_2, i.e., across the moat.

Although the two types of instability are well-separated when $\zeta_1/\zeta_3 = 5.7$ (and larger), they begin to overlap in the central part of the diagram as ζ_1/ζ_3 decreases to approximately 2. Type 1 instability is discussed in chapter 6 and type 2 instability in chapter 7.

The analysis presented here is an extension of previous work by Dritschel (1989) and Carton and Legras (1994). Dritschel considered the thin-strip limit $r_2 - r_1 \gg r_3 - r_2$ where instabilities across the ring strongly dominate instabilities across the moat. The region of Fig. A.2 which is pertinent in this limit is restricted to the upper-left corner and in this case, instabilities which serve as a precursor to tripole formation are suppressed. Carton and Legras considered the special case of the four-region model applied to shielded monopoles. They present solutions to the eigenvalue problem

Reproduced with permission of the copyright owner. Further reproduction prohibited without permission.

(A.10) where the vorticity of the ring is restricted to be negative and given by $\zeta_3 = -\zeta_1[r_1^2/(r_3^2 - r_2^2)]$.

Reproduced with permission of the copyright owner. Further reproduction prohibited without permission.

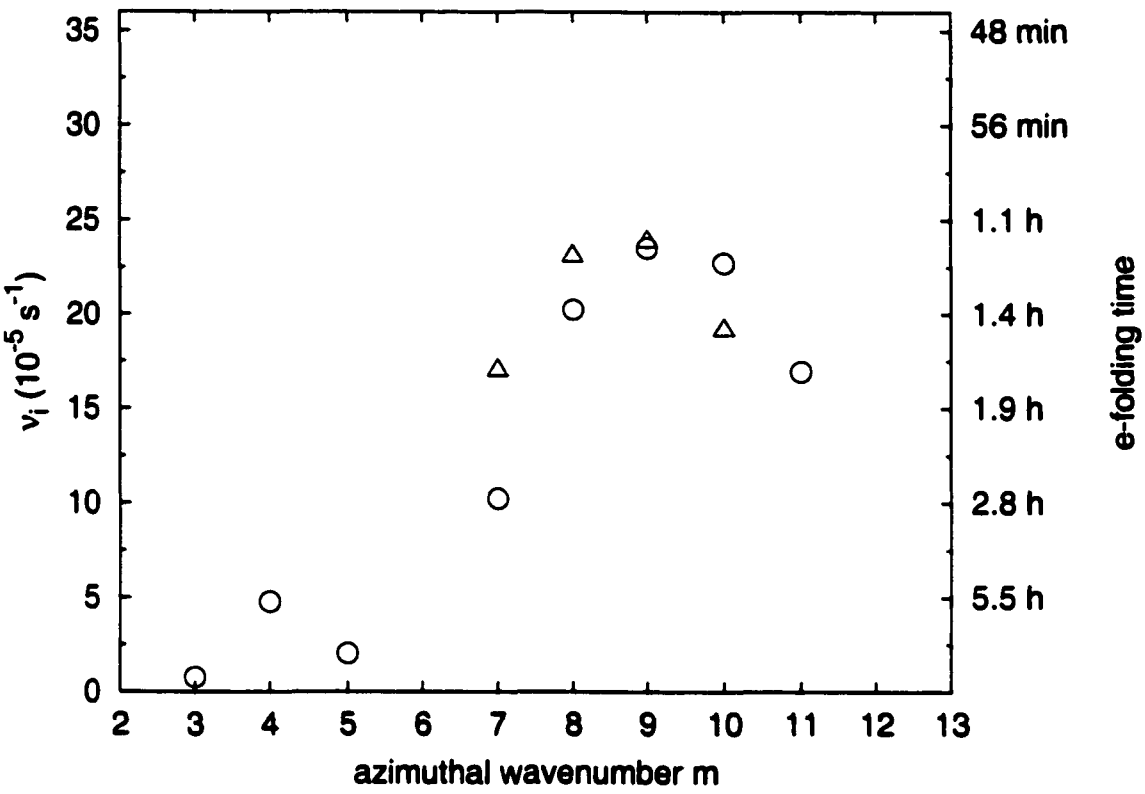

Figure A.1: Linear analysis predictions of instability growth rates and e–folding times. The triangles display the results using (A.9) and the circles show the results based on an analogous continuous basic state.

Reproduced with permission of the copyright owner. Further reproduction prohibited without permission.

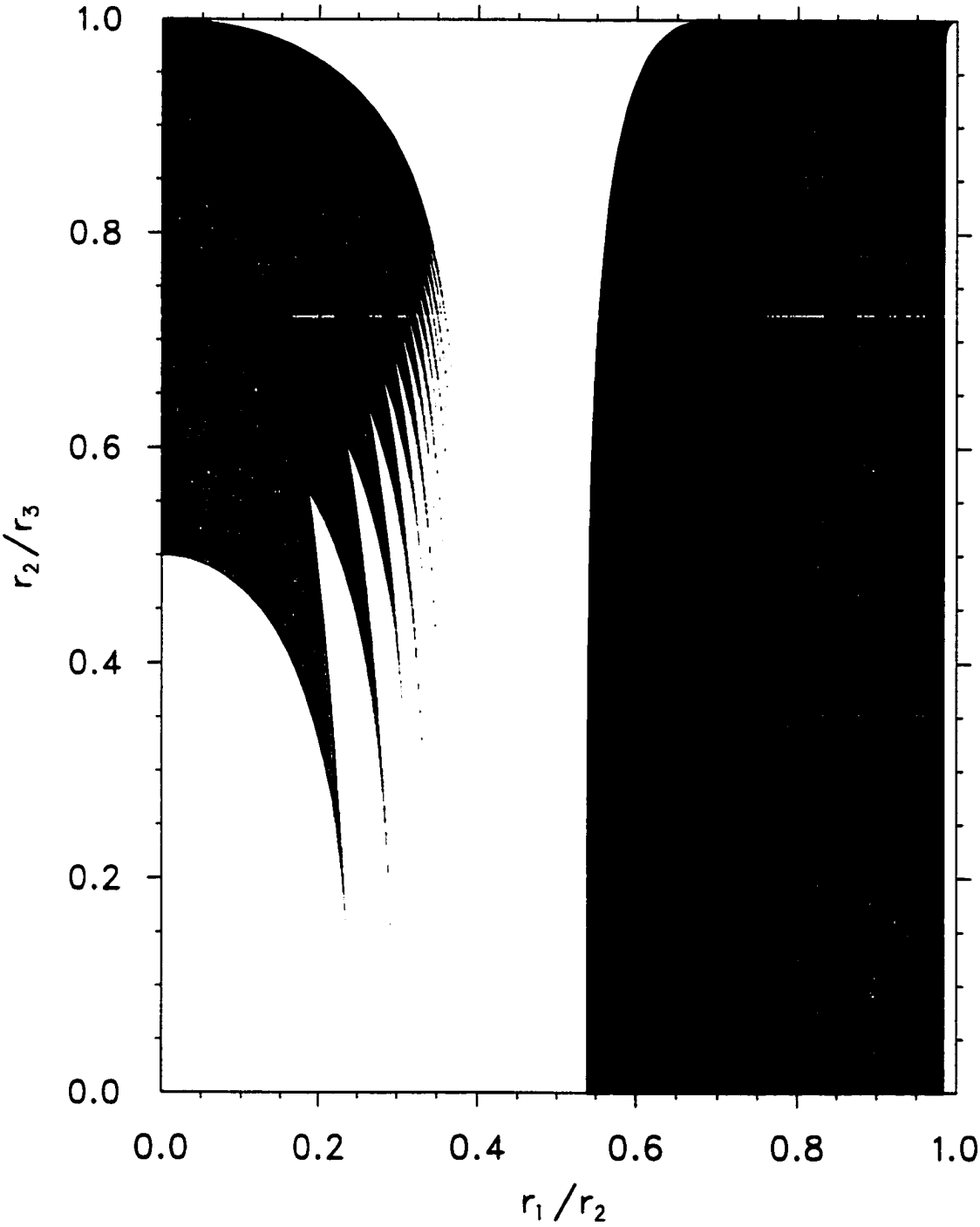

Figure A.2: Isolines of the maximum value of the dimensionless growth rate ν_i/ζ_3, computed from Eq. (A.10), as a function of r_1/r_2 and r_2/r_3 for the case $\zeta_1/\zeta_3 = 5.7$ and for azimuthal wavenumbers up to $m = 16$. Type 1 instability (for $m = 3, 4, \ldots, 16$) occurs on the left side of the diagram and type 2 instability (for $m = 2, 3, \ldots, 16$) occurs on the right side. The azimuthal wavenumber associated with the most unstable mode is indicated by the alternating grey scales. The white region is stable, and the isolines are $\nu_i/\zeta_3 = 0.01, 0.03, 0.05, \ldots$.

Reproduced with permission of the copyright owner. Further reproduction prohibited without permission.

Appendix B

NONDIVERGENT BAROTROPIC MODEL

To isolate the barotropic aspects of the nonlinear evolution, we consider the nondivergent barotropic model with spectral discretization and ordinary diffusion. Expressing the velocity components[7] in terms of the streamfunction by $u = -\partial\psi/\partial y$ and $v = \partial\psi/\partial x$, we can write the vorticity equation as

$$\frac{\partial\zeta}{\partial t} + \frac{\partial(\psi,\zeta)}{\partial(x,y)} = \nu\nabla^2\zeta, \tag{B.1}$$

where

$$\nabla^2\psi = \zeta \tag{B.2}$$

is the invertibility principle. Two integral properties associated with (B.1) and (B.2) on a closed or periodic domain are the energy and enstrophy relations

$$\frac{d\mathcal{E}}{dt} = -2\nu\mathcal{Z}, \tag{B.3}$$

$$\frac{d\mathcal{Z}}{dt} = -2\nu\mathcal{P}, \tag{B.4}$$

where $\mathcal{E} = \iint \frac{1}{2}\nabla\psi\cdot\nabla\psi\,dxdy$ is the energy, $\mathcal{Z} = \iint \frac{1}{2}\zeta^2\,dxdy$ is the enstrophy, and $\mathcal{P} = \iint \frac{1}{2}\nabla\zeta\cdot\nabla\zeta\,dxdy$ is the palinstrophy. The diffusion term on the right hand side of (B.1) controls the spectral blocking associated with the enstrophy cascade to higher wavenumbers.

[7]Throughout this work the symbols u, v are used to denote eastward and northward components of velocity when working in Cartesian coordinates and to denote radial and tangential components when working in cylindrical coordinates.

Reproduced with permission of the copyright owner. Further reproduction prohibited without permission.

B.1 Pseudospectral model

All of the solutions presented in this work were obtained with a double Fourier pseudospectral code having $n \times n$ equally spaced collocation points on a doubly periodic Cartesian domain of size L km $\times L$ km. The code was run with a dealiased calculation of the quadratic nonlinear terms in (B.1). This results in $n/3 \times n/3$ resolved Fourier modes. Although the collocation points are only L/n km apart, a more realistic estimate of resolution is the wavelength of the highest Fourier mode, which is $3L/n$ km. Time differencing was accomplished with a standard 4^{th} order Runge-Kutta scheme. The time step and the value of ν was chosen according to each particular initial condition, the former in accordance with the Courant-Friedrichs-Lewy condition for stability, and the latter in a less formal manner depending on the palinstrophy evolution. In cases where the palinstrophy production is large, a larger value of ν was used in order to minimize the appearance of spurious vorticity caused by Gibb's phenomena. A description of the chosen model parameters for each experiment is shown in Table B.1, where individual experiments are identified by the figure number in which they are displayed.

B.2 Initial conditions

As the initial condition for (B.1), we use $\zeta(r,\phi,0) = \bar{\zeta}(r) + \zeta'(r,\phi)$ where $\bar{\zeta}(r)$ is an axisymmetric vorticity field and $\zeta'(r,\phi)$ is some small perturbation. For the three-region type experiment of chapter 3, we use

$$\bar{\zeta}(r) = \begin{cases} \zeta_1, & 0 \le r \le r_1 - d_1 \\ \zeta_1 S\left((r - r_1 + d_1)/2d_1\right) + \zeta_2 S\left((r_1 + d_1 - r)/2d_1\right), & r_1 - d_1 \le r \le r_1 + d_1 \\ \zeta_2, & r_1 + d_1 \le r \le r_2 - d_2 \\ \zeta_2 S\left((r - r_2 + d_2)/2d_2\right) + \zeta_3 S\left((r_2 + d_2 - r)/2d_2\right), & r_2 - d_2 \le r \le r_2 + d_2 \\ \zeta_3, & r_2 + d_2 \le r \end{cases} \tag{B.5}$$

where $r_1, r_2, d_1, d_2, \zeta_1$, and ζ_2 are independently specified quantities. The constant ζ_3 will be determined in order to make the domain average of $\zeta(r,\phi,0)$ vanish. Here

Reproduced with permission of the copyright owner. Further reproduction prohibited without permission.

$S(s) = 1 - 3s^2 + 2s^3$ is the basic cubic Hermite shape function satisfying $S(0) = 1$, $S(1) = 0$, $S'(0) = S'(1) = 0$.

For the four-region type of experiments of chapters 6 and 7 (excluding the experiments using shielded vortices in 7.1), we use

$$\bar{\zeta}(r) = \begin{cases} \zeta_1, & 0 \le r \le r_1 - d_1 \\ \zeta_1 S\left((r - r_1 + d_1)/2d_1\right) + \zeta_2 S\left((r_1 + d_1 - r)/2d_1\right), & r_1 - d_1 \le r \le r_1 + d_1 \\ \zeta_2, & r_1 + d_1 \le r \le r_2 - d_2 \\ \zeta_2 S\left((r - r_2 + d_2)/2d_2\right) + \zeta_3 S\left((r_2 + d_2 - r)/2d_2\right), & r_2 - d_2 \le r \le r_2 + d_2 \\ \zeta_3, & r_2 + d_2 \le r \le r_3 - d_3 \\ \zeta_3 S\left((r - r_3 + d_3)/2d_3\right) + \zeta_4 S\left((r_3 + d_3 - r)/2d_3\right), & r_3 - d_3 \le r \le r_3 + d_3 \\ \zeta_4, & r_3 + d_3 \le r \le r_4 - d_4 \\ \zeta_4 S\left((r - r_4 + d_4)/2d_4\right) + \zeta_5 S\left((r_4 + d_4 - r)/2d_4\right), & r_4 - d_4 \le r \le r_4 + d_4 \\ \zeta_5, & r_4 + d_4 \le r \end{cases} \tag{B.6}$$

where $r_1, r_2, r_3, r_4, d_1, d_2, d_3, d_4, \zeta_1, \zeta_2, \zeta_3$, and ζ_4 are independently specified quantities. In this case, the constant ζ_5 will be determined in order to make the domain average of $\zeta(r, \phi, 0)$ vanish. Since ζ_5 must generally be weakly negative to satisfy the zero circulation requirement, but no negative vorticity is expected in the region of hurricanes, we apply a small but positive 'far field' vorticity ζ_4 to a radius beyond the area of expected mixing processes.

In all experiments (except those of section 7.1), we apply an azimuthally broad-banded perturbation across some annular region $r_j - d_j \le r \le r_{j+1} + d_{j+1}$, that is

$$\zeta'(r, \phi) = \zeta_{\text{amp}} \sum_{m=1}^{12} \cos(m\phi) \begin{cases} 0, & 0 \le r \le r_j - d_j \\ S\left((r_j + d_j - r)/2d_j\right), & r_j - d_j \le r \le r_j + d_j \\ 1, & r_j + d_j \le r \le r_{j+1} - d_{j+1} \\ S\left((r - r_{j+1} + d_{j+1})/2d_{j+1}\right), & r_{j+1} - d_{j+1} \le r \le r_{j+1} + d_{j+1} \\ 0, & r_{j+1} + d_{j+1} \le r \end{cases} \tag{B.7}$$

where ζ_{amp} is a specified constant less than 1% of the maximum vorticity in the annulus. The index j specifies which annular region of $\bar{\zeta}(r)$ has $\zeta'(r, \phi)$ applied to it. For the experiment of chapter 3, we use $j = 1$ which specifies the primary eyewall, chapter 6 uses $j = 2$ which specifies the secondary eyewall, and chapter 7 uses $j = 1$ which specifies the moat.

Reproduced with permission of the copyright owner. Further reproduction prohibited without permission.

For the shielded vortex experiments of section 7.1, the initial condition $\bar{\zeta}(r)$ is given by Eq. (7.3) and an initial perturbation of proportional (1%) random noise is imposed across the moat.

Reproduced with permission of the copyright owner. Further reproduction prohibited without permission.

Table B.1: Model execution parameters in relation to figure number where the experiment is shown.

Figure	n	L (km)	Max Mode Kept	Resolution (km)	Δt (s)	ν (m^2 s^{-1})
3.6	512	200	170	1.18	5	15
6.6	1024	600	340	1.76	7.5	4
6.8	1024	600	340	1.76	15	32
7.2	1024	600	340	1.76	15	25
7.3	1024	600	340	1.76	15	25
7.5	1024	600	340	1.76	7.5	5
7.7	1024	600	340	1.76	7.5	8

Reproduced with permission of the copyright owner. Further reproduction prohibited without permission.

Appendix C

TURKINGTON AND WHITAKER (1996) ALGORITHM

Turkington and Whitaker (1996) have developed an iterative algorithm in order to solve the variational problem:

Maximize

$$S[\rho_1(r,\phi),\ldots,\rho_L(r,\phi)] = -\int_0^a \int_0^{2\pi} \left(\sum_{\ell=1}^{L} \rho_\ell(r,\phi) \ln \rho_\ell(r,\phi) \right) r dr d\phi,$$

subject to the constraints

$$\int_0^a \int_0^{2\pi} \rho_\ell(r,\phi) r dr d\phi = \mathcal{A}_\ell, \qquad \ell = 1,2,\ldots,L,$$

$$-\tfrac{1}{2} \int_0^a \int_0^{2\pi} \psi \left(\sum_{\ell=1}^{L} \hat{\zeta}_\ell \rho_\ell \right) r dr d\phi = \mathcal{E},$$

and

$$\int_0^a \int_0^{2\pi} r^2 \left(\sum_{\ell=1}^{L} \hat{\zeta}_\ell \rho_\ell \right) r dr d\phi = \mathcal{I},$$

where

$$\rho_\ell(r,\phi) = Z^{-1} \exp[-\alpha_\ell + \hat{\zeta}_\ell(\beta\psi - \gamma r^2)],$$

$$Z = \sum_{\ell=1}^{L} \exp[-\alpha_\ell + \hat{\zeta}_\ell(\beta\psi - \gamma r^2)],$$

and

$$\nabla^2\psi = Z^{-1} \sum_{\ell=1}^{L} \hat{\zeta}_\ell \exp[-\alpha_\ell + \hat{\zeta}_\ell(\beta\psi - \gamma r^2)].$$

The iterative step generates $\rho_\ell^{(k+1)}(r,\phi)$ from $\rho_\ell^{(k)}(r,\phi)$ by solving the constrained optimization subproblem:

Reproduced with permission of the copyright owner. Further reproduction prohibited without permission.

Maximize

$$S[\rho_1^{(k+1)}(r,\phi),\ldots,\rho_L^{(k+1)}(r,\phi)] = -\int_0^a \int_0^{2\pi} \sum_{\ell=1}^{L} \left[\rho_\ell^{(k+1)}(r,\phi)\ln\rho_\ell^{(k+1)}(r,\phi)\right] r dr d\phi, \tag{C.1}$$

subject to the constraints

$$\int_0^a \int_0^{2\pi} \rho_\ell^{(k+1)}(r,\phi) r dr d\phi = \mathcal{A}_\ell, \qquad \ell = 1,2,\ldots,L \tag{C.2}$$

$$\int_0^a \int_0^{2\pi} r^2 \left(\sum_{\ell=1}^{L} \hat{\zeta}_\ell \rho_\ell^{(k+1)}\right) r dr d\phi = \mathcal{I}, \tag{C.3}$$

and

$$-\tfrac{1}{2}\int_0^a \int_0^{2\pi} \psi^{(k)} \left(\sum_{\ell=1}^{L} \hat{\zeta}_\ell \rho_\ell^{(k+1)}\right) r dr d\phi = \tfrac{1}{2}\left[\mathcal{E} - \tfrac{1}{2}\int_0^a \int_0^{2\pi} \psi^{(k)} \left(\sum_{\ell=1}^{L} \hat{\zeta}_\ell \rho_\ell^{(k)}\right)\right] r dr d\phi. \tag{C.4}$$

Introducing the Lagrange multipliers $\alpha_\ell^{(k+1)}$, $\beta^{(k+1)}$, $\gamma^{(k+1)}$, the variational problem is

$$\begin{aligned} 0 \;=\; & \int_0^a \int_0^{2\pi} \sum_{\ell=1}^{L} \Big\{ \Big[-1 - \ln\rho_\ell^{(k+1)} - \alpha_\ell^{(k+1)} + \\ & \hat{\zeta}_\ell \left(\beta^{(k+1)}\psi^{(k)} - \gamma^{(k+1)} r^2\right)\Big] \delta\rho_\ell^{(k+1)} \Big\} r dr d\phi. \end{aligned} \tag{C.5}$$

For arbitrary variations $\delta\rho_\ell^{(k+1)}$ we obtain

$$1 + \ln\rho_\ell^{(k+1)} = -\alpha_\ell^{(k+1)} + \hat{\zeta}_\ell \left(\beta^{(k+1)}\psi^{(k)} - \gamma^{(k+1)} r^2\right). \tag{C.6}$$

Imposing the normalization condition

$$\sum_{\ell=1}^{L} \rho_\ell^{(k+1)}(r,\phi) = 1,$$

at every point (r,ϕ), (C.6) can be written as

$$\rho_\ell^{(k+1)}(r,\phi) = \frac{1}{Z^{(k+1)}} \exp\left[-\alpha_\ell^{(k+1)} + \hat{\zeta}_\ell \left(\beta^{(k+1)}\psi^{(k)} - \gamma^{(k+1)} r^2\right)\right], \tag{C.7}$$

where

$$Z^{(k+1)} = \sum_{\ell=1}^{L} \exp\left[-\alpha_\ell^{(k+1)} + \hat{\zeta}_\ell \left(\beta^{(k+1)}\psi^{(k)} - \gamma^{(k+1)} r^2\right)\right]. \tag{C.8}$$

Reproduced with permission of the copyright owner. Further reproduction prohibited without permission.

The invertibility principle is

$$\begin{aligned}\zeta^{(k+1)}(r,\phi) &= \sum_{\ell=1}^{L} \hat{\zeta}_\ell \rho_\ell^{(k+1)}(r,\phi) \\ &= \nabla^2 \psi^{(k+1)}. \end{aligned} \tag{C.9}$$

Substituting (C.7) and (C.8) into (C.9) we have

$$\begin{aligned}&\frac{\partial^2 \psi^{(k+1)}}{\partial r^2} + \frac{\partial \psi^{(k+1)}}{r \partial r} + \frac{\partial^2 \psi^{(k+1)}}{r^2 \partial \phi^2} = \\ &\left\{ \sum_{\ell=1}^{L} \exp\left[-\alpha_\ell^{(k+1)} + \hat{\zeta}_\ell \left(\beta^{(k+1)} \psi^{(k)} - \gamma^{(k+1)} r^2 \right) \right] \right\}^{-1} \times \\ &\sum_{\ell=1}^{L} \hat{\zeta}_\ell \exp\left[-\alpha_\ell^{(k+1)} + \hat{\zeta}_\ell \left(\beta^{(k+1)} \psi^{(k)} - \gamma^{(k+1)} r^2 \right) \right]. \end{aligned} \tag{C.10}$$

Note that (C.10) is now a *linear* partial differential equation for $\psi^{(k+1)}$ since $\psi^{(k)}$ is known from the previous iteration.

The equations for $\alpha_\ell^{(k+1)}$, $\beta^{(k+1)}$, and $\gamma^{(k+1)}$ are obtained by enforcing the constraints (C.2)–(C.4) which, after using (C.7), may be written as

$$\int_0^a \int_0^{2\pi} \frac{1}{Z^{(k+1)}} \exp\left[-\alpha_\ell^{(k+1)} + \hat{\zeta}_\ell \left(\beta^{(k+1)} \psi^{(k)} - \gamma^{(k+1)} r^2 \right) \right] r dr d\phi = \mathcal{A}_\ell, \tag{C.11}$$

$$\int_0^a \int_0^{2\pi} r^2 \frac{1}{Z^{(k+1)}} \left(\sum_{\ell=1}^{L} \hat{\zeta}_\ell \exp\left[-\alpha_\ell^{(k+1)} + \hat{\zeta}_\ell \left(\beta^{(k+1)} \psi^{(k)} - \gamma^{(k+1)} r^2 \right) \right] \right) r dr d\phi = \mathcal{I}, \tag{C.12}$$

and

$$\begin{aligned}&\tfrac{1}{2} \left[\mathcal{E} - \tfrac{1}{2} \int_0^a \int_0^{2\pi} \psi^{(k)} \frac{1}{Z^{(k)}} \left(\sum_{\ell=1}^{L} \hat{\zeta}_\ell \exp\left[-\alpha_\ell^{(k)} + \hat{\zeta}_\ell \left(\beta^{(k)} \psi^{(k)} - \gamma^{(k)} r^2 \right) \right] \right) r dr d\phi \right] = \\ &-\tfrac{1}{2} \int_0^a \int_0^{2\pi} \psi^{(k)} \frac{1}{Z^{(k+1)}} \left(\sum_{\ell=1}^{L} \hat{\zeta}_\ell \exp\left[-\alpha_\ell^{(k+1)} + \hat{\zeta}_\ell \left(\beta^{(k+1)} \psi^{(k)} - \gamma^{(k+1)} r^2 \right) \right] \right) r dr d\phi. \end{aligned} \tag{C.13}$$

Given an initial vorticity field $\zeta^{(0)}(r,\phi)$, the iteration proceeds as follows:

Reproduced with permission of the copyright owner. Further reproduction prohibited without permission.

1. Invert the initial vorticity to obtain the initial streamfunction $\psi^{(0)}(r, \phi)$. For the solutions presented in this work, this was performed at each iteration using a fast elliptic solver within a disk with Dirichlet boundary conditions. The solver is part of the FISHPACK software package developed by John Adams, Paul Swarztrauber, and Roland Sweet.

2. Calculate $\mathcal{A}_\ell$, $\mathcal{I}$, and $\mathcal{E}$.

3. Solve the $(L+2) \times (L+2)$ system (C.11)–(C.13) for $\alpha_\ell^{(k+1)}$, $\beta^{(k+1)}$, and $\gamma^{(k+1)}$. At the first iteration, $k = 0$.

4. With $\alpha_\ell^{(k+1)}$, $\beta^{(k+1)}$, $\gamma^{(k+1)}$, and $\psi^{(k)}$ in hand, use (C.7) to obtain the probability functions $\rho_\ell^{(k+1)}$.

5. Use (C.9) to obtain $\zeta^{(k+1)}$ from $\rho_\ell^{(k+1)}$ and start again at step 1. The iteration is stopped when the energy calculated at the current iteration is within some specified tolerance from the initial energy.

Reproduced with permission of the copyright owner. Further reproduction prohibited without permission.